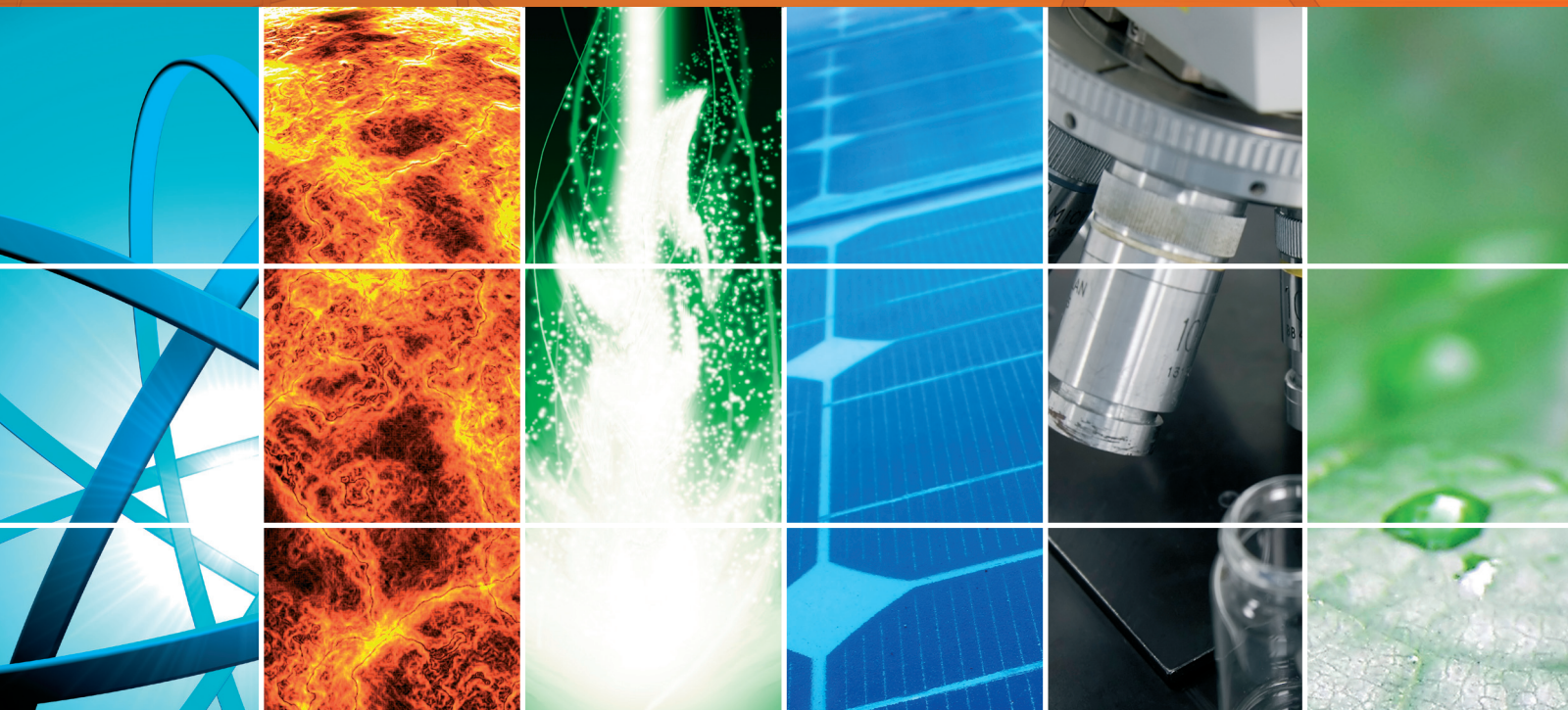


TiO₂ Photocatalytic Materials 2013

Guest Editors: Jiaguo Yu, Mietek Jaroniec, Gongxuan Lu,
Christos Trapalis, and Gang Liu





TiO₂ Photocatalytic Materials 2013

International Journal of Photoenergy

TiO₂ Photocatalytic Materials 2013

Guest Editors: Jiaguo Yu, Mietek Jaroniec, Gongxuan Lu,
Christos Trapalis, and Gang Liu



Copyright © 2013 Hindawi Publishing Corporation. All rights reserved.

This is a special issue published in "International Journal of Photoenergy." All articles are open access articles distributed under the Creative Commons Attribution License, which permits unrestricted use, distribution, and reproduction in any medium, provided the original work is properly cited.

Editorial Board

M. Sabry Abdel-Mottaleb, Egypt
Nihal Ahmad, USA
Nicolas Alonso-Vante, France
Wayne A. Anderson, USA
Vincenzo Augugliaro, Italy
Detlef W. Bahnemann, Germany
Mohammad A. Behnajady, Iran
Ignazio Renato Bellobono, Italy
Raghu N. Bhattacharya, USA
Pramod H. Borse, India
Gion Calzaferri, Switzerland
Adriana G. Casas, Argentina
Wonyong Choi, Korea
Vra Cimrova, Czech Republic
Vikram Dalal, USA
D. (Dion) D. Dionysiou, USA
Mahmoud M. El-Nahass, Egypt
Ahmed Ennaoui, Germany
Chris Ferekides, USA
Beverley Glass, Australia
M. A. Gondal, Saudi Arabia
Shinya Higashimoto, Japan
Chun-Sheng Jiang, USA

Yadong Jiang, China
Shahed Khan, USA
Cooper Harold Langford, Canada
Yuexiang Li, China
Stefan Lis, Poland
N. Mohammad Mahmoodi, Iran
Dionissios Mantzavinos, Greece
Ugo Mazzucato, Italy
Jacek Miller, Poland
Jarugu N. Moorthy, India
Franca Morazzoni, Italy
Fabrice Morlet-Savary, France
Ebinazar B. Namdas, Australia
Maria da Graça P. Neves, Portugal
Leonidas Palilis, Greece
Leonardo Palmisano, Italy
Ravindra K. Pandey, USA
David Lee Phillips, Hong Kong
Pierre Pichat, France
Gianluca Li Puma, UK
Xie Quan, China
Tijana Rajh, USA
Peter Robertson, UK

Avigdor Scherz, Israel
Lukas Schmidt-Mende, Germany
Panagiotis Smirniotis, USA
Zofia Stasicka, Poland
Juliusz Sworakowski, Poland
Nobuyuki Tamaoki, Japan
Gopal N. Tiwari, India
Nikolai V. Tkachenko, Finland
Veronica Vaida, USA
Roel van De Krol, Germany
Mark van Der Auweraer, Belgium
Ezequiel Wolcan, Argentina
Man Shing Wong, Hong Kong
David Worrall, UK
Fahrettin Yakuphanoglu, Turkey
Minjoong Yoon, Korea
Hongtao Yu, USA
Jimmy C. Yu, Hong Kong
Jun-Ho Yum, Switzerland
Klaas Zachariasse, Germany
Lizhi Zhang, China
Jincai Zhao, China

Contents

TiO₂ Photocatalytic Materials 2013, Jiaguo Yu, Mietek Jaroniec, Gongxuan Lu, Christos Trapalis, and Gang Liu
Volume 2013, Article ID 534164, 2 pages

Dyes Degradation with Fe-Doped Titanium Nanotube Photocatalysts Prepared from Spent Steel Slag, Chih Ming Ma, Yu Jung Lin, Ren Wei Shiue, and Chang Tang Chang
Volume 2013, Article ID 350698, 7 pages

Photocatalytic Degradation of 2,4-Dichlorophenol Using Nanosized Na₂Ti₆O₁₃/TiO₂ Heterostructure Particles, Zicong Jian, Shaobin Huang, and Yongqing Zhang
Volume 2013, Article ID 606291, 7 pages

Nanocrystalline N-Doped TiO₂ Powders: Mild Hydrothermal Synthesis and Photocatalytic Degradation of Phenol under Visible Light Irradiation, Junna Xu, Feng Wang, Wenxiu Liu, and Wenbin Cao
Volume 2013, Article ID 616139, 7 pages

Photoelectrocatalytic Performance of Benzoic Acid on TiO₂ Nanotube Array Electrodes, Hongchong Chen, Jinhua Li, Quanpeng Chen, Di Li, and Baoxue Zhou
Volume 2013, Article ID 567426, 7 pages

Fabrication and Photocatalytic Property of One-Dimensional SrTiO₃/TiO_{2-x}N_x Nanostructures, Huarong Zhang, Miao Guashuai, Ma Xingping, and Wang Bei
Volume 2013, Article ID 413507, 6 pages


Characterization and Photocatalytic Activity of TiO₂ Nanotube Films Prepared by Anodization, Wen-Yu Wang and Bo-Ruei Chen
Volume 2013, Article ID 348171, 12 pages

The Synergistic Effect of Nitrogen Dopant and Calcination Temperature on the Visible-Light-Induced Photoactivity of N-Doped TiO₂, Yao-Tung Lin, Chih-Huang Weng, Hui-Jan Hsu, Yu-Hao Lin, and Ching-Chang Shiesh
Volume 2013, Article ID 268723, 13 pages

Synthesis, Characterization, and Photocatalysis of Well-Dispersible Phase-Pure Anatase TiO₂ Nanoparticles, Xiuzhen Wei, Guangfeng Zhu, Jinfeng Fang, and Jinyuan Chen
Volume 2013, Article ID 726872, 6 pages

Photocatalytic Degradation of Methyl Violet with TiSiW₁₂O₄₀/TiO₂, Shuijin Yang, Yulin Xu, Yongkui Huang, Guohui Zhou, Zhiyuan Yang, Yun Yang, and Guohong Wang
Volume 2013, Article ID 191340, 5 pages

Physicochemical Study of Photocatalytic Activity of TiO₂ Supported Palygorskite Clay Mineral, Lahcen Bouna, Benaissa Rhouta, and Francis Maury
Volume 2013, Article ID 815473, 6 pages



Synthesis of Nanostructured Anatase Mesoporous Membranes with Photocatalytic and Separation Capabilities for Water Ultrafiltration Process, Vahideh Tajer-Kajinebaf, Hossein Sarpoolaky, and Toraj Mohammadi

Volume 2013, Article ID 509023, 11 pages

Correlation of Photocatalysis and Photoluminescence Effect in Relation to the Surface Properties of $\text{TiO}_2\text{:Tb}$ Thin Films, Damian Wojcieszak, Danuta Kaczmarek, Jaroslaw Domaradzki, and Michal Mazur

Volume 2013, Article ID 526140, 9 pages

Release of Volatile Compounds from Polymeric Microcapsules Mediated by Photocatalytic Nanoparticles, J. Marques, L. F. Oliveira, R. T. Pinto, P. J. G. Coutinho, P. Parpot, J. R. Góis, J. F. J. Coelho, F. D. Magalhães, and C. J. Tavares

Volume 2013, Article ID 712603, 9 pages

The Photocatalytic Property of Nitrogen-Doped TiO_2 Nanoball Film, Haiying Wang and Yanchun Hu

Volume 2013, Article ID 179427, 6 pages

Editorial

TiO₂ Photocatalytic Materials 2013

Jiaguo Yu,¹ Mietek Jaroniec,² Gongxuan Lu,³ Christos Trapalis,⁴ and Gang Liu⁵

¹ State Key Laboratory of Advanced Technology for Material Synthesis and Processing, Wuhan University of Technology, Luoshi Road 122, Wuhan 430070, China

² Department of Chemistry, Kent State University, Kent, OH 44242, USA

³ State Key Laboratory for Oxo Synthesis and Selective Oxidation, Lanzhou Institute of Chemical Physics, Chinese Academy of Sciences, Lanzhou 730000, China

⁴ Institute of Materials Science, National Centre for Scientific Research "Demokritos," Agia Paraskevi, Attikis, Greece

⁵ National Center for Nanoscience and Technology, 11 Zhongguancun Beiyitiao, Beijing 100190, China

Correspondence should be addressed to Jiaguo Yu; jiaguoyu@yahoo.com

Received 23 October 2013; Accepted 23 October 2013

Copyright © 2013 Jiaguo Yu et al. This is an open access article distributed under the Creative Commons Attribution License, which permits unrestricted use, distribution, and reproduction in any medium, provided the original work is properly cited.

Semiconductor photocatalysis has been intensively studied in recent years and has been shown to be an effective method for solving the serious environmental pollution and energy shortage problems. Among various semiconductor photocatalysts, titania has attracted more and more attention because of its biological and chemical inertness, strong oxidation and reduction power, and long-term stability against photocorrosion. However, the high recombination rate of the photoinduced electron-hole pairs and narrow light-response range for TiO₂ significantly reduces its photocatalytic performance. To enhance the photocatalytic performance of TiO₂, some modification methods including doping, noble metal deposition, surface sensitization, and coupling of two semiconductors have been proposed.

This special issue contains 14 papers, which are mainly related to pollutant decomposition and environmental purification. Among them, 5 papers are about doping of TiO₂, 3 papers deal with the composite of two semiconductors, 3 papers are devoted to TiO₂ nanoparticles, 2 papers focus on TiO₂ nanotube array films, and 1 paper is related to mesoporous membranes. A brief summary of all fourteen accepted papers is provided below.

In "*The photocatalytic property of nitrogen-doped TiO₂ nanoball film*," the authors describe the fabrication and photocatalytic performance of N-doped TiO₂ nanoball film by anodic oxidation method. The results indicate that N-doping greatly enhances visible light absorption of TiO₂ and

reduces nanoball diameter. N-doped TiO₂ nanoball films exhibit a stronger photocatalytic activity than pure TiO₂ films.

The paper "*photocatalytic degradation of methyl violet with TiSiW₁₂O₄₀/TiO₂*" reports the photocatalytic degradation of methyl violet using TiSiW₁₂O₄₀/TiO₂ as a novel ecofriendly catalyst under simulated natural light irradiation. The results demonstrate that at optimal conditions, the degradation rate of methyl violet is as high as 82.4% after 3 h simulated natural light irradiation. The photocatalytic reaction of methyl violet can be expressed as first-order kinetic model.

The paper "*The synergistic effect of nitrogen dopant and calcination temperature on the visible light-induced photoactivity of N-doped TiO₂*" presents the synergistic effect of nitrogen content and calcination temperatures on the photocatalytic performance of TiO₂ catalysts prepared by solgel method. The results indicate that N-doping enhances the visible light photocatalytic activity of TiO₂. N-dopant retards the anatase to rutile phase transformation. Nitrogen atoms are incorporated into the interstitial positions of the TiO₂ lattice. The N-doped TiO₂ catalyst prepared with ammonia to titanium isopropoxide molar ratio of 2.0 and calcined at 400°C shows the best photocatalytic activity.

The paper "*Characterization and photocatalytic activity of TiO₂ nanotube films prepared by anodization*" describes fabrication of TiO₂ nanotube (TNT) array films by anodization

method in NH_4F electrolyte solution. Photocatalytic decomposition of methylene blue indicates that the reaction rate constants by TNT films are higher than P-25 films at comparable thickness. Reaction rate constants by TNT films increase with increasing film thickness, but the enhancement is retarded when the length of TNT reaches 2200 nm due to the limited penetration of incident UV light.

The paper “*Dyes degradation with Fe-doped titanium nanotube photocatalysts prepared from spend steel slag*” reports fabrication of the TiO_2 nanotube (TNT) and Fe-doped TNT photocatalysts. The decolorizing efficiency decreases with increasing initial MB concentration, and a higher efficiency is observed under UV-light illumination. However, excessive Fe loading reduces the efficiency, and 1.13 wt% Fe loading is found to be the optimal addition.

The paper “*Fabrication and photocatalytic property of one-dimensional $\text{SrTiO}_3/\text{TiO}_{2-x}\text{N}_x$ nanostructures*” describes preparation and photocatalytic performance of one-dimensional $\text{SrTiO}_3/\text{TiO}_{2-x}\text{N}_x$ nanostructures by the hydrothermal method. As compared with the $\text{TiO}_{2-x}\text{N}_x$ nanoparticles, the absorption performance of $\text{SrTiO}_3/\text{titanate}$ nanotubes or $\text{SrTiO}_3/\text{TiO}_{2-x}\text{N}_x$ nanorods is depressed. The $\text{SrTiO}_3/\text{TiO}_{2-x}\text{N}_x$ nanorods present better photocatalytic activity than the $\text{TiO}_{2-x}\text{N}_x$ nanoparticles or nanorods.

In “*Synthesis of nanostructured anatase mesoporous membranes with photocatalytic and separation capabilities for water ultrafiltration process*,” the mesoporous anatase membranes are fabricated for water ultrafiltration (UF) process with photocatalytic and physical separation capabilities. Photocatalytic activity of the membranes is evaluated by the photodegradation of methyl orange. The anatase membranes exhibit good homogeneity, with the surface area of $32.8 \text{ m}^2/\text{g}$, the mean pore size of 8.17 nm, and the crystallite size of 9.6 nm. The methyl orange removal efficiencies by the mesoporous membrane based on physical separation and coupling photocatalytic technique are 52 and 83%, respectively.

In “*Correlation of photocatalysis and photoluminescence effect in relation to the surface properties of $\text{TiO}_2:\text{Tb}$ thin films*,” the structural, optical, photoluminescence, and photocatalytic properties of TiO_2 and $\text{TiO}_2:(2.6 \text{ at. \% Tb})$ thin films are investigated and compared. Optical properties measurements indicate that the incorporation of Tb into TiO_2 matrix does not change significantly the thin films transparency. The incorporation of 2.6 at. % Tb increases the photocatalytic activity more than two times as compared to undoped TiO_2 .

The paper “*photoelectrocatalytic performance of benzoic acid on TiO_2 nanotube array electrodes*” reports the adsorption, degradation rate, and reaction characteristics of benzoic acid degradation by analyzing the changes in the photogenerated $I-t$ profiles. This work will provide new insights into the degradation characteristics, reaction mechanism, and reaction kinetics of aromatic organic compounds on the TNA electrode surface.

The paper “*Photocatalytic degradation of 2,4-dichlorophenol using nanosized $\text{Na}_2\text{Ti}_6\text{O}_{13}/\text{TiO}_2$ heterostructure particles*” reports preparation of $\text{Na}_2\text{Ti}_6\text{O}_{13}/\text{TiO}_2$ composite particles by a reverse microemulsion method. The photocatalytic activity of the samples is evaluated by degradation of

2,4-dichlorophenol (2,4-DCP) under 40 W ultraviolet lamp irradiation. The results show that the synthesized nanobelts $\text{Na}_2\text{Ti}_6\text{O}_{13}/\text{TiO}_2$ heterostructures have typical width from 80 to 100 nm, thickness less than 40 nm, and length up to $5 \mu\text{m}$. Such $\text{Na}_2\text{Ti}_6\text{O}_{13}/\text{TiO}_2$ composite particles exhibit better photocatalytic activity than P25- TiO_2 .

In “*Nanocrystalline N-doped TiO_2 powders: mild hydrothermal synthesis and photocatalytic degradation of phenol under visible light irradiation*,” N-doped TiO_2 powders are prepared using technical guanidine hydrochloride, titanyl sulfate, and urea as precursors by hydrothermal method. The UV-visible absorption spectra show that the absorption edge of the N-doped TiO_2 powders red shifts into the visible light region.

In “*Release of volatile compounds from polymeric microcapsules mediated by photocatalytic nanoparticles*,” a suitable method is proposed for the solar-activated controlled release of volatile compounds from polymeric microcapsules bonded with photocatalytic nanoparticles. These reservoirs can find potential application including controlled release of insecticides, repellents, or fragrances. The surface of the microcapsules is functionalized with TiO_2 nanoparticles. Upon ultraviolet irradiation, redox mechanisms are initiated on the semiconductor surface, resulting in the dissociation of the polymer chains of the capsule wall and, finally, volatilization of the encapsulated compounds.

In “*Synthesis, characterization, and photocatalysis of well-dispersible phase-pure anatase TiO_2 nanoparticles*,” high-purity anatase TiO_2 nanoparticles are fabricated by an improved sol-hydrothermal method. The photocatalytic performance of TiO_2 nanoparticles is evaluated by using photocatalytic degradation of X-3B and X-BR solutions. The results indicate that the as-prepared TiO_2 exhibits higher photocatalytic activity than P25. Also, the as-synthesized TiO_2 can settle down and be separated easily after the photocatalytic reaction.

The paper “*Physicochemical study of photocatalytic activity of TiO_2 supported palygorskite clay mineral*” reports the influence of physicochemical parameters, namely, the photocatalyst loading, dye concentration, and pH of polluted solutions on the degradation efficiency of Orange G (OG) solutions in the presence of clay mineral containing TiO_2 .

Acknowledgment

We wish to express our sincere thanks to all the authors for submitting interesting contributions to this special issue.

Jianguo Yu
Mietek Jaroniec
Gongxuan Lu
Christos Trapalis
Gang Liu

Research Article

Dyes Degradation with Fe-Doped Titanium Nanotube Photocatalysts Prepared from Spent Steel Slag

Chih Ming Ma,¹ Yu Jung Lin,² Ren Wei Shiue,² and Chang Tang Chang²

¹ Department of Cosmetic Application and Management, St. Mary's Medicine Nursing and Management College, Number 100, Lane 265, Section 2, Sansing Road, Sansing Township, Yilan County 266, Taiwan

² Department of Environmental Engineering, National I-Lan University, Number 1, Section 1, Shen-Lung Road, Ilan 260, Taiwan

Correspondence should be addressed to Chang Tang Chang; ctchang@niu.edu.tw

Received 22 January 2013; Revised 20 April 2013; Accepted 23 April 2013

Academic Editor: Jiaguo Yu

Copyright © 2013 Chih Ming Ma et al. This is an open access article distributed under the Creative Commons Attribution License, which permits unrestricted use, distribution, and reproduction in any medium, provided the original work is properly cited.

TiO₂ has been studied most commonly because it has high stability, nontoxicity, high catalytic activity, and high conductivity. Many studies have shown that TiO₂ would generate electron-hole pairs illuminated with UV and surround more energy than that before being illuminated. In this study, the titanium nanotube (TNT) photocatalysts were prepared to increase the surface area and adsorption capacity. The Fe TNT was also prepared from a slag iron since many slag irons cause waste treatment problems. In this study, a different Fe loading was also assessed since TNT doped with metals can be used to improve the degradation efficiency. Furthermore, five kinds of dye concentration, including 10, 20, 100, 200, and 400 ppm, and five kinds of Fe-doped content, including 0, 0.77, 1.13, 2.24, and 4.50%, were tested. Different kinds of reaction time and dye species were also assessed. In this result, Direct Black 22 was the most difficult to be degraded, although the concentration was decreased or the dose amount was increased. The degradation efficiency of 10 ppm Direct Black 22 was below 40% with 0.04 gL⁻¹ TNT under 365 nm UV irradiation.

1. Introduction

About 15% of the total world production of dyes is lost during textile dyeing when dyes are released as textile effluents [1]. Dyes are widely used in the textile industry and cause polluted water. The disposal of this colored wastewater into the environment leads to many ecological problems as well as diminished natural aesthetics [2]. How to efficiently solve this urgent environmental issue has become a challenging and indispensable topic of modern research.

The traditional methods for treating dye wastewater include adsorption, coagulation, and biological treatment, but they do not have good performance [3]. In contrast, photocatalytic degradation is considered to be an efficient and economical alternative for controlling dye wastewater. Currently, several new photocatalysts, most impregnated with metal oxide and composite metal oxide semiconductors have been used to overcome the drawbacks of TiO₂, which has low surface area and adsorption capacity [4]. The photocatalysts commonly used are TiO₂, ZnO, WO₃, CdS, ZnS, SrTiO₃, and Fe₂O₃, with TiO₂ being frequently reported as the most

active in organic degradation experiments [5]. For example, in suitable irradiation sunlight, using titanium dioxide can decrease costs significantly [6]. Photocatalysts have several obvious advantages in technique, including cleaner air, an extraction stream, and carbon adsorption. In these processes, oxygens occur OH[•] hit, and a rate constant is higher than the oxidation of a normal state ten billion times. Ultraviolet irradiation can be obtained from sunlight or a simulated light source.

The photocatalytic activity of the S-TiO₂ photocatalyst at 400°C for the photodegradation of L-acid is better than that of pure TiO₂ [7]. A novel In³⁺-doped TiO₂ and TiO₂/In₂S₃ nanocomposites for photocatalytic degradation of environmental pollutants and stoichiometric degradation of warfare agents is prepared using homogeneous hydrolysis with urea and thioacetamide [8]. Through high-energy ball-milling technique, the nanostructured (20 nm) TiO₂ photocatalysts with different quantities of Cr doping were synthesized for 3 hours [9]. Early studies primarily focused on TiO₂-based photocatalysts, though TiO₂ only responds

to ultraviolet (UV) irradiation, which accounts for only about 4% of all solar energies which greatly hinders wider application [10].

In our experiment, TiO_2 was chosen for modification into TNT (titanium nanotube) because it shows relatively high chemical stability, exhibits high activity for photocatalysis, and is relatively inexpensive [11]. This study used hydrothermal methods to modify the titanium dioxide into TNT. The largest difference is in the structure and surface area. The former is a spherical particle with a surface area of $50 \text{ m}^2 \text{ g}^{-1}$. The latter is a mesoporous tube shape with a surface area of roughly $400 \text{ m}^2 \text{ g}^{-1}$. The surface area, closely related to adsorption efficiency, is about eight times that of TiO_2 manufactured using the hydrothermal method [12]. Further, TNT can simultaneously generate photodegradation and adsorption in wastewater. TNT has vast pore structures and large surface areas owing to its unique tubular nanostructure [13]. This mesoporous catalyst is suitable for treating high dye concentrations in wastewater.

In this study, TNT was doped with different Fe contents to increase its absorption visible light. The Fe was extracted from slag iron in steel plant to reuse the iron. The aim of this study was to investigate the performance of TNT and Fe TNT for methyl blue (MB), Direct Blue (DB22), and Reactive Black (RBK5) removal using a photocatalytic reaction. In particular, factors such as doped Fe content, light source, initial dye concentrations, and dye species were assessed to establish the optimum operating conditions. Furthermore, the reaction kinetics analysis was also investigated in this study.

2. Materials and Methods

2.1. Preparation of TNT. Commercial TiO_2 (P25) nanoparticles (5 g) were mixed in an aqueous 10 M NaOH solution and charged into a Teflon-lined autoclave. The autoclave was then oven-heated at 135°C for 3 days. The precipitate was filtered, and the pH value of the slurry was adjusted with a diluted 0.1 M HNO_3 by washing. The final products were obtained by filtration with subsequent drying at 100°C overnight. Finally, the TNT samples were obtained through calcination at the temperatures of 400°C .

2.2. Preparation of Fe TNT by Photodeposition. An appropriate amount of TNT suspension solution was weighed in a Pyrex glass container and then purged with nitrogen for 2 h to remove any dissolved oxygen (DO) from the solution. Then an appropriate amount of Fe solution was weighed and mixed with 10 mL methanol and dissolved in TNT solution. Photodeposition was performed for 12 h under a continuous nitrogen purge using a 254-nm ultraviolet light. Once the Fe-TNT suspension solution was formed, the subsequent clearing was applied using methods similar to those used with the TNT photocatalyst.

2.3. Characterization of TNT and Fe TNT. A UV spectrometer (Hitachi, U-3900) was applied to analyze the reflectance spectra of TNT samples, ranging from 200 nm

to 800 nm in wavelength. High-resolution transmission electron microscopy (HR-TEM, JEOL, EM2100 High Resolution TEM) was used for morphological observations of the TNT. Specifically, surface areas and pore volumes of the derived nanotubes were determined by N_2 adsorption/desorption isotherm (Micromeritics, BET ASAP 2020N).

2.4. The Performance Assessment of TNT and Fe TNT. The photocatalytic degradation of MB, DB22, and RBK5 for initial concentrations (10, 20, 100, 200, and 400 ppm), Fe-doped content (0, 0.77, 1.13, 2.24, and 4.50%) and light source (254 nm UV, 365 nm UV, 380 nm, and 490 nm) was determined by means of UV-Vis spectrophotometer analysis through indication of color disappearance. A calibration curve of methyl blue solution was obtained at 600 nm wavelength in order to correlate the concentration of MB at different reaction times by converting the absorbance of the sample to MB concentration. During the reaction time the solutions were centrifuged at 300 rpm to mix the dye well.

2.5. Kinetics Analysis. Pseudo-first-order reaction kinetics is the most commonly used kinetic expression to explain the kinetics of the heterogeneous catalytic processes. The Pseudo-first-order expression that explains the kinetics of heterogeneous catalytic systems is given by (1) [14]

$$r = -\frac{dC}{dt} = \frac{K_r KC}{1 + KC}, \quad (1)$$

where K_r is the reaction rate constant ($\text{mol dm}^{-3} \text{ min}^{-1}$), K is the adsorption coefficient of the reactant on catalyst (mol dm^{-3}) $^{-1}$, and C is the concentration of the solute (ppm or mg L^{-1}).

Pseudo-first-order expression reduces to first-order equation when C is small:

$$-\ln\left(\frac{C}{C_0}\right) = k_1 t, \quad (2)$$

where $k_1 = K_r K$.

Yielding half-life, $t_{1/2}$ (min) can be calculated as below (Habibi et al., 2005) [15]:

$$t_{1/2} = \frac{0.693}{k_1}. \quad (3)$$

3. Results and Discussion

3.1. UV-Visible Spectrum. In order to determine the photo absorbance properties, the commercial Fe TNT and TNT were analyzed by UV-Vis for wavelengths of 200–800 nm. The band gap (E , eV) of the six samples was calculated by (4) [16] as follows:

$$E = \frac{1240}{\lambda}, \quad (4)$$

where λ is the wavelength of UV absorption thresholds.

After calculation, P25, TNT (0% Fe TNT), and 1.13% Fe TNT had band gaps of 3.20, 3.10, and 2.7 eV, respectively,

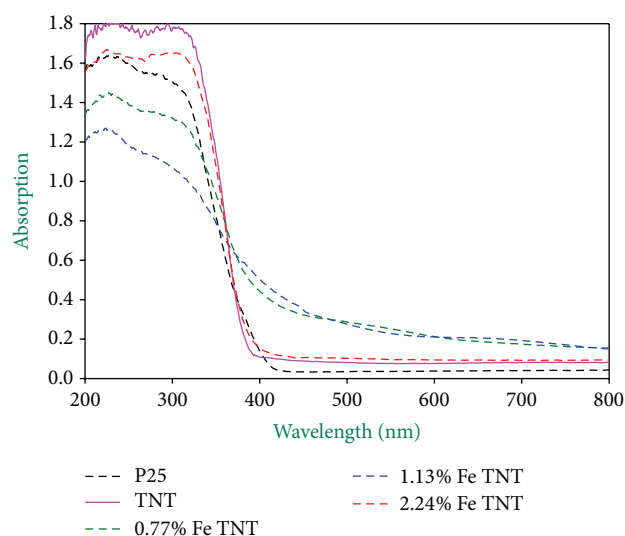


FIGURE 1: The UV absorption of P25 and Fe-doped TNT.

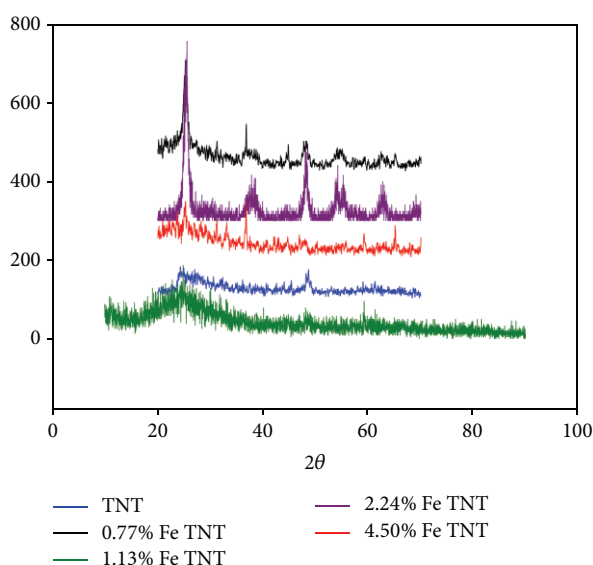


FIGURE 2: XRD spectra of the different Fe-doping catalyst.

as shown in Figure 1. The results showed that less energy was needed for reacting with pollutants with the 1.13% Fe TNT. It was found that the Fe-doped TiO_2 can get higher photocatalytic activity with visible light than that of P25. The differences between photocatalytic activity of different Fe-doped TiO_2 and pure TiO_2 were illustrated in Figure 7 and described later.

The TNT surface can be blocked with increasing the Fe content. It causes the surface of Fe TNT and band gap to decrease because the amount of Fe increases with increasing red shift.

X-ray diffraction was used to identify the Fe-TNT structures and compositions, as shown in Figure 2. From JCPDS-ICDD database, Fe particle was identified with five root

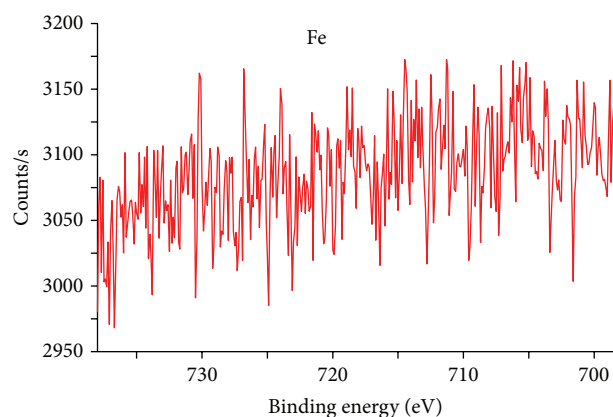


FIGURE 3: XPS spectra of the 4.50% Fe-TNT catalyst.

significantly diffraction peaks at (104), (110), (024), (116), and (214) crystal surface.

The peaks of $\text{Fe } 2p^{3/2}$ can be decomposed into two contributions corresponding to the different oxidation of iron, respectively. The main contribution is attributed to Fe^{3+} ions (binding energy at 709.1 eV), and the other is to Fe^{2+} ion (binding energy at 710.9 eV) [17]. However, the Fe cannot be detected with no element diffraction peak since the Fe content is too small as shown in Figure 3.

The typical tube structure of the TNT was shown in the TEM image. The tube size, judged from the TEM image, ranged from 5–10 nm and was smaller than the results of Park et al. [18], but similar to the results of Song et al. [19]. The end of the tube was open, which is extremely critical for TNT absorption and photocatalysis ability [20]. This shows that the hydrothermal method successfully changed the p25 nanopowder into nanotubes. As observed in Figure 4, the nanotubes were scrolls which can be explained by the hydrothermal mechanism.

3.2. N_2 Adsorption and Desorption Analyzer. The catalyst surface area was determined by an accelerated surface area and porosimetry analyzer (ASAP 2000) from Micromeritics company using nitrogen at a constant temperature (-196°C). The data obtained from the N_2 adsorption and desorption analyzer showed that the surface area of the TNT was $331 \text{ m}^2 \text{ g}^{-1}$, which was larger than that of 4.50% Fe TNT.

3.3. Degradation of MB

3.3.1. The Effect of Initial Concentration. The temperature and catalysis loading were controlled at 25°C and 0.04 g L^{-1} , respectively, to test the effect of initial concentration. Five kinds of concentrations, including 10, 20, 100, 200, and 400 ppm (mg L^{-1}), were assessed to understand the effects of initial concentrations on the degradation of MB. The effect of initial concentration on degradation efficiency is shown in Figure 6.

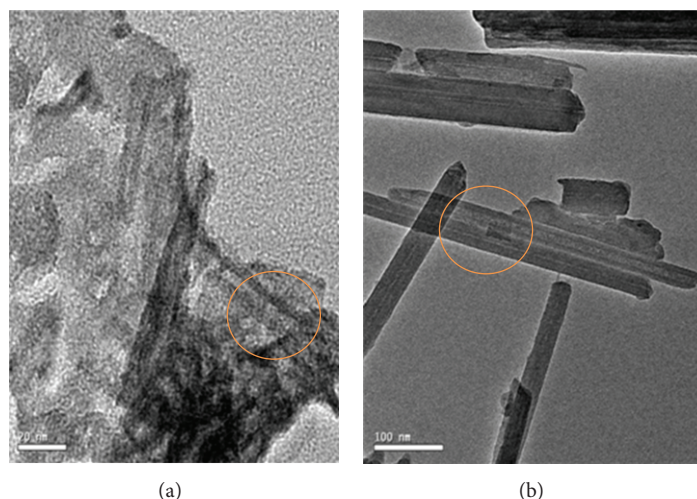
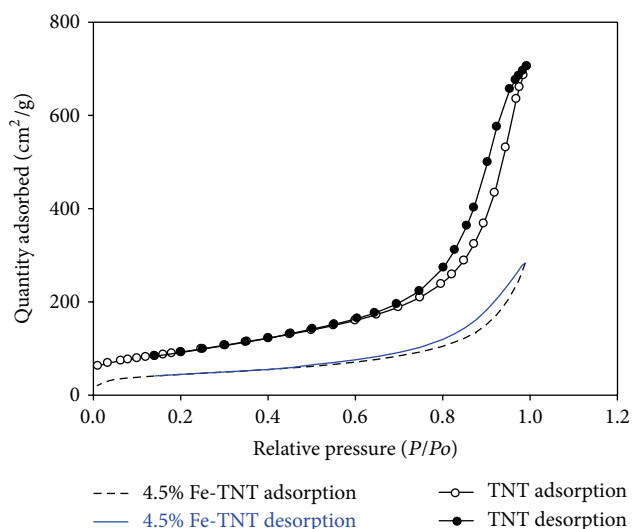


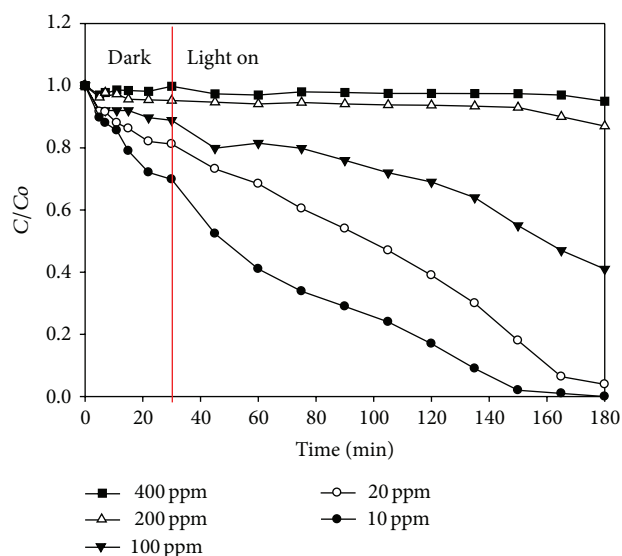
FIGURE 4: TEM images of (a) TNT and (b) 2.24% Fe TNT.

FIGURE 5: The curve of N_2 adsorption/desorption.

It can be seen that the photodegradation efficiency of methylene blue was inversely proportional to its concentration, which means that the lower the dye concentration, the higher the efficiency of the dye photodegradation [21]. In addition, the degradation efficiency of the MB decreased with increasing solution concentration [20].

3.3.2. The Effect of Dye Species. The three types of dyes were analyzed in this study. The degradation results under UV light are shown in Figure 5. After 180 min, the degradation efficiency of MB reached 99%, but the degradation efficiency of RBK5 was only 68% under 254 nm with and 0.04 gL^{-1} of 1.13% Fe TNT. These phenomena can be explained by the chemical structure of RBK5.

The test results under illuminated UV light with the three types of dyes are shown in Figure 7. The photodegradation efficiency of the three dyes ranked in order was MB, RBK5,

FIGURE 6: The effect of initial concentration on degradation efficiency under 254 nm UV and 1.13 % Fe-TNT of 0.04 gL^{-1} .

and DB22. The MB degradation efficiency reached almost 100% after 180 min, whereas, the DB22 decolorizing efficiency was only 38% after 180 min because the chemical bonds of DB22 are longer. To increase degradation efficiency, length of exposure to UV light needs to be increased.

3.3.3. The Effect of Fe Content. The photocatalytic degradation of methylene blue (MB, 10 ppm) by 0.77–4.5 wt% Fe-doped TNT was conducted under a 14-W UV and visible light. The power of a 14-W UV and visible light is a very low source compared to conventional visible sources or solar light at 300–500 watts [22]. The 1.13% Fe TNT displayed the best properties in this experiment, as shown in Figure 8. The photodegradation efficiency abruptly decreased to 62% due to an agglomeration and sedimentation of the catalyst

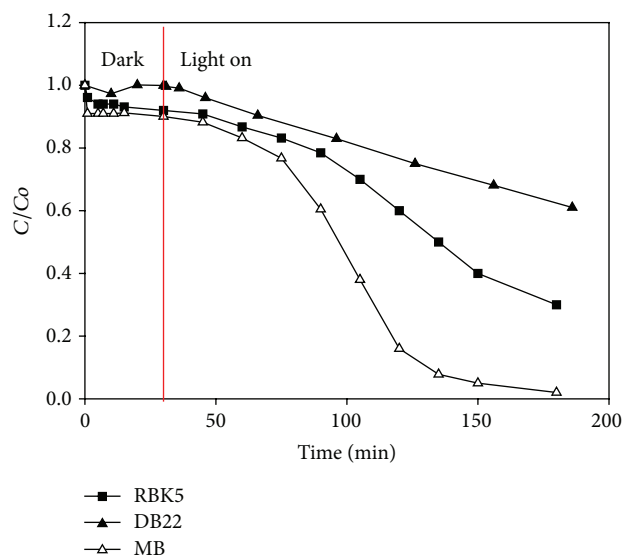


FIGURE 7: The effect of dye species on degradation efficiency under 254 nm UV and 1.13% Fe TNT of 0.04 gL^{-1} .

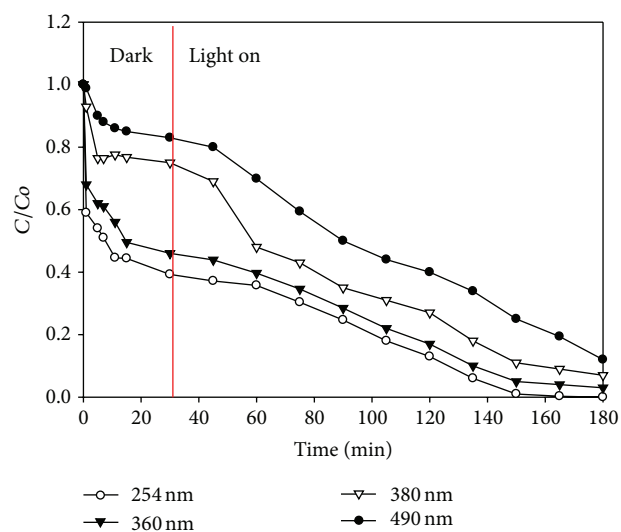


FIGURE 9: The effect of light source on degradation efficiency for 10 ppm MB removal and catalysts loading of 0.04 gL^{-1} with 1.13% Fe TNT.

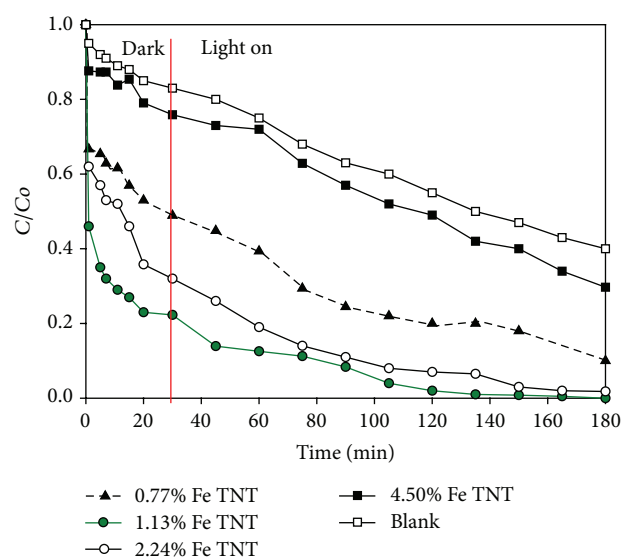


FIGURE 8: The effect of Fe content on degradation efficiency under 254 nm UV and catalysts loading of 0.04 gL^{-1} .

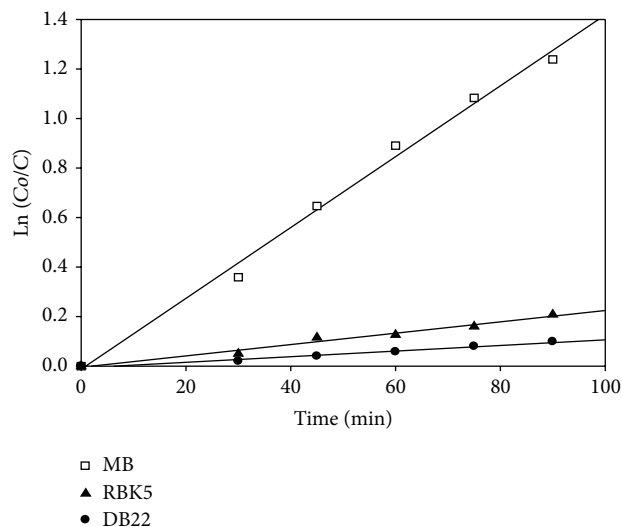


FIGURE 10: Pseudo-first-order kinetics plot for decolorization of 10 ppm MB, RBK5, and DB22 with 0.13 gL^{-1} catalyst under 254 nm light source.

particles when the Fe content exceeded 4.50%. This caused an increase in the particle size and a decrease in a specific surface area which lead to a decrease in the number of surface active sites [23].

El-Sharkawy et al. [24]. indicate that MB was not degraded completely when irradiated with UV in the absence of catalyst after 25 hr. This study has the same r .

3.3.4. The Effect of Light Source. There are four kinds of light sources, including 254 nm UV, 365 nm, 380 nm, and 490 nm light, for assessing the effect of light sources. The decolorizing efficiency reached almost 100% after 180 min of illumination time under 254 nm UV, as shown in Figure 9. Decolorizing

efficiency reached 90% after 180 min under near visible light ($\lambda = 380 \text{ nm}$). In addition, the decolorizing efficiency was 95% under 365 nm UV. Several minutes were spent before each reaction to maintain the temperature stability. The temperature was kept at 25°C by constant temperature water bath circulation system.

3.3.5. Kinetic Analysis. The photocatalytic degradation of MB, RBK5, and DB22 dyes as a function of the irradiation time was observed to follow an exponential decay as depicted in Figure 10. These results suggest that the photodegradation reaction follows the pseudo-first-order reaction kinetics. The pseudo-first-order reaction rate constant and half-life

TABLE 1: Pseudo-first-order kinetic parameters of different dyes.

Catalyst	R^2	k_1 (min ⁻¹)	$t_{1/2}$ (min)
MB	0.993	0.014	49.5
RBK5	0.937	0.005	21.0
DB22	0.947	0.002	18.3

parameters for MB dyes are listed in Table 1. The values of R^2 for different dyes show that a good compliance with the pseudo-first-order equation and the regression coefficients for the linear plots all exceeded 0.94.

4. Conclusion

In this study, the characterization of TNT and Fe TNT prepared using a hydrothermal and photodeposition method was performed. The time of decolorization increased with an increase in the initial MB concentration. The decolorizing efficiency decreased with increasing initial MB concentration, and a higher efficiency was obtained under UV-light illumination. However, excessive loading decreased the efficiency, and 1.13% weight Fe loading was found to be the optimal addition. Fe TNT using different Fe loadings was well characterized by the pseudo-first-order kinetic model.

Acknowledgment

Financial support from the National Science Council through Grant NSC-100-2622-E-562-002-CC3 and NSC-101-2221-E-562-003-MY3 is gratefully acknowledged.

References

- [1] N. M. Mahmoodi and M. Arami, "Decolorization and aromatic ring degradation kinetics of Direct Red 80 by UV oxidation in the presence of hydrogen peroxide utilizing TiO₂ as a photocatalyst," *Chemical Engineering Journal*, vol. 112, pp. 191–196, 2005.
- [2] Q. Zhang, "Photocatalytic degradation of methyl blue dye by pure and Platinum doped Titanium Dioxide Nanotube photocatalysts," *Advanced Science Letters*, vol. 18, no. 8, pp. 213–220, 2012.
- [3] N. Daneshvar, A. Oladegaragoze, and N. Djafarzadeh, "Decolorization of basic dye solutions by electrocoagulation: an investigation of the effect of operational parameters," *Journal of Hazardous Materials*, vol. 129, no. 1–3, pp. 116–122, 2006.
- [4] C. Pan and Y. Zhu, "New Type of BiPO₄ Oxy-acid salt photocatalyst with high photocatalytic activity on degradation of dye," *Environmental Science and Technology*, vol. 44, no. 14, pp. 5570–5574, 2010.
- [5] Y. Hu, Y. Tang, X. Tang, H. Li, and D. Liu, "The photocatalytic degradation of methylene blue in wastewater by nano-structured Cr-doped TiO₂ under low power visible-light irradiation," in *Proceedings of the 5th International Conference on Bioinformatics and Biomedical Engineering (iCBBE '11)*, May 2011.
- [6] S. P. Kamble, S. B. Sawant, and J. C. Schouten, "Photocatalytic and photochemical degradation of aniline using concentrated solar radiation," *Journal of Chemical Technology and Biotechnology*, vol. 78, pp. 865–872, 2003.
- [7] Y. Wang, J. Li, P. Peng, T. Lu, and L. Wang, "Preparation of S-TiO₂ photocatalyst and photodegradation of L-acid under visible light," *Applied Surface Science*, vol. 254, no. 16, pp. 5276–5280, 2008.
- [8] V. Štengl, F. Opluštil, and T. Nemec, "In³⁺-doped TiO₂ and TiO₂/In₂S₃ nanocomposite for photocatalytic and stoichiometric degradations," *Photochemistry and Photobiology*, vol. 88, no. 2, pp. 265–276, 2012.
- [9] Y. Hu, Y. Tang, X. Tang, H. Li, and D. Liu, "The photocatalytic degradation of methylene blue in wastewater by nano-structured Cr-doped TiO₂ under low power visible-light irradiation," in *Proceedings of the 5th International Conference on Bioinformatics and Biomedical Engineering (iCBBE '11)*, May 2011.
- [10] A. Fujishima and K. Honda, "Electrochemical photolysis of water at a semiconductor electrode," *Nature*, vol. 238, no. 5358, pp. 37–38, 1972.
- [11] C. Zhang, L. Gu, Y. Lin, Y. Wang, D. Fu, and Z. Gu, "Degradation of X-3B dye by immobilized TiO₂ photocatalysis coupling anodic oxidation on BDD electrode," *Journal of Photochemistry and Photobiology A*, vol. 207, no. 1, pp. 66–72, 2009.
- [12] C. C. Tsai, *Structure analysis of nanotubes synthesized from hydrothermal treatment on TiO₂* [Ph.D. thesis], National Cheng Kung University Department of Chemical Engineering, Tainan City, Taiwan, 2005.
- [13] M. Boroski, A. C. Rodrigues, J. C. Garcia, L. C. Sampaio, J. Nozaki, and N. Hioka, "Combined electrocoagulation and TiO₂ photoassisted treatment applied to wastewater effluents from pharmaceutical and cosmetic industries," *Journal of Hazardous Materials*, vol. 162, no. 1, pp. 448–454, 2009.
- [14] K. V. Kumar, K. Porkodi, and F. Rocha, "Langmuir-Hinshelwood kinetics-a theoretical study," *Catalysis Communications*, vol. 9, no. 1, pp. 82–84, 2008.
- [15] M. H. Habibi, A. Hassanzadeh, and S. Mahdavi, "The effect of operational parameters on the photocatalytic degradation of three textile azo dyes in aqueous TiO₂ suspensions," *Journal of Photochemistry and Photobiology A*, vol. 172, no. 1, pp. 89–96, 2005.
- [16] S. Song, J. Tu, Z. He, F. Hong, W. Liu, and J. Chen, "Visible light-driven iodine-doped titanium dioxide nanotubes prepared by hydrothermal process and post-calcination," *Applied Catalysis A*, vol. 378, no. 2, pp. 169–174, 2010.
- [17] J. G. Yu, H. G. Yu, C. H. Ao, S. C. Lee, J. C. Yu, and W. Ho, "Preparation, characterization and photocatalytic activity of in situ Fe-doped TiO₂ thin films," *Thin Solid Films*, vol. 496, no. 2, pp. 273–280, 2006.
- [18] D. Park, T. Sekino, S. Tsukuda, and S. Tanaka, "Synthesis of Sm-doped TiO₂ nanotubes and analysis of their methylene blue-removal properties under dark and UV-irradiated conditions," *Research on Chemical Intermediates*, vol. 39, no. 4, pp. 1581–1591, 2013.
- [19] S. Song, J. Tu, Z. He, F. Hong, W. Liu, and J. Chen, "Visible light-driven iodine-doped titanium dioxide nanotubes prepared by hydrothermal process and post-calcination," *Applied Catalysis A*, vol. 378, no. 2, pp. 169–174, 2010.
- [20] C. T. Hsieh, W. S. Fan, W. Y. Chen, and J. Y. Lin, "Adsorption and visible-light-derived photocatalytic kinetics of organic dye on Co-doped titania nanotubes prepared by hydrothermal synthesis," *Separation and Purification Technology*, vol. 67, no. 3, pp. 312–318, 2009.
- [21] R. M. Mohamed, I. A. Mkhaliid, E. S. Baeissa, and M. A. Al-Rayyani, "Photocatalytic degradation of methylene blue by

- Fe/ ZnO/SiO₂ nanoparticles under visible light,” *Journal of Nanotechnology*, vol. 2012, Article ID 329082, 5 pages, 2012.
- [22] Y. Hu, Y. Tang, X. Tang, H. Li, and D. Liu, “The photocatalytic degradation of methylene blue in wastewater by nano-structured Cr-doped TiO₂ under low power visible-light irradiation,” in *Proceedings of the 5th International Conference on Bioinformatics and Biomedical Engineering (iCBBE '11)*, pp. 1–4, School of Technical Physics, Xidian University, Shaanxi, China, 2011.
- [23] D. Zhao, J. Wang, Z. Zhang, and J. Zhang, “Photocatalytic degradation of omethoate using NaY zeolite-supported TiO₂,” *Frontiers of Chemical Engineering in China*, vol. 3, no. 2, pp. 206–210, 2009.
- [24] E. A. El-Sharkawy, A. Y. Soliman, and K. M. Al-Amer, “Comparative study for the removal of methylene blue via adsorption and photocatalytic degradation,” *Journal of Colloid and Interface Science*, vol. 310, no. 2, pp. 498–508, 2007.

Research Article

Photocatalytic Degradation of 2,4-Dichlorophenol Using Nanosized $\text{Na}_2\text{Ti}_6\text{O}_{13}/\text{TiO}_2$ Heterostructure Particles

Zicong Jian,^{1,2} Shaobin Huang,^{1,2,3,4} and Yongqing Zhang^{1,2}

¹ College of Environment and Energy, South China University of Technology, Guangzhou 510006, China

² Guangdong Provincial Key Laboratory of Atmospheric Environment and Pollution Control, Guangzhou 510006, China

³ State Key Laboratory of Pulp and Paper Engineering, South China University of Technology, Guangzhou 510006, China

⁴ The Key Laboratory of Environmental Protection and Eco-Remediation of Guangdong Regular Higher Education Institutions, Guangzhou 510006, China

Correspondence should be addressed to Shaobin Huang; chshuang@scut.edu.cn

Received 10 January 2013; Revised 9 May 2013; Accepted 10 May 2013

Academic Editor: Jiaguo Yu

Copyright © 2013 Zicong Jian et al. This is an open access article distributed under the Creative Commons Attribution License, which permits unrestricted use, distribution, and reproduction in any medium, provided the original work is properly cited.

$\text{Na}_2\text{Ti}_6\text{O}_{13}/\text{TiO}_2$ composite particles were synthesized through the hydrolyzation of tetrabutyl titanate in a reverse microemulsion and characterized by thermogravimetry and differential scanning calorimetry (TG-DSC), X-ray diffraction (XRD), and scanning electron microscope (SEM). The photocatalytic property of $\text{Na}_2\text{Ti}_6\text{O}_{13}/\text{TiO}_2$ was evaluated by degradation of 2,4-dichlorophenol (2,4-DCP) under 40 W ultraviolet lamp ($\lambda = 365 \text{ nm}$) irradiation and compared with commercial P25- TiO_2 in the same condition. The results showed that the synthesized nanobelts $\text{Na}_2\text{Ti}_6\text{O}_{13}/\text{TiO}_2$ heterostructures had typical width from 80 to 100 nm, with thickness less than 40 nm and length up to 5 μm . Such $\text{Na}_2\text{Ti}_6\text{O}_{13}/\text{TiO}_2$ nanosized particles exhibited better photocatalytic activity than that of P25- TiO_2 , and the degradation rate of 2,4-DCP with initial concentration of 0.02 g/L reached 99.4% at the end of 50 min.

1. Introduction

Chlorophenols, as significantly harmful environmental pollutants [1–3], are of high toxicity, recalcitrance, bioaccumulation, and persistence in the environment. These compounds, which have been widely used as insecticides, bactericides, herbicides, fungicides, and wood preservative, are difficult to be biodegraded [4, 5]; thus, they are environmental residue. Chlorophenols are considered to be harmful for human health [6, 7] and have been listed as priority pollutants by the US EPA and the EU. Conventional processes [8–10], such as physical, chemical, and biological methods, are used to remove chlorophenols. These techniques, however, are difficult to degrade such refractory biodegradation organic pollutants completely. In recent years, several advanced oxidation processes (AOPs) are put forward for the degradation of chlorophenols [11, 12], including electrochemical anodic oxidation [13, 14], Fenton oxidation [15, 16], and photocatalytic oxidation [17, 18]. Such AOPs generate free radicals, which have strong oxidation capability; thus, the organic

pollutants can be destructed easily. Photocatalytic oxidation is one of the AOPs widely used to degrade organic pollutants into harmless final products.

The present researches focusing on the materials of photocatalytic oxidation are semiconductors included oxides [19, 20], sulfides [21], nitrides [22], and oxynitrides [23]. These semiconductors provide a promising strategy for environmental pollutants control or hydrogen generation. One of the most important photocatalysts is titanium dioxide (TiO_2) [24, 25], which has been known as the most preferable photocatalyst due to its stability, nontoxicity, and low cost. However, there are disadvantages, such as low separation rate of the photoexcited electrons and holes, which lead to the limited quantum efficiency of TiO_2 . Therefore, many scholars have been devoted to prepare a TiO_2 photocatalyst that is capable of efficient generation and separation of photo-induced electron-hole pairs. These investigations include doping with cation or anion ions, coupling TiO_2 with other semiconductors [26], depositing precious metal, and so on. For example, Yu et al. synthesized novel carbon self-doped

TiO₂ sheets with exposed {001} facets, which exhibited an excellent absorption in the whole visible-light region, due to the exposed {001} facets which were much more reactive than the thermodynamically more stable {101} surface [27].

It was reported [28, 29] that alkali titanates, general formula as A₂O-*n*TiO₂ (3 ≤ *n* ≤ 8, A = Li, Na, K), exhibited good photocatalytic activity and ion conductivity. According to Billik et al. [30], Na₂Ti₆O₁₃ could be prepared by mechanochemical reaction of the TiC₁₄-Na₂SO₄·10H₂O-Na₂CO₃ mixture followed by a molten salt synthesis.

The present work is based on the idea that heterostructures of Na₂Ti₆O₁₃ coupling with TiO₂ would perform outstanding photocatalytic properties. To our knowledge, Na₂Ti₆O₁₃ is hard to be obtained at the temperature lower than 800°C. Since the costs are high and the process of crystallization is difficult to control, we proposed a simple and rapid method to obtain such heterostructures. In this paper, *x*-Na₂Ti₆O₁₃/TiO₂ (*x* = 0, 1.0, 1.5, 2.5) composite particles were synthesized in reverse microemulsions system at room temperature and ambient pressure followed by heat treatments from 500°C to 800°C. The photocatalytic activity of these samples was evaluated and compared with the commercial P25-TiO₂ on the degradation of 2,4-DCP in aqueous solution under ultraviolet light irradiation. The forming conditions of Na₂Ti₆O₁₃/TiO₂ heterostructures and their photocatalytic property were discussed based on characterization results.

2. Materials and Methods

2.1. Preparation of Na₂Ti₆O₁₃/TiO₂ Composite Particles. The nanostructured Na₂Ti₆O₁₃/TiO₂ photocatalyst was synthesized by a microemulsion approach. The *n*-hexanol (chemically pure, CP) was considered as both the oil phase and the cosurfactant, and cetyltrimethylammonium bromide (CTAB) (CP) was chosen as the surfactant. Sodium hydroxide (CP) solution with specific molar concentration of 0, 1.0, 1.5, and 2.5 mol/L, respectively, acted as the water phase.

Stock solutions of *n*-hexanol and CTAB with a quality ratio of 2:1 were mixed under stirring. Sodium hydroxide solution was added drop-wise to the glass vial containing the mixtures aforementioned, and the mass of sodium hydroxide solution was 10% of the bulk quality. After stirring for 60 min, a steady microemulsion was obtained. A desired amount of Ti(OBut)₄ (CP) was injected into the microemulsion. The resultant suspension was stirred for 120 min until it became milk white. In the system, the quality ratio of CTAB to Ti(OBut)₄ was 2.5:1. The solid products were separated in a centrifuge at 4000 r min⁻¹ and washed with anhydrous ethanol (AP) to remove the organic compounds and surfactants from the particles and dried in an oven at 105°C for 12 h. The obtained precursors were calcined for 3 h at 500, 600, 700, and 800°C, respectively. The final products were milled before characterization. Samples were labeled as *x*-Na₂Ti₆O₁₃/TiO₂, where *x* = 0, 1.0, 1.5, and 2.5 mol/L was the molar concentration of NaOH. All the products were synthesized at room temperature and ambient pressure without thermal treatment, if not otherwise stated.

2.2. Characterization of Na₂Ti₆O₁₃/TiO₂ Composite Particles. X-ray powder diffraction (XRD) patterns were recorded on a Bruker D8 ADVANCE X-ray diffractometer with Cu Kα radiation (λ = 0.15406 nm) at a high voltage of 40 kV with a step of 0.02°. The particle size and morphology were observed on a field emission scanning electron microscope (FESEM, LEO 1530 VP, Germany). The TG analysis of precursors was measured by an STA449c/1/41G thermal analyzer (Netzsch, Germany).

2.3. Photocatalytic Studies. The photocatalytic reaction was conducted in a 200 mL cylindrical glass vessel fixed in the XPA photochemical reactor (Nanjing Xujiang Machine-electronic Plant). The XPA reactor consists of a magnetic stirrer, quartz cool trap, and a condenser to keep the reaction temperature steady and to prevent the evaporation of water. A 40 W Hg lamp (365 nm) was used as the UV light source. 2,4-Dichlorophenol (2,4-DCP) with certain concentration (0.02 g/L) was used as reactant.

Prior to illumination, various quantities of photocatalyst powder were dispersed in 200 mL reaction solution and stirred in the dark for 30 min in order to obtain an optimally dispersed system and to ensure complete adsorption/desorption equilibration. Subsequently, the Hg lamp was turned on, and the catalysts began to decompose 2,4-DCP.

During the course of illumination, 1.0 mL of suspensions was withdrawn periodically from the reactor and filtered (Millipore Millex25 0.45 mm membrane filter) previously to HPLC measurements.

The concentrations of 2,4-DCP were monitored with a high performance liquid chromatography (HPLC, Shimadzu, Japan) equipped with a UV detector (SPD-10AV) and a Symmetry C18 column (250 mm × 4.6 mm). Mobile phase: methanol (HPLC grade) and water (80:20, volume); flow rate: 1.0 mL/min; injection volume: 20 μL; absorbance detection: 284 nm. The concentration of the remaining 2,4-DCP was measured by its area of characteristic peak (*A*). The degradation ratio (*X*) of the reactant was calculated using $X(\%) = 100(A_0 - A_t)/A_0$.

3. Results and Discussion

3.1. Characterization of Na₂Ti₆O₁₃/TiO₂ Composite Particles. The TG-DSC curves for 1.5-Na₂Ti₆O₁₃/TiO₂ precursor are shown in Figure 1. The TG results indicate that the sample lost weight slowly from 25 to 80°C, which could be attributed to the volatilization of physically absorbed oil phase and water. There is a sharp weight loss from 80 to 270°C due to the evaporation of water and the desorption of hexanol (boiling point 156°C), and this is supported by the exothermic peak at 119°C in the DSC curve. As the temperature increases from 270 to 320°C, the sample exhibits further and faster weight loss, which corresponds to the burning of residual surfactant, and this could be explained well by an exothermic peak detected in the DSC curve at 272°C. Beyond 320°C, the curve becomes almost flat, implying that the weight of the precursor has little changed. Combining with the DSC curve, phase transition may be the mainly occurring at this process.

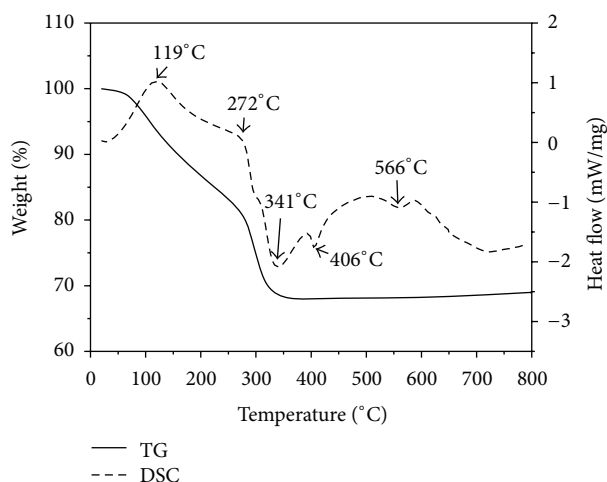


FIGURE 1: TG-DSC curves of 1.5- $\text{Na}_2\text{Ti}_6\text{O}_{13}/\text{TiO}_2$ precursor.

The DSC curve of the precursor shows two main exothermic peaks: one of which is the evaporation of water and oil phase, and the other is the decomposition of surfactant as discussed earlier. Three endothermic peaks appear at 341, 406, and 566°C, which could be ascribed to the crystallization of TiO_2 from amorphous to anatase, and from anatase to rutile, and the crystallization of $\text{Na}_2\text{Ti}_6\text{O}_{13}$, respectively.

The typical SEM images of 1.5- $\text{Na}_2\text{Ti}_6\text{O}_{13}/\text{TiO}_2$ are presented in Figure 2. As can be seen in Figure 2(a), the 1.5- $\text{Na}_2\text{Ti}_6\text{O}_{13}/\text{TiO}_2$ precursor without heat treatment is amorphous and bonding loosely, appearing to be large and bubbles-like, which might reflect the situation of the water droplet in the microemulsion. While the precursors were calcined at 500 or 600°C, the loose bubbles-like structures break into small particles, and the diameter was less than 100 nm. Comparing with Figures 2(b) and 2(c), particles calcined at 600°C dispersed better than that at 500°C. Subcircular and well-crystallized particles with diameter of around 50 nm were obtained in Figure 2(c). Combining with XRD pattern, it can be known that the precursors were dehydrated and they would be transformed into the crystalline anatase and $\text{Na}_2\text{Ti}_6\text{O}_{13}$, under calcinations at 500 and 600°C, respectively.

The SEM micrographs of $\text{Na}_2\text{Ti}_6\text{O}_{13}$ powders calcined at 700 and 800°C are shown in Figures 2(d) and 2(e). The belt-like morphology of the product calcined at 700°C is well documented in the SEM image shown in Figure 2(d). $\text{Na}_2\text{Ti}_6\text{O}_{13}$ nanobelts have typical width from 80 to 100 nm, thickness less than 40 nm, and length up to 5 μm . The phase of the obtained sample was supported by XRD. It is also found that the nanobelts were fractured under calcination at 800°C, though the fragments have higher degree of crystallinity, as shown obviously in Figure 2(e).

Figure 3 shows the XRD patterns of 1.5- $\text{Na}_2\text{Ti}_6\text{O}_{13}/\text{TiO}_2$ precursor and the composite particles which were calcined for 3 h at 500, 600, 700, and 800°C, respectively. As can be seen, no characteristic diffraction peaks are observed from the pattern of precursor, indicating that the precursor is amorphous. The XRD pattern of 1.5- $\text{Na}_2\text{Ti}_6\text{O}_{13}/\text{TiO}_2$ calcined at 500°C shows a strong peak at $2\theta = 25.34^\circ$ and a

weak one at $2\theta = 27.50^\circ$, implying that TiO_2 is crystallized as the anatase and rutile phase coexistence after calcined at 500°C. Curves of 1.5- $\text{Na}_2\text{Ti}_6\text{O}_{13}/\text{TiO}_2$ calcined at 600–800°C show that $\text{Na}_2\text{Ti}_6\text{O}_{13}$ could be obtained by calcining the microemulsion-resulted precursor at relatively low temperature (<800°C). The pattern of 1.5- $\text{Na}_2\text{Ti}_6\text{O}_{13}/\text{TiO}_2$ calcined at 600°C shows the characteristic diffraction peak of both rutile and $\text{Na}_2\text{Ti}_6\text{O}_{13}$; however, the samples calcined at 700, and 800°C have no characteristic diffraction peak of TiO_2 .

Although the formation mechanisms of the titanate nanobelts are still under debate, we believe that the formation of $\text{Na}_2\text{Ti}_6\text{O}_{13}$ nanobelts may be affected by the crystallite size or chemical activity of the precursor and the condition of crystallization. In our work, the precursor is considered to be $\text{Ti}(\text{OH})_4$. Under heat treatment, $-\text{OH}$ from the surface of $\text{Ti}(\text{OH})_4$ combined with each other to produce H_2O and $-\text{O}-\text{Ti}-$ bond. With the calcined temperature increase and the existence of Na^+ , more $-\text{OH}$ were removed and $\text{Na}-\text{O}-\text{Ti}-$ bonds were formed, which means that $\text{Na}_2\text{Ti}_6\text{O}_{13}$ were formed. As it was supported by SEM and XRD, at the temperature of 600°C, the crystallization of $\text{Na}_2\text{Ti}_6\text{O}_{13}$ which are the prerequisites for the nanobelts formation was obtained. According to Dominko et al. [31], $\text{Na}_2\text{Ti}_6\text{O}_{13}$ crystallizes in a monoclinic crystalline structure with continuous tunnel channels along c axis (Figure 4). Such tunnel channels suppressed the possible delamination into sheets or nanotubes [30].

In a word, the amorphous precursor forms anatase and rutile phase at 500°C, and the anatase phase transits into rutile phase at 600°C; meanwhile, $\text{Na}_2\text{Ti}_6\text{O}_{13}$ crystal formed. However, when the temperature is higher than 600°C, no TiO_2 exists. Thus, the optimum temperature for heterostructure particles is 600°C.

3.2. Degradation Activities of $\text{Na}_2\text{Ti}_6\text{O}_{13}/\text{TiO}_2$. In this investigation, 2,4-dichlorophenol (2,4-DCP) was chosen as a representative model pollutant ($C_0 = 20 \text{ mg/L}$, 200 mL) to study the adsorption and photocatalytic activity of the $\text{Na}_2\text{Ti}_6\text{O}_{13}/\text{TiO}_2$ composite particles (10 mg) under UV-light (40 W Hg lamp) irradiation and the results can be seen in Figure 5. The degradation efficiency of 2,4-DCP increased with time. After 50 min UV-light irradiation, the degradation rate reached 99.4%, 96.0%, 83%, and 56.2%, by the photocatalyst synthesized in 1.5, 1.0, 0, and 2.5 mol/L sodium hydroxide solution, respectively, while the commercial P25 has the degradation rate of 76.9%, and the degradation rate of 11.5% was obtained without any photocatalysts.

The different molar ratios of $\text{Na}_2\text{Ti}_6\text{O}_{13}/\text{TiO}_2$ have significant differences in photoactivity. While the ratio raises from 0 to 1.5, the degradation rate raises obviously; however, the 2.5 sample has the weakest activity. The sample of 1.5- $\text{Na}_2\text{Ti}_6\text{O}_{13}/\text{TiO}_2$ has the best efficiency for decomposing 2,4-DCP, which is about 1.3 times higher than commercial P25. Thus, 1.5- $\text{Na}_2\text{Ti}_6\text{O}_{13}/\text{TiO}_2$ was chosen as the standard photocatalyst.

Figure 6 shows the photoactivity of 1.5- $\text{Na}_2\text{Ti}_6\text{O}_{13}/\text{TiO}_2$ calcined at different temperatures. After 50 min UV-light irradiation, the degradation rate reached 99.4%, 83.8%, 56.3%, and 37.2%, by the photocatalyst calcined at 600, 500,

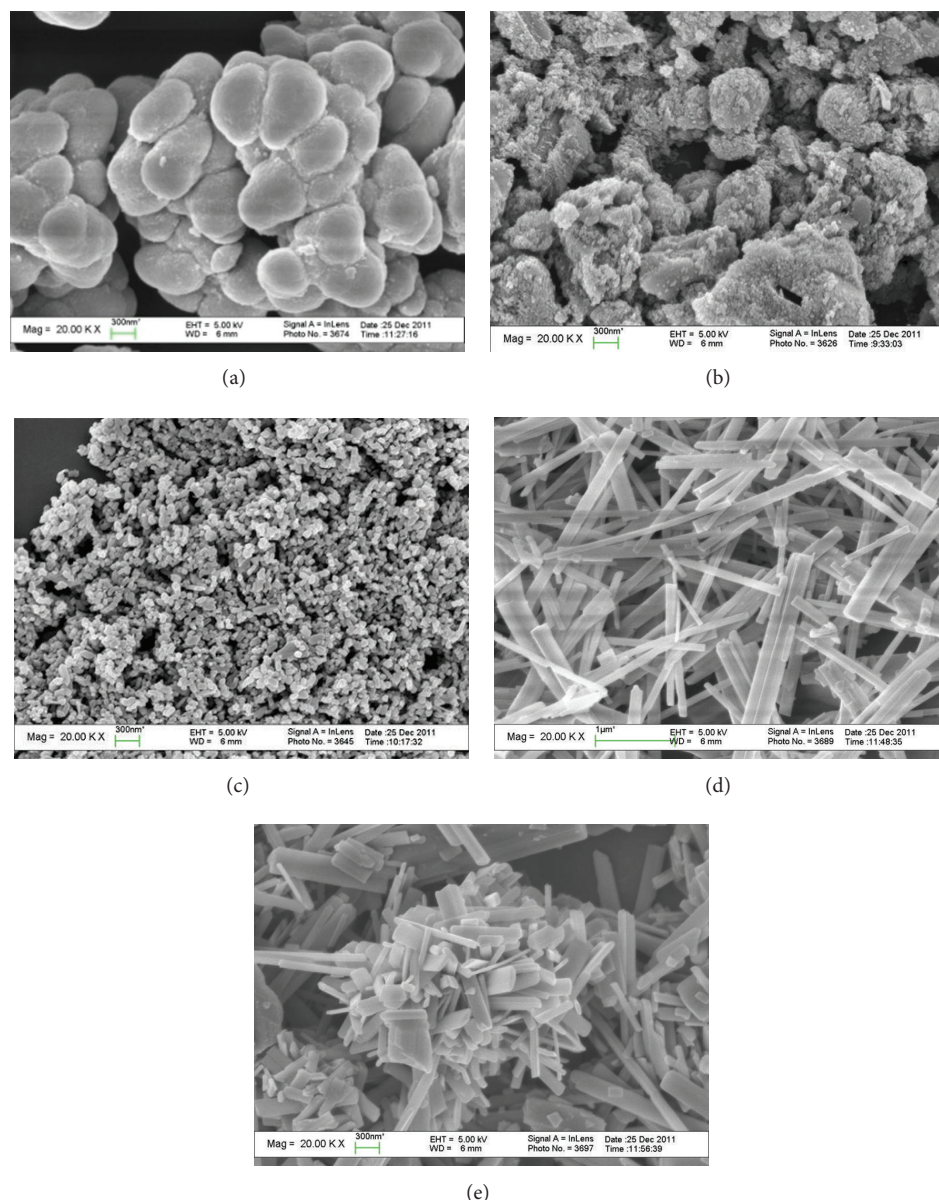


FIGURE 2: SEM image of $\text{Na}_2\text{Ti}_6\text{O}_{13}/\text{TiO}_2$ composite particles. (a) $1.5\text{-Na}_2\text{Ti}_6\text{O}_{13}/\text{TiO}_2$ precursor; (b) $1.5\text{-Na}_2\text{Ti}_6\text{O}_{13}/\text{TiO}_2$ calcined at 500°C ; (c) $1.5\text{-Na}_2\text{Ti}_6\text{O}_{13}/\text{TiO}_2$ calcined at 600°C ; (d) $1.5\text{-Na}_2\text{Ti}_6\text{O}_{13}/\text{TiO}_2$ calcined at 700°C ; (e) $1.5\text{-Na}_2\text{Ti}_6\text{O}_{13}/\text{TiO}_2$ calcined at 800°C .

700°C , and 800°C , respectively. The commercial P25 has the degradation rate of 76.9%, and the blank experiment showed the degradation rate of 11.5%.

Combining with SEM and XRD characterization, the temperature of calcinations determines the crystal line, the morphology, and the components of the photocatalyst. At 500°C the component of the photocatalyst mainly is TiO_2 . Such photocatalyst formed by anatase and rutile exhibits a general photoactivity. At 600°C $\text{Na}_2\text{Ti}_6\text{O}_{13}/\text{TiO}_2$ heterostructure formed and the particles were well crystalline. These microstructures improve the separation efficiency of photogenerated electrons and holes, increase the contact area,

and allow more efficient transport for the reactant molecules to get to the active sites on the framework walls, enhance the adsorption of light, and reduce the reflection of light. Therefore, the photocatalytic activity was enhanced.

In order to observe the photo degradation process of 2,4-DCP, the concentrations of possible intermediates, such as phenol, 4-CP, and 2-CP, were measured with HPLC. Figure 7 represents these three intermediates generation from the system. It is clear that 2,4-DCP was not completely mineralized and was residue as phenol and chlorophenol; meanwhile, the concentration of phenol is much higher than 4-CP and 2-CP. After 40 min photoreaction, the concentration

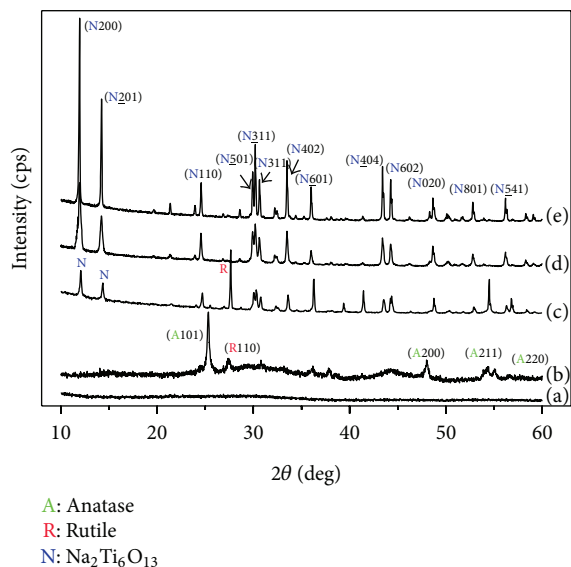


FIGURE 3: XRD pattern of 1.5-Na₂Ti₆O₁₃/TiO₂ composite particles: (a) 1.5-Na₂Ti₆O₁₃/TiO₂ precursor; (b) 1.5-Na₂Ti₆O₁₃/TiO₂ calcined at 500°C; (c) 1.5-Na₂Ti₆O₁₃/TiO₂ calcined at 600°C; (d) 1.5-Na₂Ti₆O₁₃/TiO₂ calcined at 700°C; (e) 1.5-Na₂Ti₆O₁₃/TiO₂ calcined at 800°C.

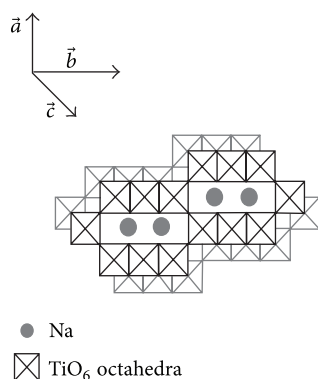


FIGURE 4: Schematic representation of the crystal structure of Na₂Ti₆O₁₃ along *a*-axis [31] (octahedral: Ti-O₆; spheres: Na).

of these three intermediates reduced obviously, indicating that Na₂Ti₆O₁₃/TiO₂ heterostructure is capable of degrading phenol and chlorophenol.

4. Conclusions

Nanobelts Na₂Ti₆O₁₃/TiO₂ heterostructure particles were synthesized in an *n*-hexanol/CTAB/sodium hydroxide solution reverse microemulsion. The samples were investigated by TG-DSC, XRD, and SEM. The results show that such belt-like photocatalyst has typical width from 80 to 100 nm, thickness of less than 40 nm, and length up to 5 μm. The photocatalytic activity of photocatalysts synthesized by 1.5 mol/L sodium hydroxide solution and calcined at 600°C for 3 h gave the greatest degradation rate towards 2,4-DCP. In summary, it

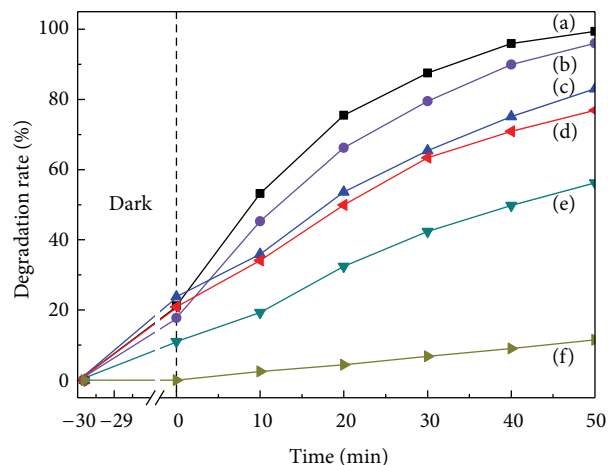


FIGURE 5: Effects of ratio of Na₂Ti₆O₁₃/TiO₂ calcined at 600°C: (a) 1.5-Na₂Ti₆O₁₃/TiO₂; (b) 1.0-Na₂Ti₆O₁₃/TiO₂; (c) 0-Na₂Ti₆O₁₃/TiO₂; (d) commercial P25; (e) 2.5-Na₂Ti₆O₁₃/TiO₂; (f) blank.

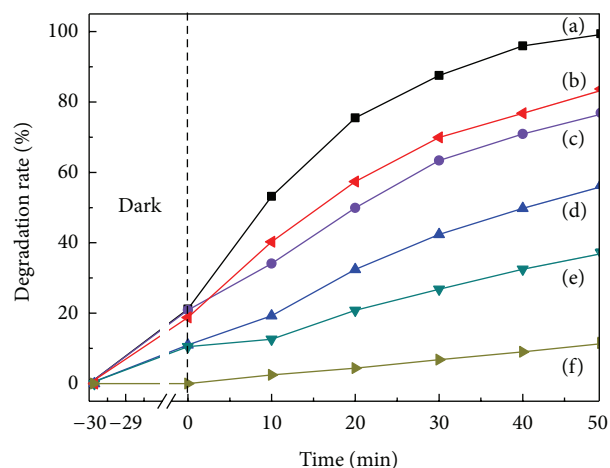


FIGURE 6: Effects of calcined temperature of 1.5-Na₂Ti₆O₁₃/TiO₂: (a) 600°C; (b) 500°C; (c) commercial P25; (d) 700°C; (e) 800°C; (f) blank.

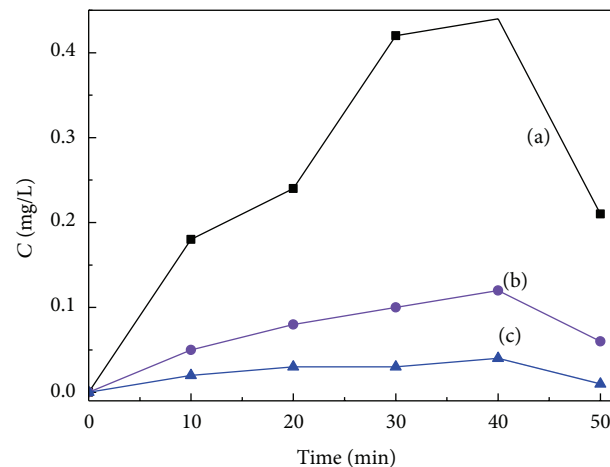


FIGURE 7: Variation of (a) phenol; (b) 4-CP; (c) 2-CP concentration during the photo degradation.

was proved that the heterostructure particles had higher photocatalytic activity than the common TiO_2 .

Acknowledgments

This research was financially supported by National Natural Science Foundations of China (Grant no. 20777019), Research Project of Guangdong Provincial Department of Science and Technology (Grant no. 2012A010800006), and Guangdong Natural Science Foundation (Grant no. S2012020010887).

References

- [1] A. O. Olaniran and E. O. Igbinosa, "Chlorophenols and other related derivatives of environmental concern: properties, distribution and microbial degradation processes," *Chemosphere*, vol. 83, no. 10, pp. 1297–1306, 2011.
- [2] M. Czaplicka, "Sources and transformations of chlorophenols in the natural environment," *Science of the Total Environment*, vol. 322, no. 1–3, pp. 21–39, 2004.
- [3] F. Galán-Cano, R. Lucena, S. Cárdenas, and M. Valcárcel, "Ionic liquid based in situ solvent formation microextraction coupled to thermal desorption for chlorophenols determination in waters by gas chromatography/mass spectrometry," *Journal of Chromatography A*, vol. 1229, pp. 48–54, 2012.
- [4] N. K. Temel and M. Sökmen, "New catalyst systems for the degradation of chlorophenols," *Desalination*, vol. 281, no. 1, pp. 209–214, 2011.
- [5] J. Chen, Y. Chan, and M. Lu, "Photocatalytic oxidation of chlorophenols in the presence of manganese ions," *Water Science and Technology*, vol. 39, no. 10–11, pp. 225–230, 1999.
- [6] B. Ozkaya, "Chlorophenols in leachates originating from different landfills and aerobic composting plants," *Journal of Hazardous Materials*, vol. 124, no. 1–3, pp. 107–112, 2005.
- [7] L. Xing, H. Liu, J. P. Giesy, X. Zhang, and H. Yu, "Probabilistic ecological risk assessment for three chlorophenols in surface waters of China," *Journal of Environmental Sciences*, vol. 24, no. 2, pp. 329–334, 2012.
- [8] S. S. Makgato and E. M. Nkhambayausi-Chirwa, "Performance evaluation of AOP/biological hybrid system for treatment of recalcitrant organic compounds," *International Journal of Chemical Engineering*, vol. 2010, Article ID 590169, 10 pages, 2010.
- [9] H. Zilouei, B. Guieysse, and B. Mattiasson, "Biological degradation of chlorophenols in packed-bed bioreactors using mixed bacterial consortia," *Process Biochemistry*, vol. 41, no. 5, pp. 1083–1089, 2006.
- [10] P. J. Dorathi and P. Kandasamy, "Dechlorination of chlorophenols by zero valent iron impregnated silica," *Journal of Environmental Sciences*, vol. 24, no. 4, pp. 765–773, 2012.
- [11] A. Dixit, A. J. Tirpude, A. K. Mungray, and M. Chakraborty, "Degradation of 2, 4 DCP by sequential biological-advanced oxidation process using UASB and UV/ $\text{TiO}_2/\text{H}_2\text{O}_2$," *Desalination*, vol. 272, no. 1–3, pp. 265–269, 2011.
- [12] L. Liu, F. Chen, and F. Yang, "Stable photocatalytic activity of immobilized $\text{Fe}^0/\text{TiO}_2/\text{ACF}$ on composite membrane in degradation of 2,4-dichlorophenol," *Separation and Purification Technology*, vol. 70, no. 2, pp. 173–178, 2009.
- [13] Y. Wang, Z. Shen, and X. Chen, "Effects of experimental parameters on 2,4-dichlorophenol degradation over Er-chitosan- PbO_2 electrode," *Journal of Hazardous Materials*, vol. 178, no. 1–3, pp. 867–874, 2010.
- [14] B. Nasr, T. Hsen, and G. Abdellatif, "Electrochemical treatment of aqueous wastes containing pyrogallol by BDD-anodic oxidation," *Journal of Environmental Management*, vol. 90, no. 1, pp. 523–530, 2009.
- [15] C. Wang, H. Liu, and Z. Sun, "Heterogeneous photo-Fenton reaction catalyzed by nanosized iron oxides for water treatment," *International Journal of Photoenergy*, vol. 2012, Article ID 801694, 10 pages, 2012.
- [16] S. Karthikeyan, A. Titus, A. Gnanamani, A. B. Mandal, and G. Sekaran, "Treatment of textile wastewater by homogeneous and heterogeneous Fenton oxidation processes," *Desalination*, vol. 281, no. 1, pp. 438–445, 2011.
- [17] H. Ilyas, I. A. Qazi, W. Asgar, M. A. Awan, and Z. Khan, "Photocatalytic degradation of nitro and chlorophenols using doped and undoped titanium dioxide nanoparticles," *Journal of Nanomaterials*, vol. 2011, Article ID 589185, 8 pages, 2011.
- [18] J. Sin, S. Lam, A. R. Mohamed, and K. Lee, "Degrading endocrine disrupting chemicals from wastewater by TiO_2 photocatalysis: a review," *International Journal of Photoenergy*, vol. 2012, Article ID 185159, 23 pages, 2012.
- [19] K. Klačanová, P. Fodran, and P. Šimon, "Formation of $\text{Fe}(0)$ -nanoparticles via reduction of $\text{Fe}(\text{II})$ compounds by amino acids and their subsequent oxidation to iron oxides," *Journal of Chemistry*, vol. 2013, Article ID 961629, 10 pages, 2013.
- [20] B. Zielińska, E. Mijowska, and R. J. Kalenczuk, "Synthesis and characterization of K-Ta mixed oxides for hydrogen generation in photocatalysis," *International Journal of Photoenergy*, vol. 2012, Article ID 525727, 7 pages, 2012.
- [21] Z. Liu, J. Fang, and W. Xu, "Low temperature hydrothermal synthesis of Bi_2S_3 nanorods using BiOI nanosheets as self-sacrificing templates," *Materials Letters*, vol. 88, pp. 82–85, 2012.
- [22] H. Yan, Y. Chen, and S. Xu, "Synthesis of graphitic carbon nitride by directly heating sulfuric acid treated melamine for enhanced photocatalytic H_2 production from water under visible light," *International Journal of Hydrogen Energy*, vol. 37, no. 1, pp. 125–133, 2012.
- [23] O. I. Yaskiv, I. M. Pohrel'yuk, V. M. Fedirko, D. B. Lee, and O. V. Tkachuk, "Formation of oxynitrides on titanium alloys by gas diffusion treatment," *Thin Solid Films*, vol. 519, no. 19, pp. 6508–6514, 2011.
- [24] A. Fujishima, X. Zhang, and D. A. Tryk, " TiO_2 photocatalysis and related surface phenomena," *Surface Science Reports*, vol. 63, no. 12, pp. 515–582, 2008.
- [25] J. Yu, G. Dai, and B. Huang, "Fabrication and characterization of visible-light-driven plasmonic photocatalyst $\text{Ag}/\text{AgCl}/\text{TiO}_2$ nanotube arrays," *Journal of Physical Chemistry C*, vol. 113, no. 37, pp. 16394–16401, 2009.
- [26] G. Dai, J. Yu, and G. Liu, "Synthesis and enhanced visible-light photoelectrocatalytic activity of p-n junction BiOI/TiO_2 nanotube arrays," *Journal of Physical Chemistry C*, vol. 115, no. 15, pp. 7339–7346, 2011.
- [27] J. Yu, G. Dai, Q. Xiang, and M. Jaroniec, "Fabrication and enhanced visible-light photocatalytic activity of carbon self-doped TiO_2 sheets with exposed $\{001\}$ facets," *Journal of Materials Chemistry*, vol. 21, no. 4, pp. 1049–1057, 2011.
- [28] L. Zhen, C. Y. Xu, W. S. Wang, C. S. Lao, and Q. Kuang, "Electrical and photocatalytic properties of $\text{Na}_2\text{Ti}_6\text{O}_{13}$ nanobelts prepared by molten salt synthesis," *Applied Surface Science*, vol. 255, no. 7, pp. 4149–4152, 2009.

- [29] S. Baliteau, A.-L. Sauvet, C. Lopez, and P. Fabry, "Controlled synthesis and characterization of sodium titanate composites $\text{Na}_2\text{Ti}_3\text{O}_7/\text{Na}_2\text{Ti}_6\text{O}_{13}$," *Solid State Ionics*, vol. 178, no. 27-28, pp. 1517–1522, 2007.
- [30] P. Billik, M. Čaplovičová, and Ľ. Čaplovič, "Mechanochemical-molten salt synthesis of $\text{Na}_2\text{Ti}_6\text{O}_{13}$ nanobelts," *Materials Research Bulletin*, vol. 45, no. 5, pp. 621–627, 2010.
- [31] R. Dominko, E. Baudrin, P. Umek, D. Arčon, M. Gaberšček, and J. Jamnik, "Reversible lithium insertion into $\text{Na}_2\text{Ti}_6\text{O}_{13}$ structure," *Electrochemistry Communications*, vol. 8, no. 4, pp. 673–677, 2006.

Research Article

Nanocrystalline N-Doped TiO₂ Powders: Mild Hydrothermal Synthesis and Photocatalytic Degradation of Phenol under Visible Light Irradiation

Junna Xu, Feng Wang, Wenxiu Liu, and Wenbin Cao

Department of Inorganic Nonmetallic Materials, School of Materials Science and Engineering, University of Science and Technology Beijing, Beijing 100083, China

Correspondence should be addressed to Wenbin Cao; wbcdo@ustb.edu.cn

Received 10 January 2013; Revised 22 April 2013; Accepted 23 April 2013

Academic Editor: Jiaguo Yu

Copyright © 2013 Junna Xu et al. This is an open access article distributed under the Creative Commons Attribution License, which permits unrestricted use, distribution, and reproduction in any medium, provided the original work is properly cited.

Nitrogen-doped TiO₂ powders have been prepared using technical guanidine hydrochloride, titanyl sulfate, and urea as precursors via a mild hydrothermal method under initial pressure of 3MPa, 150°C holding for 2h without any postheat treatment for crystallization. The nanocrystalline N-doped TiO₂ powders were composed of anatase TiO₂ by XRD. The grain size was estimated as about 10 nm, and the BET specific surface area of the powder was measured as 154.7 m²/g. The UV-visible absorption spectra indicated that the absorption edge of the N-doped TiO₂ powders had been red shifted into the visible light region. The photocatalytic performance of the synthesized powders was evaluated by degradation of phenol under visible light irradiation. And the effects of the catalyst load and the initial pH value on the photodegradation were also investigated.

1. Introduction

Water pollution has become a major problem in recent years. The biological, chemical, and physical-chemical water treatment methods are often ineffectively or environmentally incompatible [1, 2]. Heterogeneous photocatalytic oxidation has been considered as one of the effective methods to treat the pollutants in water through the photo-generated hydroxyl radicals and super oxygen species [3, 4]. TiO₂ photocatalyst has attracted much attention due to its low cost, high stability, nontoxicity, and environmental friendly properties [5, 6]. However, TiO₂ can only be excited by UV light ($\lambda < 387$ nm, accounts only about 5% of sunlight) because of its large band gap of 3.2 eV for anatase which limits its application in practical use. Many methods have been adopted to extend its optical response to visible light (accounts about 45% of sunlight), such as doping with impurities [7–10], sensitizing by dyes [11], and coupling with semiconductors [12].

Doping TiO₂ with various elements is the most effective way to narrow its band gap. Among these dopants, nitrogen has attracted much attention in recent years due to its small ionization energy, comparable atomic size with

oxygen, metastable center formation, and enhanced UV-Vis photocatalytic performance [7]. Many works on the preparation of N-TiO₂ by physical or chemical methods have been published [13–22]. Among these methods, N-TiO₂ powders were mainly prepared either by calcination of TiO₂ powders under nitrogen containing atmosphere or by postheat treatment of the Sol-Gel/hydrothermally prepared amorphous TiO₂ with nitrogen agents at high temperature for both doping nitrogen atoms into the TiO₂ lattice and crystallization. However, calcination under high temperature may cause agglomeration and abnormal growth of crystals which results in small surface area and decreases the number of photoactive sites. So, it is necessary to seek an appropriate route to synthesize N-TiO₂ effectively under mild conditions. However, it is not so easy to dope nitrogen into TiO₂ under mild hydrothermal conditions because the bond energy between Ti–O is greater than that of Ti–N bond [23]. Some researchers have tried to synthesize N-TiO₂ powders by one-step hydrothermal method without postheat treatment in a relatively lower temperature [24]. It was found that N-TiO₂ could be synthesized through one-step hydrothermal method at 150°C for 8 h [25]. N-TiO₂ nanoparticles were prepared

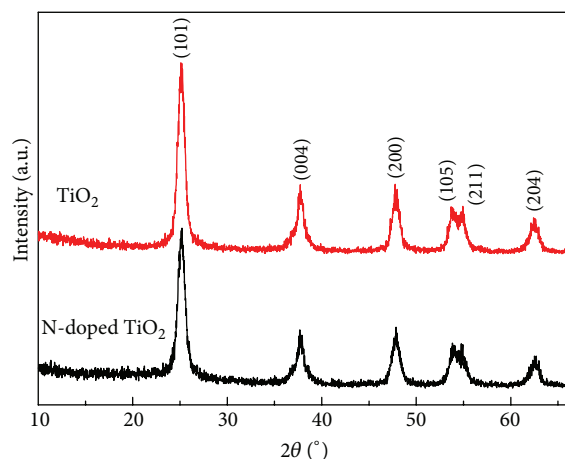


FIGURE 1: XRD patterns of the undoped and N-doped TiO_2 powders.

by using Degussa P25 and triethanol amine as precursors via hydrothermal method at 140°C holding for 24 h [26]. So, it always needs longer reaction time in the one-step hydrothermal method to prepare N-doped TiO_2 .

In this paper, well crystallized N-doped TiO_2 powders with enhanced visible light absorption have been prepared by a mild hydrothermal method at 150°C holding for 2 h without any postheat treatment for crystallization. The photocatalytic performance of the synthesized powders was evaluated by degradation of phenol in aqueous solution under visible light irradiation.

2. Experimental

N-doped TiO_2 powders were prepared via a hydrothermal method at 150°C holding for 2 h. Technical grade $\text{TiOSO}_4 \cdot 2\text{H}_2\text{O}$, $\text{CO}(\text{NH}_2)_2$ and $\text{CH}_5\text{N}_3 \cdot \text{HCl}$ were used as received and without any further purification. In a typical synthesis process, titanyl sulfate (1 M), urea (1.5 M), and guanidine hydrochloride (3 M) were dissolved in 1 L distilled water and stirred for 30 min, and then the mixed solution was transferred into an autoclave with an internal volume of 2 L. The initial pressure was set at 3 MPa, and the stirring speed was fixed at 300 r/min. The autoclave was heated to 150°C holding for 2 h. The obtained suspension was centrifuged and washed with deionized water until no SO_4^{2-} was detected in the washes. After drying at 90°C in air, the yellow colored N-doped powders were obtained. The white undoped TiO_2 was also synthesized under the same processing parameters.

The synthesized N-doped powders were characterized by X-ray diffraction, Brunauer-Emmett-Teller (BET), Transmission electron microscopy, UV-Visible diffuse reflectance spectra, and X-ray photoelectron spectroscopy. The photocatalytic activity of N-doped powders was evaluated by photodegradation of phenol in aqueous solution under 400~650 nm visible light irradiation with illuminant intensity of 15.54 mW/cm^2 . Firstly, 0.25 g of N-doped powders were mixed into 100 mL phenol aqueous solution with a concentration of 25 mg/L, and then the suspension was stirred in the

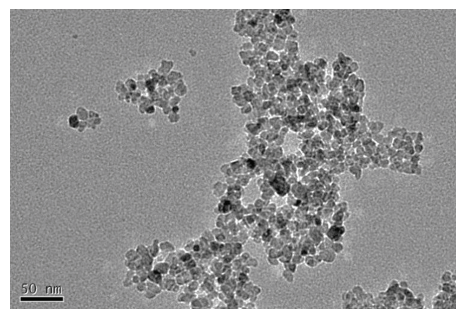


FIGURE 2: TEM micrograph of N-doped TiO_2 powders.

dark for 2 h to reach the balance of adsorption/desorption. The balanced concentration of phenol was treated as the initial phenol concentration. Then, the light was turned on to start photodegradation. The suspension was sampled at an interval of 2 h and centrifuged to remove the N-doped TiO_2 particles. The concentration of phenol was measured on a UV-Visible spectrophotometer (TU-1901) at the wavelength of 270 nm to obtain the absorbance of the solution.

3. Results and Discussion

Figure 1 shows the XRD patterns of the synthesized pure and N-doped TiO_2 powders. All the peaks are corresponding to those of anatase. The intensity of the peaks of N- TiO_2 is slightly weakened compared with that of undoped TiO_2 . From the line broadening of the (101) diffraction peak by Scherrer's method, the grain sizes of undoped and N-doped TiO_2 are about 9.7 and 10.0 nm, respectively. The specific surface areas for undoped and N-doped TiO_2 are 150.6 and $154.7 \text{ m}^2/\text{g}$, respectively.

Figure 2 shows the TEM micrograph of N-doped TiO_2 powders. The particles are approximately spherical in shape and 10 nm in size, which is consistent with the results calculated by Scherrer's method.

The UV-Visible absorption spectra of undoped and N-doped TiO_2 powders are shown in Figure 3(a). It is clear that N-doped TiO_2 powders exhibit stronger visible light absorption while the undoped TiO_2 can absorb only UV light. The straight-line extrapolation method was used to determine the light absorption edge of the powders, as indicated in Figure 3(a). The absorption edge of the undoped TiO_2 is approximately 390 nm while that of N-doped TiO_2 is around 420 nm. According to the equation $E_g = 1240/\lambda$ (eV), the band gap energies of the undoped and N-doped TiO_2 are 3.18 and 2.95 eV, respectively. As TiO_2 has been considered as an indirect semiconductor [27, 28], the band gap energy of the samples can be estimated by Kubelka-Munk function [29, 30], as shown in Figure 3(b). Band gap energy calculated from the intercept of the tangent lines in the plots are 3.10 and 2.90 eV for undoped and N-doped TiO_2 , respectively, which is in accordance with the UV-Vis results.

The concentration and the electronic state of nitrogen at the surface of the N-doped TiO_2 powders were measured by XPS, as shown in Figure 4. The XPS survey spectra as

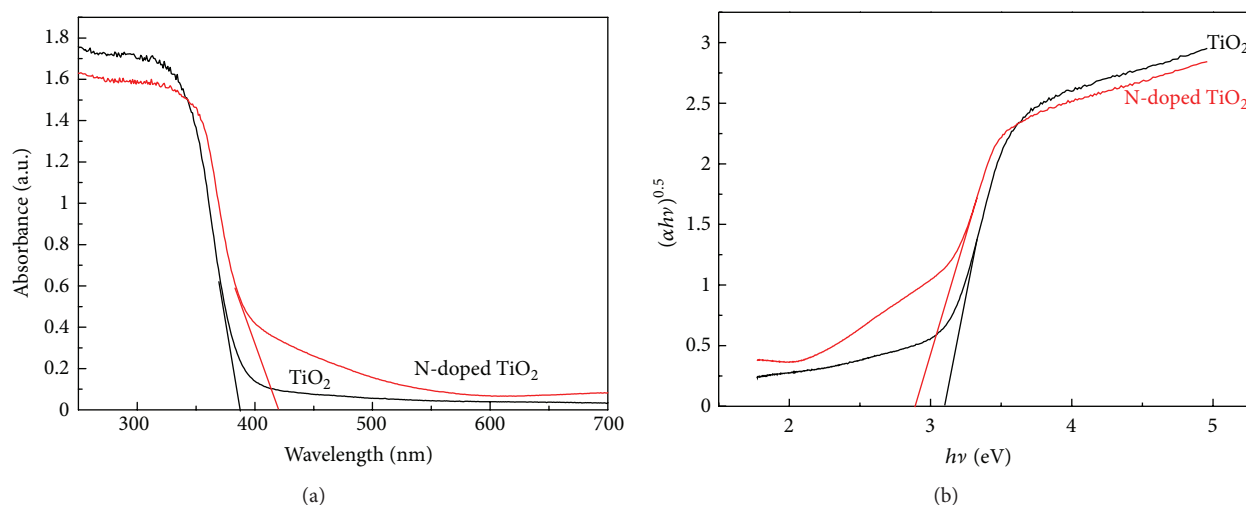


FIGURE 3: (a) UV-Visible absorption spectra of undoped and N-doped TiO_2 powders and (b) plots of $(\alpha h\nu)^{0.5}$ versus photoenergy of the synthesized samples.

indicated in Figure 4(a) show that the surface of N-doped TiO_2 is composed of Ti, O, N, and carbon. The concentration of nitrogen is about 1.6% (atomic percent). Yang et al. [31] suggested that when the doping concentration of nitrogen was less than 2.1% (atomic percent), an isolated $\text{N}2p$ states would be created above the $\text{O}2p$ valance band, which might contribute to the visible light sensitivity. Figure 4(b) shows the binding energy of N1s located at both 396.0 and 399.9 eV. The weaker peak located at 396.0 eV can be attributed to the Ti-N bond which indicates that nitrogen atoms have been incorporated into the lattice of TiO_2 [32, 33]. The stronger peak located at 399.9 eV can be assigned to Ti-O-N linkage which is considered as the interstitial nitrogen atoms in the lattice of TiO_2 and has been reported in many literatures [34–36].

The photodegradation of phenol aqueous solution under different conditions is shown in Figure 5. In order to confirm any possible self-degradation of phenol under visible light irradiation, the light irradiation of phenol solution with the same illumination intensity was processed. It can be seen in Figure 5 that the phenol concentration remains almost unchanged with the elapse of irradiation time. That is, the phenol will not be degraded by the visible light irradiation.

The effect of the phenol adsorption by the catalysts on the photocatalytic degradation process has been investigated by stirring the phenol-catalysts suspensions in the dark for 10 h. The concentration of phenol was decreased only 2% during the 10 h black stirring as indicated in Figure 5. So, the decrease of the concentration of the phenol caused by the adsorption of the catalysts can be ignored. Forty-seven percent of phenol has been degraded by N- TiO_2 powders while that by undoped TiO_2 is 15%. N-doped TiO_2 exhibits better photoactivity than that of undoped TiO_2 , which indicates that nitrogen doping has improved the photocatalytic activity of TiO_2 in the visible light region.

Catalyst load is an important factor that affects the photocatalytic degradation of phenol. The influence of the load

of photocatalyst was performed by varying the amount of N-doped TiO_2 from 0.1 to 2.0 g, as indicated in Figure 6. The maximum photocatalytic degradation is obtained when using 0.25 g N-doped TiO_2 powders. Further increase or decrease, the amount of catalysts will reduce the photodegradation. The results are in agreement with the data published by other researchers [37, 38]. When the amount of the charged catalyst is too high, turbidity will hinder the light penetration and enhance the light scattering [39]; thus, the photocatalytic activity of the catalyst will be reduced due to the decreased light intensity. Besides, the aggregation of particles increases with the increase of the amount of the photocatalyst which may also decrease the total active sites for the adsorption of photos and phenol [34], resulting in the decrease of photodegradation.

The pH value of the aqueous solution affects the surface charge of the catalyst as well as phenol. The effect of pH value on photodegradation of phenol was investigated in the range of 4 to 10 by adjusting the solution with 1 mol/L HCl and NaOH, as shown in Figure 7. The maximum photodegradation is observed at $\text{pH} = 4$, and it can reach 81% after 10 h of visible light irradiation. The similar results were also reported in [40]. Figure 8 shows the zeta potential of N-doped TiO_2 in phenol aqueous solution at different pH values. The isoelectric point of N-doped TiO_2 particle is 6.4. According to the isoelectric point of N-doped TiO_2 , the following reactions may occur on the surface of N-doped TiO_2 at different pH values:



That is, the surface of N-doped TiO_2 will be positively charged at $\text{pH} < 6.4$ and negatively charged at $\text{pH} > 6.4$. As the dissociation constants ($\text{p}K_a$) of phenol are 9.96 ($t = 25^\circ\text{C}$) [41], the phenol will mainly exist as neutral species when pH value is less than the $\text{p}K_a$, while it will be negatively

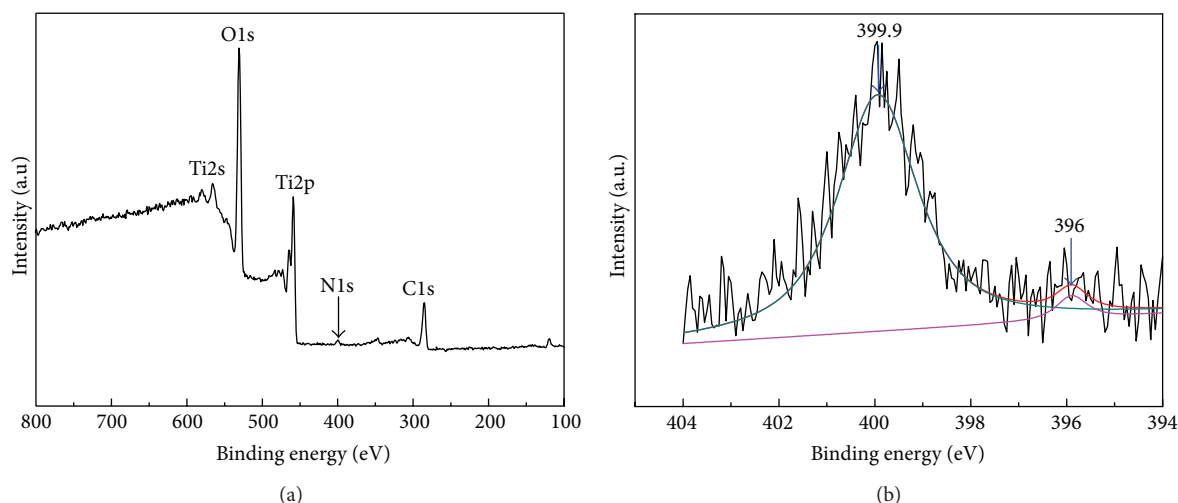


FIGURE 4: XPS survey spectra of (a) survey spectrum and (b) N1s.

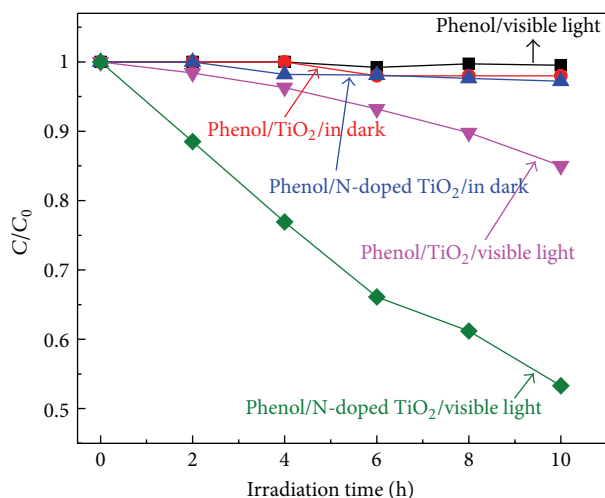


FIGURE 5: Photodegradation of phenol with 0.25 g catalysts at pH = 6 under different conditions.

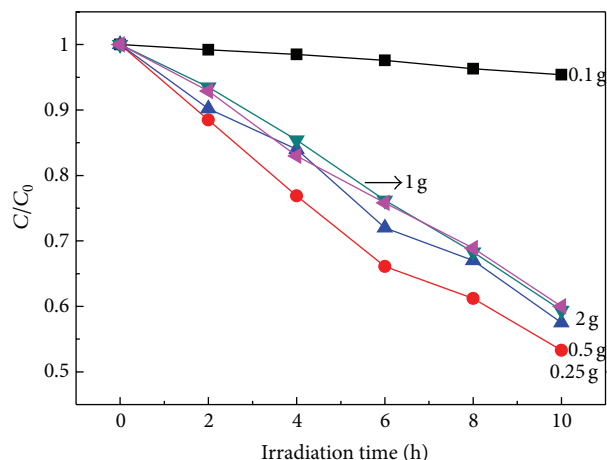


FIGURE 6: Effects of N-doped TiO₂ powders load on the photodegradation of phenol at pH = 6.

charged when the pH is larger than the pK_a . That is, phenol molecules can be scarcely adsorbed on the surface of N-doped TiO₂ particles due to the columbic repulsion between them as the surface of N-doped TiO₂ particles and phenol molecules are both negatively charged when pH = 10. Therefore, very little phenol could be decomposed. At the case when pH < 10, phenol is primarily presented in neutral molecular form while the surface of TiO₂ particles are positively (or negatively when pH > 6.4) charged. The electrostatic attraction between TiO₂ particles and phenol molecule increases the amount of adsorbed phenol and then enhances the photodegradation. Besides, agglomeration has also been considered as one of the key factors that affect the photocatalytic activity. When the pH is relatively low, large repulsive forces between the TiO₂ particles may occur due to the positive charges caused by the reaction (1); thus, the dispersion of the TiO₂ particles in the suspension could be improved and the photocatalytic performance could be enhanced as well due to the decreased agglomeration of the particles. Therefore, the better photodegradation occurs at the case when pH value is 4.

The photodegradation of phenol is complex and may produce complex intermediates such as toxic aromatic intermediates as reported in many researches [42, 43]. Generally, phenol is firstly oxidized to aromatic intermediates such as hydroquinone, catechol, benzoquinone, and 4, 4'-dihydroxybiphenyl, and then phenyl rings of these aromatic intermediates break up to form aliphatic acid which is further oxidized to short-chain organic acid such as oxalic acid, acetic acid, and formic acid. Finally, they are decomposed to carbon dioxide and water completely [11, 37]. The aromatic intermediates always have colors. For example, the color of the mixture of catechol and hydroquinone aqueous solution is pink, while that of m-dihydroxybenzene and benzoquinone are yellow and brown, respectively [44]. The absorption peaks corresponding to aromatic intermediates and ring cleavage products have been detected in the UV-Vis absorption spectra of phenol degradation by researchers [45, 46]. However,

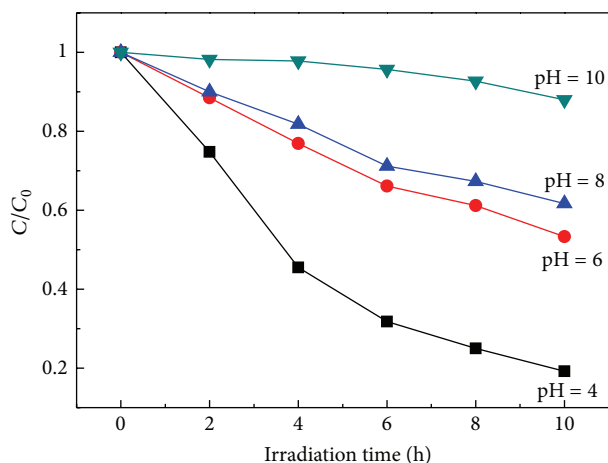


FIGURE 7: Effect of pH value on the photodegradation of phenol with 0.25 g N-TiO₂ powders.

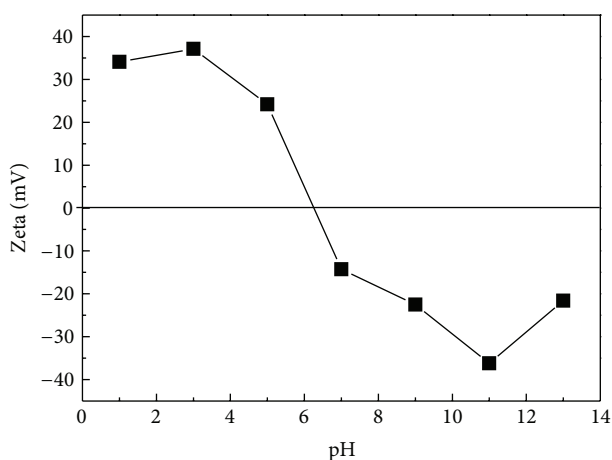


FIGURE 8: Zeta potential of N-doped TiO₂ powders in phenol aqueous solution at different pH values.

in our experiments, the solution after photodegradation is colorless, and no clear absorption peaks corresponding to aromatic intermediates and ring cleavage products are detected in the spectra, as shown in Figure 9, which indicates that there is little photodegradation intermediates produced in the photodegradation of phenol process and the good photocatalytic performance of our samples.

4. Conclusion

N-doped TiO₂ was successfully synthesized by a mild hydrothermal method at 150°C and holding for 2 h without any postheat treatment for crystallization. The grain size of the powders was about 10 nm, and the specific surface area of N-doped TiO₂ was 154.7 m²/g. The absorption edge of N-doped TiO₂ had been shifted to 420 nm, and the band energy was about 2.90 eV estimated by Kubelka-Munk function after nitrogen doping. Nitrogen atoms have been successfully incorporated into the lattice of TiO₂. The amount of catalyst

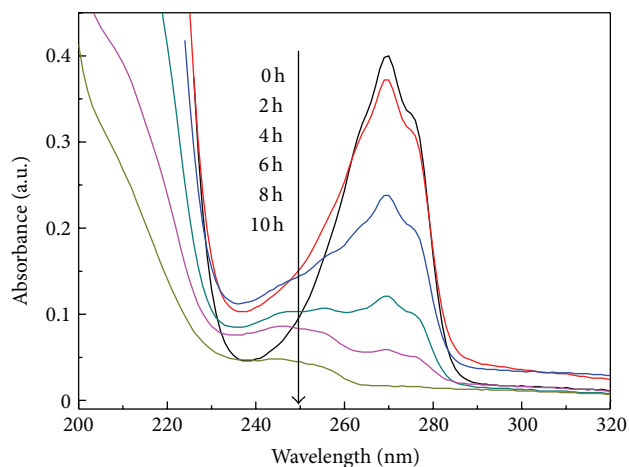


FIGURE 9: UV-Vis absorption spectra of phenol degradation with 0.25 g N-doped TiO₂ at pH 4.

and pH value was optimized as 0.25 g and 4, respectively, for better photocatalytic performance in our experiment conditions. The photodegradation reached 81% after 10 h of visible light irradiation.

Acknowledgments

This work has been financially supported by the National High Technology Research and Development Program of China (Grant no. 2012AA030302), the National Natural Science Foundation of China (Grant no. 51072019), and the Opening Project of State Key Laboratory of High Performance Ceramics and Superfine Microstructure under Grant SKL201112SIC.

References

- [1] D. Gümüş and F. Akbal, "Photocatalytic degradation of textile dye and wastewater," *Water, Air, and Soil Pollution*, vol. 216, no. 1–4, pp. 117–124, 2011.
- [2] A. M. De Luis, J. I. Lombraña, A. Menéndez, and J. Sanz, "Analysis of the toxicity of phenol solutions treated with H₂O₂/UV and H₂O₂/Fe oxidative systems," *Industrial and Engineering Chemistry Research*, vol. 50, no. 4, pp. 1928–1937, 2011.
- [3] N. Kashif and F. Ouyang, "Parameters effect on heterogeneous photocatalysed degradation of phenol in aqueous dispersion of TiO₂," *Journal of Environmental Sciences*, vol. 21, no. 4, pp. 527–533, 2009.
- [4] S. Ahmed, M. G. Rasul, W. N. Martens, R. Brown, and M. A. Hashib, "Advances in heterogeneous photocatalytic degradation of phenols and dyes in wastewater: a review," *Water, Air, and Soil Pollution*, vol. 215, no. 1–4, pp. 3–29, 2011.
- [5] A. Fujishima and K. Honda, "Electrochemical photolysis of water at a semiconductor electrode," *Nature*, vol. 238, no. 5358, pp. 37–38, 1972.
- [6] A. Fujishima, T. N. Rao, and D. A. Tryk, "Titanium dioxide photocatalysis," *Journal of Photochemistry and Photobiology C*, vol. 1, no. 1, pp. 1–21, 2000.

- [7] X. Qiu and C. Burda, "Chemically synthesized nitrogen-doped metal oxide nanoparticles," *Chemical Physics*, vol. 339, no. 1-3, pp. 1-10, 2007.
- [8] Y. Li, W. Cao, F. Ran, and X. Zhang, "Photocatalytic degradation of methylene blue aqueous solution under visible light irradiation by using N-doped titanium dioxide," *Key Engineering Materials*, vol. 336-338, pp. 1972-1975, 2007.
- [9] H. Q. Wang, Z. B. Wu, and Y. Liu, "A simple two-step template approach for preparing carbon-doped mesoporous TiO₂ hollow microspheres," *Journal of Physical Chemistry C*, vol. 113, no. 30, pp. 13317-13324, 2009.
- [10] K. Huang, L. Chen, M. Liao, and J. Xiong, "The photocatalytic inactivation effect of Fe-doped TiO₂ nanocomposites on Leukemic HL60 cells-based photodynamic therapy," *International Journal of Photoenergy*, vol. 2012, Article ID 367072, 8 pages, 2012.
- [11] P. Chowdhury, J. Moreira, H. Goma, and A. K. Ray, "Visible-solar-light-driven photocatalytic degradation of phenol with dye-sensitized TiO₂: parametric and kinetic study," *Industrial & Engineering Chemistry Research*, vol. 51, no. 12, pp. 4523-4532, 2012.
- [12] R. Khan and T. J. Kim, "Preparation and application of visible-light-responsive Ni-doped and SnO₂-coupled TiO₂ nanocomposite photocatalysts," *Journal of Hazardous Materials*, vol. 163, no. 2-3, pp. 1179-1184, 2009.
- [13] M. H. Chan and F. H. Lu, "Characterization of N-doped TiO₂ films prepared by reactive sputtering using air/Ar mixtures," *Thin Solid Films*, vol. 518, no. 5, pp. 1369-1372, 2009.
- [14] W. Guo, Y. Shen, G. Boschloo, A. Hagfeldt, and T. Ma, "Influence of nitrogen dopants on N-doped TiO₂ electrodes and their applications in dye-sensitized solar cells," *Electrochimica Acta*, vol. 56, no. 12, pp. 4611-4617, 2011.
- [15] Y. Wang, C. Feng, M. Zhang, J. Yang, and Z. Zhang, "Visible light active N-doped TiO₂ prepared from different precursors: origin of the visible light absorption and photoactivity," *Applied Catalysis B*, vol. 104, no. 3-4, pp. 268-274, 2011.
- [16] D. Huang, S. Liao, S. Quan et al., "Synthesis and characterization of visible light responsive N-TiO₂ mixed crystal by a modified hydrothermal process," *Journal of Non-Crystalline Solids*, vol. 354, no. 33, pp. 3965-3972, 2008.
- [17] R. Asahi, T. Morikawa, T. Ohwaki, K. Aoki, and Y. Taga, "Visible-light photocatalysis in nitrogen-doped titanium oxides," *Science*, vol. 293, no. 5528, pp. 269-271, 2001.
- [18] S. Z. Hu, F. Y. Li, and Z. P. Fan, "The influence of preparation method, nitrogen source, and post-treatment on the photocatalytic activity and stability of N-doped TiO₂ nanopowder," *Journal of Hazardous Materials*, vol. 196, pp. 248-254, 2011.
- [19] B. Kosowska, S. Mozia, A. W. Morawski, B. Grzmil, M. Janus, and K. Kałucki, "The preparation of TiO₂-nitrogen doped by calcination of TiO₂·xH₂O under ammonia atmosphere for visible light photocatalysis," *Solar Energy Materials and Solar Cells*, vol. 88, no. 3, pp. 269-280, 2005.
- [20] B. Baruwati and R. S. Varma, "Synthesis of N-doped nano TiO₂ using guanidine nitrate: an excellent visible light photocatalyst," *Journal of Nanoscience and Nanotechnology*, vol. 11, no. 3, pp. 2036-2041, 2011.
- [21] S. Livraghi, A. M. Czoska, M. C. Paganini, and E. Giamello, "Preparation and spectroscopic characterization of visible light sensitized N doped TiO₂ (rutile)," *Journal of Solid State Chemistry*, vol. 182, no. 1, pp. 160-164, 2009.
- [22] M. D'Arienzo, R. Scotti, L. Wahba et al., "Hydrothermal N-doped TiO₂: explaining photocatalytic properties by electronic and magnetic identification of N active sites," *Applied Catalysis B*, vol. 93, no. 1-2, pp. 149-155, 2009.
- [23] H. Diker, C. Varlikli, K. Mizrak, and A. Dana, "Characterizations and photocatalytic activity comparisons of N-doped nc-TiO₂ depending on synthetic conditions and structural differences of amine sources," *Energy*, vol. 36, no. 2, pp. 1243-1254, 2011.
- [24] D. Wu, M. Long, W. Cai, C. Chen, and Y. Wu, "Low temperature hydrothermal synthesis of N-doped TiO₂ photocatalyst with high visible-light activity," *Journal of Alloys and Compounds*, vol. 502, no. 2, pp. 289-294, 2010.
- [25] N. Bao, J. J. Niu, Y. Li, G. L. Wu, and X. H. Yu, "Low-temperature hydrothermal synthesis of N-doped TiO₂ from small-molecule amine systems and their photocatalytic activity," *Environmental Technology*, vol. iFirst, pp. 1-11, 2012.
- [26] F. Peng, L. Cai, L. Huang, H. Yu, and H. Wang, "Preparation of nitrogen-doped titanium dioxide with visible-light photocatalytic activity using a facile hydrothermal method," *Journal of Physics and Chemistry of Solids*, vol. 69, no. 7, pp. 1657-1664, 2008.
- [27] G. Wang, L. Xu, J. Zhang, T. Yin, and D. Han, "Enhanced photocatalytic activity of TiO₂ powders (P25) via calcination treatment," *International Journal of Photoenergy*, vol. 2012, Article ID 265760, 9 pages, 2012.
- [28] G. Shang, H. Fu, S. Yang, and T. Xu, "Mechanistic study of visible-light-induced photodegradation of 4-chlorophenol by TiO_{2-x}N_x with low nitrogen concentration," *International Journal of Photoenergy*, vol. 2012, Article ID 759306, 9 pages, 2012.
- [29] X. W. Cheng, X. J. Yu, Z. P. Xing, and L. S. Yang, "Enhanced visible light photocatalytic activity of mesoporous anatase TiO₂ co-doped with nitrogen and chlorine," *International Journal of Photoenergy*, vol. 2012, Article ID 593245, 6 pages, 2012.
- [30] K. Villa, A. Black, X. Domnech, and J. Peral, "Nitrogen doped TiO₂ for hydrogen production under visible light irradiation," *Solar Energy*, vol. 86, no. 1, pp. 558-566, 2012.
- [31] K. Yang, Y. Dai, and B. Huang, "Study of the nitrogen concentration influence on N-doped TiO₂ anatase from first-principles calculations," *Journal of Physical Chemistry C*, vol. 111, no. 32, pp. 12086-12090, 2007.
- [32] H. Irie, Y. Watanabe, and K. Hashimoto, "Nitrogen-concentration dependence on photocatalytic activity of TiO_{2-x}N_x powders," *Journal of Physical Chemistry B*, vol. 107, no. 23, pp. 5483-5486, 2003.
- [33] M. Kurtoglu, T. Longenbach, K. Sohlberg, and Y. Gogotsi, "Strong coupling of Cr and N in Cr-N-doped TiO₂ and its effect on photocatalytic activity," *Journal of Physical Chemistry C*, vol. 115, no. 35, pp. 17392-17399, 2011.
- [34] H. Sun, Y. Bai, H. Liu et al., "Mechanism of nitrogen-concentration dependence on pH value: experimental and theoretical studies on nitrogen-doped TiO₂," *Journal of Physical Chemistry C*, vol. 112, no. 34, pp. 13304-13309, 2008.
- [35] X. Zhang, K. Udagawa, Z. Liu et al., "Photocatalytic and photoelectrochemical studies on N-doped TiO₂ photocatalyst," *Journal of Photochemistry and Photobiology A*, vol. 202, no. 1, pp. 39-47, 2009.
- [36] J. Fang, F. Shi, J. Bu et al., "One-step synthesis of bifunctional TiO₂ catalysts and their photocatalytic activity," *Journal of Physical Chemistry C*, vol. 114, no. 17, pp. 7940-7948, 2010.
- [37] H. J. Jung, J. S. Hong, and J. K. Suh, "A study on removal efficiency of phenol and humic acid using spherical activated

- carbon doped by TiO_2 ,” *Korean Journal of Chemical Engineering*, vol. 28, no. 9, pp. 1882–1888, 2011.
- [38] C. C. Chen, C. S. Lu, Y. C. Chung, and J. L. Jan, “UV light induced photodegradation of malachite green on TiO_2 nanoparticles,” *Journal of Hazardous Materials*, vol. 141, no. 3, pp. 520–528, 2007.
- [39] W. Bahnemann, M. Muneer, and M. M. Haque, “Titanium dioxide-mediated photocatalysed degradation of few selected organic pollutants in aqueous suspensions,” *Catalysis Today*, vol. 124, no. 3–4, pp. 133–148, 2007.
- [40] D. Zhao, J. Cheng, and M. R. Hoffmann, “Kinetics of microwave-enhanced oxidation of phenol by hydrogen peroxide,” *Frontiers of Environmental Science & Engineering in China*, vol. 5, no. 1, pp. 57–64, 2011.
- [41] S. H. Lin, C. H. Chiou, C. K. Chang, and R. S. Juang, “Photocatalytic degradation of phenol on different phases of TiO_2 particles in aqueous suspensions under UV irradiation,” *Journal of Environmental Management*, vol. 92, no. 12, pp. 3098–3104, 2011.
- [42] Z. Guo, R. Ma, and G. Li, “Degradation of phenol by nanomaterial TiO_2 in wastewater,” *Chemical Engineering Journal*, vol. 119, no. 1, pp. 55–59, 2006.
- [43] E. B. Azevedo, F. R. D. A. Neto, and M. Dezotti, “ TiO_2 -photocatalyzed degradation of phenol in saline media: lumped kinetics, intermediates, and acute toxicity,” *Applied Catalysis B*, vol. 54, no. 3, pp. 165–173, 2004.
- [44] B. Yang, “Study on intermediates variation in the course of phenol degradation,” *Sci-Tech Information Development & Economy*, vol. 7, no. 13, pp. 129–123, 2003.
- [45] L. Xiong, L. Zheng, J. Xu et al., “Photocatalytic degradation of phenol with mesoporous $\text{TiO}_{2-x}\text{B}_x$,” *Environmental Chemistry Letters*, vol. 9, no. 2, pp. 251–257, 2011.
- [46] L. Liu, H. Liu, Y. P. Zhao et al., “Directed synthesis of hierarchical nanostructured TiO_2 catalysts and their morphology-dependent photocatalysis for phenol degradation,” *Environmental Science and Technology*, vol. 42, no. 7, pp. 2342–2348, 2008.

Research Article

Photoelectrocatalytic Performance of Benzoic Acid on TiO₂ Nanotube Array Electrodes

Hongchong Chen, Jinhua Li, Quanpeng Chen, Di Li, and Baoxue Zhou

School of Environmental Science and Engineering, Shanghai Jiao Tong University, Shanghai 200240, China

Correspondence should be addressed to Baoxue Zhou; zhoubaoxue@sjtu.edu.cn

Received 4 February 2013; Revised 22 April 2013; Accepted 22 April 2013

Academic Editor: Jiaguo Yu

Copyright © 2013 Hongchong Chen et al. This is an open access article distributed under the Creative Commons Attribution License, which permits unrestricted use, distribution, and reproduction in any medium, provided the original work is properly cited.

The photoelectrocatalytic performance of benzoic acid on TiO₂ nanotube array electrodes was investigated. A thin-cell was used to discuss the effect of the bias voltage, illumination intensity, and electrolyte concentration on the photoelectrocatalytic degradation efficiency of benzoic acid. The photogenerated current-time (*I-t*) profiles were found to be related to the adsorption and the degradation process. The relationship between the initial concentration and the photocurrent peaks (*I*_{0ph}) fits the Langmuir-type adsorption model, thus confirming that the adsorption of benzoic acid on TiO₂ nanotube arrays (TNAs) was single monolayer adsorption. At low concentrations, the *I-t* profiles simply decay after the initial transient peak due to the sufficient holes on the TNAs which would oxidize the benzoic acid quickly. However, the *I-t* profiles varied with increasing benzoic acid concentrations because the rate of diffusion in the bulk solution and the degradation of the intermediate products affect the photoelectrocatalysis on the electrode surface.

1. Introduction

For nearly three decades, the photocatalytic and photoelectrocatalytic degradation of organic substances on wide-bandgap semiconductive TiO₂ nanomaterials have drawn considerable attention because of their high photocatalytic efficiency, nontoxicity, nonphotocorrosiveness, favorable biological and chemical inertness, and low cost [1–5]. However, conventional TiO₂ nanoparticles also exhibit defects such as a high electron-hole recombination rate, low photocatalytic degradation efficiency, and difficult follow-up process [6].

To overcome these defects, considerable effort has been devoted to improving the photocatalytic ability of TiO₂ catalysts, including the synthesis of new TiO₂ structures [7–11]. TiO₂ nanotube arrays (TNAs) have gained attention and have been successfully applied to the photoelectrocatalytic degradation of a variety of organic pollutants because of their peculiar architecture, large surface area, high adsorption capacity, easy teleportation, and highly efficient degradation of organics [12–15].

Traditional studies on the photoelectrocatalytic oxidation of organic compounds were mainly performed in bulk

reactors, wherein the pollutant concentration was repeatedly determined over a certain period via absorption spectrophotometry [16–18]. However, this method limits the in-depth investigation of the reaction mechanism because of the relatively large body solution and long diffusion channel [19]. The use of a thin-cell with a small-volume cavity facilitated the study of the adsorption characteristics of organic substances and their interactions with the catalyst because of the subsequent increase in the ratio of the photoanode area to the organic solution volume. These studies led to the rapid completion of the exhaustive redox reaction [19, 20].

Benzoic acid was typical aromatic ring acid compound. It was the most commonly used food preservative and antibacterial agent [21]. It was also extensively used in the printing and dyeing industry (as a mordant of dyeing and printing) as well as in the pharmaceutical (as the intermediate) [22], steel (as an antirust agent) [23], and other industries [24]. In addition, benzoic acid is the intermediate metabolic product of various aromatic compounds and also the degradation intermediate product of many complex refractory organics [25]. However, few reports on the photoelectrocatalytic performance of benzoic acid compounds have been released.

In this paper, the photoelectrocatalytic performance of benzoic acid on TNA electrodes was investigated using a thin-cell reactor. The adsorption properties, microcosmic degradation process, and reaction characterization of benzoic acid on TNAs were investigated by analyzing the change in the photogenerated current-time ($I_{ph}-t$) profiles. The result of this study provides a solid foundation for future research into the reaction mechanism and reaction kinetics of aromatic organic compounds on TNA electrode surfaces.

2. Materials and Methods

2.1. Materials. Titanium sheets (0.25 mm thick, 99.9% purity) were purchased from Sumitomo Chemical (Japan). Unless otherwise indicated, reagents were obtained from Sinopharm Chemical Reagent Company and were used as received. High-purity deionised water was used in the preparation of all solutions.

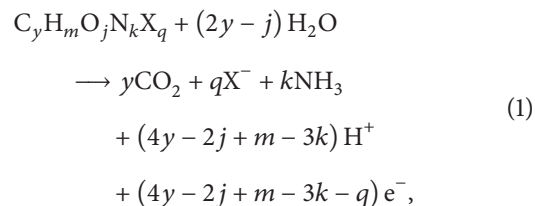
2.2. Preparation of TiO_2 Nanotube Array Electrode. The preparing method of TiO_2 nanotube array electrodes has been published in our previous work [18]. Hence, only key points of the fabrication process were summarized here. The electrolyte contain 0.1 mol/L NaF, 1 mol/L $NaHSO_4$ and 0.2 mol/L trisodium citrate, also with NaOH added to adjust the pH. The TiO_2 nanotube array electrodes are prepared under constant stirring for 4 h. After anodization, the as-prepared sample was washed with high-purity deionized water and dried at room temperature. Then it was annealed in a laboratory muffle furnace at 500°C to crystallize in the air ambience. X-ray diffraction (Bruker, D8 ADVANCE, Germany) analysis showed that the crystal structure of TNA is anatase [18].

2.3. Apparatus and Methods. All experiments were performed at room temperature in a three-electrode electrochemical cell with a quartz window (0.82 cm²). The thickness of the spacer was 0.1 mm, which defined the cell volume of 8.2 μ L. The structure of thin-cell reactor has been reported in our previous paper [18]. The TiO_2 nanotube array electrode was used as a working electrode; a saturated Ag/AgCl electrode and a platinum foil were used as the reference and the counter electrodes, respectively. Also 2 mol/L $NaNO_3$ was chosen as the supporting electrolyte in the experiment. The supply bias and work current are controlled by a CHI (CH Instrument, Inc., CHI601d, USA) electrochemical analyzer; 2W LED UV lamp (365 nm) was chosen as UV light source. The light intensity in experiment was measured by UV-A ultraviolet irradiator.

3. Results and Discussion

3.1. The Photocurrent-Time Profile Property and Net Charge Determined in Thin-Cell. In the photoelectrochemical reaction, the oxidation of organic compounds at the electrodes

can be represented by the following electrode reaction equation:



where X represents the halogen atom. The numbers of carbon, hydrogen, oxygen, nitrogen, and halogen atoms in the organic compound are represented by y , m , j , k , and q .

Faraday's law can be used to quantify the concentration by measuring the charge passed if the organics is completely oxidized. That is,

$$Q_{net} = \int I dt = nFVC, \quad (2)$$

where I is the photocurrent from the oxidation of the organics and t is the time elapsed upon illumination; Q_{net} is the direct measure of net charge of the organics; n is the number of electrons transferred and C is the concentration of the organics, while the volume (V) and the Faraday constant (F) are known constants.

Figure 1 shows a set of typical photocurrent-time profiles in the exhaustive mode in thin-cell at the fixed applied bias potential of 2.5 V. Figures 1(c) and 1(d) show the photocurrent response of a blank solution of 2.0 mol/L $NaNO_3$ and a 2.0 mol/L $NaNO_3$ solution containing 0.4 mmol/L benzoic acid in a thin-cell in the absence of illumination (electrocatalytic performances). The results show that there is no photocurrent under dark conditions which indicate that the benzoic acid in thin-cell cannot be oxidized. Figure 1(a) shows the typical photocurrent response of a blank solution of 2.0 mol/L $NaNO_3$ under the illumination conditions (7.9 mW/cm²). The even photocurrent (I_{blank}) observed for the blank solution originated from the stable oxidation of water. Figure 1(b) shows the photocurrent response of a 2.0 mol/L $NaNO_3$ solution containing 0.4 mmol/L benzoic acid in a thin-cell under the same illumination (7.9 mW/cm²). The total photocurrent (I_{total}) observed for the benzoic acid solution was the total of two different components: one originates from the photoelectrocatalytic oxidation of benzoic acid, whereas the other was from water oxidation, which was the same as I_{blank} (Figure 1(a)). When the I_{total} decreases to the level of I_{blank} , the oxidation of organics was finished. Hence, the processes of the photoelectrochemical reaction in thin-cell were described by the change of $I-t$ profile.

The net charge which originated from the oxidation of organics was defined as Q_{net} , which can be obtained by subtracting Q_{blank} from Q_{total} . The net charge which obtained by (2) was defined as ThQ_{net} . Because the change of net charge is directly related to concentration of organics during the photoelectrochemical reaction. The degradation efficiency (DE) of the photoelectrochemical reaction can be defined as the ratio of Q_{net} to ThQ_{net} , which can be used in describing the property of thin-cell.

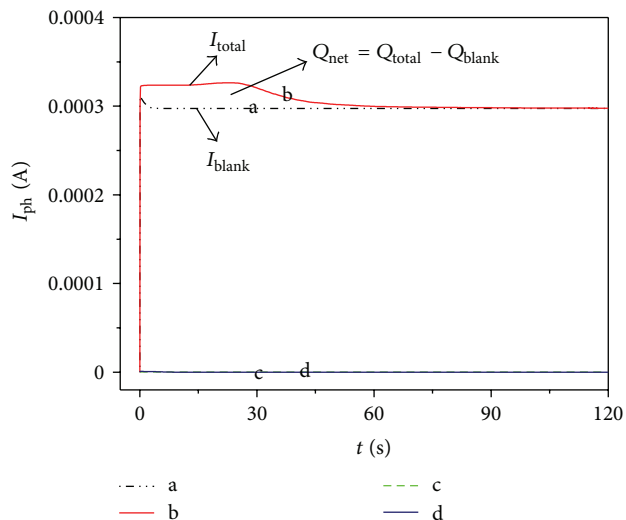


FIGURE 1: Typical photocurrent-time responses obtained from the thin-cell (a) 2.0 mol/L NaNO_3 solution under illumination; (b) 2.0 mol/L NaNO_3 with 0.4 mmol/L benzoic acid under illumination; (c) 2.0 mol/L NaNO_3 solution under no illumination; (d) 2.0 mol/L NaNO_3 with 0.4 mmol/L benzoic acid under no illumination.

According to (1), the stoichiometric oxidation of benzoic acid can be represented as



That is, if the complete mineralisation of benzoic acid has been achieved, 1 mol of benzoic acid requires 30 mol of electrons. The relationship between the net charge and the concentration should be written as follows with the cell volume, $V = 8.2 \mu\text{L}$, being used:

$$ThQ_{\text{net}} = 30FVC = 0.0237C. \quad (4)$$

Hence, the ThQ_{net} of 0.2 mmol/L, 0.4 mmol/L, and 0.8 mmol/L were 0.00474 mC, and 0.00948 mC, 0.01896 mC.

3.2. Effect of Photoelectrocatalytic Degradation on Benzoic Acid

3.2.1. Effect of the Bias Voltage. The cyclic voltammograms of a 2.0 mol/L NaNO_3 solution is shown in Figure 2. The photocurrent increases with the bias voltage, indicating that the bias voltage can improve the electronic transmission performance of TNAs in the thin-cell. This increase may affect the photoelectrocatalytic degradation efficiency of benzoic acid. In the low-bias voltage range ($<2\text{ V}$), the photocurrent rapidly increases with the bias voltage, thus demonstrating that the photogenerated electrons cannot be completely exported to the external circuit. When the bias voltage is between 2 and 4 V, the photocurrent appears in a saturated platform, indicating that the photogenerated electrons have been completely exported and that the recombination of electrons and holes has been restricted. After the platform becomes saturated ($>4\text{ V}$), the photocurrent again increases with the bias voltage and can cause the water molecules

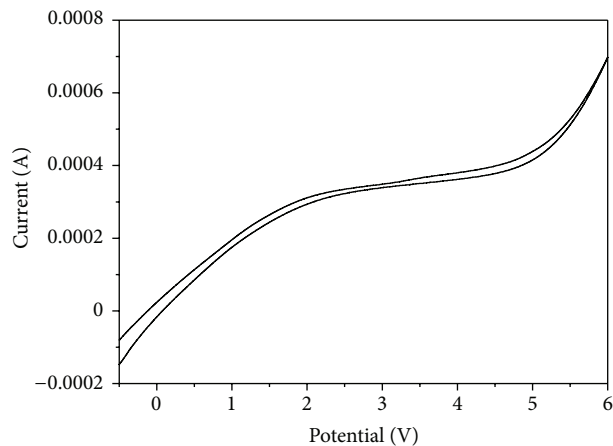


FIGURE 2: Cyclic voltammograms of a 2.0 mol/L NaNO_3 blank solution in a thin-cell reactor based on the TNA electrodes under illuminations of 7.9 mW/cm^2 .

to decompose when the bias voltage reaches the oxygen evolution potential of the TNA electrode. The results in Figure 3 support this view.

Figure 3 shows the photocurrent-time profile of benzoic acid (0.4 mmol/L) degradation at different bias voltages and under 7.9 mW/cm^2 ultraviolet (UV) illuminations. As show in Figure 3, when the bias voltage is below 3 V, the degradation time of benzoic acid decreased as the bias voltage increased. This was indicated that the increase in the bias voltage can also improve the degradation rate of benzoic acid on TNAs. However, the photocurrent curve continuously increases when the bias voltage is 4 V, which leads to failure in identifying the reaction termination using a computer. This result indicates that the degradation of benzoic acid is significantly perturbed by the water decomposition when the bias voltage is too high.

Table 1 shows the Q_{net} value and degradation efficiency (DE) of benzoic acid under different bias voltages. When the bias voltage is below 2 V, the DE of benzoic acid increases with the bias voltage, indicating that the application of a bias voltage can enhance the photoelectrocatalytic capability of TNAs for benzoic acid. When the bias voltage is set between 2 and 3 V, the degradation efficiency of benzoic acid exceeds 99.5%, indicating that the benzoic acid is completely degraded. The Q_{net} value remains stable in this condition, indicating that the value of Q_{net} is related only to the transferred electronics during the photoelectrocatalytic oxidation. Therefore, the bias voltage should be set within the electrochemical window (2 V to 3 V).

3.2.2. Effect of Light Intensity. Figure 4 shows the photocurrent responses of a 2 mol/L NaNO_3 blank solution containing benzoic acid (0.4 mmol/L) under different light intensities. The more intense the light, the shorter the time for complete degradation, indicating that an increase in the intensity of light is conducive to promoting the photoelectrocatalytic degradation rate.

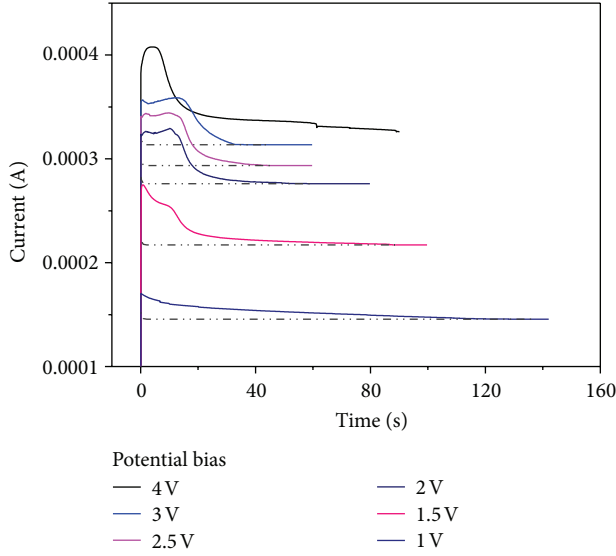


FIGURE 3: Photocurrent responses of a 2 mol/L NaNO_3 blank solution containing benzoic acid (0.4 mmol/L) in the thin-cell reactor based on the TNA electrodes at different fixed applied bias potentials under bias voltages under illuminations of 7.9 mW/cm^2 .

Figure 4 shows that the photocurrent increases with the light intensity, indicating that the increases of light intensity can improve the electronic transmission performance of TNAs. The photocurrent-time curve shapes vary with the light intensity, demonstrating that the light intensity affects the photoelectrocatalysis of benzoic acid on TNAs.

Table 2 shows that the Q_{net} and degradation efficiency of 0.8 mmol/L benzoic acid increase with the light intensity when the light intensity is below 5.53 mW/cm^2 . This result indicates that benzoic acid is not completely mineralized because of the insufficient light intensity not inducing enough electron-hole pairs of TNAs in the thin-cell.

However, the Q_{net} of benzoic acid at low concentrations (0.2 and 0.4 mmol/L) and at 0.8 mmol/L under sufficient light intensity (above 5.53 mW/cm^2) remain comparatively constant, confirming that Q_{net} is not related to the light intensity but is associated with the transferred electrons in the photoelectric catalytic oxidation when benzoic acid is completely mineralized.

3.2.3. Effect of Electrolyte Concentration. The transfer of electrons in the thin-cell reactor was affected by the electrolyte solution. The voltammograms of 0.4 mmol/L benzoic acid with different NaNO_3 concentrations under light (7.9 mW/cm^2) are shown in Figure 5. The photocurrent rapidly increases with the voltage when the NaNO_3 concentration is below 1 mol/L, indicating that the photoinduced electrons are not completely exported to the external circuit. When the concentration exceeds 1.5 mol/L, the photocurrent exhibits a saturated platform, indicating that the photo-generated electrons are completely exported and that the recombination of electrons and holes is restricted. The higher the electrolyte concentration, the stronger the conductivity.

TABLE 1: Q_{net} value and degradation efficiency (DE) under different bias voltages.

Bias voltage (V)	1	1.5	2	2.5	3
Q_{net} (mC)	0.008511	0.009048	0.009433	0.009469	0.009443
DE (%)	90.20	95.45	99.50	99.88	99.61

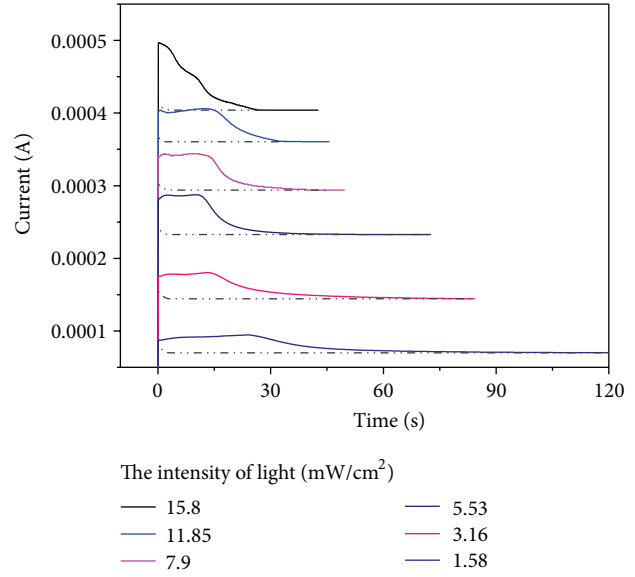


FIGURE 4: Photocurrent responses of a 2 mol/L NaNO_3 blank solution containing benzoic acid (0.4 mmol/L) in the thin-cell reactor based on the TNA electrodes at the fixed applied bias potential of 2.5 V under different light intensities.

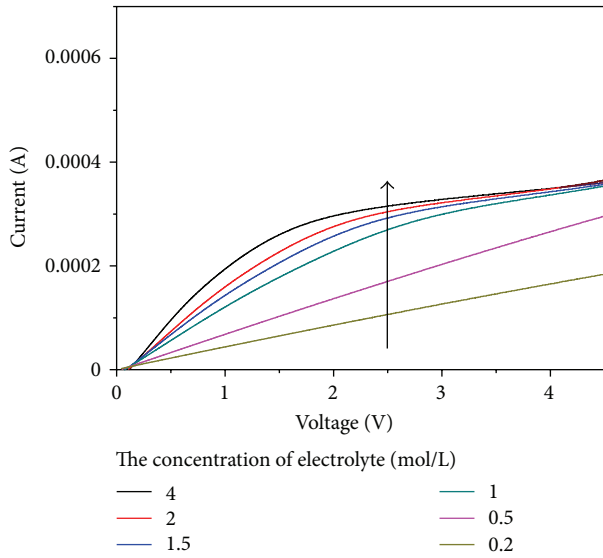
Table 3 shows that Q_{net} gradually increases with the electrolyte concentration and is lower than ThQ_{net} when the NaNO_3 electrolyte concentration is below 1 mol/L. These results indicate that benzoic acid cannot be completely degraded because of the insufficient number of hole on TNAs. When the NaNO_3 electrolyte concentration exceeds 1.5 mol/L, Q_{net} remains stable and close to ThQ_{net} , indicating that benzoic acid has been completely degraded because of the sufficient number of holes in this condition.

3.3. Photoelectrocatalytic Degradation Property and Mechanism of Benzoic Acid. The photocurrent response profiles of benzoic acid for seven different concentrations in the thin-cell reactor are shown in Figure 6. A comparison between Q_{net} and ThQ_{net} shows that the different concentrations of benzoic acid have all been completely degraded in a photoelectrocatalytic manner.

The relationship between the initial organic concentrations and I_{0ph} was used to analyze the adsorption properties of benzoic acid on TNAs because the I_{0ph} value corresponds to the initial degradation rate according to the principle of photoelectric catalysis. Figure 6(a) shows that the peak photocurrent (I_{0ph}) increases with C_0 . At low organic concentrations, I_{0ph} is proportional to C_0 , possibly because of the photohole capture process during benzoic acid mineralization. However, as the benzoic acid concentration

TABLE 2: Q_{net} value and degradation efficiency (DE) of different concentrations of benzoic acid under varying light intensities.

Concentration (mmol/L)	Light intensities (mW/cm ²)	1.58	3.16	5.53	7.9	11.85	15.8
0.2	Q_{net} (mC)	0.009423	0.009434	0.009421	0.009467	0.009449	0.009409
	DE (%)	99.47	99.52	99.38	99.86	99.67	99.25
0.4	Q_{net} (mC)	0.009471	0.009454	0.009513	0.009470	0.009406	0.009433
	DE (%)	99.90	99.72	100.34	99.89	99.21	99.50
0.8	Q_{net} (mC)	0.008552	0.009075	0.009434	0.009445	0.009466	0.009429
	DE (%)	90.21	95.73	99.52	99.63	99.85	99.46

FIGURE 5: Voltammograms of different concentrations of NaNO_3 blank solution containing benzoic acid (0.4 mmol/L) in the thin-cell reactor based on the TNA electrodes under illumination of 7.9 mW/cm^2 .TABLE 3: Q_{net} and degradation efficiency of 0.4 mmol/L benzoic acid with different NaNO_3 concentrations under illumination of 7.9 mW/cm^2 and a fixed applied bias voltage of 2.5 V.

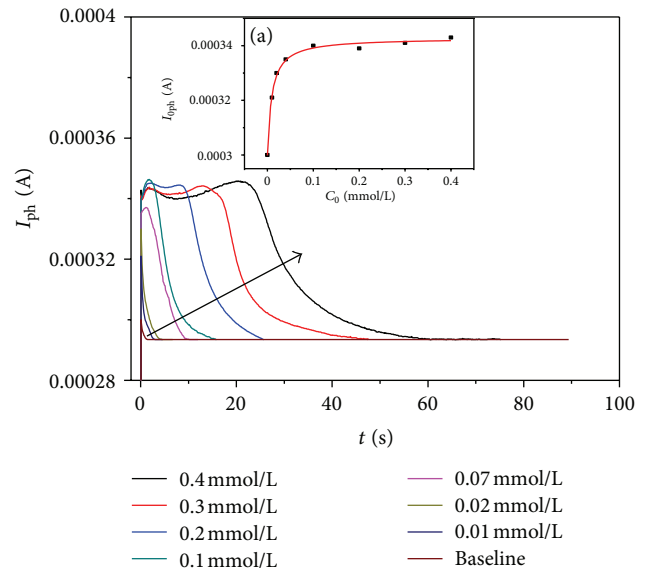
Electrolyte concentration (mol/L)	0.5	1	1.5	2
Q_{net} (mC)	0.008112	0.009260	0.009415	0.009436
DE (%)	85.57	97.68	99.31	99.54

increases to a certain level, photohole generation becomes the rate-limiting step, and the increase in I_{oph} begins to slow down.

The relationship between I_{oph} and C_0 was simulated using a computer as follows:

$$I_{\text{oph}} = \frac{4 \times 10^{-5} \times 106C_0}{1 + 106C_0} + 0.0003, \quad R^2 = 0.9945. \quad (5)$$

The data (4) fit the *Langmuir* adsorption isotherm. These results confirm that the adsorption behavior of benzoic acid on the TNAs is that of a monolayer adsorption.

FIGURE 6: Photocurrent response profiles derived from the photoelectrocatalytic oxidation of different concentrations of benzoic acid in the thin-cell reactor based on the TNA electrodes. (a) Relationship between the initial concentration (C_0) and the net peak photocurrent (I_{oph}) of the TNA electrode for benzoic acid.

The photocurrent response profiles of benzoic acid at seven different concentrations are shown in Figure 6. The degradation $I-t$ profiles all show decay to a stable value. However, this decay varies with increasing concentrations, thereby illustrating the disparities in the photoelectrocatalytic process as well as the mechanism of benzoic acid degradation at different concentrations.

At low concentrations (0 mmol/L to 0.02 mmol/L), the transient photocurrent rapidly reaches its peak at the initial stage because of the rapid degradation of the benzoic acid originally adsorbed on the TNA surface. The photocurrent then begins to decrease because of benzoic acid mineralization. After a certain period, the photocurrent finally reaches a stable value and overlaps with I_{blank} . This result indicates that the photoelectrocatalytic degradation of benzoic acid in the thin-cell reactor is complete.

When the benzoic acid concentration reaches an intermediate level (0.07 mmol/L to 0.1 mmol/L), the curve continues increasing after the initial peak, possibly because of the

degradation of the intermediates. Figure 6(a) shows that the adsorption of the electrode surface has not reached saturation at that point, indicating that the number of photogenerated holes on the electrode surface is sufficient. Thus, the rapid oxidation of intermediate products, which can be more easily oxidized than benzoic acid, may have caused the current to increase.

As the concentration increases to levels above 0.2 mmol/L (0.1 mmol/L, e.g.), the I - t profiles can be divided into five major processes: a rapid increase to the transient photocurrent spikes, a continuous increase, a rapid decrease, a re-increase, and a decrease to a stable value. Meanwhile, Figure 6(a) shows that the adsorption on the TNAs has reached saturation, indicating that the holes on the TNA electrode surface cannot oxidate all benzoic acid on the TNAs simultaneously. This photoelectrocatalytic process can be explained as follows. In the initial stage, the benzoic acid molecule on the surface of the TNA electrode is rapidly oxidized, and the photocurrent rapidly reaches the initial peak. After the first oxidization, the resting benzoic acid absorbed on the TNA surface at elevated concentrations as well as the intermediate products is oxidized, which results in the continuous increase of the curve for benzoic acid after the initial peak. The benzoic acid concentration cannot be supplemented in time because the rate of adsorption may be slower than the speed of degradation. Therefore, the optical current rapidly decreases. After a certain period, the area covered by the benzoic acid absorbents begins to increase, which results in a re-increase in the current. Afterward, the benzoic acid concentration decreases, which results in the decrease in the photocurrent. These findings indicate that when the benzoic acid concentration is high, the diffusion of benzoic acid in the bulk solution of the reactor as well as the degradation of intermediate products from benzoic acid decomposition would affect the photoelectrocatalysis on the electrode surface.

4. Conclusions

The photoelectrocatalytic performance of benzoic acid on the TiO_2 nanotube array electrode was investigated using a thin-cell reactor. The adsorption, degradation rate, and reaction characteristics of benzoic acid degradation were discussed by analyzing the changes in the photogenerated I - t profiles. The result of this paper provides a solid foundation for future research into the degradation characteristics, reaction mechanism, and reaction kinetics of aromatic organic compounds on the TNA electrode surface.

Acknowledgments

The project was supported by the National High Technology Research and Development Program of China (863) (2009AA063003), the National Natural Science Foundation of China (no. 20 677039), and R&D Foundation of Shanghai Jiaotong University. The authors are for support of XRD lab in Instrumental Analysis Center of SJTU.

References

- [1] J. H. Carey, J. Lawrence, and H. M. Tosine, "Photodechlorination of PCB's in the presence of titanium dioxide in aqueous suspensions," *Bulletin of Environmental Contamination and Toxicology*, vol. 16, no. 6, pp. 697–701, 1976.
- [2] D. H. Kim and M. A. Anderson, "Photoelectrocatalytic degradation of formic acid using a porous TiO_2 thin-film electrode," *Environmental Science and Technology*, vol. 28, no. 3, pp. 479–483, 1994.
- [3] X. Z. Li, H. L. Liu, P. T. Yue, and Y. P. Sun, "Photoelectrocatalytic oxidation of rose Bengal in aqueous solution using a Ti/TiO_2 mesh electrode," *Environmental Science and Technology*, vol. 34, no. 20, pp. 4401–4406, 2000.
- [4] H. L. Liu, D. Zhou, X. Z. Li, and P. T. Yue, "Photoelectrocatalytic degradation of Rose Bengal," *Journal of Environmental Sciences*, vol. 15, no. 5, pp. 595–599, 2003.
- [5] S. Dezh, C. Sheng, J. S. Chung, D. Xiaodong, and Z. Zhibin, "Photocatalytic degradation of toluene using a novel flow reactor with Fe-doped TiO_2 catalyst on porous nickel sheets," *Photochemistry and Photobiology*, vol. 81, no. 2, pp. 352–357, 2005.
- [6] J. Bai, J. H. Li, Y. B. Liu, B. X. Zhou, and W. M. Cai, "A new glass substrate photoelectrocatalytic electrode for efficient visible-light hydrogen production: CdS sensitized TiO_2 nanotube arrays," *Applied Catalysis B*, vol. 95, no. 3–4, pp. 408–413, 2010.
- [7] Y. X. Li, Y. Xiang, S. Q. Peng, X. W. Wang, and L. Zhou, "Modification of Zr-doped titania nanotube arrays by urea pyrolysis for enhanced visible-light photo electrochemical H_2 generation," *Electrochimica Acta*, vol. 87, no. 1, pp. 794–800, 2013.
- [8] D. W. Gong, C. A. Grimes, O. K. Varghese et al., "Titanium oxide nanotube arrays prepared by anodic oxidation," *Journal of Materials Research*, vol. 16, no. 12, pp. 3331–3334, 2001.
- [9] Z. H. Xu and J. G. Yu, "Visible-light-induced photoelectrochemical behaviors of Fe-modified TiO_2 nanotube arrays," *Nanoscale*, vol. 3, no. 8, pp. 3138–3144, 2011.
- [10] G. P. Dai, J. G. Yu, and G. Liu, "Synthesis and enhanced visible-light photoelectrocatalytic activity of p-N junction BiOI/TiO_2 nanotube arrays," *Journal of Physical Chemistry C*, vol. 115, no. 15, pp. 7339–7346, 2011.
- [11] Z. H. Xu, J. G. Yu, and G. Liu, "Enhancement of ethanol electrooxidation on plasmonic Au/TiO_2 nanotube arrays," *Electrochemistry Communications*, vol. 13, no. 11, pp. 1260–1263, 2011.
- [12] W. B. Zhang, T. C. An, X. M. Xiao et al., "Photoelectrocatalytic degradation of reactive brilliant orange K-R in a new continuous flow photoelectrocatalytic reactor," *Applied Catalysis A*, vol. 255, no. 2, pp. 221–229, 2003.
- [13] T. An, G. Li, X. Zhu, J. Fu, G. Sheng, and Z. Kun, "Photoelectrocatalytic degradation of oxalic acid in aqueous phase with a novel three-dimensional electrode-hollow quartz tube photoelectrocatalytic reactor," *Applied Catalysis A*, vol. 279, no. 1–2, pp. 247–256, 2005.
- [14] Q. Q. Meng, J. G. Wang, Q. Xie, H. Q. Dong, and X. N. Li, "Water splitting on TiO_2 nanotube arrays," *Catalysis Today*, vol. 165, no. 1, pp. 145–149, 2011.
- [15] C. H. Wang, X. T. Zhang, C. L. Shao et al., "Rutile TiO_2 nanowires on anatase TiO_2 nanofibers: a branched heterostructured photocatalysts via interface-assisted fabrication approach," *Journal of Colloid and Interface Science*, vol. 363, no. 1, pp. 157–164, 2011.

- [16] L. Gu, F. Y. Song, and N. W. Zhu, "An innovative electrochemical degradation of 1-diazo-2-naphthol-4-sulfonic acid in the presence of $\text{Bi}_2\text{Fe}_4\text{O}_9$," *Applied Catalysis B*, vol. 110, no. 2, pp. 186–194, 2011.
- [17] J. Krýsa, G. Waldner, H. Měšt'ánková, J. Jirkovský, and G. Grabner, "Photocatalytic degradation of model organic pollutants on an immobilized particulate TiO_2 layer. Roles of adsorption processes and mechanistic complexity," *Applied Catalysis B*, vol. 64, no. 3-4, pp. 290–301, 2006.
- [18] X. J. Yu, Y. Q. Wang, Z. L. Li, S. Bai, and D. Sun, "Study on deactivated mechanism and regeneration methods of TiO_2 during photocatalytic benzoic acid," *Acta Scientiae Circumstantiae*, vol. 26, no. 3, pp. 433–437, 2006.
- [19] Q. Zheng, B. X. Zhou, J. Bai et al., "Self-organized TiO_2 nanotube array sensor for the determination of chemical oxygen demand," *Advanced Materials*, vol. 20, no. 5, pp. 1044–1049, 2008.
- [20] J. L. Zhang, B. X. Zhou, Q. Zheng et al., "Photoelectrocatalytic COD determination method using highly ordered TiO_2 nanotube array," *Water Research*, vol. 43, no. 7, pp. 1986–1992, 2009.
- [21] D. S. Ling, H. Y. Xie, Y. Z. He, W. E. Gan, and Y. Gao, "Determination of preservatives by integrative coupling method of headspace liquid-phase microextraction and capillary zone electrophoresis," *Journal of Chromatography A*, vol. 1217, no. 49, pp. 7807–7811, 2010.
- [22] A. Ali, S. S. Somayeh, and S. Abbas, "Synthesis and antimycobacterial activity of 2-(phenylthio) benzoylarylhydrazones derivatives servicesIranian," *Journal of Pharmaceutical Research*, vol. 10, no. 4, pp. 727–731, 2011.
- [23] Z. M. Chen, P. Lu, Y. L. Su, and M. He, "Preparation and performance evaluation of water-based rust inhibitor for iron and steel," *Materials Protection*, vol. 44, no. 6, pp. 58–59, 2011.
- [24] T. Jyothi and C. AKe, "Rasmuson Particle engineering of benzoic acid by spherical agglomeration," *European Journal of Pharmaceutical Sciences*, vol. 45, no. 5, pp. 657–667, 2012.
- [25] C. G. Silva and J. L. Faria, "Photocatalytic oxidation of benzene derivatives in aqueous suspensions: synergic effect induced by the introduction of carbon nanotubes in a TiO_2 matrix," *Applied Catalysis B*, vol. 101, no. 1-2, pp. 81–89, 2010.

Research Article

Fabrication and Photocatalytic Property of One-Dimensional $\text{SrTiO}_3/\text{TiO}_{2-x}\text{N}_x$ Nanostructures

Huarong Zhang, Miao Guashuai, Ma Xingping, and Wang Bei

Institute of Microsystemic Physics and School of Physics & Electronics, Henan University, Kaifeng 475001, China

Correspondence should be addressed to Huarong Zhang; zhanghake@yahoo.com

Received 31 January 2013; Revised 18 April 2013; Accepted 19 April 2013

Academic Editor: Gang Liu

Copyright © 2013 Huarong Zhang et al. This is an open access article distributed under the Creative Commons Attribution License, which permits unrestricted use, distribution, and reproduction in any medium, provided the original work is properly cited.

One-dimensional $\text{SrTiO}_3/\text{TiO}_{2-x}\text{N}_x$ nanostructures were prepared by the hydrothermal method and investigated by X-ray diffraction (XRD), transmission electron microscopy (TEM), X-ray photoelectron spectroscopy (XPS), and ultraviolet-visible diffuse reflectance spectroscopy (UV-vis DRS) measurements. The photocatalytic activities of the prepared samples were evaluated by photodegrading the methylene blue (MB) solution. According to the characterizations, the intermediate product of SrTiO_3 /titanate nanotubes was presented after hydrothermal processing of the $\text{TiO}_{2-x}\text{N}_x$ nanoparticles with the mixed solution of NaOH and $\text{Sr}(\text{NO}_3)_2$. The final product of $\text{SrTiO}_3/\text{TiO}_{2-x}\text{N}_x$ nanorods was obtained after calcining the intermediate. As compared to the $\text{TiO}_{2-x}\text{N}_x$ nanoparticles, the absorption performance of SrTiO_3 /titanate nanotubes or $\text{SrTiO}_3/\text{TiO}_{2-x}\text{N}_x$ nanorods was depressed, instead of improving it. The mechanisms of the absorption property changes were discussed. The $\text{SrTiO}_3/\text{TiO}_{2-x}\text{N}_x$ nanorods presented better photocatalytic activity than the $\text{TiO}_{2-x}\text{N}_x$ nanoparticles or nanorods. However, due to overmuch adsorption, the SrTiO_3 /titanate nanotubes gave ordinary photocatalytic performances.

1. Introduction

TiO_2 has been extensively investigated for several decades in photocatalysis and photovoltaic areas. Anatase-type TiO_2 has attracted great interest as one of the most promising photocatalysts due to its impressed advantages such as high degradation capability, chemical stability, and low cost. However, the application potential of TiO_2 photocatalyst is restricted for its low quantum efficiency which is mainly caused by its low light absorption efficiency and high photogenerated charge carrier recombination rate. One-dimensional (1D) nanostructures can facilitate transport of charge carriers and minimize the loss of charge carriers at grain boundaries [1–3]. Hence, the charge carrier recombination of TiO_2 is expected to be held back by fabricating 1D nanostructure. Another efficient method to increase the charge separation efficiency of TiO_2 is modifying the photocatalyst with some other semiconductors because of the charge carrier transfer between valence or conduction band of two different semiconductors [4–6].

Recently, TiO_2 photocatalyst was reported to be modified by various materials such as graphene [7], Fe_3O_4 [8], C_{60}

[9], CdS, and Bi_2S_3 [10], by which the photocatalytic activity of TiO_2 was enhanced. Moreover, to further improve the photogenerated charge carrier separation rate, some semiconductors were coupled with prepared 1D nanostructures (such as nanotube, nanofiber, and nanorod). Zhai et al. reported high photoactivities in the visible light responsive graphene/titanate nanotubes photocatalysts fabricated by hydrothermal method [11]. Yi et al. fabricated the silver nanoparticles, decorated nanobranched TiO_2 nanofibers, and presented that the photocatalytic degradation rates of silver loaded on nanobranched TiO_2 nanofibers were 1.6 and 1.7 times as those of pure TiO_2 nanofibers in the presence of methylene blue and methyl orange, respectively [12].

Cubic-perovskite-type SrTiO_3 , a multimetallc oxide semiconductor with a band gap of 3.4 eV comparable to TiO_2 , has drawn considerable interest because of its applications in storage batteries, thermoelectric property, solar cell, and photocatalysis [13–16]. SrTiO_3 is a good candidate for coupling TiO_2 and improving the photocatalytic performance of the photocatalyst because its conduction band edge is more negative than TiO_2 . Due to the potential differences between

the band edges of these two semiconductors, the photogenerated electrons transfer from the conduction band of SrTiO_3 to that of TiO_2 . Conversely, the photogenerated electrons transfer from the conduction band of SrTiO_3 to that of TiO_2 . Then the photogenerated charge carriers can be efficiently separated by these processes, resulting in the enhancement of the photocatalytic property in the photocatalyst. Recently, some research work about $\text{SrTiO}_3/\text{TiO}_2$ photocatalysts has been reported [17–19]. On the other hand, it has been extensively reported that N-doping could obviously improve the photocatalytic activity of TiO_2 [20, 21]. In this work, we fabricated one-dimensional $\text{SrTiO}_3/\text{TiO}_{2-x}\text{N}_x$ nanostructures by the hydrothermal method. The photocatalytic activity for the degradation of methylene blue (MB) solution in the N-doped TiO_2 was greatly enhanced after coupling with SrTiO_3 .

2. Materials and Methods

2.1. Sample Preparation. Anatase nanocrystalline $\text{TiO}_{2-x}\text{N}_x$ was synthesized by a simple sol-gel method as our previous work described [22]. Different amounts of $\text{Sr}(\text{NO}_3)_2$ were dissolved in 40 mL of 10 mol/L NaOH solution. Then 0.78 g N- TiO_2 powder was dispersed into the mixture solution to form a suspension which was heated at 180°C for 24 h under hydrothermal condition in a PTFE-lined stainless steel vessel. The observed sediment at the bottom of the vessel was washed with 0.1 mol/L HCl solutions until pH is less than 7, followed by washing with DI water and drying at 80°C in air overnight. The dried powder was milled and calcined at 400°C under air for 2 h. $\text{SrTiO}_3/\text{N-TiO}_2$ samples with different ratios of SrTiO_3 were then prepared.

2.2. Characterization and Measurements. X-ray diffraction (XRD) patterns were recorded on a DX-2500 diffractometer (Fangyuan, Dandong) with $\text{Cu K}\alpha$ radiation with $\lambda = 0.154145$ nm. Transmission electron microscopy (TEM) measurements were carried out on a JEOL-2010 TEM at an acceleration voltage of 200 kV. X-ray photoelectron spectroscopy (XPS) measurements were recorded on an Axis Ultra system with monochromatic Al $\text{K}\alpha$ X-rays (1486.6 eV) operated at 45 W and 15 kV with a background pressure of approximately 5.0×10^{-9} Torr. A survey spot size and 40 eV pass energy were used for the analysis. Emitted photoelectrons perpendicular to the sample surface were collected. The binding energy of all investigated elements was referenced by the C 1s peak at 284.8 eV of the surface adventitious carbon, respectively. The diffuse reflection spectra were obtained on an UV-vis spectrophotometer (Varian Cary 5000) using BaSO_4 as the reference standard and were converted to the absorbance data through the Kubelka-Munk method.

Photocatalytic experiments were carried out in an inner-irradiation-type reactor. A cylindrical reaction cell was used to contain the reaction solution, and a 500 W long-arc xenon lamp surrounded with a water cooling system was fixed in the center of the reaction cell. 30 mg of photocatalyst was suspended in 200 mL of a methylene blue (MB) solution (10 mg/L) under stirring magnetically. The mixture was kept in the dark for 30 minutes to establish an

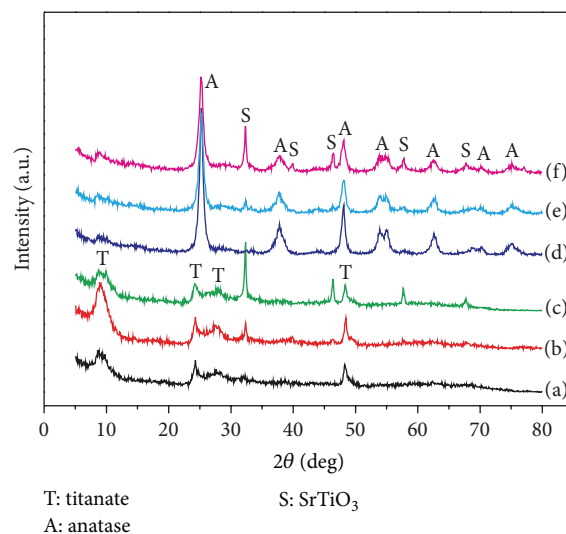


FIGURE 1: XRD patterns for the uncalcined ((a): 1%; (b): 2%; (c): 5%) and calcined ((d): 1%; (e): 2%; (f): 5%) samples with different Sr/Ti ratios.

adsorption-desorption equilibrium before the light radiation. The amount of MB in the solution was determined on the basis of its characteristic optical absorption at 665 nm using a visible light spectrophotometer (Model: 723C) based on Lambert-Beer's law.

3. Results and Discussion

3.1. Crystal Structure and Morphology. The XRD patterns of the uncalcined and calcined samples are presented in Figure 1. The main diffraction peaks at about 9.1° , 24.3° , 28.0° , and 48.3° in the patterns of the uncalcined samples (Figures 1(a), 1(b), and 1(c)) are designated to the protonic titanate phase [23]. Additionally, with the increase of the Sr/Ti ratio, the intensity of the diffraction peaks contributed by SrTiO_3 at about 32.3° , 46.4° , 57.5° , and 67.6° gradually increases. From Figures 1(d), 1(e), and 1(f), it can be found that main crystalline phases in the calcined samples involve the anatase and SrTiO_3 phase. Figure 2 shows the morphologies of the uncalcined and calcined samples. From the TEM results as shown in Figures 2(a), 2(b), and 2(c), it is found that the uncalcined samples are all composed of nanotubes with lengths about 200–300 nm and diameters about 10 nm. After the calcination, the nanotubes in the uncalcined samples morph into nanorods with diameters of 5–10 nm and different lengths as Figures 2(d), 2(e), and 2(f) show.

3.2. XPS Measurements. Figure 3 shows the XPS spectra of O 1s, N 1s, Ti 2p, and Sr 3d for the $\text{SrTiO}_3/\text{TiO}_{2-x}\text{N}_x$ with the Sr/Ti ratio of 5%. After fitting the result of O 1s XPS, it can be found that two peaks centered at 529.8 eV and 531.2 eV are observed in the O 1s XPS peak, attributing to bulk oxygen bonded to titanium and surface hydroxyl oxygen in TiO_2 , respectively [22, 24]. From Figure 3, a similar broad peak from 397 eV to 403 eV is displayed in the XPS pattern of N

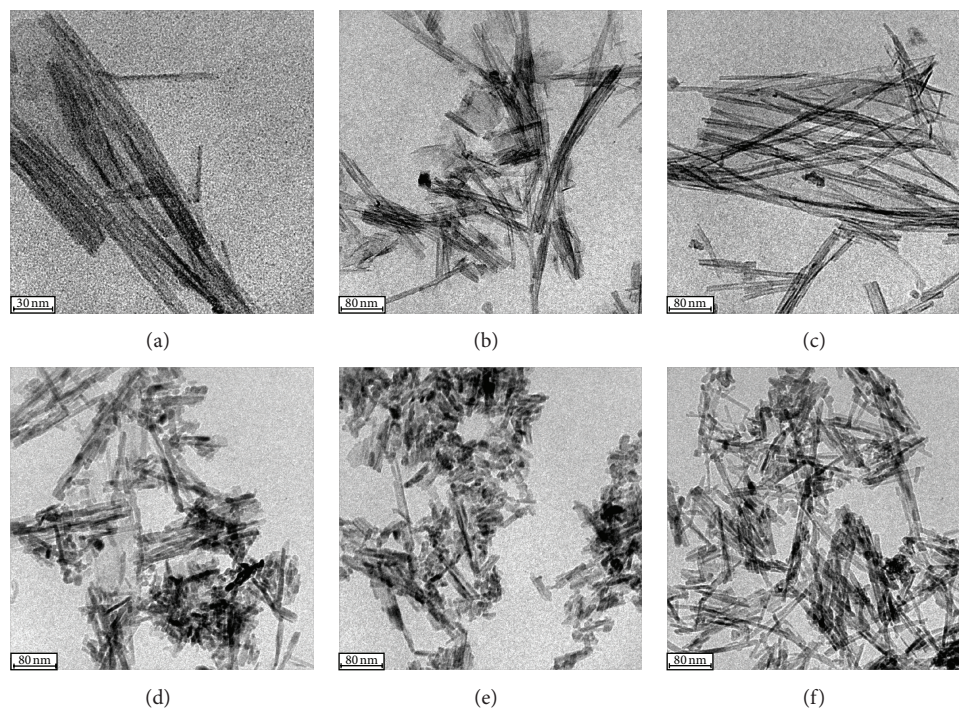


FIGURE 2: TEM images of the uncalcined ((a): 1%; (b): 2%; (c): 5%) and calcined ((d): 1%; (e): 2%; (f): 5%) samples with different Sr/Ti ratios.

Is state with our previous work where the broad N *Is* peak in the XPS pattern of the (Y, N)-codoped TiO_2 was attributed to the formation of the O–Ti–N (substitutional N) and Ti–O–N (interstitial N) structures in the lattice of TiO_2 during the nitridation process [22]. The XPS result of N *Is* also indicates that N still exists in the lattice of TiO_2 after the hydrothermal process. As shown in Figure 3, two peaks at 458.6 and 464.6 eV are observed in the spectrum of Ti *2p*, which corresponds to the $2p_{3/2}$ and Ti $2p_{1/2}$ states of Ti^{4+} , respectively [22]. By fitting the XPS result of Sr *3d*, two peaks at about 133.0 and 134.7 eV are revealed, assigning to the Sr *3d* electronic states in the SrTiO_3 perovskite material and SrO complexes, respectively [24–26].

3.3. UV-Vis Spectroscopy. Figure 4 shows the UV-vis spectra of the uncalcined and calcined samples. It can be observed that all the absorption spectra in Figure 4 exhibit typical absorption behavior of the wide band gap oxide semiconductor, having an intense absorption band with a steep edge. From the spectra, the absorption edges of the uncalcined (SrTiO_3 /titanate) samples with the Sr/Ti ratio of 0%, 1%, 2%, and 5%, respectively, lie at 390.9, 392.5, 408.4, and 396.7 nm as shown in Figure 4 (curves (a)–(d)). The absorption edges of the calcined ($\text{SrTiO}_3/\text{TiO}_{2-x}\text{N}_x$) samples with the Sr/Ti ratio of 0%, 1%, 2%, and 5%, respectively, lie at 424.5, 408.9, 418.8, and 402.1 nm (see curves (e)–(h) in Figure 4). Compared with the absorption edges of uncalcined samples, the absorption edges of the calcined samples shift slightly toward lower energy, respectively, which can be attributed to the differences of band structure and morphologies between titanate nanotubes and anatase nanorods. On the other hand, slight

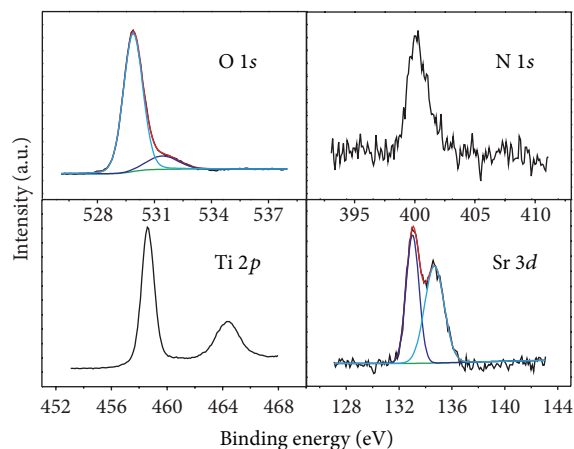


FIGURE 3: XPS spectra of O *1s*, N *1s*, Ti *2p*, and Sr *3d* for the $\text{SrTiO}_3/\text{TiO}_{2-x}\text{N}_x$ with the Sr/Ti ratio of 5%.

red shifts can be observed in the SrTiO_3 /titanate samples after decorating titanate with SrTiO_3 . However, different absorption edge blue shifts occur in the $\text{SrTiO}_3/\text{TiO}_{2-x}\text{N}_x$ samples as compared to the undecorated $\text{TiO}_{2-x}\text{N}_x$. The origins of absorption edge shifts after the decoration of SrTiO_3 are still under discussion. It is known that the N-doping in TiO_2 nanoparticles can result in obvious visible photocatalytic activity because the band narrowing and oxygen vacancies caused by the N-doping can greatly extend the optical absorption range to visible light region. The inset of Figure 4 shows the absorption spectrum of the $\text{TiO}_{2-x}\text{N}_x$

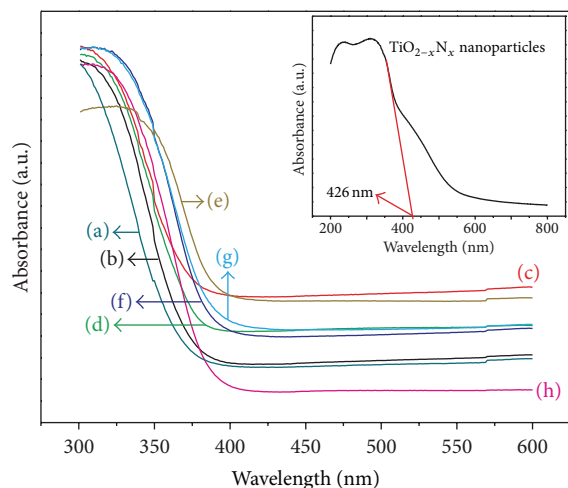


FIGURE 4: UV-vis absorption spectra of the uncalcined ((a): 0%; (b): 1%; (c): 2%; (d): 5%) and calcined ((e): 0%; (f): 1%; (g): 2%; (h): 5%) samples with different Sr/Ti ratios.

nanoparticles which reveals that the absorption edge lies at 426.0 nm, and a broad absorption shoulder is observed from 380 to 550 nm. According to the calculational results by Dong et al. [27], the highest localized state for the substitutional N state is 0.14 eV above the top of the valence band and 0.73 eV for the interstitial N state. N-doping simultaneously favored the formation of oxygen vacancy whose electronic states are located 0.8 eV below the conduction band minimum. Herein, in our opinion, the absorption edge at 426.0 nm can be attributed to the electron transition from the substitutional N states to the conduction band, and the absorption shoulder is contributed by the electron transition between the valence (or conduction) band and the oxygen vacancy (or interstitial N) states. It should be noted that the absorption shoulder is not presented in the spectra of the uncalcined or calcined samples, indicating the decrease or vanishing of oxygen vacancies and interstitial N after the hydrothermal process.

3.4. Photocatalytic Activity. The photocatalytic activities of the prepared samples were evaluated by monitoring the degradation of MB solution, where the concentration of MB was obtained from the linear relation between the absorbance and the concentration of MB solution. Figure 5 displays the degradation rate of MB as a function of light irradiation time without any photocatalyst (the blank test) and over the photocatalysts of $\text{TiO}_{2-x}\text{N}_x$ nanoparticles, $\text{TiO}_{2-x}\text{N}_x$ nanorods, and $\text{SrTiO}_3/\text{TiO}_{2-x}\text{N}_x$ nanorods with different amounts of SrTiO_3 and $\text{SrTiO}_3/\text{titanate}$ nanotube with 5% Sr/Ti ratio. Firstly, the $\text{TiO}_{2-x}\text{N}_x$ nanorods sample presents a similar photocatalytic performance with the sample of $\text{TiO}_{2-x}\text{N}_x$ nanoparticles even though the photoabsorption efficiency of the former is obviously lower than that of the latter. According to the C/C_0 values of these two samples after 30 of minutes dark reaction, the adsorption capability of the $\text{TiO}_{2-x}\text{N}_x$

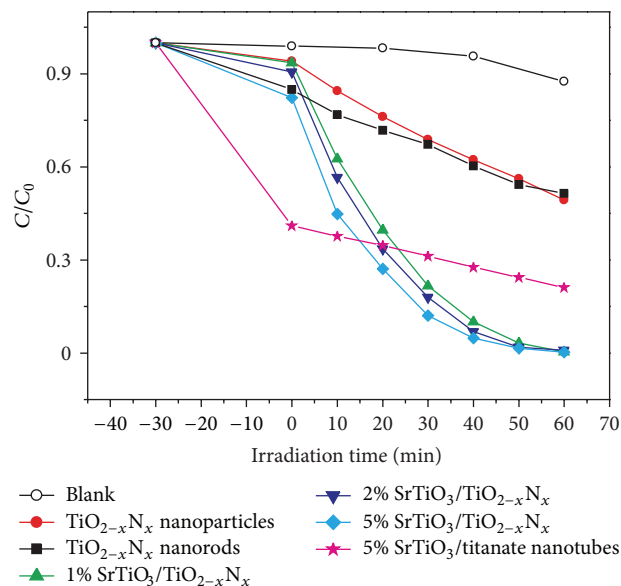


FIGURE 5: Photodegradation of MB under light irradiation without any photocatalyst (blank) and over the prepared photocatalysts.

nanorods is better than that of the nanoparticles. Moreover, as described above, the charge carrier recombination of TiO_2 is expected to be held back by fabricating 1D nanostructure. The above two factors are both positive to the photocatalytic activity of $\text{TiO}_{2-x}\text{N}_x$ nanorods. Secondly, the photocatalytic property of $\text{TiO}_{2-x}\text{N}_x$ nanorods was greatly enhanced after the decoration of SrTiO_3 as shown in Figure 5. With the increase of the amount of SrTiO_3 , the photocatalytic properties of the $\text{SrTiO}_3/\text{TiO}_{2-x}\text{N}_x$ samples are improved gradually. Here, the visible light photodegradation experiments using a light source with a UV cut were also performed which revealed that there was almost no visible light photocatalytic activity in the samples of $\text{SrTiO}_3/\text{TiO}_{2-x}\text{N}_x$. This result is expected; after all, the decoration of SrTiO_3 cannot enhance the visible light absorption in the $\text{TiO}_{2-x}\text{N}_x$ photocatalyst. As described above, SrTiO_3 is a good candidate for coupling TiO_2 to improve the photocatalytic performance of the photocatalyst because the photogenerated charge carriers can be efficiently separated after the modification of SrTiO_3 . As a result, better photocatalytic properties were presented in the composite samples than the sample of $\text{TiO}_{2-x}\text{N}_x$. Lastly, as Figure 5 shows, the photocatalytic activity of the $\text{SrTiO}_3/\text{titanate}$ nanotubes is obviously inferior to the other samples even though its adsorption capability is best among all the samples. From the C/C_0 values of all the samples after the dark reaction, the adsorption capability of the nanotubes is obviously more prominent than the other samples. Generally, the better adsorption capability will indicate a better photocatalytic performance in a type of photocatalyst. However, overmuch adsorbed degrading dye will cover the photocatalytic active sites existing on the photocatalyst surface which is detrimental to the photocatalytic activity of photocatalyst. Herein, in our opinion, overmuch adsorption on the nanotubes surface causes the decrease of photocatalytic property in the $\text{SrTiO}_3/\text{titanate}$ sample.

4. Conclusions

In summary, $\text{SrTiO}_3/\text{TiO}_{2-x}\text{N}_x$ nanostructures were fabricated by the hydrothermal method and characterized by XRD, TEM, XPS, and UV-vis DRS measurements. After hydrothermal processing of the $\text{TiO}_{2-x}\text{N}_x$ nanoparticles with the mixed solution of NaOH and $\text{Sr}(\text{NO}_3)_2$, SrTiO_3 /titanate nanotubes were obtained and presented ordinary photocatalytic performances even though their adsorption properties were greatly improved, indicating that overmuch adsorption is detrimental to the photocatalytic activity of photocatalysts. After calcining the SrTiO_3 /titanate nanotubes, $\text{SrTiO}_3/\text{TiO}_{2-x}\text{N}_x$ nanorods were produced and showed greatly enhanced photocatalytic activities even though their optical absorption performances were depressed as compared to the $\text{TiO}_{2-x}\text{N}_x$. The mechanisms about the absorption and photocatalytic properties in the prepared samples were discussed in detail.

Acknowledgments

This work is financially supported by the Scientific and Technological Research Project of Henan Province (Grant no. 122102210229) and the Research Project of Province-ministry Coconstructing Henan University (SBGJ090505).

References

- [1] J. Zhang, J. H. Bang, C. C. Tang, and P. V. Kamat, "Tailored TiO_2 - SrTiO_3 heterostructure nanotube arrays for improved photoelectrochemical performance," *ACS Nano*, vol. 4, no. 1, pp. 387–395, 2010.
- [2] A. Kongkanand, K. Tvrđy, K. Takechi, M. K. Kuno, and P. V. Kamat, "Quantum dot solar cells. Tuning photoresponse through size and shape control of CdSe-TiO_2 architecture," *Journal of the American Chemical Society*, vol. 130, no. 12, pp. 4007–4015, 2008.
- [3] Q. Wang, K. Zhu, N. R. Neale, and A. J. Frank, "Constructing ordered sensitized heterojunctions: bottom-up electrochemical synthesis of p-type semiconductors in oriented n- TiO_2 nanotube arrays," *Nano Letters*, vol. 9, no. 2, pp. 806–813, 2009.
- [4] T. Tsumura, K. Sogabe, and M. Toyoda, "Preparation of SrTiO_3 -supported TiO_2 photocatalyst," *Materials Science and Engineering B*, vol. 157, no. 1–3, pp. 113–115, 2009.
- [5] B. Zielinska and A. W. Morawski, " TiO_2 photocatalysts promoted by alkali metals," *Applied Catalysis B*, vol. 55, no. 3, pp. 221–226, 2005.
- [6] H. L. Meng, C. Cui, H. L. Shen et al., "Synthesis and photocatalytic activity of TiO_2/CdS and CdS/TiO_2 double-shelled hollow spheres," *Journal of Alloys and Compounds*, vol. 527, pp. 30–35, 2012.
- [7] P. N. Zhu, A. S. Nair, S. J. Peng, S. Y. Yang, and S. Ramakrishna, "Facile fabrication of TiO_2 -graphene composite with enhanced photovoltaic and photocatalytic properties by electrospinning," *ACS Applied Materials & Interfaces*, vol. 4, no. 2, pp. 581–585, 2012.
- [8] M. S. Islam, Y. Kusumoto, M. Abdulla-Al-Mamun, and Y. Horie, "Photocatalytic and AC magnetic-field induced enhanced cytotoxicity of Fe_3O_4 - TiO_2 core-shell nanocomposites against HeLa cells," *Catalysis Communications*, vol. 16, no. 1, pp. 39–44, 2011.
- [9] Z. D. Meng, M. M. Peng, L. Zhu, W. C. Oh, and F. J. Zhang, "Fullerene modification CdS/TiO_2 to enhancement surface area and modification of photocatalytic activity under visible light," *Applied Catalysis B*, vol. 113–114, pp. 141–149, 2012.
- [10] Y. Bessekhouad, D. Robert, and J. V. Weber, " $\text{Bi}_2\text{S}_3/\text{TiO}_2$ and CdS/TiO_2 heterojunctions as an available configuration for photocatalytic degradation of organic pollutant," *Journal of Photochemistry and Photobiology A*, vol. 163, no. 3, pp. 569–580, 2004.
- [11] Q. Q. Zhai, T. Bo, and G. X. Hu, "High photoactive and visible-light responsive graphene/titanate nanotubes photocatalysts: preparation and characterization," *Journal of Hazardous Materials*, vol. 198, pp. 78–86, 2011.
- [12] C. Yi, R. Nirmala, N. A. M. Barakat, R. Navamathavan, and H. Y. Kim, "Photocatalytic properties of silver nanoparticles decorated nanobranched TiO_2 nanofibers," *Journal of Nanoscience and Nanotechnology*, vol. 11, no. 8, pp. 6886–6892, 2011.
- [13] N. Iwata, K. Yamaguchi, T. B. Nishimura, K. Takemura, and Y. Miyasaka, "Li-ion battery operated power amplifier MMICs utilizing SrTiO_3 capacitors and heterojunction FETs for PDC and CDMA cellular phones," *Solid-State Electronics*, vol. 43, no. 4, pp. 747–753, 1999.
- [14] Y. J. Cui, J. He, G. Amow, and H. Kleinke, "Thermoelectric properties of n-type double substituted SrTiO_3 bulk materials," *Dalton Transactions*, vol. 39, no. 4, pp. 1031–1035, 2010.
- [15] I. Hod, M. Shalom, Z. Tachan, S. Rühle, and A. Zaban, " SrTiO_3 recombination-inhibiting barrier layer for type II dye-sensitized solar cells," *Journal of Physical Chemistry C*, vol. 114, no. 21, pp. 10015–10018, 2010.
- [16] U. Sulaeman, S. Yin, and T. Sato, "Visible light photocatalytic activity induced by the carboxyl group chemically bonded on the surface of SrTiO_3 ," *Applied Catalysis B*, vol. 102, no. 1–2, pp. 286–290, 2011.
- [17] T. P. Cao, Y. J. Li, C. H. Wang, C. L. Shao, and Y. C. Liu, "A facile in situ hydrothermal method to $\text{SrTiO}_3/\text{TiO}_2$ nanofiber heterostructures with high photocatalytic activity," *Langmuir*, vol. 27, no. 6, pp. 2946–2952, 2011.
- [18] J. Zhang, J. H. Bang, C. C. Tang, and P. V. Kamat, "Tailored TiO_2 - SrTiO_3 heterostructure nanotube arrays for improved photoelectrochemical performance," *ACS Nano*, vol. 4, no. 1, pp. 387–395, 2010.
- [19] J. H. Yan, Y. R. Zhu, Y. G. Tang, and S. Q. Zheng, "Nitrogen-doped $\text{SrTiO}_3/\text{TiO}_2$ composite photocatalysts for hydrogen production under visible light irradiation," *Journal of Alloys and Compounds*, vol. 472, no. 1–2, pp. 429–433, 2009.
- [20] R. Asahi, T. Morikawa, T. Ohwaki, K. Aoki, and Y. Taga, "Visible-light photocatalysis in nitrogen-doped titanium oxides," *Science*, vol. 293, no. 5528, pp. 269–271, 2001.
- [21] Z. H. Zhao, J. M. Fan, J. Y. Wang, and R. F. Li, "Effect of heating temperature on photocatalytic reduction of CO_2 by N- TiO_2 nanotube catalyst," *Catalysis Communications*, vol. 21, pp. 32–37, 2012.
- [22] H. R. Zhang, K. Q. Tan, H. W. Zheng, Y. Z. Gu, and W. F. Zhang, "Preparation, characterization and photocatalytic activity of TiO_2 codoped with yttrium and nitrogen," *Materials Chemistry and Physics*, vol. 125, no. 1–2, pp. 156–160, 2011.
- [23] X. B. Chen, H. Q. Wang, S. Gao, and Z. B. Wu, "Effect of pH value on the microstructure and deNO_x catalytic performance of titanate nanotubes loaded CeO_2 ," *Journal of Colloid and Interface Science*, vol. 377, no. 1, pp. 131–136, 2012.
- [24] J. W. Ng, S. P. Xu, X. W. Zhang, H. Y. Yang, and D. D. Sun, "Hybridized nanowires and cubes: a novel architecture of

- a heterojunctioned $\text{TiO}_2/\text{SrTiO}_3$ thin film for efficient water splitting,” *Advanced Functional Materials*, vol. 20, no. 24, pp. 4287–4294, 2010.
- [25] W. D. Yang, “X-ray photoelectron spectroscopy and electrical properties studies of La_2O_3 -doped strontium titanate ceramics prepared by sol-precipitation method,” *Journal of Materials Science*, vol. 34, no. 14, pp. 3533–3544, 1999.
- [26] R. P. Vasquez, “X-ray photoelectron spectroscopy study of Sr and Ba compounds,” *Journal of Electron Spectroscopy and Related Phenomena*, vol. 56, no. 3, pp. 217–240, 1991.
- [27] F. Dong, W. R. Zhao, Z. B. Wu, and S. Guo, “Band structure and visible light photocatalytic activity of multi-type nitrogen doped TiO_2 nanoparticles prepared by thermal decomposition,” *Journal of Hazardous Materials*, vol. 162, no. 2-3, pp. 763–770, 2009.

Research Article

Characterization and Photocatalytic Activity of TiO_2 Nanotube Films Prepared by Anodization

Wen-Yu Wang and Bo-Ruei Chen

Department of Environmental Engineering and Management, Chaoyang University of Technology, 168, Jifeng E. Rd., Wufeng District, Taichung 41349, Taiwan

Correspondence should be addressed to Wen-Yu Wang; wywang@cyut.edu.tw

Received 10 February 2013; Revised 15 April 2013; Accepted 16 April 2013

Academic Editor: Gang Liu

Copyright © 2013 W.-Y. Wang and B.-R. Chen. This is an open access article distributed under the Creative Commons Attribution License, which permits unrestricted use, distribution, and reproduction in any medium, provided the original work is properly cited.

Titanium dioxide nanotube (TNT) arrays were prepared in electrolytes containing fluoride by anodic oxidation. Different preparation parameters were investigated in order to evaluate their effects on length and inner diameter of nanotube, including weight ratio of glycerol to water, anodization voltage, electrolysis time, bath temperature, and electrolyte solution pH. The well defined and highly ordered TNT arrays were formed in electrolyte containing 40, and 20% water. The inner diameter of TNT was observed to increase as anodization voltage increased across the range of 10–40 V. The length of TNT was affected simultaneously by both anodization voltage and electrolysis time. The inner diameter and length depend on bath temperature below 60°C. The morphology of TNT was well defined and highly ordered only at electrolyte solution pH of 6 across the pH range of 2–10. Photocatalysis of methylene blue showed that reaction rate constants by TNT films were higher than P-25 films at comparable thickness. Reaction rate constants by TNT films increased as film thickness increased, but the enhancement was retarded when the length of TNT reached 2200 nm which appeared to be the limited penetration of incident UV light.

1. Introduction

In the past decade, considerable attention has been focused on using nanocrystalline TiO_2 as a photocatalyst for the degradation of organic pollutants [1]. The photocatalyst titanium dioxide is a wide bandgap semiconductor, corresponding to radiation in the near-UV range. An electron-hole pair formation occurs within the conduction and valence bands of TiO_2 after the absorption of UV radiation. The positive hole is apparently able to oxidize a water molecule to hydroxyl radical [2]. The hydroxyl radical, in turn, is a powerful oxidant. The oxidation of organic contaminants seems to be mediated by a series of reactions initiated by hydroxyl radical on the TiO_2 surface. However, recombination of the separated electron and hole can occur either in the volume or on the surface of the semiconductor particle accompanied with heat releasing [3].

Highly ordered TiO_2 nanotube (TNT) arrays have been regarded as potential superior photocatalyst due to their valuable high surface area structure. The one-dimensional

nanostructures with tubular symmetries possessed low recombination of light-induced electron-hole pairs and high photocurrent conversion efficiency [4]. Quan et al. [5], and Wang et al. [6] indicated that TNT attached to the parent titanium substrate improved the transport of the photo-induced electrons from photoanode to cathode and enhanced the photocatalytic activity of TNT.

In recent years, numerous researchers have paid their attention on developing new techniques for fabrication of TNT, such as template [7], hydrothermal [8] and anodic oxidation method [9]. The electrochemical oxidation and chemical dissolution rates of TiO_2 were the keys to fabricate TNT by anodic oxidation method. The thin layer of TiO_2 was formed on the titanium surface in the onset of anodization. The pores could be observed on the surface of TiO_2 layer after the localized dissolution of the TiO_2 by fluoride ions. When the pores became deeper, the electric field at the bottom of pores was increased to enhance the electrochemical oxidation and chemical dissolution rates of TiO_2 and to form the tubular structure of TiO_2 . The length

of TNT remained constant when electrochemical oxidization rate and chemical dissolution rate reached dynamic balance [10].

Although various studies on the preparation of TNT had been reported, this study widely investigated the effects of various preparation parameters on length and inner diameter of TNT. These parameters included weight ratio of glycerol to water, anodization voltage, electrolysis time, bath temperature, and electrolyte solution pH. Photocatalytic efficiency was affected by diameter and length of TNT. Alivov and Fan [11] reported on the performance of dye sensitized solar cells (DSSCs) based on different diameters of TNT filled with TiO_2 nanoparticles. It is shown that the efficiency of DSSCs significantly increased with relative increasing of diameter of TNT. Macák et al. [4] revealed that higher light-induced photocurrent can be achieved by TNT with longer tube length.

As to our knowledge there was comparatively little research on the preparation parameter of electrolyte solution pH and the comparison of photocatalysis efficiency among comparable thickness of TNT films and P-25 films. In order to examine the relation between photocatalysis rate and the length of TNT film, photocatalytic reactions of methylene blue with various thicknesses of TNT and P-25 films were also performed.

2. Experimental

2.1. Preparation and Characterization of TiO_2 Nanotube Arrays. A 25×15 mm Ti foil (99.53%) was subsequently immersed in acetone, isopropanol, methanol and deionized water for 10 minutes to remove the impurities and then dried at room temperature. Ti and Pt foils connected by Pt wire were used as anode and cathode, respectively. The glycerol solution containing 0.5 wt% NH_4F and water content ranging from 0 to 90 wt% was used as electrolyte and transferred to an electrolytic reactor along with electrodes for the anodization of Ti foil. Anodization voltage and electrolysis time were controlled by a programmable DC power supply (CDP-350-005PB, Chyng Hong Electronic) across the range of 10–70 V and 1–8 hours, respectively. Bath temperature was controlled via a water jacket with a thermostatic circulating water bath (BL-720, Yihder Technology). Electrolyte solution pH was adjusted among 2 to 10. The complete preparation parameters are listed in Table 1. The anodized Ti foils were put into a muffle furnace at different temperatures ranged from 200 to 800°C for 3 hours to induce crystallization. Because of the TNT films calcined at 600°C presented the best photocatalytic activity (as experimental procedure described in Section 2.2), the calcination temperature of 600°C was chosen in all experiments in this study. The surface dimensions of anodized Ti foil were determined by a field-emission scanning electron microscopy (JSM-6500F, JEOL).

2.2. Photocatalytic Activity Tests. The photocatalytic reaction system was composed of a photoreactor, UV-LED lamp,

TABLE 1: Experimental design matrix for preparation of TNT.

Weight ratio of glycerol to water	Anodization voltage (V)	Electrolysis time (hours)	Bath temperature ($^\circ\text{C}$)	Electrolyte solution pH
1:9	30	2	40	6
2:8	30	2	40	6
4:6	30	2	40	6
6:4	30	2	40	6
8:2	30	2	40	6
10:0	30	2	40	6
6:4	10	2	40	6
6:4	20	2	40	6
6:4	40	2	40	6
6:4	50	2	40	6
6:4	60	2	40	6
6:4	70	2	40	6
6:4	30	1	40	6
6:4	30	4	40	6
6:4	30	6	40	6
6:4	30	8	40	6
6:4	30	10	40	6
6:4	30	2	10	6
6:4	30	2	20	6
6:4	30	2	50	6
6:4	30	2	60	6
6:4	30	2	80	6
6:4	30	2	40	2
6:4	30	2	40	4
6:4	30	2	40	8
6:4	30	2	40	10

dye solution flask, peristaltic pump, and UV-Vis spectrophotometer and operated in recirculation mode. Silicone pipes connected the above equipment for circulation of the dye solution. The peristaltic pump transported methylene blue solution from the dye solution flask to photoreactor and recycled back to the dye solution flask. Major components of the photoreactor were made entirely of teflon. The photoreactor contained two hollow fillisters at the top fixture and the bottom fixture, respectively. The photocatalyst film (TNT or Degussa P-25) was attached under the top fixture. A quartz plate was mounted on the bottom fixture to penetrate the UV light. A UV-LED lamp with wavelength of 365 nm and irradiation power of $2\text{ mW}/\text{cm}^2$ was put under the photoreactor. Dye solution was pumped through the flow channel hold between the top fixture and the bottom fixture. The initial concentration of methylene blue solution was 10 mg/L for all experiments. The photocatalytic reactions were carried out with various thicknesses of TNT and P-25 films. The TNT films were prepared by anodic oxidation method, and the P-25 films were prepared by dipcoating of suspension [12]. Concentrations of methylene blue

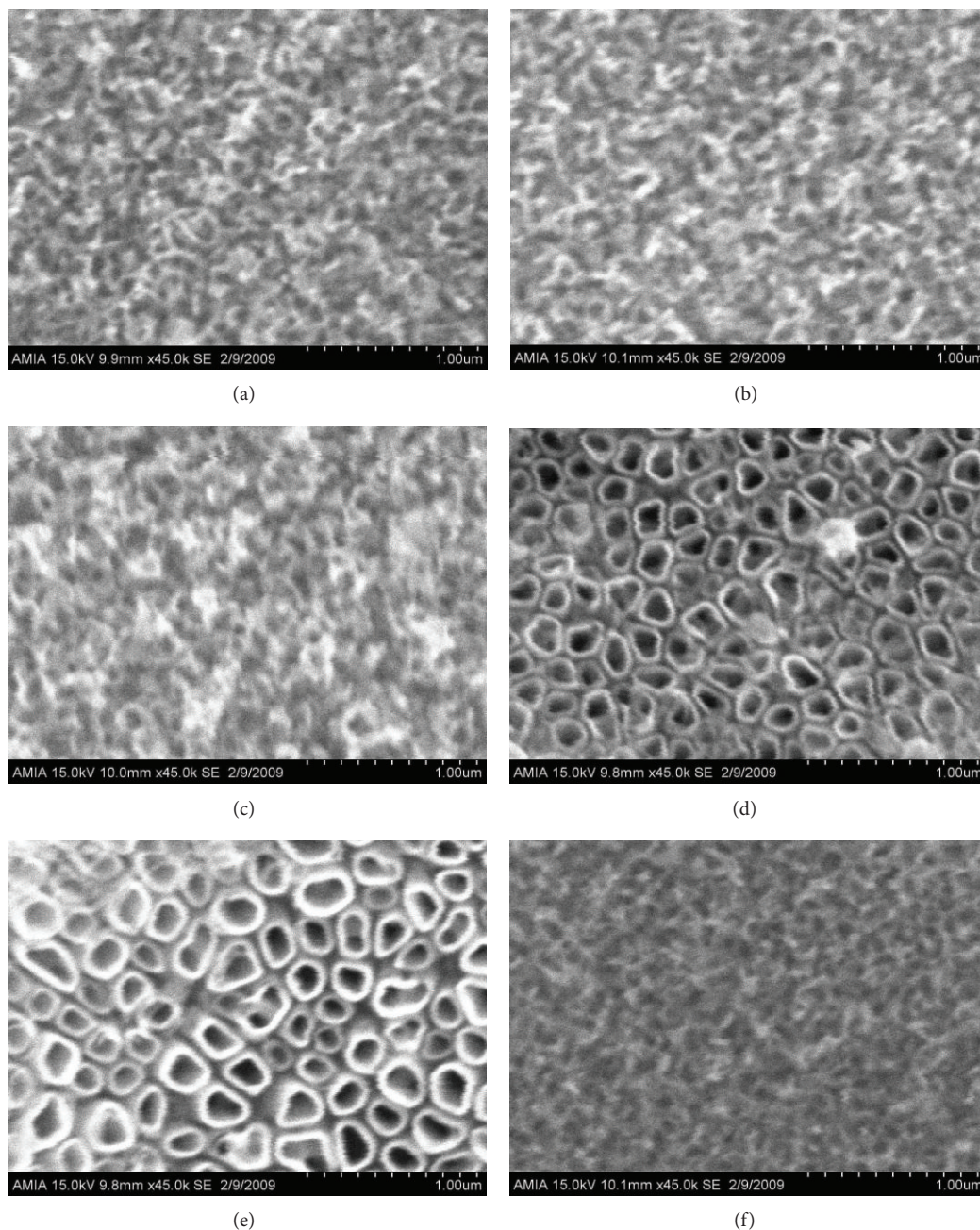


FIGURE 1: Top view of SEM images of TNT synthesized at different weight ratios of glycerol and water: (a) 1 : 9, (b) 2 : 8, (c) 4 : 6, (d) 6 : 4, (e) 8 : 2, and (f) 10 : 0.

were determined at the desired intervals of reaction time by a UV-Vis spectrophotometer (Spectra Academy, K-MAC).

3. Results and Discussion

3.1. Effect of Weight Ratio of Glycerol to Water. Effect of glycerol and water ratio on the dimensions of fabricated TNT is illustrated in Figure 1. Anodization was carried out at 30 V for 2 hours in electrolyte solution containing glycerol, water, and 0.5 wt% NH_4F . The water content in electrolyte solution is 90, 80, 60, 40, 20, and 0%, respectively. Anodization

process was performed at electrolyte solution pH of 6 and bath temperature of 40°C. TiO_2 with tubular structure was observed in glycerol electrolyte with water content of 40 and 20% (Figures 1(d) and 1(e)). Hence, the glycerol/water ratio of 60 : 40% was chosen to perform those anodizations at various anodization voltages, electrolysis time, bath temperature, and electrolyte solution pH. Partially well-formed TNT or collapsed TNT prepared by water contents of 90, 80, 60, and 0% was also shown in Figure 1. The result is consistent with the research finding by Valota et al. [13]. They proposed that electric current densities increases as water content

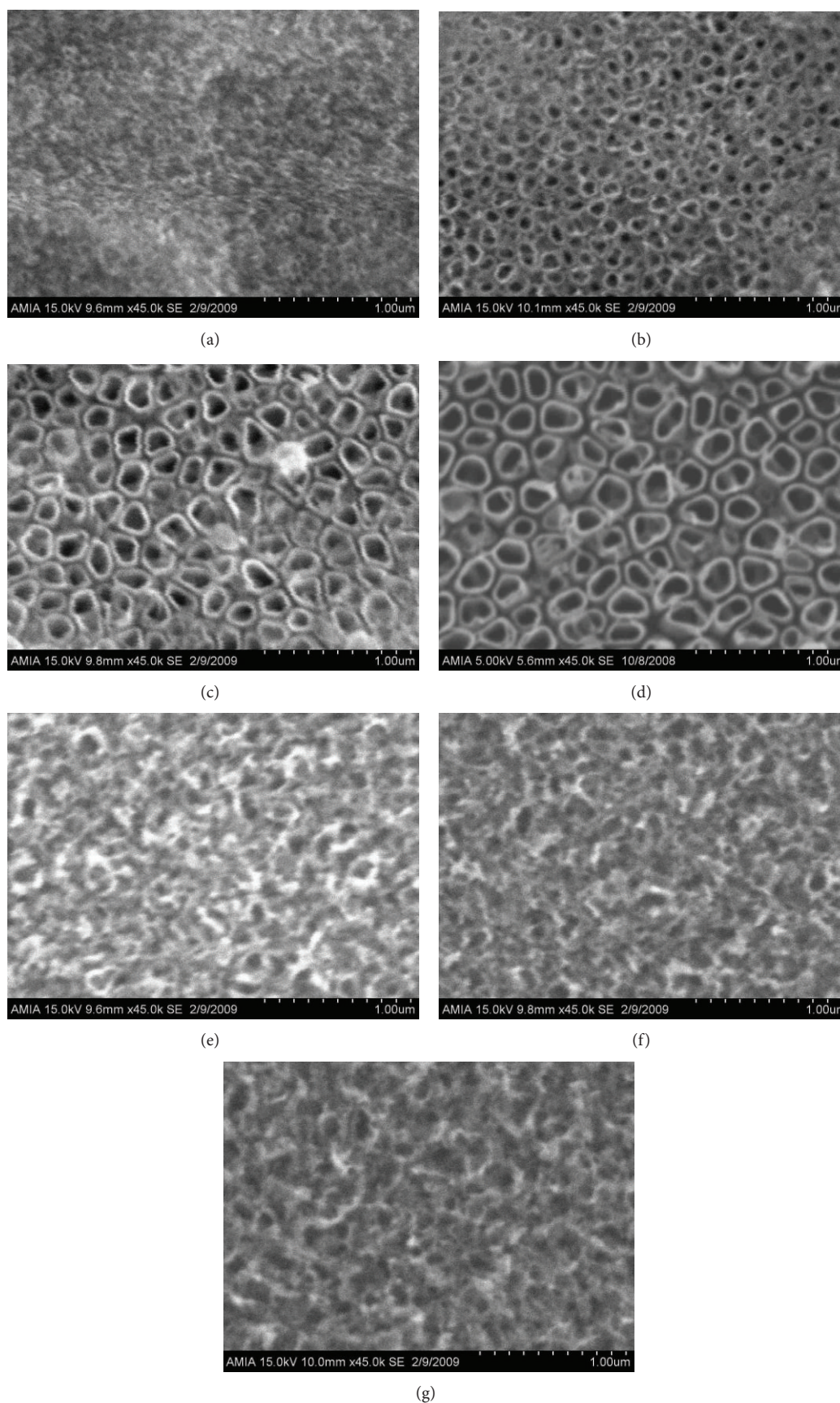


FIGURE 2: Top view of SEM images of TNT synthesized at different anodization voltages: (a) 10 V, (b) 20 V, (c) 30 V, (d) 40 V, (e) 50 V, (f) 60 V, and (g) 70 V.

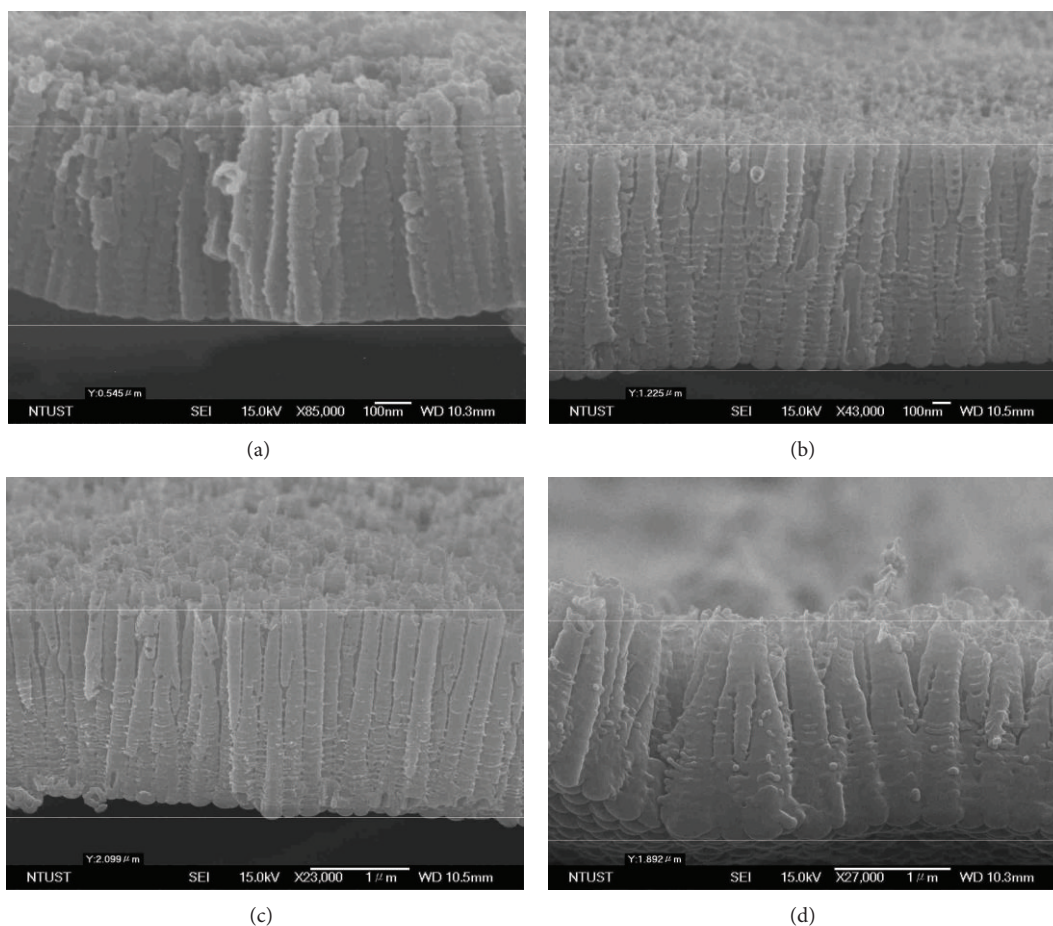


FIGURE 3: Front view of SEM images of TNT synthesized at different anodization voltages: (a) 10 V, (b) 20 V, (c) 30 V, and (d) 40 V.

increase and high electric current densities further result in the collapse and dissolve of TNT.

3.2. Effect of Anodization Voltage. Figure 2 illustrates SEM images for the influence of applied anodization voltage on the fabrication of TiO_2 nanotube arrays. These samples were prepared at water contents of 40 wt% in glycerol containing 0.5 wt% NH_4F , anodization voltage ranged from 10–70 V, electrolysis time of 2 hours, electrolyte solution pH of 6, and bath temperature of 40°C. The TNT structure was observed at applied anodization voltage of 10–40 V but disappeared above 50 V. As shown in Figures 2 and 3, Inner diameter and length of TNT prepared with applied anodization voltage of 10–40 V were determined by SEM cross-section images. Figure 4(a) illustrates that the average inner diameter of TNT was ranged from 50 to 210 nm and increased almost linearly with the increasing applied anodization voltage from 10 to 40 V. Average length of TNT was also linearly increased from 608 to 2100 nm with the increasing applied anodization voltage but decreased above 30 V.

Applied anodization voltage and fluoride concentration in electrolyte solution are proposed to play important roles during anodization to carry out electrochemical oxidation and chemical dissolution reactions. Lee et al. [14] recorded

current-time curves during anodization with 20 V at water contents of 30 wt% in glycerol containing different amounts of NH_4F . The current densities increased with increasing the fluoride content in the range of 0–2%. They proposed that the dissolution reaction of the anodic oxide is induced by F^- ions. The growth of TNT is a result of competition between electrochemical oxide formation and chemical dissolution of oxide by fluoride ions. In this study, anodization of Ti foil was conducted in electrolyte solutions containing 0.5 wt% NH_4F , indicating that the chemical dissolution rate of TiO_2 coating was supposed to be roughly the same for all experiments regarding to the anodization of Ti foil, while the electrochemical oxidation rate to form TiO_2 layers was varied with different applied anodization voltages. Hence, the growth of TNT was mainly determined by applied anodization voltage.

Some similar results were reported in the literature. Gong et al. [9] fabricated TNT in 0.5–3.5% HF solutions by applying various anodization voltages. The length of TiO_2 nanotube was approximately 500 nm, and the average inner diameter was 25 to 65 nm. Macak et al. [15] studied the effect of anodization voltage on the fabrication of TNT by anodization in water/glycerol solution (50:50 vol%) containing 0.27 M NH_4F . The authors indicated that the inner diameter was linearly increased with increasing anodization voltage.

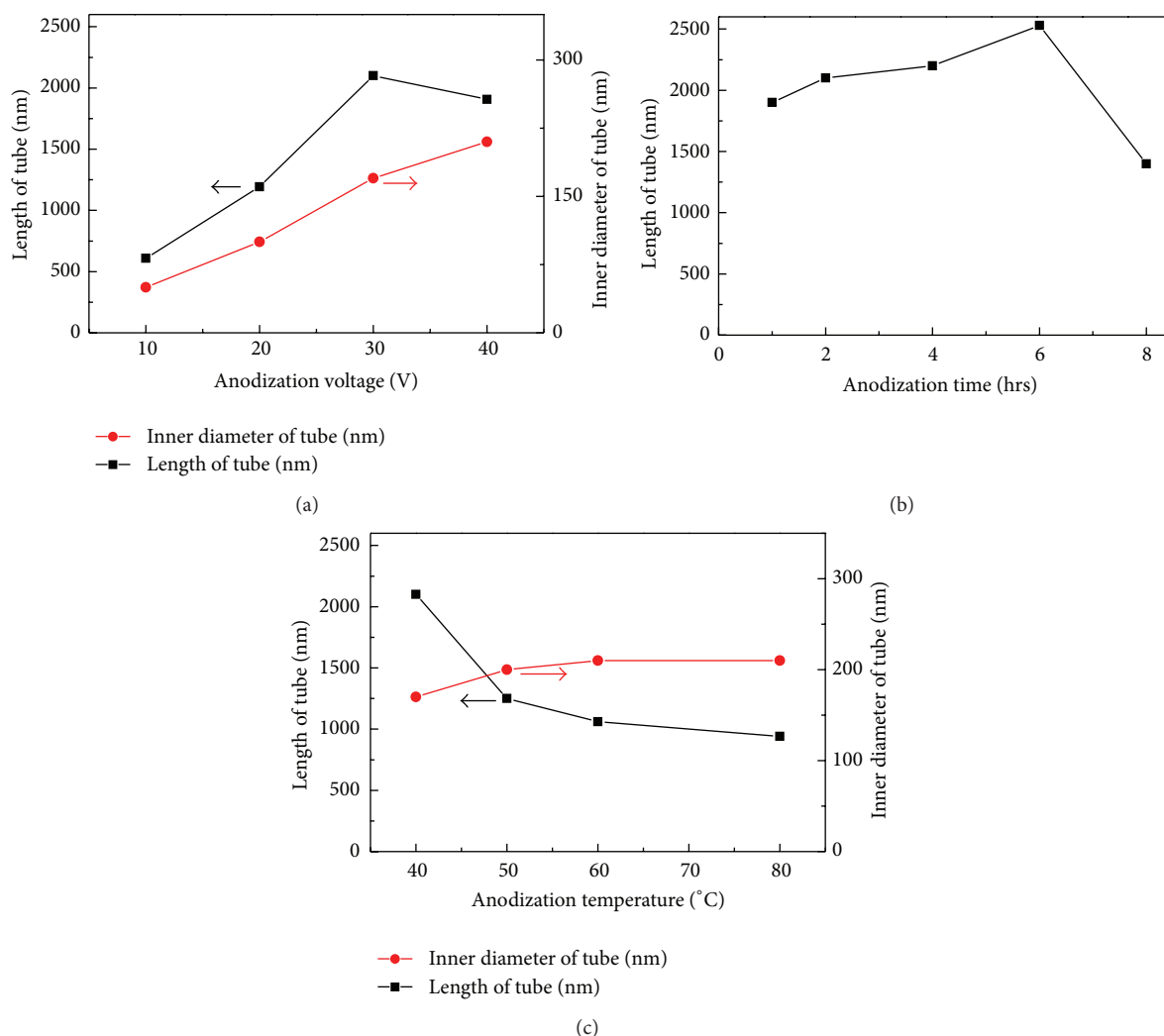


FIGURE 4: Dimensional control of titanium dioxide nanotube arrays with different preparation parameters of (a) anodization voltage, (b) electrocatalysis times, and (c) bath temperature.

The length of TNT fabricated with anodization voltage less than 20 V was found to be increased with anodization voltage and then gradually approached to a constant value with continuously increasing anodization voltage.

3.3. Effect of Electrolysis Time. Figure 5 illustrates SEM images for the influence of electrolysis time ranged from 1 to 10 hours on the fabrication of TiO_2 nanotube arrays. These samples were prepared at water contents of 40 wt% in glycerol containing 0.5 wt% NH_4F , anodization voltage of 30 V, anodization time of 2 hours, electrolyte solution pH of 6, and bath temperature of 40°C. Figures 5 and 4(b) depict the relationship between the dimensions of TNT and electrolysis duration periods. The average length of nanotube increased with increasing anodization time, but the average inner diameter of nanotube was not affected with anodization time for experiments conducted with the same applied anodization voltage. The length of TNT rapidly grew

to 1900 nm at the first hour then was enhanced with growth rate of 126 nm/hour for anodization duration periods from the second to the sixth hour, and thereafter the length of TNT decreased drastically to less than 1400 nm at the eighth hour.

As shown in Figures 5(e) and 5(f), at the eighth hour the length of TNT decreased drastically. At the tenth hour the structure of nanotube arrays could not stay highly ordered and vertically oriented due to collapse of nanotubes. These observations indicate that the anodization of Ti foil has three stages in this study. At the first stage (the first hour), the formation and erosion of titanium dioxide layer arose simultaneously. TNT layer was established initially with a very fast speed. A very high current density at the initial 50 seconds of anodization showed the fast formation of an oxide layer. At the second stage (the second to the sixth hour), the growth of TNT slowed down due to high electric resistance gradually induced by thicker oxide layer; meanwhile, the chemical erosion also slowed down due to the long diffusion path of corrosion agents. The results arose in a slow growing

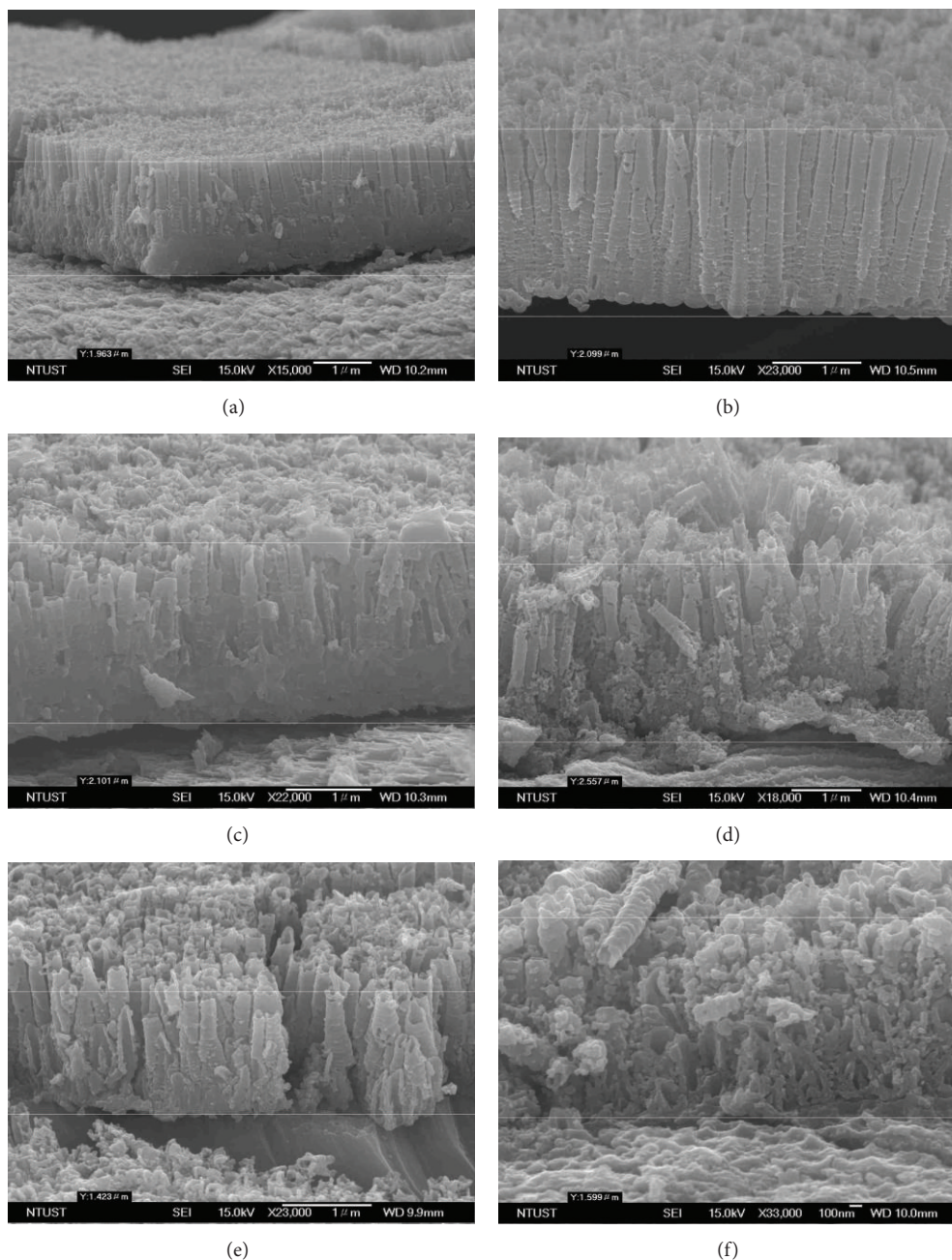


FIGURE 5: Front view of SEM images of TNT synthesized at different electrocatalysis time: (a) 1 hr, (b) 2 hr, (c) 4 hr, (d) 6 hr, (e) 8 hr, and (f) 10 hr.

rate of nanotubes layer at the second stage. Finally, at the third stage of longer anodization time, the erosion rate was a little faster than the inhibited growth of oxide layer and caused the collapse of nanotubes as anodization time increased. It is assumed that the length of nanotube is continually increased with anodization time until the rates of electrochemical oxidation of Ti foil and chemical dissolution of TiO_2 film reached dynamically equilibrium.

The experimental results are consistent with Cai et al. [16]. With the application of anodization voltage higher than 30 V, the length of TNT was rapidly enhanced with growth rate

greater than 300 nm/hour for anodization time less than 4 hours, and thereafter growth rate was decreased drastically to less than 60 nm/hour. For experiments conducted with lower anodization voltages, the length of TNT was gradually increased at steady growth rate of about 40 nm/hour even for anodization time of 12 hours. Normally, the decrease of tube length after a long time of electrolysis in our study (Figure 4(b)) is less reported in the literature. Crawford et al. [17] prepared TNT by anodization in a NaF electrolyte and indicated that the length of TNT increased with increasing anodization time for anodization time less than 2 hours

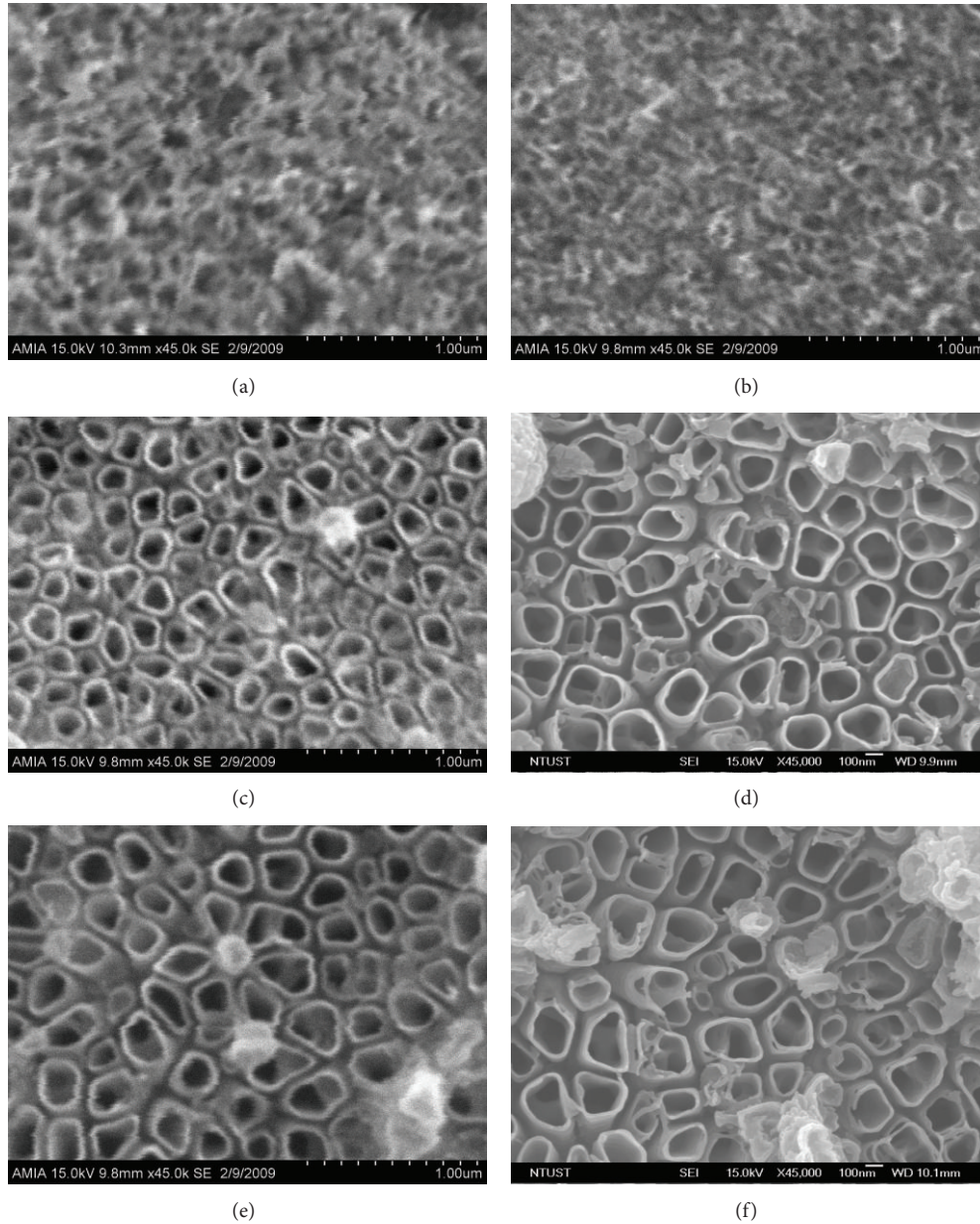


FIGURE 6: Top view of SEM images of TNT synthesized at different bath temperatures: (a) 10°C, (b) 20°C, (c) 40°C, (d) 50°C, (e) 60°C, and (f) 80°C.

and remained constant thereafter. Macak and Schmuki [18] and Kim et al. [19] examined the effect of anodization time on the dimension of TNT and revealed that the tube diameter and wall thickness were not varied with anodization time.

3.4. Effect of Bath Temperature. Effect of bath temperature on the dimensions of fabricated TNT is illustrated in Figures 6 and 7. These samples were prepared at water contents of 40 wt% in glycerol containing 0.5 wt% NH_4F , bath temperature ranged from 10 to 80°C, anodization voltage of 30 V for 2 hours, and electrolyte solution pH of 6. The TNT was observed at bath temperature ranged from 80 to 40°C but disappeared below 20°C. As shown in Figure 4(c), inner

diameter and length of TNT prepared with bath temperature from 40 to 80°C were determined by SEM cross-section images. Figure 4(c) showed that average inner diameter of TNT increased from 170 to 210 nm as bath temperature increased from 40 to 50°C but had comparable diameters as bath temperature was above 50°C. Average length of TNT was inversely decreased from 2100 to 940 nm with increasing bath temperature but had comparable lengths as bath temperature was above 60°C.

Unlike anodization voltage and electrolysis time, the effects of bath temperature and electrolyte solution pH only attracted a few researchers' attention. Lim et al. [20] examined the effect of bath temperature on the dimension of TNT

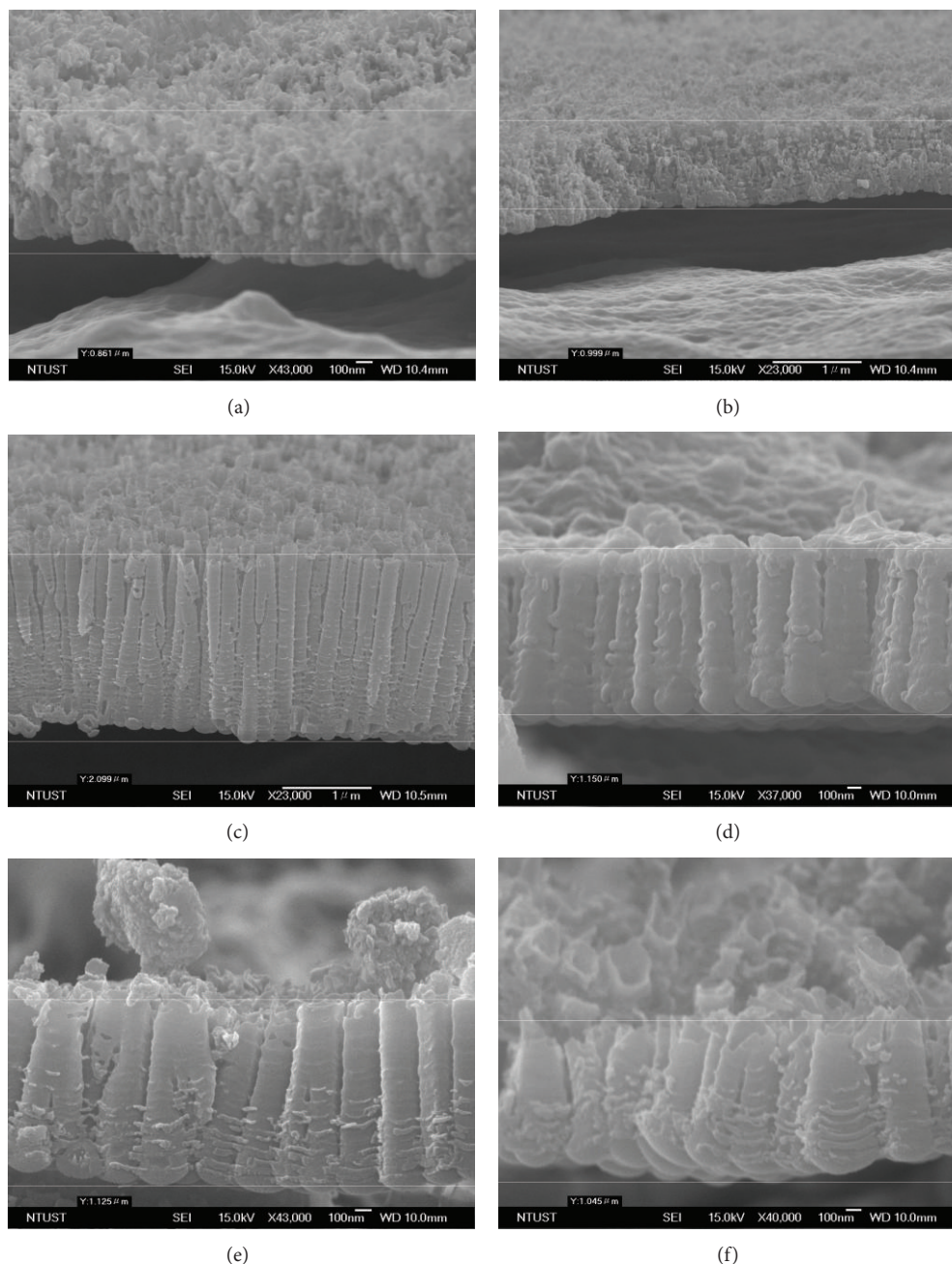


FIGURE 7: Front view of SEM images of TNT synthesized at different bath temperatures: (a) 10°C, (b) 20°C, (c) 40°C, (d) 50°C, (e) 60°C, and (f) 80°C.

and found that TNT can still be fabricated at 35°C; however, the tube length decreases whereas tube diameter increases with elevated temperature from 10 to 35°C. Some different results were reported by various studies. Macak and Schmuki [18] anodized Ti in mixture of glycerol and water (50:50) containing 0.5 wt% NH_4F at various bath temperatures of 20, 40, 60, and 80°C with 20 V for 6 hours. Their result showed that the length of TNT increased as bath temperature increased.

There are some differences between the literature and our study including electrolyte composition, anodization

voltage, and electrolysis time, and therefore the results of these studies are different. It appears that TNT could form at low bath temperature for a longer electrolysis time, but our study performs 2 hours of electrolysis time and only gets a random oxide layer. On other hands, our result is consistent with the study of Mor et al. [21]. They studied the TNT prepared at different bath temperatures by 10 V anodization in an electrolyte of 0.5% HF and acetic acid mixed in a 7:1 ratio. The result shows that the length of the nanotubes increases from 120 nm to 224 nm with decreasing bath temperature from 50°C to 5°C. The electric density

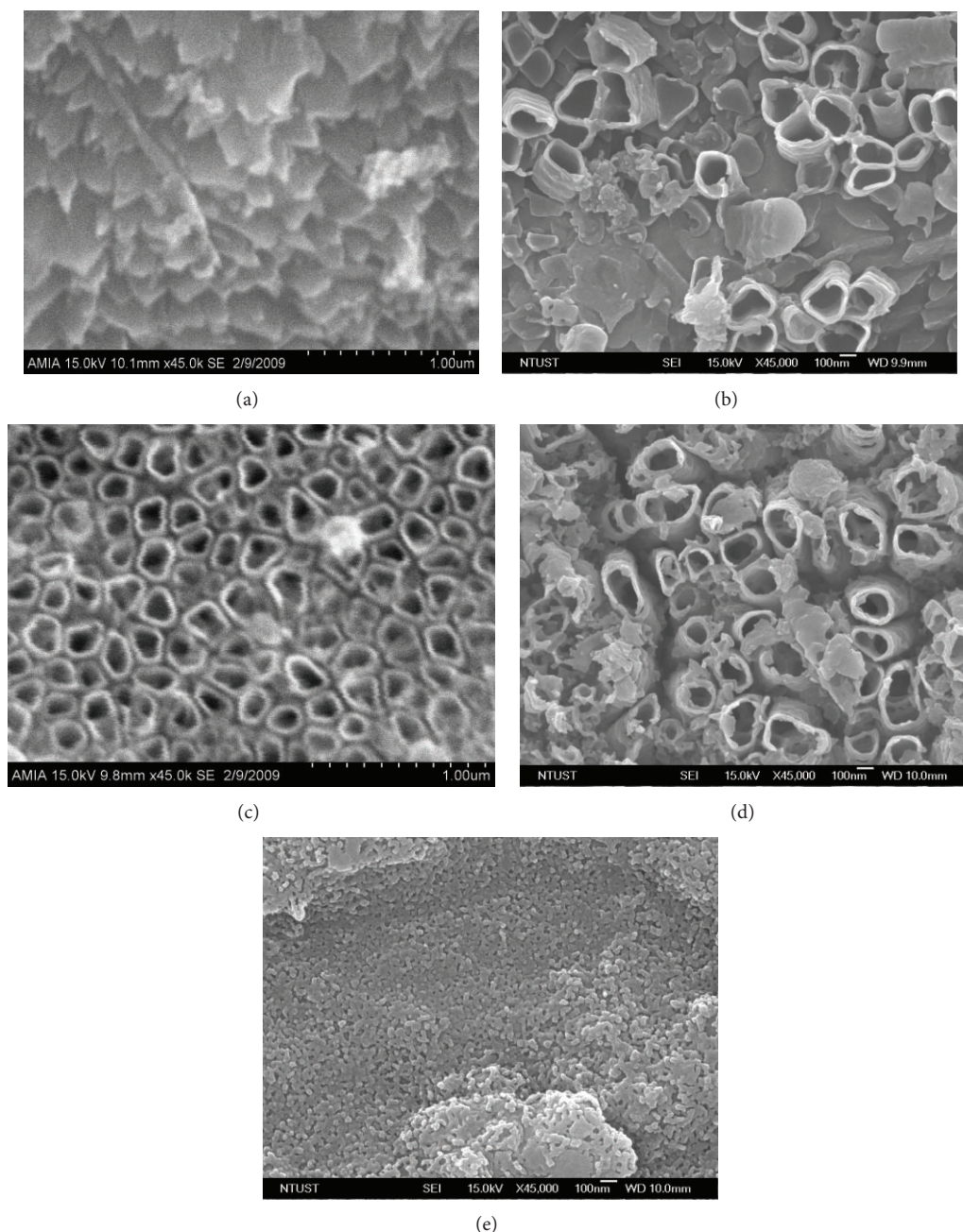


FIGURE 8: Top view of SEM images of TNT synthesized at different electrolyte solution pH: (a) 2, (b) 4, (c) 6, (d) 8, and (e) 10.

of anodization bath will increase with rising bath temperature. At the same time, the electric field formed in titanium anode will also increase. High electric current density and appropriate chemical etching will match up and make a fast transform of oxidize layer to nanotubes at the initial oxidizing stage. The nanotubes formed in this situation got a bigger diameter and a longer length.

3.5. Effect of Electrolyte Solution pH. Figure 8 illustrates SEM images for the influence of electrolyte solution pH on the fabrication of TiO_2 nanotube arrays. These samples were

prepared at water contents of 40 wt% in glycerol containing 0.5 wt% NH_4F , electrolyte solution pH ranged from 2 to 10, anodization voltage of 30 V for 2 hours, and bath temperature of 40°C . The results showed that a flaky layer was formed at pH 2 (Figure 8(a)). Nanotube structure is produced at PH 4, but nanotube was not formed around the entire Ti foil. There was some flaky oxidizing layer structure disperses behind the nanotube structure (Figure 8(b)). At PH 6, well-defined and highly ordered TNT was formed (Figure 8(c)). At PH 8, nanotube structure was not well developed (Figure 8(d)). At PH 10, a fine concave and convex porous surface was formed (Figure 8(e)). Electrolyte solution pH influences oxidation

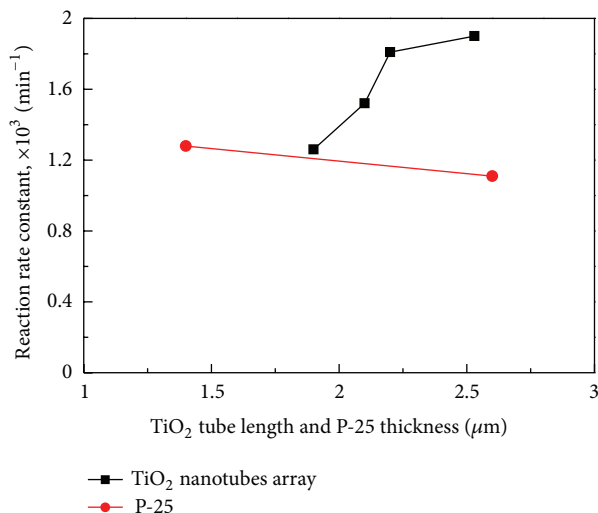


FIGURE 9: Photocatalytic reaction rate constants of TiO₂ nanotube arrays film and P-25 film as a function of film thickness.

rate and chemical etching rate of oxidizing layer. It will further control the surface morphology of TiO₂ film and whether TNT will be formed or not.

At too low pH, chemical etching rate of fluorine ion was too big. Drastic chemical etching on surface resulted in a deep flaky layer, and TNT was unable to be formed. As electrolyte solution pH rises gradually, oxidation and chemical etching rates reached a dynamic equilibrium and promoted the form of TNT. At too high pH, oxidation rate of titanium slowed down but the chemical etching rate slowed down even more and resulted in a concave and convex porous surface. Macák et al. [22] proposed that transition and diffusion of H⁺ ion at low pH resulted in acidic solution accumulated in the bottom of concave. Chemical etching of the accumulated acidic solution caused a deep flaky layer. Cai et al. [16] proposed that high pH caused a low oxidation rate. It needs much time to establish the dynamic equilibrium between oxidation of titanium and chemical etching of oxide layer.

3.6. Comparison of Rate Constants for TNT Film and P-25 Film. This study compared the effect of thicknesses of TNT film and P-25 film on the photocatalysis rates of methylene blue. Figure 9 showed the photocatalytic reaction rate constants of 10 mg/L methylene blue with comparable thicknesses of TNT film and P-25 film under illumination of UV-LED in a recirculation flow system as described in Experimental section. The photocatalytic reaction rate constants with TNT film thicknesses of 1900, 2100, 2200, 2530 nm are 1.26×10^{-3} , 1.52×10^{-3} , 1.81×10^{-3} , and $1.90 \times 10^{-3} \text{ min}^{-1}$, respectively. As lengths of TNT increased the reaction rate constants increased, but the enhancement was retarded when the length of TNT reaching 2200 nm appeared to be the limited penetration of incident UV light. The photocatalytic reaction rate with TNT film was higher than P-25 film at above the film thicknesses range.

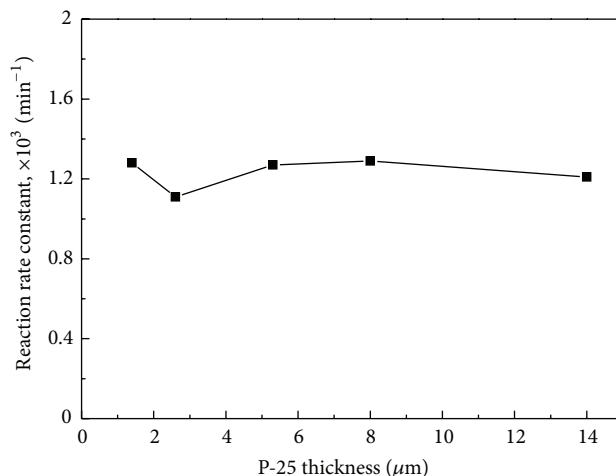


FIGURE 10: Photocatalytic reaction rate constants of different thicknesses of P-25 film ranged from 1400 to 14000 nm.

This result is similar to Macak et al.'s [23]. They prepared TNT film with different tube lengths of 500, 2500, and 4500 nm to study photocatalytic reaction of methylene blue and acid orange 7. The result showed that the photocatalytic reaction ratio is better for TNT films than 2500 nm thickness of P-25 film. Furthermore, the photocatalytic reaction ratio had a positive dependence on the length of nanotubes. Wu et al. [24] studied the photoelectrocatalytic degradation of methylene blue. A reaction rate constant of $2.97 \times 10^{-3} \text{ min}^{-1}$ was observed at a low bias level of 0.6 V. Because of the electric field enhancement, the reaction constant of photoelectrocatalysis is bigger than that of our study on photocatalysis. As shown in Figure 10, the photocatalytic reaction rate constants of different thicknesses of P-25 film ranging from 1400 to 14000 nm had no obvious variation. It could be proposed that only the top layer of particle-packed P-25 film contacts with dye solution and results in photocatalytic reaction. Other P-25 below the top layer has no contribution to photocatalysis. On other hand, because of the porous structure of TNT film, the dye solution has more opportunities to contact with TiO₂. The porous nanotube structure causes the photocatalysis rate constants to increase as the lengths of TNT increase.

4. Conclusion

In summary, self-organized TNT films were synthesized using anodization method in NH₄F containing electrolyte. The growth of TNT was mainly determined by applied anodization voltage rather than bath temperature. The inner diameter of TNT was mainly determined by the anodization voltage while the length of TNT was affected by both anodization voltage, and anodization time. With the photocatalysis of methylene blue, It was found that the best well-defined, highly ordered, and uniform TNT film was prepared in glycerol electrolyte with water content of 40%, anodization voltage of 30 V, electrolysis time of 6 hours, bath temperature of 40°C, and electrolyte solution pH of 6. The photocatalytic reaction rate constants with TNT film thicknesses ranged from 1900

to 2530 nm were higher than with P-25 film at comparable thicknesses.

Acknowledgment

The authors gratefully acknowledge the financial support to this work from the National Science Council of Taiwan, Taiwan (NSC 99-2221-E-324-004).

References

- [1] D. M. Blake, "Bibliography of work on the heterogeneous photocatalytic removal of hazardous compounds from water and air," Tech. Rep., U.S. National Renewable Energy Laboratory, Golden, Colo, USA, 2001.
- [2] A. Fujishima and K. Honda, "Electrochemical photolysis of water at a semiconductor electrode," *Nature*, vol. 238, no. 5358, pp. 37–38, 1972.
- [3] A. L. Linsebigler, G. Lu, and J. T. Yates, "Photocatalysis on TiO_2 surfaces: principles, mechanisms, and selected results," *Chemical Reviews*, vol. 95, no. 3, pp. 735–758, 1995.
- [4] J. M. Macák, H. Tsuchiya, A. Ghicov, and P. Schmuki, "Dye-sensitized anodic TiO_2 nanotubes," *Electrochemistry Communications*, vol. 7, no. 11, pp. 1133–1137, 2005.
- [5] X. Quan, X. Ruan, H. Zhao, S. Chen, and Y. Zhao, "Photoelectrocatalytic degradation of pentachlorophenol in aqueous solution using a TiO_2 nanotube film electrode," *Environmental Pollution*, vol. 147, no. 2, pp. 409–414, 2007.
- [6] N. Wang, X. Li, Y. Wang, X. Quan, and G. Chen, "Evaluation of bias potential enhanced photocatalytic degradation of 4-chlorophenol with TiO_2 nanotube fabricated by anodic oxidation method," *Chemical Engineering Journal*, vol. 146, no. 1, pp. 30–35, 2009.
- [7] P. Hoyer, "Formation of a titanium dioxide nanotube array," *Langmuir*, vol. 12, no. 6, pp. 1411–1413, 1996.
- [8] T. Kasuga, M. Hiramatsu, A. Hoson, T. Sekino, and K. Niihara, "Formation of titanium oxide nanotube," *Langmuir*, vol. 14, no. 12, pp. 3160–3163, 1998.
- [9] D. Gong, C. A. Grimes, O. K. Varghese et al., "Titanium oxide nanotube arrays prepared by anodic oxidation," *Journal of Materials Research*, vol. 16, no. 12, pp. 3331–3334, 2001.
- [10] G. K. Mor, O. K. Varghese, M. Paulose, K. Shankar, and C. A. Grimes, "A review on highly ordered, vertically oriented TiO_2 nanotube arrays: fabrication, material properties, and solar energy applications," *Solar Energy Materials and Solar Cells*, vol. 90, no. 14, pp. 2011–2075, 2006.
- [11] Y. Alivov and Z. Y. Fan, "Efficiency of dye sensitized solar cells based on TiO_2 nanotubes filled with nanoparticles," *Applied Physics Letters*, vol. 95, no. 6, Article ID 063504, 2009.
- [12] W. Y. Wang and Y. Ku, "Photocatalytic degradation of reactive red 22 in aqueous solution by UV-LED radiation," *Water Research*, vol. 40, no. 12, pp. 2249–2258, 2006.
- [13] A. Valota, D. J. LeClere, P. Skeldon et al., "Influence of water content on nanotubular anodic titania formed in fluoride/glycerol electrolytes," *Electrochimica Acta*, vol. 54, no. 18, pp. 4321–4327, 2009.
- [14] B. G. Lee, J. W. Choi, S. E. Lee, Y. S. Jeong, H. J. OH, and C. S. Chi, "Formation behavior of anodic TiO_2 nanotubes in fluoride containing electrolytes," *Transactions of Nonferrous Metals Society of China*, vol. 19, no. 4, pp. 842–845, 2009.
- [15] J. M. Macak, H. Hildebrand, U. Marten-Jahns, and P. Schmuki, "Mechanistic aspects and growth of large diameter self-organized TiO_2 nanotubes," *Journal of Electroanalytical Chemistry*, vol. 621, no. 2, pp. 254–266, 2008.
- [16] Q. Cai, M. Paulose, O. K. Varghese, and C. A. Grimes, "The effect of electrolyte composition on the fabrication of self-organized titanium oxide nanotube arrays by anodic oxidation," *Journal of Materials Research*, vol. 20, no. 1, pp. 230–236, 2005.
- [17] G. A. Crawford, N. Chawla, K. Das, S. Bose, and A. Bandyopadhyay, "Microstructure and deformation behavior of biocompatible TiO_2 nanotubes on titanium substrate," *Acta Biomaterialia*, vol. 3, no. 3, pp. 359–367, 2007.
- [18] J. M. Macak and P. Schmuki, "Anodic growth of self-organized anodic TiO_2 nanotubes in viscous electrolytes," *Electrochimica Acta*, vol. 52, no. 3, pp. 1258–1264, 2006.
- [19] E. Y. Kim, J. H. Park, and G. Y. Han, "Design of TiO_2 nanotube array-based water-splitting reactor for hydrogen generation," *Journal of Power Sources*, vol. 184, no. 1, pp. 284–287, 2008.
- [20] Y. C. Lim, Z. Zainal, W. T. Tan, and M. Z. Hussein, "Anodization parameters influencing the growth of titania nanotubes and their photoelectrochemical response," *International Journal of Photoenergy*, vol. 2012, Article ID 638017, 9 pages, 2012.
- [21] G. K. Mor, K. Shankar, M. Paulose, O. K. Varghese, and C. A. Grimes, "Enhanced photocleavage of water using titania nanotube arrays," *Nano Letters*, vol. 5, no. 1, pp. 191–195, 2005.
- [22] J. M. Macák, H. Tsuchiya, and P. Schmuki, "High-aspect-ratio TiO_2 nanotubes by anodization of titanium," *Angewandte Chemie*, vol. 44, no. 14, pp. 2100–2102, 2005.
- [23] J. M. Macak, M. Zlamal, J. Krysa, and P. Schmuki, "Self-organized TiO_2 nanotube layers as highly efficient photocatalysts," *Small*, vol. 3, no. 2, pp. 300–304, 2007.
- [24] X. Wu, Z. Huang, Y. Liu, and M. Fang, "Investigation on the photoelectrocatalytic activity of well-aligned TiO_2 nanotube arrays," *International Journal of Photoenergy*, vol. 2012, Article ID 832516, 7 pages, 2012.

Research Article

The Synergistic Effect of Nitrogen Dopant and Calcination Temperature on the Visible-Light-Induced Photoactivity of N-Doped TiO₂

Yao-Tung Lin,¹ Chih-Huang Weng,² Hui-Jan Hsu,¹ Yu-Hao Lin,¹ and Ching-Chang Shiesh³

¹ Department of Soil and Environmental Sciences and Center of Nanoscience and Nanotechnology, National Chung Hsing University, TaiChung 402, Taiwan

² Department of Civil and Ecological Engineering, I-Shou University, Kaohsiung 84001, Taiwan

³ Department of Horticulture, National Chung Hsing University, TaiChung 402, Taiwan

Correspondence should be addressed to Yao-Tung Lin; yaotung@nchu.edu.tw

Received 9 January 2013; Revised 28 March 2013; Accepted 29 March 2013

Academic Editor: Jiaguo Yu

Copyright © 2013 Yao-Tung Lin et al. This is an open access article distributed under the Creative Commons Attribution License, which permits unrestricted use, distribution, and reproduction in any medium, provided the original work is properly cited.

The synergistic effect of nitrogen content and calcinations temperature on the N-doped TiO₂ catalysts prepared by sol-gel method was investigated. The phase and structure, chemical state, optical properties, and surface area/pore distribution of N-doped TiO₂ were characterized using X-ray diffraction spectrometer, high-resolution transmission electron microscope, X-ray photoelectron spectroscopy, UV-vis diffusion reflectance spectroscopy, and Brunauer-Emmett-Teller specific surface area. Finding showed that the photocatalytic activity of N-doped TiO₂ was greatly enhanced compared to pure TiO₂ under visible irradiation. N dopants could retard the transformation from anatase to rutile phase. Namely, N-doping effect is attributed to the anatase phase stabilization. The results showed nitrogen atoms were incorporated into the interstitial positions of the TiO₂ lattice. Ethylene was used to evaluate the photocatalytic activity of samples under visible-light illumination. The results suggested good anatase crystallization, smaller particle size, and larger surface are beneficial for photocatalytic activity of N-doped TiO₂. The N-doped TiO₂ catalyst prepared with ammonia to titanium isopropoxide molar ratio of 2.0 and calcinated at 400°C showed the best photocatalytic ability.

1. Introduction

Titanium dioxide (TiO₂) is an effective photocatalyst due to its inexpensiveness, chemical stability, nontoxicity, biological and chemical inertness, and long-term stability against photo-corrosion and chemical corrosion [1, 2]. In the last two decades, many works have been done on expanding and augmenting the utility of TiO₂ in heterogeneous photocatalysis (e.g., water purification, air cleaning, and water splitting for the production of hydrogen) [2–5], self-cleaning surfaces [6], inactivation of bacteria and fungi [7, 8], solar cells [9], anticorrosive coatings [10], and Li-ion batteries [11]. TiO₂ has three phases in nature, brookite (orthorhombic), anatase (tetragonal), and rutile (tetragonal). It is amorphous at temperature up to 300°C, becoming anatase and rutile typically at 350 and 800°C, respectively [3]. Anatase powder with good crystallinity, small grain size, and high specific

surface area is desirable as long as the photocatalytic activity is concerned. However, its wide band gap of 3.2 and 3.0 eV for anatase and rutile polymorphs, respectively, requires UV light for the excitation of electron-hole pairs. It only uses 4–5% of the UV light in the solar irradiation. To utilize solar energy effectively, many attempts have been made to modify the properties of TiO₂, such as doping with transition metal ions [12–14] or nonmetal anions [3, 15–23], and sensitization with organic dyes [24, 25]. Among the nonmetal-doping TiO₂ photocatalysts, the simplest and most feasible TiO₂ modification approaches for achieving visible-light-driven photocatalysis seem to be N-doping, that is, doping nitrogen atoms into interstitial (or substitutional) sites in the crystal structure of TiO₂. Sato [4] was the first to report on nitrogen-doped TiO₂. It was treated with various nitrogen sources such as urea, ammonia, ammonium chloride, and nitric acid. Asahi et al. have prepared TiO_{2-x}N_x films whose

absorption activity not only was shifted toward the longer visible wavelength but also had higher thermal stability and less recombination centers of charge carriers than the metal-doped TiO_2 [5]. However, to date, little research has been conducted on gaining in-depth information on the properties of the interstitial (or substitutional) N-doped TiO_2 , as well as its photocatalytic activity. Different dopants result in TiO_2 of different properties and consequently alter the photocatalytic activity of the materials. Currently, few works have focused on the synergistic effects of nitrogen dopant and calcination temperature on the characteristics and visible-light-induced photoactivity of N-doped TiO_2 [6].

In this study, we focused on sol-gel synthesis process for the preparation of nitrogen-doped TiO_2 catalysts (N- TiO_2) because the wet processes have the advantages of low cost, ease of scale-up, and stability for practical applications. The effects of N atom and calcination temperature on the structural, optical, and photocatalytic properties of N- TiO_2 were assessed. The gel samples were calcined at 400, 500, 600, 700, and 800°C. The photocatalysts were characterized using X-ray diffraction (XRD), high-resolution transmission electron microscope (HRTEM), X-ray photoelectron spectroscopy (XPS), UV-vis diffusion reflectance spectroscopy (UV-vis DRS), Brunauer-Emmett-Teller (BET) specific surface area (S_{BET}), and thermogravimetric-differential thermal analysis (TG-DTA). The transition from amorphous to anatase and rutile phases at different calcination temperatures was also explored. Ethylene was chosen as a probe reactant because it is structurally simple, has relatively high reactivity, and is the parent compound of many widespread volatile organic compounds (VOCs) of environmental concern (e.g., TCE and tetrachloroethylene). The object of this study is to investigate the synergistic effects of nitrogen content and calcination temperatures in the synthesis process of N-doped TiO_2 prepared by sol-gel process and to investigate the influence of ethylene on photocatalytic decomposition.

2. Materials and Methods

2.1. Preparation of N-Doped TiO_2 Catalyst. Titanium isopropoxide (TTIP, $\text{C}_{12}\text{H}_{28}\text{O}_4\text{Ti}$, 97%, Aldrich), a highly reactive alkoxide, was used as precursor. Aqua ammonia (NH_4OH) was used as nitrogen source. A given amount of aqua ammonia was added to the distilled water while being stirred until it completely dissolved at room temperature. Then, the solution was added dropwise to a constant amount of titanium isopropoxide as to obtain an aqua ammonia to TTIP molar ratio (A/T) of 1:1; the TiO_2 sample was designated as N- TiO_2 . While the mixture was being stirred vigorously, the urea solution was introduced to the TTIP. Hydrolysis and polycondensation reactions occurred. The reactant was stirred continuously for one hour after all aqua ammonia solution was dissipated. The sol was aged in air for 24 hr to allow further hydrolysis. The final sol was left on the bench top to allow thickening. After aging, the sol was dried at 70°C for 24 hr to evaporate the solvent. The residual xerogel was crushed to fine powder before calcined in a furnace at 400, 500, 600, 700, and 800°C, respectively, for 3 hr. Pure

TiO_2 powder was also prepared without the presence of aqua ammonia following the same procedures as described above. The nitrogen-doped samples were labeled AxTy , where x and y refer to the aqua ammonia to TTIP molar ratio (A/T) and calcining temperature, respectively. For example, A20T4 means the N- TiO_2 prepared with A/T molar ratio 2.0 and calcinated at 400°C.

2.2. Characterization. The S_{BET} of the samples was determined using nitrogen adsorption method measured with a Micromeritics ASAP 2020 adsorption apparatus. Pore size and pore volume were calculated by the BJH isotherm. The crystallization behavior and stability of N atoms in N- TiO_2 were monitored using a TG-DTA (STA 6000, PerkinElmer), while the sample was being heated from room temperature to 1000°C at 10°C/min. The morphology, structure, and grain size of the samples were characterized by a high-resolution transparent electromicroscopy (HRTEM, JEM-2010, JEOL). To study the optical response of N- TiO_2 samples ($\lambda = 200\text{--}800\text{ nm}$), UV-vis DRS (U3900H, Hitachi) were recorded using a spectrophotometer with an integrating sphere attachment and Al_2O_3 was used as the reference. The chemical environment information and the N concentration of all of the samples were measured by X-ray photoelectron spectra (XPS) (PHI 5000, VersaProbe/Scanning ESCA Microprobe with a C_{60} ion gun). All samples were collected in vacuum and transferred to the main ultrahigh-vacuum (UHV) chamber for measurements. The shift of binding energy due to relative surface charging was corrected to the C 1s level at 285 eV as an internal standard. The XPS peaks were assumed to have Gaussian line shapes and were resolved into components by a nonlinear least-squares procedure after proper subtraction of the baseline. The crystallinity and phase of the samples were analyzed by XRD (PANalytical X'Pert-Pro MPD PW3040/60) with Cu-K α radiation at a scan rate of 0.05°/s in the range from 20 to 80°.

2.3. Photooxidation Performance. The experiment setup and operating conditions for photocatalytic activity tests were the same as those reported previously [7]. The catalyst was prepared by depositing suspension of the as-prepared catalyst at the bottom surface of the reactor that was subsequently dried at ambient condition. The obtained catalyst film density on the bottom surface of reactor was kept at 4 mg/cm². The experiment setup and operating conditions for photocatalytic activity tests were the same as those in our previous reports [7]. The photocatalytic activity experiments of the as-prepared catalysts for the oxidation of ethylene in gas phase were performed at room temperature using a 250 mL photocatalytic reactor. Air with 60% relative humidity was passed through the reactor with the sample inside for 1 hr to reach equilibrium, and then a desired amount of ethylene was injected into the reactor with a gastight syringe. The ethylene inside the reactor was taken at regular intervals with gas-tight syringe and analyzed using gas chromatographs (PerkinElmer, Clarus 500, USA) equipped with a flame ionization detector (FID) and a thermal conductivity detector (TCD) detection. The GC instrument was equipped with an

Elite-Plot-Q capillary column (Agilent Technologies). The ethylene was allowed to reach adsorption equilibrium with the catalyst in the reactor prior to irradiation. Two 500-W horizontal halogen lamps (9.5 cm in length, PHILIPS) were used to simulate the solar light. The lamp equipped with a cut-off filter ($\lambda > 400$ nm) was vertically placed outside the photocatalytic reactor. Light intensity at the catalyst surface was 16 mW/cm^2 . Blank experiments using an uncoated (no catalyst) glass plate had no effect on the ethylene concentration and did not generate any carbon monoxide or carbon dioxide (see supplementary material online at <http://dx.doi.org/10.1155/2013/268723>). The photocatalytic activity of the catalyst can be quantitatively evaluated by comparing the apparent reaction rate constants.

3. Results and Discussion

3.1. Thermal Analysis. To investigate the process of phase transformation of titanium(IV)-oxide-hydroxide to titanium oxide and the effect of nitrogen doping content on the transformation from anatase to rutile, thermoanalytic techniques including TGA and DTA were conducted. Typically, the hydrothermal weight loss is attributed to a multistep of polycondensation of titanium(IV)-oxide-hydroxide and phase transformation of anatase into rutile or brookite from room temperature to $700\text{--}800^\circ\text{C}$ as shown in Figure 1 and Table 1. DTA measurements established the transformation of $\text{TiO}_x(\text{OH})_y$ into TiO_2 including two endothermic and one exothermic peaks from room temperature to 398°C (Figure 1). A sharp endothermic peak at 105°C due to the release of adsorbed water, while the other minor peak at 253°C is referred to as the desorption of organic. There was a corresponding weight loss from TGA of about 19.8 and 9.4 wt%, respectively. In the region mentioned above, the finely exothermic peak around 276°C is ascribed to the thermal decomposition of unhydrolyzed TTIP with about 0.8 wt% weight loss. The weak thermal effect at $276\text{--}730^\circ\text{C}$ is accompanied by obvious exothermic peak at 451°C which can be assigned to the crystallization of the amorphous phase to anatase. At around 730°C , an obvious exothermic peak was observed owing to the oxidation of carbon residue and evaporation of chemisorbed water, which can be assigned to the phase transformation from anatase titania to rutile TiO_2 . It can be concluded from the DTA result that the as-prepared TiO_2 sample was amorphous. According to TGA, the weight loss roughly consists of three distinct stages. The first stage was up to 276°C , over which the mass loss is the greatest. A mass loss of up to 30% was observed, which is attributed to the evaporation of the physical adsorbed water and the release of organic. The second stage is from 276 to 451°C , where the mass loss is about 1.7%. This corresponds to the thermal decomposition of unhydrolyzed TTIP. The third stage is from 451 to 730°C and the mass loss is about 0.7%, which is attributed to the removal of chemisorbed water. At about 730°C , no mass loss was observed. The exothermic peaks of N- TiO_2 prepared at 0.5, 1.0, and 2.0 A/T ratios were at 710, 720, and 730°C , respectively (Table 1). The results indicated that nitrogen atoms doped in TiO_2 could prevent

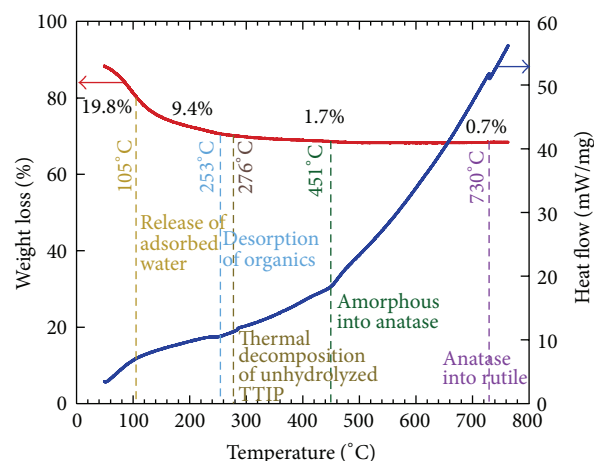


FIGURE 1: TG-DTA curve of N- TiO_2 samples prepared with 2.0 ammonia/TTIP ratio.

phase transition of anatase to rutile, because as far as pure TiO_2 was concerned, most TiO_2 particles were transformed into rutile at 700°C .

3.2. Phase and Structure. The characteristics of N- TiO_2 at various calcination temperatures and molar ratios of A/T are summarized in Table 1. Figure 2 shows the XRD pattern of the N- TiO_2 samples at various A/T ratios and annealed at different temperatures. The presence of peaks ($2\theta = 25.44^\circ, 38.06^\circ$, and 48.24°) was regarded as an attributive indicator of anatase titania, and the presence of peaks ($2\theta = 27.54^\circ, 36.14^\circ$, and 41.20°) was regarded as an attributive indicator of rutile titania. The diffraction peaks for the anatase (JCPDS no. 21-1272) and rutile (JCPDS no. 21-1276) phases are marked with "A" and "R," respectively, and the corresponding diffraction planes are given in parenthesis. No N-derived peaks were detected in all the patterns. This may be caused by the lower concentration of the doped species, and the limited dopants may have moved into either the interstitial positions or the substitutional sites of the TiO_2 crystal structure, which is consistent with [8, 9]. The average grain size was estimated at 28–131 nm, comparable to that from the HRTEM image. A comparison of XRD patterns clearly shows that nitrogen doping significantly changes the crystalline size and the crystal structure of TiO_2 .

The transformation from the amorphous to the crystalline form of TiO_2 usually requires temperatures close to 300°C [8]. For the samples prepared with 2.0 A/T and calcinated at $400\text{--}500^\circ\text{C}$ (Figure 2(a)), the intensities of the anatase peak are increased and the width of the (101) plane diffraction peak becomes narrower as the calcination temperature increases, implying an improvement and growth in crystallinity. Increasing the temperature to 800°C , the intensity of anatase peak decreases, but the rutile peaks appear, suggesting the transformation of anatase to rutile phase. The average crystalline size was 32, 85, and 103 nm and the mass percentage of anatase was 90, 60, and 6% for samples prepared at 2.0 A/T and calcination temperature

TABLE 1: Characteristics for N-TiO₂ at various ammonia/TTIP molar ratios under different calcination temperatures.

Sample ^a	XRD				BET	TG-DTA	TEM	Optical properties			
	Phase ratio		Crystallite size		Surface area (m ² /g)	A ^b → R ^c Temp. (°C)	Size (nm)	λ _{g,1} (nm)	E _{g,1} (nm)	λ _{g,2} (nm)	E _{g,2} (nm)
	A ^b %	R ^c %	A ^b (nm)	R ^c (nm)							
A00T4	90	10	32	—	93	703	11 ± 1	392	3.16	—	—
A05T4	89	11	28	—	108	710	12 ± 1	392	3.16	505	2.46
A10T4	90	10	28	—	119	720	12 ± 1	391	3.17	506	2.45
A15T4	87	13	29	—	119	728	11 ± 1	388	3.20	513	2.42
A20T4	90	10	32	—	98	730	12 ± 1	390	3.18	510	2.43
A25T4	90	10	37	—	98	728	12 ± 1	392	3.16	515	2.41
A30T4	92	8	37	—	86	729	12 ± 1	392	3.16	514	2.41
A00T5	94	6	46	—	50	703	13 ± 2	402	3.08	—	—
A05T5	89	11	46	98	64	710	13 ± 1	404	3.07	503	2.47
A10T5	90	10	41	87	68	720	15 ± 2	400	3.10	508	2.44
A15T5	91	9	40	—	71	728	15 ± 2	396	3.13	517	2.40
A20T5	94	6	45	—	62	730	15 ± 2	394	3.15	513	2.42
A25T5	94	6	49	—	55	728	17 ± 2	397	3.12	507	2.45
A30T5	94	6	47	—	53	729	17 ± 2	397	3.12	510	2.43
A00T6	34	66	106	156	7	703	24 ± 2	420	2.95	—	—
A05T6	14	86	86	128	8	710	40 ± 3	422	2.94	—	—
A10T6	14	86	81	132	9	720	40 ± 4	425	2.92	—	—
A15T6	22	78	79	141	14	728	35 ± 3	424	2.92	—	—
A20T6	60	40	85	184	17	730	34 ± 3	415	2.99	—	—
A25T6	78	22	90	184	16	728	35 ± 4	416	2.98	—	—
A30T6	74	26	97	169	12	729	36 ± 4	415	2.99	—	—
A00T7	6	94	131	177	2	703	80 ± 5	424	2.92	—	—
A05T7	3	97	95	148	5	710	145 ± 10	428	2.90	—	—
A10T7	3	97	102	149	6	720	145 ± 10	429	2.89	—	—
A15T7	3	97	92	159	6	728	150 ± 11	428	2.90	—	—
A20T7	6	94	103	163	4	730	170 ± 13	428	2.90	—	—
A25T7	15	85	108	178	8	728	60 ± 6	426	2.91	—	—
A30T7	15	85	117	182	6	729	60 ± 6	427	2.90	—	—
A00T8	1	99	—	174	3	703	200 ± 17	424	2.92	—	—
A05T8	1	99	—	161	3	710	190 ± 15	428	2.90	—	—
A10T8	1	99	—	159	3	720	160 ± 13	429	2.89	—	—
A15T8	1	99	—	171	3	728	170 ± 15	428	2.90	—	—
A20T8	1	99	—	164	2	730	160 ± 14	428	2.90	—	—
A25T8	3	97	106	184	4	728	200 ± 18	427	2.90	—	—
A30T8	3	97	127	179	3	729	170 ± 15	429	2.89	—	—

^aAXXTY: ammonia/TTIP molar ratio = 0.XX; calcination temperature = Y00°C.^bAnatase.^cRutile.

of 400, 600, and 700°C, respectively. The maximum mean size of anatase and rutile crystallites was observed at 800°C. Results agreed with those reported that the crystalline size grows and the content of anatase diminishes as calcination temperature increases [8, 10–13]. For the samples prepared at 0.5 A/T, the anatase peaks appear at temperatures 400 and 500°C. Increasing the temperature to 500°C, the intensity of anatase peak decreases, but the rutile peaks appear. When temperature is increased further to 600°C, rutile becomes a main phase. In this case, the anatase-to-rutile phase transformation temperature is between 400 and 500°C. XRD

patterns of samples prepared at 3.0 A/T and annealed at 700°C show both anatase and a rutile phase, indicating that anatase-to-rutile phase transformation is shifted to higher temperature. It can be seen that the presence of nitrogen can restrain the formation and growth of TiO₂ crystal phase, thereby retarding the anatase-to-rutile phase transformation. This result is further supported by the appearance of rutile in XRD patterns of sample prepared at 0.5 and 1.5 G/T at 600°C and disappearance for samples prepared at G/T greater than 2.0 at 600°C (data not shown). Compared with P25, the peak position of the (101) plane of N-doped

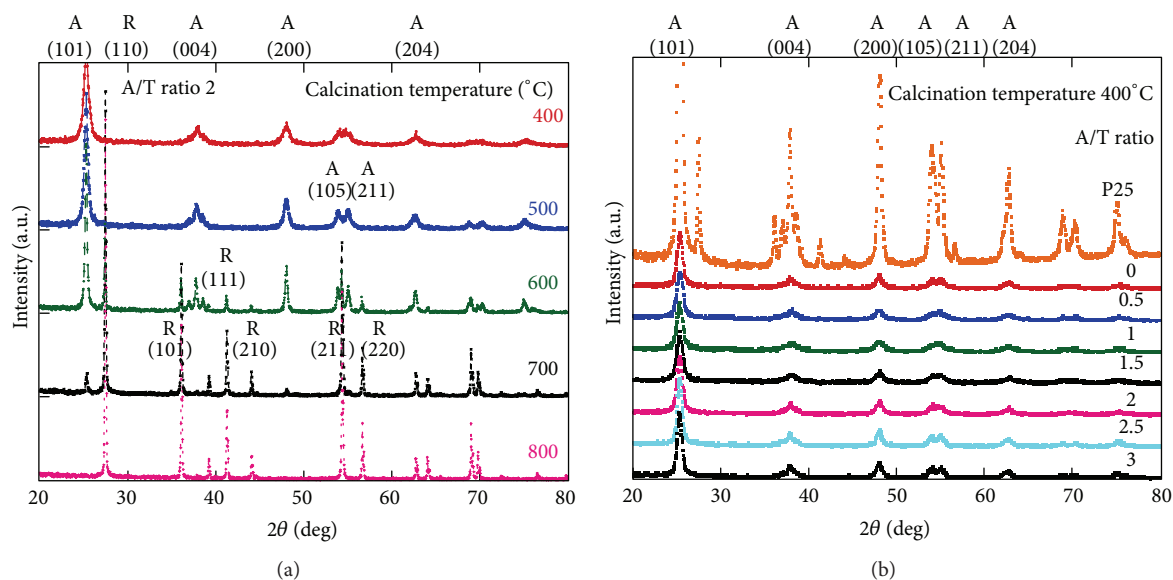


FIGURE 2: XRD patterns of N-TiO₂ samples prepared (a) at various calcination temperatures and (b) with various ammonia/TTIP ratios.

TiO₂ shifted slightly to higher 2θ value, and the peak was broader as N/T ratio increases, suggesting distortion of the crystal lattice of TiO₂ by the incorporation of nitrogen. The crystalline sizes of samples calcined at 400 °C and prepared at 0.5, 1.5, 2.0, and 3.0 A/T were 28, 29, 32, and 37 nm, respectively. The average crystalline size of samples increases with increase in A/T, revealing that nitrogen can enhance the growth of N-TiO₂ crystals. Results agreed with those reported that the crystalline size grows as nitrogen to Ti proportion increases [14]. The results reveal that the phase transformation temperature of anatase to rutile was progressively increased when the amount of N dopant was increased. Clearly, calcination temperature and A/T ratio play a significant role in the formed crystal structure and particle size (Figure 3). Higher temperature favors the growth of rutile structure and produces N-TiO₂ nanoparticles with larger particle size. Thus, a fine control of calcination temperature and A/T ratio is crucial for obtaining a pure phase of N-TiO₂.

Further insights into the effect of calcination and doping on the morphology and structure of the N-TiO₂ samples can be obtained from HRTEM image (Figure 4). The selected area electron diffraction pattern and TEM confirmed its highly crystalline anatase or rutile structure. The observed d -spacing from HRTEM image is 3.522 Å and is comparable to 3.52 Å previously reported for (101) crystallographic plane of undoped anatase [15–18]. The HRTEM image showed the nanocrystallines with primary grain size around 11–200 nm. From the TEM images, the particles in N-TiO₂ samples are monodispersed. The crystalline form aggregates with a mesoporous structure. The formation of mesoporous structure is similar to that reported in the literature [19, 20]. First, monodispersed amorphous titanium oxide sol particles are formed by the hydrolysis processes. Then the monodispersed sol particles are crystallized and aggregated under calcination treatment to form mesoporous crystalline. Based on the HRTEM results, the calcination temperature

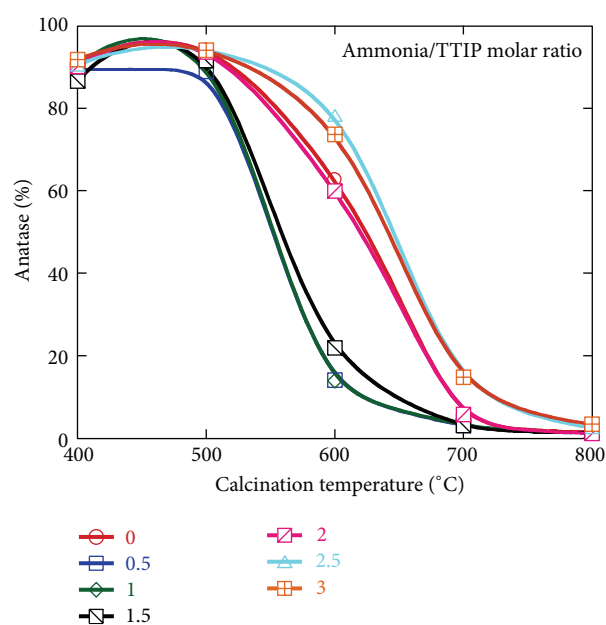


FIGURE 3: The anatase content of N-TiO₂ samples as a function of the various ammonia/TTIP molar ratios.

significantly changes the size of particles (Table 1). The grain size of crystalline is in consistent with the calculated value obtained from XRD patterns (Table 1). The grain size of samples increases with the calcination temperature. Morphological observation by TEM and XRD calculations reveals that the large particle size of A20T8 was mainly caused by agglomeration and the growth of crystallite size.

3.3. Surface Area and Pore Size Distribution. Typical nitrogen adsorption-desorption isotherms of N-TiO₂ photocatalyst

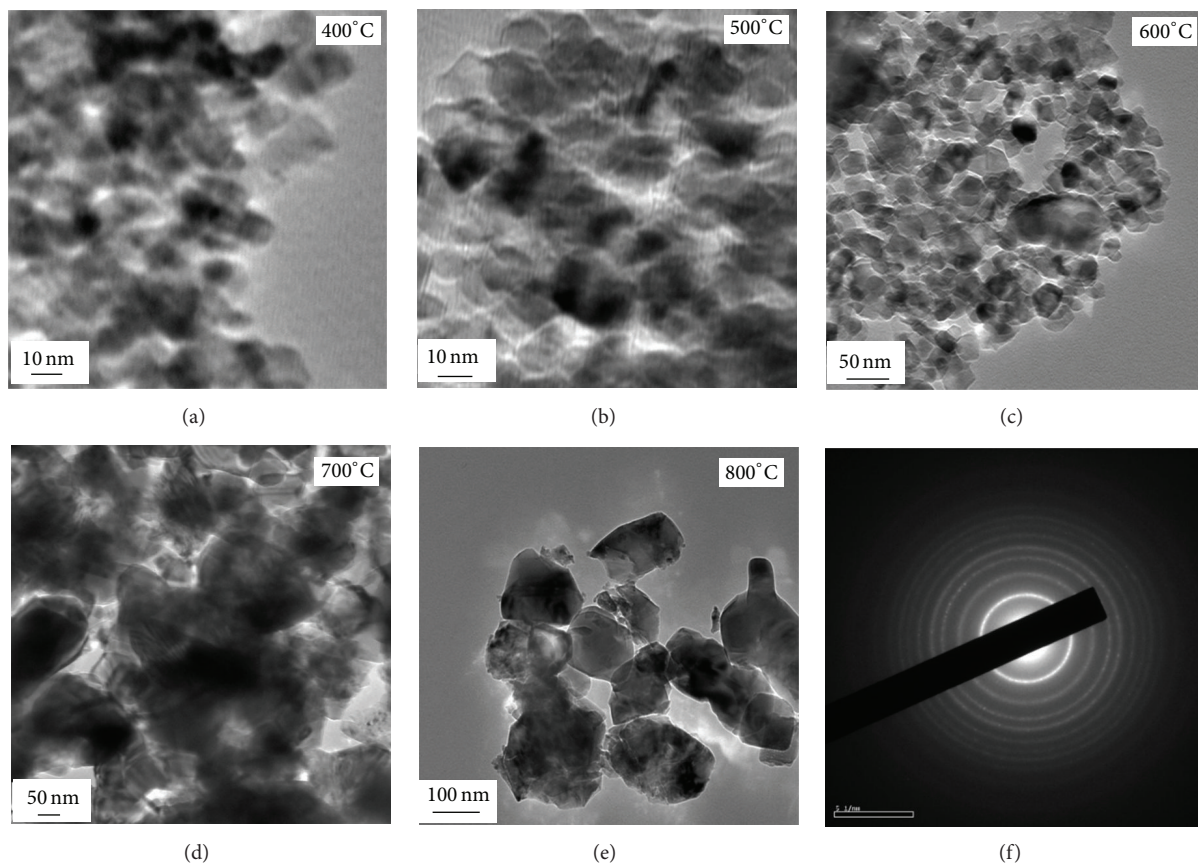


FIGURE 4: TEM images of N-TiO₂ prepared (a)–(e) at various calcination temperatures with 2.0 ammonia/TiP ratio and (f) the selected area electron diffraction of A20T4.

are shown in Figure 5. The S_{BET} of N-TiO₂ prepared with 2.0 A/T ratio at calcined 400, 500, 600, 700, and 800°C was 98, 62, 17, 4, and 2 m²/g, respectively. Obviously, the values of S_{BET} and pore volume of N-TiO₂ prepared with the same A/T ratio decreased with increasing calcination temperatures. Such phenomenon could be attributed to the collapse of the mesoporous structure, the growth of TiO₂ crystallites, and the removal process of nitrogen core by high-temperature calcination. Consequently, N-TiO₂ calcined at 800°C has the least S_{BET} . Based on the results obtained, the hysteresis loop of N-TiO₂ is significantly shifted in direction of higher relative pressures as calcination temperature increases, indicating much larger mesopore. The average pore size of N-TiO₂ increased with increasing calcination temperature due to the formation of slit-like pores [21].

The N-TiO₂ samples obtained at various calcination temperatures gave different nitrogen adsorption isotherms (Figure 5), implying differences in their porous structure. The N-TiO₂ samples prepared at low calcination temperature (i.e., 400 and 500°C) exhibited a type IV isotherm and a type H2 hysteresis loop at lower relative pressure region, which are typical characteristics of mesoporous structure with ink bottle pores. Note that the adsorption branches of these isotherms resembled type II, indicating the presence of some macropores. Otherwise the N-TiO₂ samples prepared

at higher calcination temperature (i.e., 600–800°C) exhibited a type V isotherm and a type H3 hysteresis loop at higher relative pressure. The hysteresis loop at lower relative pressure region ($0.4 < P/P_0 < 0.8$) was attributed to a smaller mesopore, while that at the higher relative pressure ($0.8 < P/P_0 < 1.0$) was of larger mesopores. Thus samples prepared at high calcination temperature ($>600^\circ\text{C}$) had a wide pore size distribution in the mesopores scale. The isotherm of N-TiO₂ prepared at higher calcination temperature was below that of lower calcination temperature (Figure 5), indicating lower surface area and pore volume of the former. Further observation from Table 1 indicated that S_{BET} for the N-TiO₂ samples at the same A/T ratio increased with increasing calcination temperature (Figure 5(c)). Results reveal that all N-TiO₂ samples calcined at various temperatures show monomodal pore size distributions and mesopores may be assigned to the pores among interaggregated particles (data not shown). With calcination temperature increasing, there is a significant tendency of pore size distribution toward to the bigger pore size. The increase of pore size is due to the corruption of smaller pores during calcination as the smaller pores endured much greater stress than the bigger pores. Formation of bigger crystalline aggregation upon increase in temperature could form bigger pores also. Consequently, the pore size increases while the pore volume decreases with

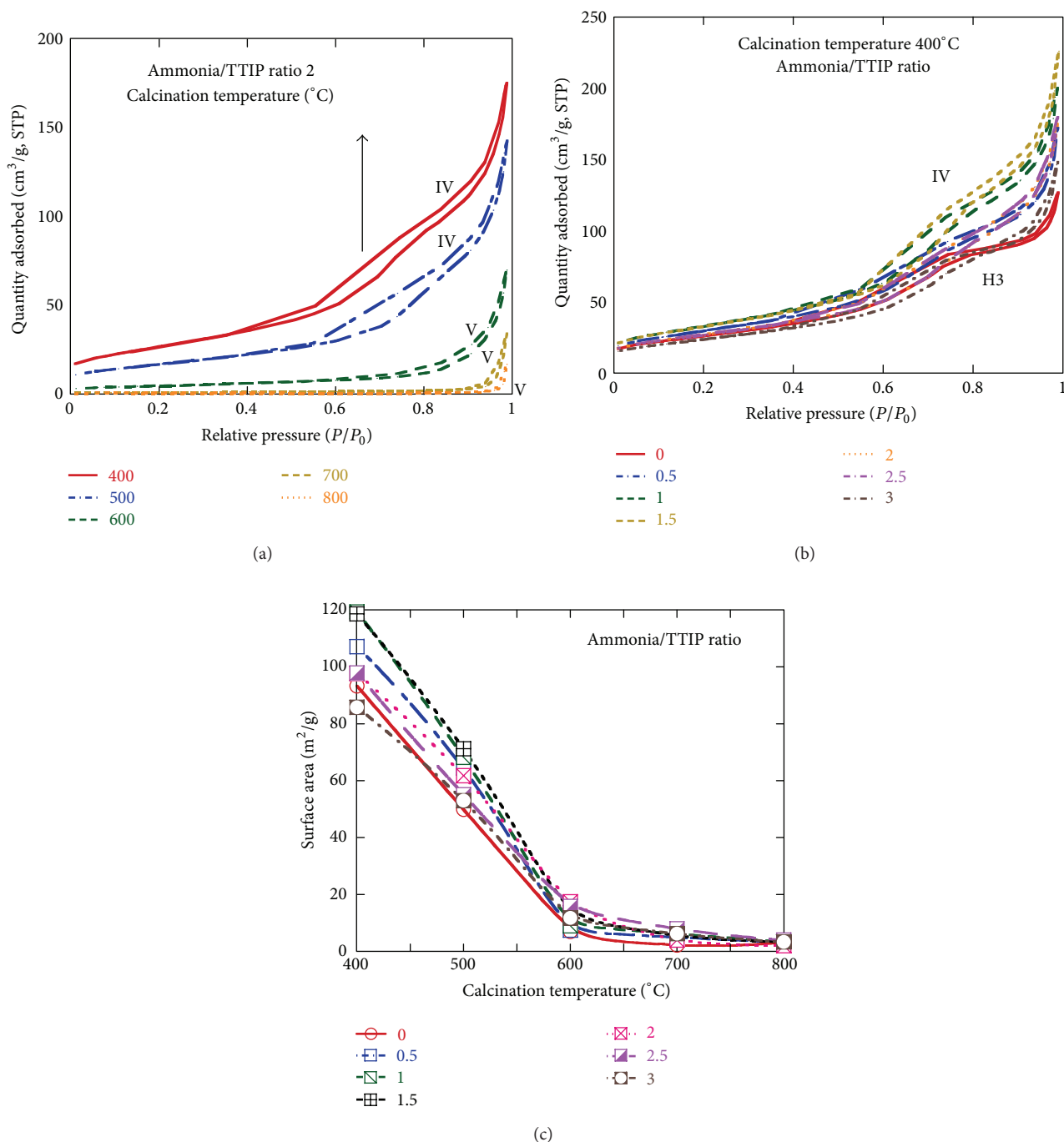


FIGURE 5: Nitrogen adsorption and desorption isotherms of N-TiO₂ samples (a) calcined at various temperatures, (b) prepared with various ammonia/TTIP molar ratios; the surface area as a function of calcination temperature.

calcinations temperature increasing. Based on the TEM and BET results, the mesopores of TiO₂ were decreased due to the heat shrinkage of calcination. The results indicated that calcination at high temperature and in the presence of nitrogen atoms will help to improve the thermal stability of the photocatalyst. While the calcination temperature was increased, both the specific surface area and the pore volume of N-TiO₂ samples decreased. This indicated that the average pore size increased while the pore volume and the

specific surface area decreased with calcination temperature increasing.

3.4. Optical Properties. The typical UV-vis diffuse reflectance spectra of N-TiO₂ are shown in Figures 6(a) and 6(b). It can be seen that nondoped TiO₂ (P25) has only one light sharp edge ($\lambda = 410$ nm) which can be assigned to the band gap of TiO₂, while part of N-TiO₂ showed two absorption edges and a noticeable shift to the visible light region as compared

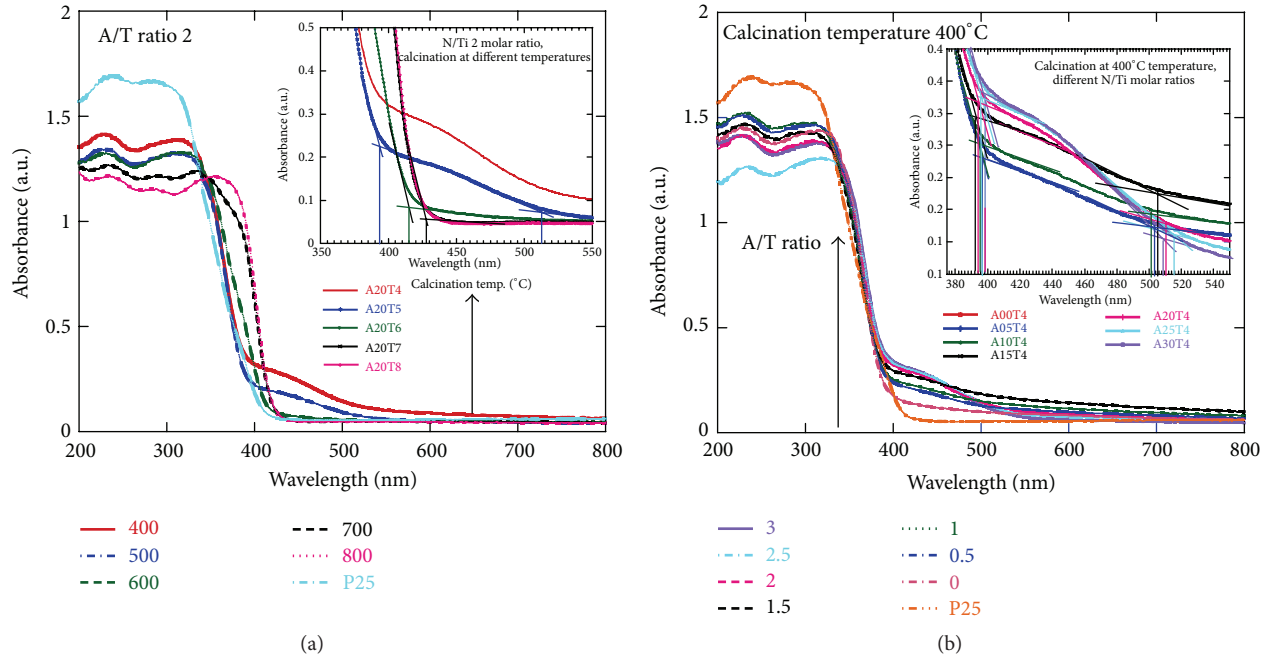


FIGURE 6: The typical UV-vis DR spectra of N-TiO₂ samples: (a) prepared with 2.0 ammonia/TTIP molar ratio and calcined at various temperatures; (b) prepared with various ammonia/TTIP molar ratios and calcined at 400 °C.

to that of the TiO₂ (i.e., P25). This phenomenon should be ascribed to either the nitrogen doping and/or sensitization by a surface-anchored group. The calcination temperature and A/T ratio are the crucial factor that can further affect the absorption as seen in Figure 6. Similar phenomenon had been reported by previous publications [17, 22–25]. The absorption edges of the N-TiO₂ samples show continuous red shift as the calcination temperature changes from 400 to 700 °C, which can be assigned to the intrinsic band gap absorption of TiO₂. The shift is too minor to be observed when the calcination temperature changes from 500 to 600 °C, which is possibly caused by the synergetic effect of the loss of the nitrogen and the increase of the TiO₂ crystallinity during the calcination process. The absorption threshold (λ_g) can be determined using the onset of the absorption edges by the section of the fitting lines on the upward and outward section of the spectrum (shown in the graph inserted in Figure 6) [23]. Table 1 lists the determined λ_g (nm) and the derived band gap energy values. The band gap of N-TiO₂ (E_g) was calculated using the $E_g = 1240/\lambda_g$ equation. It also can be seen that N-TiO₂ samples have two characteristic light absorption edges. One of them corresponds to the band gap of TiO₂ ($\lambda_{g1} = 390\sim 430$ nm) while the other originates from the N-induced midgap level ($\lambda_{g2} = 505\sim 517$ nm). The color of the samples was different with calcination temperature and A/T ratio. The color of N-TiO₂ samples prepared with 2.0 A/T ratio and calcinated at 400, 600, and 700 °C was vivid yellow, yellow, and white, respectively. There is no λ_{g2} when N-TiO₂ calcinated above 600 °C. It can be ascribed to the amount of N dopant decreased. The color of N-TiO₂ prepared with 0.0, 1.0, 2.0, and 3.0 A/T ratio and calcinated at 400 °C was white, pale yellow, yellow, and vivid yellow,

respectively. The phenomenon that the A/T ratio increases the shifting of the spectra towards visible region was clearly observed (Figure 6(a)). The absorption threshold (λ_g) was increased with increasing A/T ratio. It reveals that more nitrogen doping in the matrix of TiO₂ structure results in a shift of absorbance region toward visible light wavelength. This is possible attribute to the nitrogen incorporated into TiO₂ lattice and formation of new electronic state above valence band caused by nitrogen doping to generate a red shift.

3.5. Analysis of Chemical State. The chemical states of doping impurity are critical to the optical property, band gap, and photocatalytic activity of nitrogen-doped TiO₂. To investigate the chemical states of the doping nitrogen, XPS spectra were applied to examine three regions: the Ti 2p core level near 460 eV, the O 1s core level near 530 eV, and the N 1s core level near 400 eV. Figure 7 shows the experimental observation of surface chemical composition and the electronic structures of N-TiO₂ samples using XPS. XPS peaks showed that the N-TiO₂ contained only Ti, O, N elements and a small quantity of carbon. The presence of carbon was ascribed to the residual carbon from the precursor solution and the adventitious hydrocarbon from the XPS instrument itself. In Figures 7(a) and 7(b), the binding energy (BE) peaks corresponding to N 1s core levels for N-TiO₂ are observed one major peak at 400 eV. The N 1s peak at 400 eV is ascribed to the presence of the oxidized nitrogen species, and the nitrogen may be incorporating into the interstitial positions of the TiO₂ lattice and to form a Ti–O–N structure [26, 27]. No other N 1s peaks were detected in N-TiO₂ samples. As shown in Figure 7, N 1s peak at 400 eV slightly decreased with increasing calcination

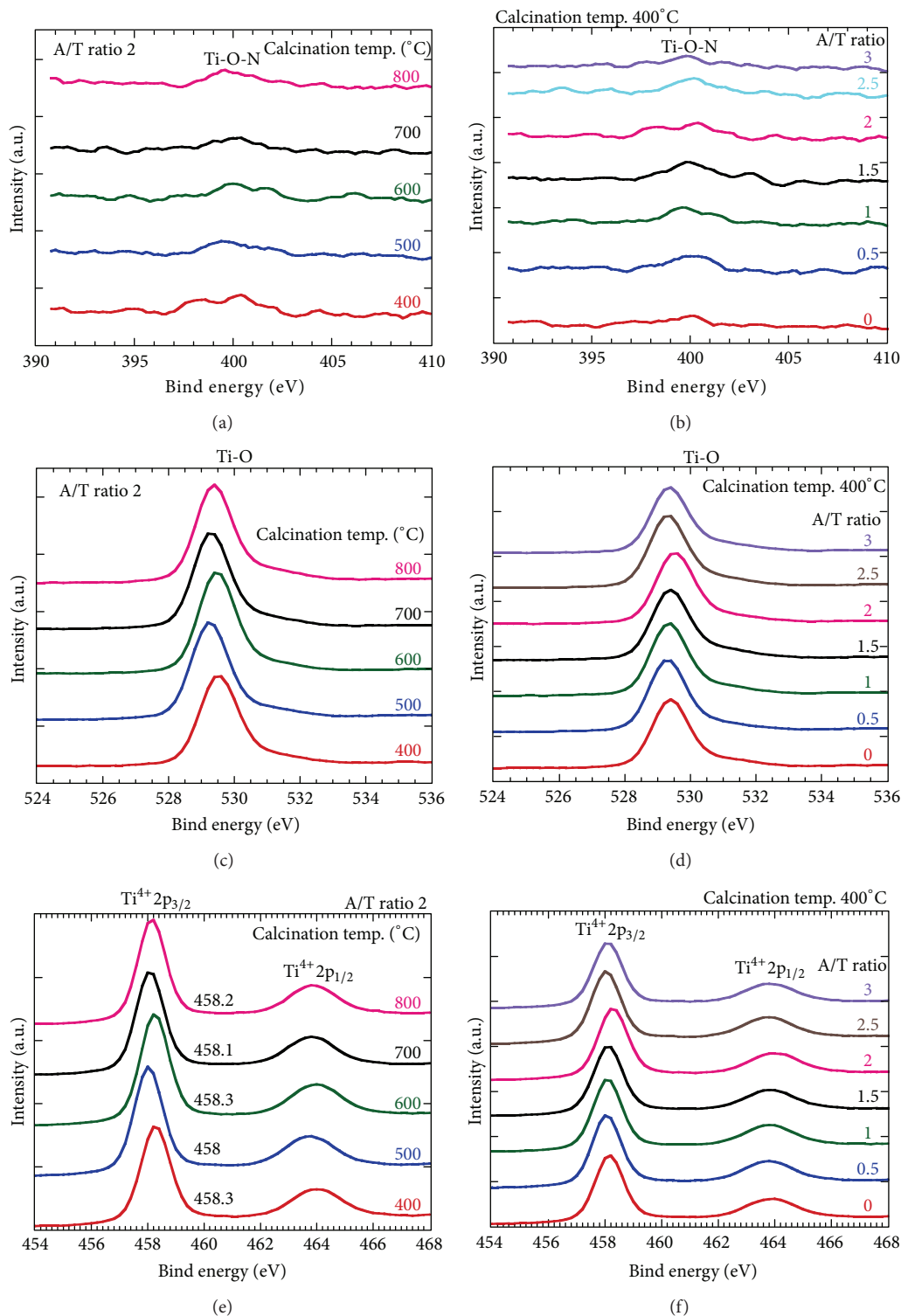


FIGURE 7: XPS survey and core level spectra of (a)-(b) N 1s, (c)-(d) Ti 2p, and (e)-(f) O 1s of N-TiO₂ samples.

temperature. This is different from the N-TiO₂ prepared by flame oxidation, in which nitrogen partially substitutes the oxygen sites in the TiO₂ [28]. The preparation method plays an important role in determining the nitrogen state in TiO₂ band structure [26, 29, 30]. Depending on the nitrogen source

and experimental conditions N species are incorporated into TiO₂ in interstitial form or substitutional form [31, 32]. The interstitial N-doping is favored when the doping is carried out under oxygen-rich conditions and the substitution-type N-doping occurs under reducing conditions [31–33]. Therefore,

from the atomic N 1s XPS spectra the interstitial sites (400 eV) were observed under air atmosphere.

The XPS spectra of Ti 2p regions are shown in Figures 7(c) and 7(d). The peaks at around 458.5 and 464.2 eV for P25 are ascribed to Ti 2p_{3/2} and Ti 2p_{1/2} of TiO₂ (data not shown). The line separation between Ti 2p_{1/2} and Ti 2p_{3/2} was 5.7 eV, which is consistent with the standard binding energy. According to Figure 7, all spectra of Ti 2p_{1/2} are symmetry. The spectra of Ti 2p_{1/2} are consistent of single state and the banding energy of peaks is 458.0–458.3 eV which shows a redshift of 0.5 eV compared to the binding energy of Ti⁴⁺ in P25. This suggests that Ti³⁺ was present in N-TiO₂ and the distance of peaks between Ti 2p_{1/2} and Ti 2p_{3/2} is 5.7–5.9 eV. The 396 eV peak is assigned to the atomic b-N state and generally proves the presence of TiAN bonds formed when N atoms replace the oxygen in the TiO₂ crystal lattice [30]. The peak characteristic for Ti–N (396 eV) is not present, indicating the absence of the TiN phase in the N-TiO₂ samples [34]. The results show that the binding energies of Ti 2p peaks shift to lower energies with a negative shift of ~0.5 eV for the N-TiO₂ due to the N doping [27]. The lower binding energy than a typical Ti 2p signal of Ti⁴⁺ oxidation state suggests that titanium cation has a considerable interaction with the doped nitrogen and thus TiO₂ lattice is modified [27, 35]. Nitrogen doping accompanies the formation of oxygen vacancies and/or Ti³⁺ defects, resulting in slight shifts of the Ti 2p peak toward the lower binding energy [36–38]. Hence, the red shifts of the Ti 2p peak in comparison with P25 are used to highlight the successful nitrogen doping into the TiO₂ lattice. The XRD results did not indicate the formation of TiN bonds. Therefore, results indicate that the titanium atom bonds with oxygen but not nitrogen. Thus, a shift toward lower binding energy of Ti 2p and the binding energy of N 1s upon nitrogen addition indicate that the nitrogen can be indeed incorporated into the interstitial positions of TiO₂ lattice and the formation of Ti–O–N bonding by partially interstitial with a carbon atom.

The incorporation of nitrogen into the oxide lattice should influence the BE of O 1s as well. The XPS spectra of the O 1s core level consists of the one peak (Figures 3(e) and 3(f)), at around 529.3–529.5 eV, which is ascribed to Ti–O bond in the TiO₂ lattice [30]. The O 1s core level moved toward lower energy state from 529.6 eV in P25 to 529.4 eV in N-TiO₂ prepared with A/T ratio 3.0 and calcined at 400°C. The peak shifts by ~0.2 eV which might be related to the creation of oxygen vacancies as a result of the nitrogen doping. The shifting of bind energy in both N 1s and O 1s region indicates that nitrogen was incorporated into the lattice. The shifts of Ti 2p_{3/2} and O 1s peaks are due to the introduction of oxygen vacancies into the TiO₂ lattice [32]. The presence of nitrogen dopant facilitates the formation of oxygen vacancies. The aforementioned results clearly indicate that nitrogen doping is accompanied by oxygen vacancy formation. The optical transitions between the dopant and dopant-induced level and Ti3d orbital explain the observed visible light absorptions of N-TiO₂ nanomaterials. The observed two absorbance edge features in the UV-vis spectra are directly related to the above modification of the electronic states from the dopants.

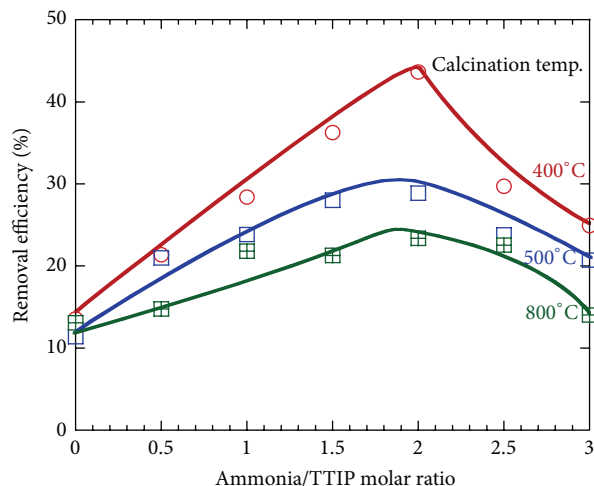


FIGURE 8: The removal efficiency of ethylene photooxidation over N-TiO₂ as function of the various ammonia/TTIP molar ratios. Experimental conditions: [C₂H₄] = 200 ppmv, [H₂O] = 25060 ppmv, [O₂] = 21%, light intensity = 16 mW/cm², temp. = 30°C, reaction time = 3 h.

3.6. Visible Light Photocatalytic Activity. To explore the photocatalytic activity of different N-doped TiO₂ at different calcination temperatures and A/T ratios, the degradation of ethylene under visible light with a cut-off wavelength of 400 nm was investigated. Carbon dioxide started being formed immediately after the visible light was turned on and ethylene was almost totally converted to CO₂ in all measurements. It is obviously that the N-TiO₂ shows significant progress in the photodegradation of ethylene compared to P25 in visible light system. P25 has no obvious photocatalytic activity (less than 1%) under visible light irradiation. Results suggest modification of TiO₂ provides visible-light-sensitive photocatalyst, which can be applied to the photooxidation of ethylene gas, as the band gap of TiO₂ was modified by nitrogen doping, evidenced by XPS and UV-visible DRS results. Figure 8 shows the activity of N-TiO₂ catalysts in the presence of visible light for photodegradation of ethylene. The reaction rate increases with the increase in the A/T ratio from 0.5 to 2.0, and then decreases in A/T ratio from 2.0 to 3.0. The enhancement of photocatalytic activity can be ascribed to an obvious improvement in anatase crystallinity and larger surface area. For the sample prepared with A/T ratio 2.0 and 3.0, however, the removal efficiency decreased rapidly, which can be due to its less surface area. The photocatalytic ability of N-TiO₂ samples calcinated at 400, 500, and 800°C is also examined. It was found that the photocatalytic activity decreased with increasing calcination temperature. The enhancement of photocatalytic activity can be ascribed to an obvious improvement in anatase crystallinity at 400°C calcination temperature. Good anatase crystallization is beneficial for reducing the recombination rate of the photogenerated electrons and holes due to the decrease in the number of the defects [39]. Zhao and Yang showed that for photocatalytic oxidation application, anatase is superior to rutile: (a) the conduction band location for anatase is more favorable for driving conjugate reactions

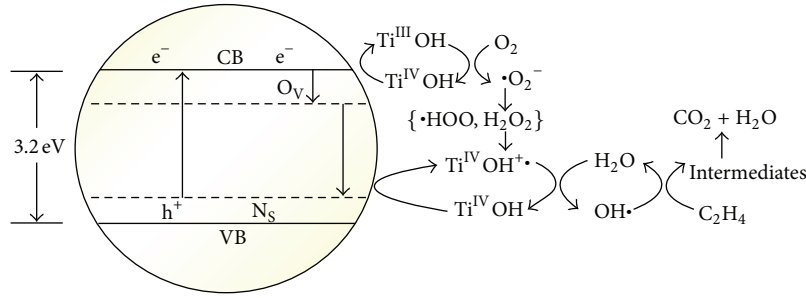
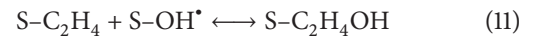
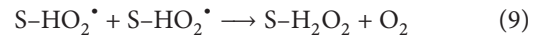
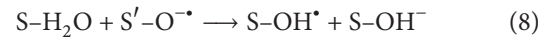
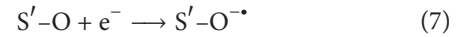
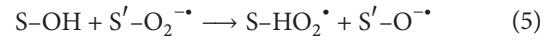
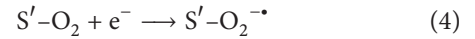
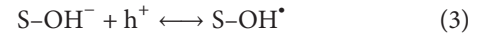
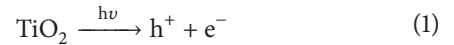


FIGURE 9: Schematic diagram for the process in the photooxidation of ethylene and electron transfer process over N-TiO₂ under visible light illumination.

involving electrons, and (b) very stable surface peroxide groups can be formed at the anatase during photo-oxidation reaction but not on the rutile surface [40]. For the sample calcined at 800°C, the removal efficiency decreased rapidly, which can be due to its fewer amounts of anatase and small S_{BET} . The result indicates that higher specific surface area, smaller crystallite size, and good anatase crystallization will promote the photocatalytic activity in visible light. The results indicate the N-TiO₂ catalyst prepared with A/T ratio 2.0 and calcinated at 400°C shows the best photocatalytic ability.

3.7. The Formation Mechanism of N-Doped TiO₂. For the pure TiO₂, the energy of the visible light is not sufficient to excite electrons from the valence band (VB), as the intrinsic band gap of pure TiO₂. Based on the results of UV-vis DRS, XRD, and XPS, the nitrogen atoms were weaved into the crystal structure of TiO₂ with structure as Ti-O-N. N-TiO₂ was active in the visible light irradiation for the degradation of ethylene. The following explanation for the photocatalytic activity of N-TiO₂ in the visible light spectra can be considered. The nitrogen existing at interstitial positions of TiO₂ lattice induces localized occupied states and forms midband gap, leading to the red shift of absorption edge and photocatalytic activity under visible light irradiation [41]. The electron (e^-) can be excited from the N-impurity level to the conduction band (CB). The exited electrons are trapped by O₂ adsorbed on the catalyst surface, producing O₂^{•-} superoxide anion radicals. After a series of reactions (1)–(12), ethylene molecules are finally mineralized into CO₂. DFT calculations and experimental results indicate that N-doping favored the formation of O vacancy (subband level O_v), which was below the bottom of the conduction band [42–47]. Therefore, the electrons (e^-) are excited from the N-impurity level bond to the subband level (O_v) and then recombine with the hole (h^+) as proved in Figure 9. The holes and electrons react with OH⁻ and O₂ molecules on the catalyst surface to form •OH radicals and O₂^{•-} superoxide anion radicals, respectively. The protonation yields the HOO• radicals, which after trapping electrons combine to produce H₂O₂. The O₂^{•-} radicals then interact with H₂O adsorbed to produce more •OH radicals. These •OH radicals then react with gaseous ethylene and mineralize it;



4. Conclusions

The observed changes in the UV-vis DRS, XRD, and XPS spectra are providing consistent structural information for Ti-O-N formation; that is, the nitrogen can be incorporated into the interstitial positions of TiO₂ lattice, which leads to the enhanced photocatalytic activity in N-TiO₂ samples. It is concluded that the photocatalytic oxidation reactivity of N-TiO₂ under visible light illumination is mainly due to the presence of localized occupied states caused by interstitial nitrogen and the electron/hole pairs generated under visible light irradiation. It has been found that N dopant retarded the anatase to rutile phase transformation by forming Ti-O-N incorporated into the interstitial position of TiO₂ lattice. Moreover, the transformation temperatures of anatase-to-rutile progressively slightly increase when N dopant content is increased. The photocatalyst, N-TiO₂ prepared with A/T ratio 2.0 and calcinated at 400°C, shows the highest photocatalytic activity in the oxidation of ethylene. This N-TiO₂ provides an effective visible-light-responsive photocatalyst for future industrial applications in pollution control.

Acknowledgment

This research was financially supported by the National Science Council of Taiwan ROC under Grant nos. NSC-100-2221-E-005-007 and NSC-100-2120-M-005-002.

References

- [1] T. Horikawa, M. Katoh, and T. Tomida, "Preparation and characterization of nitrogen-doped mesoporous titania with high specific surface area," *Microporous and Mesoporous Materials*, vol. 110, no. 2-3, pp. 397-404, 2008.
- [2] K. Yang, Y. Dai, and B. Huang, "Study of the nitrogen concentration influence on N-doped TiO₂ anatase from first-principles calculations," *Journal of Physical Chemistry C*, vol. 111, no. 32, pp. 12086-12090, 2007.
- [3] K. Pomoni, A. Vomvas, and C. Trapalis, "Dark conductivity and transient photoconductivity of nanocrystalline undoped and N-doped TiO₂ sol-gel thin films," *Thin Solid Films*, vol. 516, no. 6, pp. 1271-1278, 2008.
- [4] S. Sato, "Photocatalytic activity of NO_x-doped TiO₂ in the visible light region," *Chemical Physics Letters*, vol. 123, no. 1-2, pp. 126-128, 1986.
- [5] R. Asahi, T. Morikawa, T. Ohwaki, K. Aoki, and Y. Taga, "Visible-light photocatalysis in nitrogen-doped titanium oxides," *Science*, vol. 293, no. 5528, pp. 269-271, 2001.
- [6] J. Ananpattarachai, P. Kajitvichyanukul, and S. Seraphin, "Visible light absorption ability and photocatalytic oxidation activity of various interstitial N-doped TiO₂ prepared from different nitrogen dopants," *Journal of Hazardous Materials*, vol. 168, no. 1, pp. 253-261, 2009.
- [7] Y. T. Lin, C. H. Weng, and T. W. Tzeng, "Photocatalysis and catalytic properties of nano-sized N-TiO₂ catalyst synthesized by Sol-gel methods," *Journal of Advanced Oxidation Technologies*, vol. 13, no. 3, pp. 297-304, 2010.
- [8] B. Kosowska, S. Mozia, A. W. Morawski, B. Grzmil, M. Janus, and K. Kałucki, "The preparation of TiO₂-nitrogen doped by calcination of TiO₂·xH₂O under ammonia atmosphere for visible light photocatalysis," *Solar Energy Materials and Solar Cells*, vol. 88, no. 3, pp. 269-280, 2005.
- [9] F. Peng, L. Cai, L. Huang, H. Yu, and H. Wang, "Preparation of nitrogen-doped titanium dioxide with visible-light photocatalytic activity using a facile hydrothermal method," *Journal of Physics and Chemistry of Solids*, vol. 69, no. 7, pp. 1657-1664, 2008.
- [10] H. Yu, X. Zheng, Z. Yin, F. Tag, B. Fang, and K. Hou, "Preparation of nitrogen-doped TiO₂ nanoparticle catalyst and its catalytic activity under visible light," *Chinese Journal of Chemical Engineering*, vol. 15, no. 6, pp. 802-807, 2007.
- [11] Z. Wang, W. Cai, X. Hong, X. Zhao, F. Xu, and C. Cai, "Photocatalytic degradation of phenol in aqueous nitrogen-doped TiO₂ suspensions with various light sources," *Applied Catalysis B*, vol. 57, no. 3, pp. 223-231, 2005.
- [12] A. Trenczek-Zajac, K. Kowalski, K. Zakrzewska, and M. Radecka, "Nitrogen-doped titanium dioxide—characterization of structural and optical properties," *Materials Research Bulletin*, vol. 44, no. 7, pp. 1547-1552, 2009.
- [13] J. S. Jang, H. G. Kim, S. M. Ji et al., "Formation of crystalline TiO_{2-x}N_x and its photocatalytic activity," *Journal of Solid State Chemistry*, vol. 179, no. 4, pp. 1067-1075, 2006.
- [14] H. L. Qin, G. B. Gu, and S. Liu, "Preparation of nitrogen-doped titania using sol-gel technique and its photocatalytic activity," *Materials Chemistry and Physics*, vol. 112, no. 2, pp. 346-352, 2008.
- [15] J. Xu, Y. Ao, D. Fu, and C. Yuan J, "Low-temperature preparation of anatase titania-coated magnetite," *Journal of Physics and Chemistry of Solids*, vol. 69, pp. 1980-1984, 2008.
- [16] D. Wu, M. Long, W. Cai, C. Chen, and Y. Wu, "Low temperature hydrothermal synthesis of N-doped TiO₂ photocatalyst with high visible-light activity," *Journal of Alloys and Compounds*, vol. 502, no. 2, pp. 289-294, 2010.
- [17] K. M. Parida and B. Naik, "Synthesis of mesoporous TiO_{2-x}N_x spheres by template free homogeneous co-precipitation method and their photo-catalytic activity under visible light illumination," *Journal of Colloid and Interface Science*, vol. 333, no. 1, pp. 269-276, 2009.
- [18] N. R. Neti, R. Misra, P. K. Bera, R. Dhodapkar, S. Bakardjieva, and Z. Bastl, "Synthesis of c-doped TiO₂ nanoparticles by novel sol-gel polycondensation of resorcinol with formaldehyde for visible-light photocatalysis," *Synthesis and Reactivity in Inorganic, Metal-Organic and Nano-Metal Chemistry*, vol. 40, no. 5, pp. 328-332, 2010.
- [19] K. Bubacz, J. Choina, D. Dolat, E. Borowiak-Paleń, D. Moszyński, and A. W. Morawski, "Studies on nitrogen modified TiO₂ photocatalyst prepared in different conditions," *Materials Research Bulletin*, vol. 45, no. 9, pp. 1085-1091, 2010.
- [20] Z. Zhang, X. Wang, J. Long, Q. Gu, Z. Ding, and X. Fu, "Nitrogen-doped titanium dioxide visible light photocatalyst: spectroscopic identification of photoactive centers," *Journal of Catalysis*, vol. 276, pp. 201-214, 2010.
- [21] X. Z. Bu, G. K. Zhang, Y. Y. Gao, and Y. Q. Yang, "Preparation and photocatalytic properties of visible light responsive N-doped TiO₂/rectorite composites," *Microporous and Mesoporous Materials*, vol. 136, no. 1-3, pp. 132-137, 2010.
- [22] C. Liu, X. Tang, C. Mo, and Z. Qiang, "Characterization and activity of visible-light-driven TiO₂ photocatalyst codoped with nitrogen and cerium," *Journal of Solid State Chemistry*, vol. 181, no. 4, pp. 913-919, 2008.
- [23] R. Kun, S. Tarján, A. Oszkó et al., "Preparation and characterization of mesoporous N-doped and sulfuric acid treated anatase TiO₂ catalysts and their photocatalytic activity under UV and Vis illumination," *Journal of Solid State Chemistry*, vol. 182, pp. 3076-3084, 2009.
- [24] Z. Pap, L. Baia, K. Mogyorósi, A. Dombi, A. Oszkó, and V. Danciu, "Correlating the visible light photoactivity of N-doped TiO₂ with brookite particle size and bridged-nitro surface species," *Catalysis Communications*, vol. 17, pp. 1-7, 2012.
- [25] X. Z. Bu, G. K. Zhang, and C. H. Zhang, "Effect of nitrogen doping on anatase-rutile phase transformation of TiO₂," *Applied Surface Science*, vol. 258, pp. 7997-8001, 2012.
- [26] Y. P. Peng, E. Yassitepe, Y. T. Yeh, I. Ruzybayev, S. I. Shah, and C. P. Huang, "Photoelectrochemical degradation of azo dye over pulsed laser deposited nitrogen-doped TiO₂ thin film," *Applied Catalysis B*, vol. 125, pp. 465-472, 2012.
- [27] H. Jie, H. B. Lee, K. H. Chae et al., "Nitrogen-doped TiO₂ nanopowders prepared by chemical vapor synthesis: band structure and photocatalytic activity under visible light," *Research on Chemical Intermediates*, vol. 38, no. 6, pp. 1171-1180, 2012.
- [28] S. U. M. Khan, M. Al-Shahry, and W. B. Ingler, "Efficient photochemical water splitting by a chemically modified n-TiO₂," *Science*, vol. 297, no. 5590, pp. 2243-2245, 2002.

- [29] X. X. Wang, S. Meng, X. L. Zhang, H. T. Wang, W. Zhong, and Q. G. Du, "Multi-type carbon doping of TiO_2 photocatalyst," *Chemical Physics Letters*, vol. 444, pp. 292–296, 2007.
- [30] N. R. Khalid, E. Ahmed, Z. L. Hong, Y. W. Zhang, and M. Ahmad, "Nitrogen doped TiO_2 nanoparticles decorated on graphene sheets for photocatalysis applications," *Current Applied Physics*, vol. 12, no. 6, pp. 1485–1492, 2012.
- [31] Q. J. Xiang, J. G. Yu, and M. Jaroniec, "Nitrogen and sulfur co-doped TiO_2 nanosheets with exposed 001 facets: synthesis, characterization and visible-light photocatalytic activity," *Physical Chemistry Chemical Physics*, vol. 13, no. 11, pp. 4853–4861, 2011.
- [32] J. Wang, D. N. Tafen, J. P. Lewis et al., "Origin of photocatalytic activity of nitrogen-doped TiO_2 nanobelts," *Journal of the American Chemical Society*, vol. 131, pp. 12290–12297, 2009.
- [33] Q. Xiang, J. Yu, W. Wang, and M. Jaroniec, "Nitrogen self-doped nanosized TiO_2 sheets with exposed 001 facets for enhanced visible-light photocatalytic activity," *Chemical Communications*, vol. 47, no. 24, pp. 6906–6908, 2011.
- [34] Y. C. Tang, X. H. Huang, H. Q. Yu, and L. H. Tang, "Nitrogen-doped TiO_2 photocatalyst prepared by mechanochemical method: doping mechanisms and visible photoactivity of pollutant degradation," *International Journal of Photoenergy*, vol. 2012, Article ID 960726, 10 pages, 2012.
- [35] D. E. Gu, Y. Lu, B. C. Yang, and Y. D. Hu, "Facile preparation of micro-mesoporous carbon-doped TiO_2 photocatalysts with anatase crystalline walls under template-free condition," *Chemical Communications*, no. 21, pp. 2453–2455, 2008.
- [36] W. Ren, Z. Ai, F. Jia, L. Zhang, X. Fan, and Z. Zou, "Low temperature preparation and visible light photocatalytic activity of mesoporous carbon-doped crystalline TiO_2 ," *Applied Catalysis B*, vol. 69, no. 3–4, pp. 138–144, 2007.
- [37] E. M. Rockafellow, X. Fang, B. G. Trewyn, K. Schmidt-Rohr, and W. S. Jenks, "Solid-state ^{13}C NMR characterization of carbon-modified TiO_2 ," *Chemistry of Materials*, vol. 21, no. 7, pp. 1187–1197, 2009.
- [38] Y. Zhang, P. Xiao, X. Zhou, D. Liu, B. B. Garcia, and G. Cao, "Carbon monoxide annealed TiO_2 nanotube array electrodes for efficient biosensor applications," *Journal of Materials Chemistry*, vol. 19, no. 7, pp. 948–953, 2009.
- [39] J. Yu, L. Zhang, B. Cheng, and Y. Su, "Hydrothermal preparation and photocatalytic activity of hierarchically sponge-like macro-/mesoporous Titania," *Journal of Physical Chemistry C*, vol. 111, no. 28, pp. 10582–10589, 2007.
- [40] J. Zhao and X. Yang, "Photocatalytic oxidation for indoor air purification: a literature review," *Building and Environment*, vol. 38, no. 5, pp. 645–654, 2003.
- [41] C. Di Valentin, G. Pacchioni, and A. Selloni, "Origin of the different photoactivity of N-doped anatase and rutile TiO_2 ," *Physical Review B*, vol. 70, no. 8, Article ID 085116, 4 pages, 2004.
- [42] S. Livraghi, M. C. Paganini, E. Giamello, A. Selloni, C. Di Valentin, and G. Pacchioni, "Origin of photoactivity of nitrogen-doped titanium dioxide under visible light," *Journal of the American Chemical Society*, vol. 128, no. 49, pp. 15666–15671, 2006.
- [43] X. Chen and C. Burda, "The electronic origin of the visible-light absorption properties of C-, N- and S-doped TiO_2 nanomaterials," *Journal of the American Chemical Society*, vol. 130, no. 15, pp. 5018–5019, 2008.
- [44] C. Di Valentin, G. Pacchioni, and A. Selloni, "Theory of carbon doping of titanium dioxide," *Chemistry of Materials*, vol. 17, no. 26, pp. 6656–6665, 2005.
- [45] H. Wang and J. P. Lewis, "Effects of dopant states on photoactivity in carbon-doped TiO_2 ," *Journal of Physics Condensed Matter*, vol. 17, no. 21, pp. L209–L213, 2005.
- [46] H. Li, D. Wang, H. Fan, P. Wang, T. Jiang, and T. Xie, "Synthesis of highly efficient C-doped TiO_2 photocatalyst and its photo-generated charge-transfer properties," *Journal of Colloid and Interface Science*, vol. 354, no. 1, pp. 175–180, 2011.
- [47] Z. Wu, F. Dong, W. Zhao, and S. Guo, "Visible light induced electron transfer process over nitrogen doped TiO_2 nanocrystals prepared by oxidation of titanium nitride," *Journal of Hazardous Materials*, vol. 157, no. 1, pp. 57–63, 2008.

Research Article

Synthesis, Characterization, and Photocatalysis of Well-Dispersible Phase-Pure Anatase TiO₂ Nanoparticles

Xiuzhen Wei, Guangfeng Zhu, Jinfeng Fang, and Jinyuan Chen

*College of Biological and Environmental Engineering, Zhejiang University of Technology,
No. 18 ChaoWang Road, Hangzhou 310014, China*

Correspondence should be addressed to Jinyuan Chen; cjy1128@zjut.edu.cn

Received 7 February 2013; Accepted 29 March 2013

Academic Editor: Gang Liu

Copyright © 2013 Xiuzhen Wei et al. This is an open access article distributed under the Creative Commons Attribution License, which permits unrestricted use, distribution, and reproduction in any medium, provided the original work is properly cited.

High-purity anatase TiO₂ nanoparticles were prepared using an improved sol-hydrothermal method. The as-prepared sample was characterized by X-ray diffraction (XRD), transmission electron microscopy (TEM), Brunauer-Emmett-Teller (BET), and UV-vis diffuse reflectance spectra. TEM results showed that the average particle size of all TiO₂ particles was calculated to be (10 ± 1) nm. The XRD analysis indicated that the present sample was fully crystallized and appeared to be highly phase-pure anatase. The BET analysis showed that the as-prepared sample had a very large specific surface area of 186.25 m²/g. The photocatalytic performance of TiO₂ nanoparticles was evaluated by photocatalytic degradation of X-3B and X-BR solutions. The degradation results revealed that the as-prepared TiO₂ showed slightly higher photocatalytic activities than P25. Whereas, the as-synthesized TiO₂ can settle down and be separated easily after the photocatalytic reaction finishes.

1. Introduction

Titanium dioxide (TiO₂) is a versatile material with novel properties suitable for a number of technologically important applications, such as catalysis, white pigment for paints or cosmetics, electrodes in lithium batteries [1], dye-sensitized solar cells [2], and photocatalyst [3]. Although TiO₂ has wide potential application in environmental management and environmental protection, the low photocatalytic efficiency and the difficulty to separate greatly hinder its process of industrialization [4, 5]. Therefore, the key important aspect for the application of TiO₂ photocatalyst is to enhance the photocatalytic efficiency and the separation efficiency.

TiO₂ has three nature crystallographic phases: anatase, rutile, and brookite. Among the three main crystal phases of TiO₂, rutile is the most thermodynamically stable phase, whereas anatase and brookite are metastable phases and easily transformed into rutile by thermal treatment. Anatase TiO₂ is generally considered to be more active than rutile phase for TiO₂ photocatalyst [6]. Anatase TiO₂ with higher crystallinity is preferred for photocatalysis, due to that the higher crystallinity offers fewer defects acting as recombination sites between photo-generated electrons and holes often [7].

The physicochemical properties of the three phases are very different from each other, and they are closely related to the synthesis conditions. Anatase is the most thermodynamically stable among the three nanocrystalline phases if the size of the particles is less than 11 nm, brookite is the most stable phase between 11 nm and 35 nm, and rutile is the most stable when all the sizes are larger than 35 nm [8]. Thus, the synthesis conditions are very important and the synthesis parameters such as the crystal structure, surface morphology, and phase stability should be controlled and optimized.

The reported synthesis methods for TiO₂ nanoparticles include gas phase method and liquid phase method. The gas phases method is very complex and high energy consumption [9], although the prepared TiO₂ has a good monodispersity, a high purity, and a small size. The advantage of simple technical devices, low cost, and easy control for the liquid phase method make it widely used. The hydrolysis, sol-hydrothermal, microemulsion, sol-gel, and liquid deposition are the most common liquid phase methods. Among these methods, the TiO₂ particles prepared by sol-hydrothermal method have good crystal model, small size, and are not easy to agglomerate. These advantages lead sol-hydrothermal method to attract vast attention in the past ten years.

The disadvantage of this method is that the TiO_2 particles need high-temperature heat treatment.

Herein, we improve the sol-hydrothermal method synthesis process which does not require high-temperature treatment, and pure anatase TiO_2 nanoparticles with nanosize are obtained. XRD, BET, and TEM analyses were carried out to elucidate the as-synthesized product. The photocatalytic activity of TiO_2 under UV light irradiation was evaluated by degradation reactive brilliant red X-3B and reactive brilliant blue X-BR aqueous solution. This study may provide useful information and an effective approach for the preparation of high-purity anatase TiO_2 nanoparticles.

2. Experimental

2.1. Chemicals. The chemicals included dehydrated alcohol ($\text{CH}_3\text{CH}_2\text{OH}$, Anhui Ante Biochemistry Co., Ltd., AR), ammonium bicarbonate (NH_4HCO_3 , Shanghai no. 4 Reagent and H.v Chemical Co., Ltd., AR), tetrabutyl titanate ($\text{C}_{16}\text{H}_{36}\text{O}_4\text{Ti}$, Shanghai Star Chemical Co., Ltd. U.S., AR), P-25 (Evonik Degussa Corporation, Parsippany, NJ, USA). All the chemicals used in the experiments were of analytical purity grade with no further purification. Deionized water was used throughout the whole experiment.

2.2. TiO_2 Powder Synthesis. The anatase TiO_2 nanoparticles were prepared by an improved simple sol-hydrothermal method. Tetrabutyl titanate ($\text{C}_{16}\text{H}_{36}\text{O}_4\text{Ti}$) was used as the titanium source. Initially 4 mL tetrabutyl titanate was added to 60 mL ethanol solution under constant stirring at room temperature. Then 80 mL deionized water was dropped into the solution under vigorous stirring. The obtained mixed solution was oyster white and kept under constant stirring for 30 min. The obtained mixture and 2.0 g ammonium bicarbonate were transferred into a 200 mL Teflon-linear steel autoclave and maintained at 160°C for 12 h and then cooled to room temperature naturally finally. This produced a snow-white colored product which was rinsed thoroughly with deionized water and dehydrated alcohol. The white product obtained was dried at 50°C for 12 h. Finally, the powder was collected and transferred to a mortar and grinded to a fine powder which was used for further investigation.

2.3. Characterization. X-ray power diffraction (XRD) patterns of the samples that performed the phase identification were recorded on a D/max 2550Pc automatic diffractometer of polycrystalline ($\text{Cu K}\alpha$ radiation, Rigaku-D/MAX-2500/PC, Japan) that operated at 40 keV and 100 mA over the range of $20^\circ < 2\theta < 90^\circ$ at a scanning rate of $0.02^\circ/\text{s}$. The surface areas (S_{BET}) of the samples were analyzed by a multipoint Brunauer-Emmett-Teller (BET) method using nitrogen adsorption/desorption isotherm measurements at -196°C on an ASAP 2010 nitrogen adsorption apparatus (Micromeritics Instruments, USA). The particle size and shape were observed using transmission electron microscopy (TEM), which was equipped with an energy-dispersive X-ray spectrometry (EDS) and which was conducted with a Tecnai G2 F30 S-Twin electron microscope (Tecnai G2 F30 S-Twin,

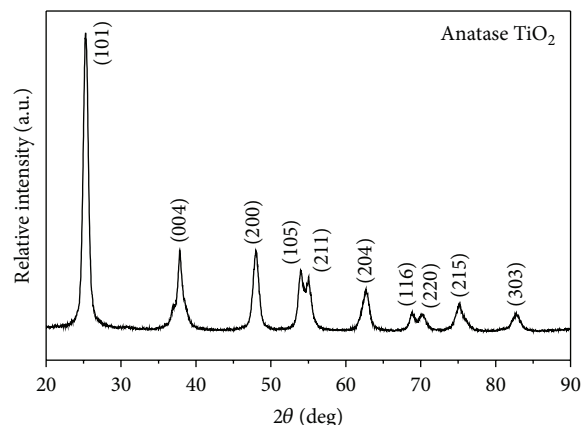


FIGURE 1: XRD patterns of the as-synthesized TiO_2 .

Holland) using a 300 kV accelerating voltage with 0.20 nm point resolution. In addition, transmittance measurements were performed using an UV-vis spectra, obtained at room temperature with an UV-vis spectrophotometer (UV-2550, Shimadzu, Japan), with BaSO_4 as the reflectance standard between 240 nm and 800 nm.

2.4. Photodegradation Experiment. The degradation of reactive brilliant red X-3B (X-3B) and reactive brilliant blue X-BR (X-BR) using anatase TiO_2 powder as photocatalyst in aqueous solution was examined by UV-vis absorption spectroscopy (TU-1810, Beijing, China). The light source employed in photoreactions was a 300 W Xe lamp (Beijing perfect light Corporation, Beijing, China). 100 mg of as-prepared TiO_2 catalyst was added into 400 mL aqueous solution containing 20 mg/L X-3B or 50 mg/L reactive brilliant blue X-BR in a glass reactor. The solution was magnetically stirred for 20 min to reach the adsorption equilibrium of dye on TiO_2 nanoparticles according to our previous study. Then it was irradiated by UV light. TiO_2 nanoparticles free dye solutions were obtained by centrifugation at 12,000 rpm. The photocatalytic activity of Degussa P25 was also measured as a reference to be compared with that of the synthesized catalysts. The degradation efficiency of catalysts after various intervals of time can be calculated using the following equation:

$$\text{degradation efficiency (\%)} = \frac{A_0 - A_t}{A_0} \times 100, \quad (1)$$

where A_0 and A_t are the initial absorbance and the absorbance after various intervals of time (t), respectively. All the experiments were done at room temperature of about 25°C .

3. Results and Discussion

3.1. X-Ray Diffraction. The XRD pattern of the as-synthesized sample was shown in Figure 1. The peaks of the powder materials are identified to corresponding (101), (004), (200), (105), (211), (204), (116), (220), (215), and (303) crystal planes.

All diffraction peaks are well defined and can be perfectly assigned to the anatase TiO_2 (JCPDS-21-1272). The anatase TiO_2 nanoparticles were known to be very photoactive and practical for water treatment and water purification [10]. No characteristic peaks associated with other crystalline forms were detected in the XRD pattern, indicating the anatase phase-pure nature of the product. The average crystallite size of as-prepared sample was calculated to be around 10 nm from the peak broadening.

3.2. Transmission Electron Microscopy. Transmission electron microscopy (TEM) was used to characterize the morphology and the average size of the synthesized TiO_2 nanoparticles. Typical low- and high-magnification TEM images of as-prepared TiO_2 sample were shown in Figure 2. The images shown in Figures 2(a) and 2(b) revealed that the as-prepared TiO_2 nanoparticles were not only uniform but also well dispersible. The well dispersible TiO_2 nanoparticles may be attributed to the decomposition of ammonium bicarbonate (NH_4Cl). When tetrabutyl titanate is hydrolyzed into TiO_2 , NH_4Cl is decomposed into NH_3 , H_2O , and CO_2 and large amounts of bubbles are produced in the mixed solution. Large amount of energy is released when the bubbles burst which is similar to the cavitations effect produced by ultrasound [11]. The energy produced by the burst of bubbles will prevent the agglomeration of synthesized TiO_2 [12].

The average particle size of the TiO_2 particles was calculated to be (10 ± 1) nm from Figures 2(c) and 2(d). The minimum and maximum particle sizes were lying close to average particle size. The particles size calculated from the TEM images was well consistent with the XRD values.

3.3. BET Surface Area Analysis. The typical plot of N_2 adsorption-desorption isotherm and pore size distribution curves of as-prepared TiO_2 sample was shown in Figure 3(a). The sample exhibited isotherm of type IV (BDDT classification) with hysteresis loops of type H3 at relative pressure range of 0.65–1.0, indicating the presence of mesoporous structure [13]. The corresponding pore size distribution of the sample was shown in Figure 3(b). The pore size distributions indicated that TiO_2 presented a relatively narrow distribution ranging from 5 nm to 25 nm. Taking into account the morphology of the material observed by TEM, the small pores should be the intra nanoparticles pores. The BET surface area of the prepared TiO_2 nanoparticles was $186.25 \text{ m}^2/\text{g}$ and the BET surface area of commercial P25 was $50 \text{ m}^2/\text{g}$. A larger surface area provides more surface active sites for the adsorption of the reactive molecules, which leads the photocatalytic process to be more efficient [14]. We can draw the conclusion that the nanoparticles prepared by us might have good photocatalytic activities.

3.4. UV-Vis Absorption Spectra of X-3B Solution Degraded by Synthesized TiO_2 . The UV-vis absorption spectrum of the X-3B aqueous solution degraded by UV-irradiation using as-prepared TiO_2 as catalyst was shown in Figure 4. The results clearly demonstrated that the X-3B aqueous solution exhibited four significant absorption peaks at 280 nm, 315 nm,

375 nm, and 535 nm, respectively. According to the theory of spectrum, we speculate that the absorption characteristic peak at 280 nm belongs to the aromatic functional group which represents benzene and naphthyl of X-3B. The absorption characteristic peaks at 315 and 375 nm represent Azo bond of X-3B. The strongest absorption characteristic peak at 535 nm is caused by conjugated structures which makes the X-3B solution appear to have the characteristic red. The results indicate that the Azo bond is easy to be broken by the influence of UV light and TiO_2 . Due to that the Azo bond is unstable, the color of X-3B solution can change easily. In this study, the concentration of X-3B was found to be less than 1% after 80 min of UV irradiation. In other words, the degradation rate was more than 99% within 80 min.

3.5. Photocatalytic Activities. Generally speaking, the high photocatalytic degradation rate corresponds to the high photocatalytic activity. The photocatalytic ability of as-synthesized sample was evaluated by UV-degradation X-3B and X-BR solutions. Figure 5 illustrates the degradation rate of X-3B and X-BR in the presence of the obtained TiO_2 and the commercial P25. The results exhibit that the obtained TiO_2 reveals slightly higher photocatalytic activities than P25. The best degradation rate of X-3B and X-BR for the obtained TiO_2 reaches 99.5% and 96.08%, respectively. Actually, it is very difficult to find a photocatalyst showing higher photocatalytic activity than P25 used as a standard titania photocatalyst [15]. As is our known, the activity of semiconductor photocatalysts depends on the specific surface area, composition, crystal size, and so on. TiO_2 has three well-known crystallographic phases in nature: anatase, rutile, and brookite. According to the reference reported, the anatase phase possesses the best photocatalyst. The phase ratio of anatase to rutile for commercial P25 used in our paper was 80 to 20 and the specific surface area was $50 \text{ m}^2/\text{g}$. However, our synthesized TiO_2 was phase-pure anatase TiO_2 and the specific surface area was $186.25 \text{ m}^2/\text{g}$. The pure anatase phase and relative high specific area endow the synthesized TiO_2 relative higher photocatalytic activity. What should be noted is that the synthesized TiO_2 can settle down and be separated easily by simple decantation in one step compared with the commercial P25. The results indicate that the prepared TiO_2 can be prepared easily and has a well promising application prospect in photocatalysis field.

The proposed photocatalytic process illuminated with UV light for TiO_2 may be as the following. When TiO_2 solution is irradiated by UV light, the conduction band electrons (e^-) and valence band holes (h^+) are generated on TiO_2 surface as long as the light energy equals or exceeds the band gap energy [16]. The holes can react with surface hydroxyl ions or water molecules producing hydroxyl radicals ($\bullet\text{OH}$), and electrons can react with adsorbed oxygen molecules yielding superoxide anion radicals ($\bullet\text{O}_2^-$) [17], which act as the oxidizing agents and the additional source of hydroxyl radicals. The hydroxyl radicals are the strongest oxidizing agent which can react with dye molecules and lead to the purification of dye wastewater.

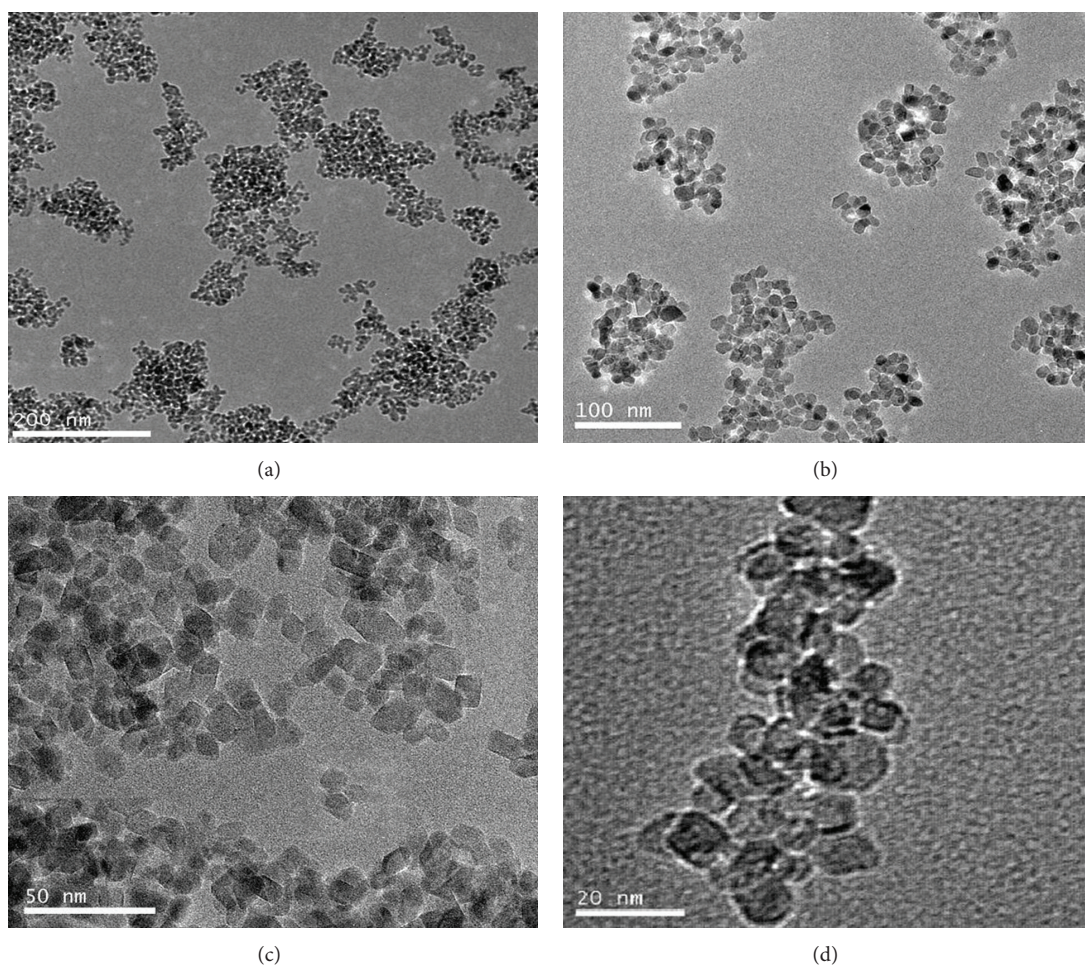


FIGURE 2: TEM images of the as-synthesized TiO_2 in different magnifications.

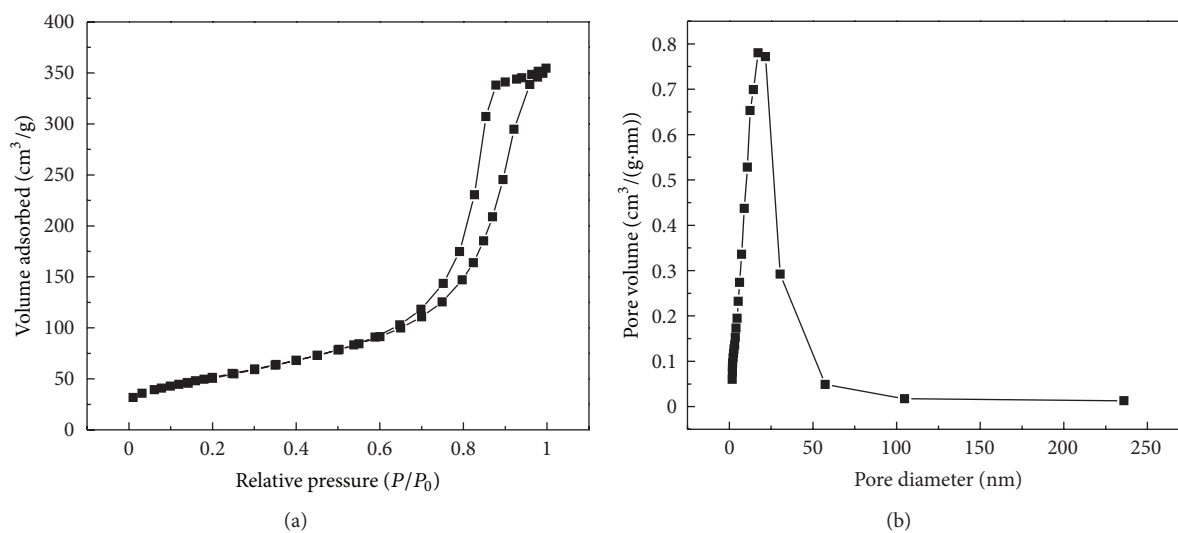


FIGURE 3: (a) Nitrogen adsorption-desorption isotherms and (b) corresponding pore size distribution curves of the as-synthesized TiO_2 .

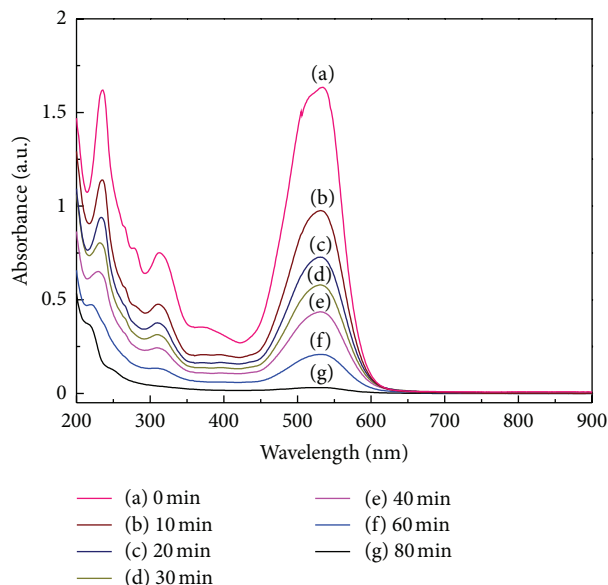


FIGURE 4: UV-vis spectra of X-3B solution as a function of wavelength for various time intervals.

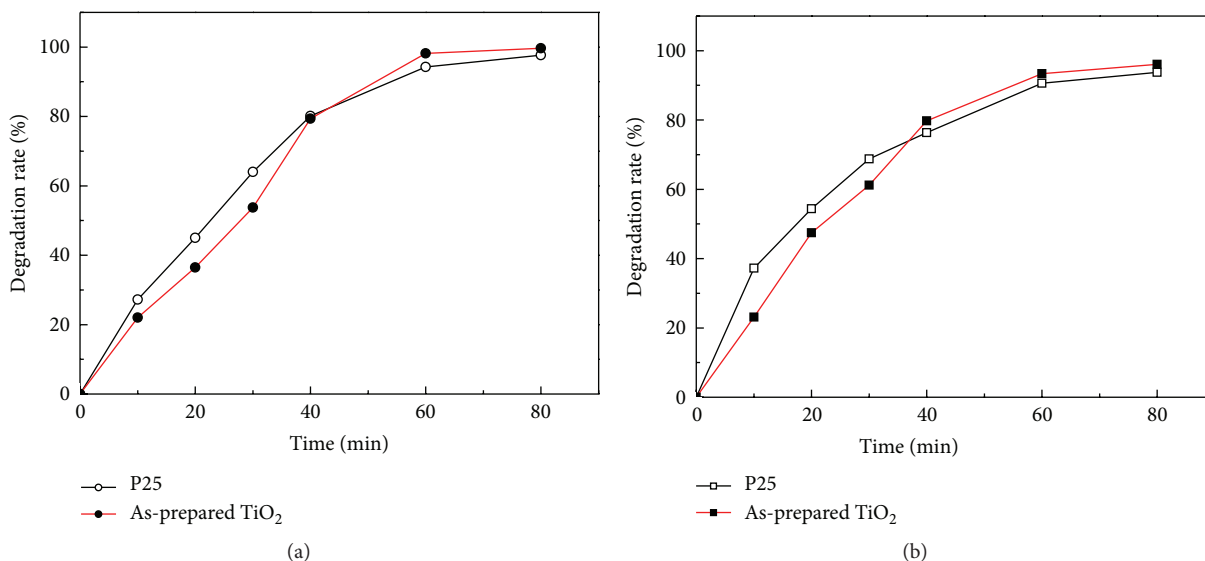


FIGURE 5: Photocatalytic degradation rate curves of different dye molecules as a function of irradiation time under UV light: (a) X-3B, (b) X-BR.

4. Conclusions

A facile method for the synthesis of pure-phase anatase TiO_2 nanoparticle has been developed. Compared with most of the prior arts, the prepared sample does not need to calcine at high temperature for this method, which can reduce energy consumption and production cost efficiently. Analysis by different characterization techniques (XRD, TEM, BET, and UV-vis) indicated that the as-prepared TiO_2 was pure-phase anatase and uniformly dispersed. The photocatalytic activity of the prepared sample was assessed using X-3B and X-BR solutions and compared with that of the commercial P25. The results indicated that X-3B and X-BR molecules were degraded effectively and the degradation rate reached 99.5%

and 96.08%, respectively, within 80 mins. And the prepared sample shows slightly better photocatalytic activity than that of P25. What is more is that the synthesized TiO_2 can settle down and be separated easily.

Acknowledgment

Financial support from the Natural Science Foundation of China (no. 20877070 and no. 21177114) is gratefully acknowledged.

References

- [1] A. R. Armstrong, G. Armstrong, J. Canales, and P. G. Bruce, "TiO₂-B nanowires as negative electrodes for rechargeable

- lithium batteries," *Journal of Power Sources*, vol. 146, no. 1-2, pp. 501-506, 2005.
- [2] H. Park, W. R. Kim, H. T. Jeong, J. J. Lee, H. G. Kim, and W. Y. Choi, "Fabrication of dye-sensitized solar cells by transplanting highly ordered TiO₂ nanotube arrays," *Solar Energy Materials and Solar Cells*, vol. 95, no. 1, pp. 184-189, 2011.
 - [3] T. Ochiai and A. Fujishima, "Photoelectrochemical properties of TiO₂ photocatalyst and its applications for environmental purification," *Journal of Photochemistry and Photobiology C*, vol. 13, no. 4, pp. 247-262, 2012.
 - [4] X. B. Chen and S. S. Mao, "Titanium dioxide nanomaterials: synthesis, properties, modifications, and applications," *Chemical Reviews*, vol. 107, no. 7, pp. 2891-2959, 2007.
 - [5] M. Anpo, "Preparation, characterization, and reactivities of highly functional titanium oxide-based photocatalysts able to operate under UV-visible light irradiation: approaches in realizing high efficiency in the use of visible light," *Bulletin of the Chemical Society of Japan*, vol. 77, no. 8, pp. 1427-1442, 2004.
 - [6] K. Tanaka, T. Hisanaga, P. Rivera, D. F. Ollis, and H. Al-Ekabi, *Photocatalytic Purification and Treatment of Water and Air*, Elsevier, Amsterdam, The Netherlands, 1993.
 - [7] D. He and F. Lin, "Preparation and photocatalytic activity of anatase TiO₂ nanocrystallites with high thermal stability," *Materials Letters*, vol. 61, no. 16, pp. 3385-3387, 2007.
 - [8] A. Furube, T. Asahi, H. Masuhara, H. Yamashita, and M. Anpo, "Charge carrier dynamics of standard TiO₂ catalysts revealed by femtosecond diffuse reflectance spectroscopy," *Journal of Physical Chemistry B*, vol. 103, no. 16, pp. 3120-3127, 1999.
 - [9] G. H. Li, D. Chen, G. X. Yao, B. Shi, and C. Ma, "Preparation of WC TiO₂ core-shell nanocomposite and its electrocatalytic characteristics," *Chinese Journal of Chemical Engineering*, vol. 19, no. 1, pp. 145-150, 2011.
 - [10] S. J. Kim, M. F. A'Hearn, D. D. Wellnitz, R. Meier, and Y. S. Lee, "The rotational structure of the B-X system of sulfur dimers in the spectra of Comet Hyakutake (C/1996 B2)," *Icarus*, vol. 166, no. 1, pp. 157-166, 2003.
 - [11] J. Y. Chen, H. J. Wang, and X. Z. Wei, "Characterization, properties and catalytic application of TiO₂ nanotubes prepared by ultrasonic-assisted sol-hydrothermal method," *Materials Research Bulletin*, vol. 47, no. 11, pp. 3747-3752, 2012.
 - [12] P. Ding and A. W. Pacek, "De-agglomeration of goethite nano-particles using ultrasonic comminution device," *Powder Technology*, vol. 187, no. 1, pp. 1-10, 2008.
 - [13] J. G. Yu, H. G. Yu, B. Cheng, and C. Trapalis, "Effects of calcination temperature on the microstructures and photocatalytic activity of titanate nanotubes," *Journal of Molecular Catalysis A*, vol. 249, no. 1-2, pp. 135-142, 2006.
 - [14] J. G. Yu, W. G. Wang, and B. Cheng, "Synthesis and enhanced photocatalytic activity of a hierarchical porous flowerlike pn junction NiO/TiO₂ photocatalyst," *Chemistry*, vol. 5, no. 12, pp. 2499-2506, 2010.
 - [15] B. Ohtani, O. O. Prieto-Mahaney, D. Li, and R. Abe, "What is Degussa (Evonic) P25? Crystalline composition analysis, reconstruction from isolated pure particles and photocatalytic activity test," *Journal of Photochemistry and Photobiology A*, vol. 216, no. 2-4, pp. 179-182, 2010.
 - [16] T. Y. Han, C. F. Wu, and C. T. Hsieh, "Hydrothermal synthesis and visible light photocatalysis of metal-doped titania nanoparticles," *Journal of Vacuum Science and Technology B*, vol. 25, no. 2, pp. 430-435, 2007.
 - [17] Y. F. Tu, S. Y. Huang, J. P. Sang, and X. W. Zou, "Preparation of Fe-doped TiO₂ nanotube arrays and their photocatalytic activities under visible light," *Materials Research Bulletin*, vol. 45, no. 2, pp. 224-229, 2010.

Research Article

Photocatalytic Degradation of Methyl Violet with $\text{TiSiW}_{12}\text{O}_{40}/\text{TiO}_2$

Shuijin Yang, Yulin Xu, Yongkui Huang, Guohui Zhou, Zhiyuan Yang, Yun Yang, and Guohong Wang

College of Chemistry and Environmental Engineering, Hubei Key Laboratory of Pollutant Analysis & Reuse Technology, Hubei Normal University, Huangshi 435002, China

Correspondence should be addressed to Shuijin Yang; yangshuijin@163.com

Received 9 January 2013; Revised 23 March 2013; Accepted 23 March 2013

Academic Editor: Jiaguo Yu

Copyright © 2013 Shuijin Yang et al. This is an open access article distributed under the Creative Commons Attribution License, which permits unrestricted use, distribution, and reproduction in any medium, provided the original work is properly cited.

The photocatalytic degradation of methyl violet using $\text{TiSiW}_{12}\text{O}_{40}/\text{TiO}_2$ as a novel eco-friendly catalyst under simulated natural light irradiation was investigated. The physical characterizations were carried out by TG/DTA, FT-IR, XRD, and UV-visible spectra. The effects of the initial methyl violet concentration, the solution pH, and catalyst dosage on the photocatalytic degradation rate of methyl violet were also examined. The results demonstrated that at optimal condition (initial concentration of methyl violet is 20 mg/L, catalyst dosage is 0.3 g, and the pH is 5.5), the degradation rate of methyl violet is as high as 82.4% after 3 h under simulated natural light irradiation. The reaction of photocatalysis for methyl violet can be expressed as first-order kinetic model.

1. Introduction

With the remarkable steady growth of people's living standard, organic dyes, which have been widely used in industry have become a concern because of their byproducts that constitute a serious risk for human health due to their high toxicity [1, 2]. However, they are difficult to be treated through generic chemical methods and biological techniques, such as condensation, ultrafiltration, membrane separation, bacterial, and adsorption [3, 4]. Hence, the treatment of organic pollutants has become a serious problem in environmental and chemical fields [5, 6]. It is noteworthy that the new opportunities and challenges in water treatment have led to the development of photocatalytic oxidation technology, which has the potential to completely oxidize organic compounds to CO_2 , H_2O , and other inorganic substances [7–9]. Photocatalytic oxidation technology with semiconductor materials such as TiO_2 , TiOX , Fe_2O_3 , and SrTiO_3 as the catalyst has been investigated widely by several authors [10–13]. Among these functional materials, TiO_2 has received the greatest interest in the field of photocatalysis technology. TiO_2 used in photocatalytic water treatment has many excellent properties such as high activity, chemical stability, and nontoxicity. Other than these, photocatalytic activity of TiO_2

can be turned by various chemical methods to obtain visible light response [14].

Polyoxometalates (POMs) constituted by transition metals in their highest oxidation states and oxoanions have been extensively studied as catalysts for a wide range of reactions. They have the similar photochemical characteristics with TiO_2 and can be activated by the light in the near ultraviolet (UV) or the visible region, and hence they are also used as photocatalysts in wastewater treatment [15]. POMs should be supported on a support like molecular sieves, carbon, or transition metal oxide to overcome their shortcomings, such as low surface area ($1\text{--}10\text{ m}^2/\text{g}$), low thermal stability, and high solubility, which limit their industrial application. TiO_2 was also an ideal support because of its higher surface area, chemical inertness, controlled porosity, and well dispersal for POMs while retaining the structure [16].

Since nearly 5% of the solar energy incident on the Earth's surface lies in the ultraviolet light region, it is essential to use natural light efficiently to drive photocatalytic oxidation of organic dyes. In order to achieve the goal, we attempt to develop novel functional materials with a visible light response. In this paper, the preparation of $\text{TiSiW}_{12}\text{O}_{40}/\text{TiO}_2$ composite was reported, and the photocatalytic degradation

of methyl violet with the catalyst under simulated natural light irradiation was investigated.

2. Experimental

2.1. Preparation of Catalyst. The catalyst was prepared using $\text{Ti}(\text{OH})_4$ and $\text{H}_4\text{SiW}_{12}\text{O}_{40} \cdot 21\text{H}_2\text{O}$ as the starting materials. $\text{H}_4\text{SiW}_{12}\text{O}_{40} \cdot 21\text{H}_2\text{O}$ (10.0 g, 3.0707 mmol) was dissolved in 40 mL of water, and the solution was heated to near 100°C . Then, $\text{Ti}(\text{OH})_4$ (1.0 g, 8.6260 mmol) was slowly added to the boiling solution, and the resulting mixture was refluxed for 3 h. In this process, water was added to the solution to prevent it from searing. After drying at 100°C for 12 h, the white catalyst was obtained.

2.2. Characterization. The thermal stability of the catalyst was examined by means of DTA with a Netzsch STA 449 thermal analysis system at a heating rate of $10^\circ\text{C}/\text{min}$ from 20 to 700°C in air atmosphere. The FT-IR spectra of the samples in KBr matrix were recorded on a Nicolet 5700 FT-IR spectrometer in the range $400\text{--}4000\text{ cm}^{-1}$. The X-ray powder diffraction pattern of the samples was measured by a Bruker AXS D8-advanced diffractometer (Bruker, Germany) employing Cu K_α radiation.

2.3. Activity Test. For the evaluation of catalyst activity, the catalyst was suspended in an aqueous solution of methyl violet in a Pyrex reactor. The photoreactor was designed with a light source surrounded by a quartz jacket. Simulated sunlight irradiation was provided by a 500 W xenon lamp (Nanjing Xujiang Electromechanical Factory, China) and the intensity of the lamp was $1200\text{ }\mu\text{mol}\cdot\text{m}^{-2}\cdot\text{s}^{-1}$. Solution pH was adjusted with dilute aqueous HCl and NaOH solutions. The system was cooled by circulating water and maintained at room temperature. Before irradiation, the suspensions were magnetically stirred in the dark for 30 min to reach the adsorption-desorption equilibrium of organic dyes on catalyst surface. At given time intervals, about 3 mL suspension was continually taken from the photoreactor for subsequent methyl violet concentration analysis after centrifuging. Decreases of the methyl violet concentrations were monitored via a UV-visible spectrometer (Hitachi U-3010, Japan). The degradation yield of organics was calculated by the following formula:

$$\text{Degradation yield (\%)} = \left(\frac{A_0 - A}{A_0} \right) \times 100, \quad (1)$$

where A_0 and A referred to the absorbance of RhB before and after reaction, respectively.

3. Results and Discussion

3.1. Characterization of the Catalysts. The DTA curve of the catalyst is shown in Figure 1. The pyrolysis proceeds mainly in three steps. The endothermic peaks on the DTA curve at about 98.3°C correspond to the loss of the adsorbed water. The broad endothermic peak at about 258.8°C is associated with the loss of coordination water in HPA, and the loss

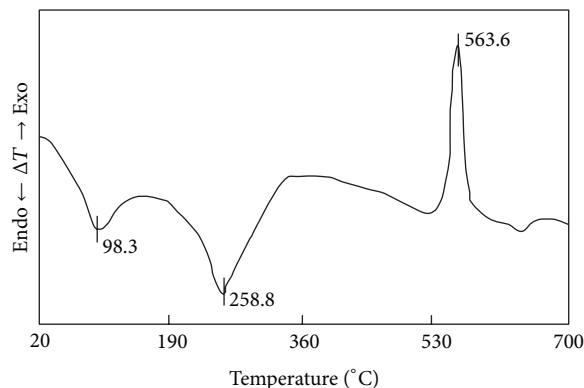


FIGURE 1: DTA curve of the catalyst.

is complete at 350°C , which is the activation temperature of $\text{TiSiW}_{12}\text{O}_{40}/\text{TiO}_2$. Finally, $\text{TiSiW}_{12}\text{O}_{40}/\text{TiO}_2$ starts to decompose and its Keggin structure collapses, as seen from the sharp exothermic peak at 563.6°C .

IR spectra of $\text{TiO}_2 \cdot x\text{H}_2\text{O}$, $\text{H}_4\text{SiW}_{12}\text{O}_{40} \cdot x\text{H}_2\text{O}$, and $\text{TiSiW}_{12}\text{O}_{40}/\text{TiO}_2$ are shown in Figure 2. The infrared spectra characteristic absorption peaks of TiO_2 are explored at 1401 cm^{-1} and of $\text{H}_4\text{SiW}_{12}\text{O}_{40} \cdot 21\text{H}_2\text{O}$ at 1631, 984, 935, 785, and 549 cm^{-1} . In the infrared spectrum of $\text{TiSiW}_{12}\text{O}_{40}/\text{TiO}_2$, the absorption bands at 1618, 1021, 984, 928, 885, 791, and 543 cm^{-1} can be assigned to the bending vibrations of H-O-H bond and the stretching vibrations of Si-O-Si, W-Od, Si-O, W-Ob-W, W-Oc-W, and Si-O-Si bonds, respectively. The stretching vibrations of Ti-O at 1401 cm^{-1} in titanium hydroxide decrease in the composite of $\text{TiSiW}_{12}\text{O}_{40}/\text{TiO}_2$. Similar bands in the region of $935\text{--}543\text{ cm}^{-1}$ confirmed the presence of red shift of absorption peaks at the base of $\text{H}_4\text{SiW}_{12}\text{O}_{40} \cdot 21\text{H}_2\text{O}$. These indicate that the Keggin structure of $\text{H}_4\text{SiW}_{12}\text{O}_{40} \cdot 21\text{H}_2\text{O}$ [17] was maintained after compounding at the surface of support.

XRD spectra of TiO_2 , $\text{H}_4\text{SiW}_{12}\text{O}_{40} \cdot x\text{H}_2\text{O}$, and $\text{TiSiW}_{12}\text{O}_{40}/\text{TiO}_2$ are shown in Figure 3. The X-ray powder patterns of TiO_2 calcinated at 350°C for 3 h show the anatase structure. The comparison of XRD patterns with $\text{H}_4\text{SiW}_{12}\text{O}_{40} \cdot 21\text{H}_2\text{O}$ reveals that the salt $\text{TiSiW}_{12}\text{O}_{40}$ also shows the Keggin structure [17], which is in accordance with the results of IR spectrum analysis.

3.2. Investigation of Photocatalytic Activity of Catalysts

3.2.1. Comparison of Photocatalytic Activity of Catalysts. In order to observe the catalytic activity of $\text{TiSiW}_{12}\text{O}_{40}/\text{TiO}_2$, comparison of photocatalytic activity of catalysts was carried out at the initial methyl violet concentration of 20 mg/L, pH 5.5, and 0.3 g of catalyst. The results showed that, after 2.5 h irradiation under the same conditions, no obvious methyl violet degradation was observed without any catalyst or light. However, in the presence of $\text{TiSiW}_{12}\text{O}_{40}/\text{TiO}_2$ without any light, the degradation yield of methyl violet is about 11.9%, while with $\text{TiSiW}_{12}\text{O}_{40}/\text{TiO}_2$ under simulated natural light irradiation the degradation yield can reach to 70.5%. So the photodegradation reaction of methyl violet in the presence

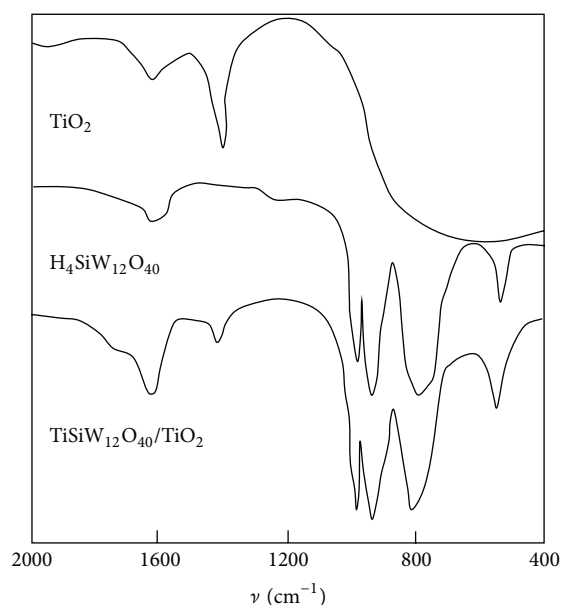


FIGURE 2: IR spectra of $\text{TiO}_2 \cdot x\text{H}_2\text{O}$, $\text{H}_4\text{SiW}_{12}\text{O}_{40} \cdot x\text{H}_2\text{O}$, and $\text{TiSiW}_{12}\text{O}_{40}/\text{TiO}_2$.

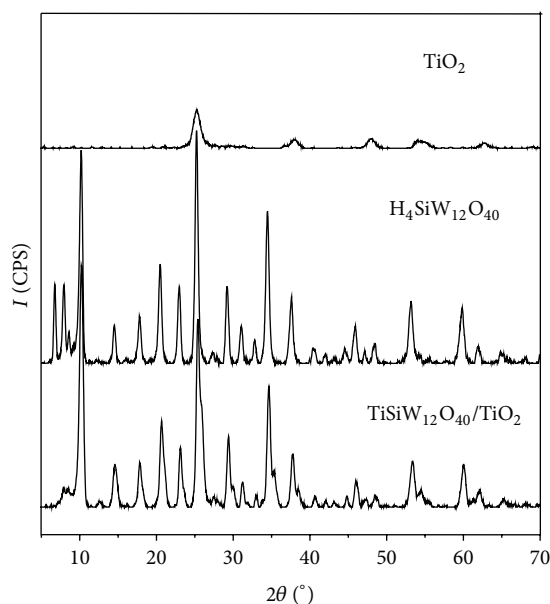


FIGURE 3: XRD spectra of TiO_2 , $\text{H}_4\text{SiW}_{12}\text{O}_{40} \cdot x\text{H}_2\text{O}$, and $\text{TiSiW}_{12}\text{O}_{40}/\text{TiO}_2$.

of $\text{TiSiW}_{12}\text{O}_{40}/\text{TiO}_2$ under simulated natural light irradiation is more effective than that of $\text{TiSiW}_{12}\text{O}_{40}/\text{TiO}_2$ without any light.

3.2.2. Effect of the Initial Concentration of Dye. To investigate the influence of initial concentration on the degradation efficiency of methyl violet, the initial concentration was varied from 5 to 40 mg/L, keeping the other experimental conditions constant.

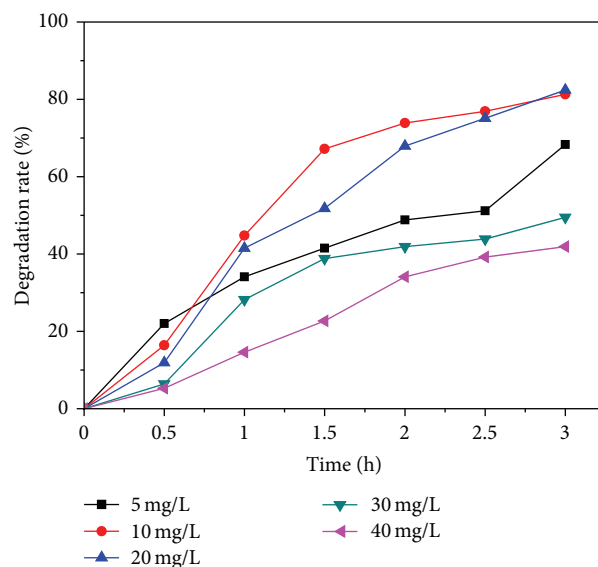


FIGURE 4: Effect of the initial methyl violet concentration on the photocatalytic degradation rate of methyl violet.

As can be seen in Figure 4, the degradation rate decreased with increase of initial concentration of methyl violet. This might be due to the excessive adsorption of the methyl violet molecules on the surface of catalyst at higher concentration. Moreover, light through the solution is reduced significantly. The results indicated that the degradation rate gradually increased with increase of the initial concentration of dye from 5 to 20 mg/L. However, the degradation efficiency gradually decreased with increase of the initial concentration of dye from 20 to 40 mg/L. Thus, the efficiency of degradation was decreased in the higher concentration. From the practical point of wastewater treatment, the initial concentration of the 20 mg/L is more appropriate.

3.2.3. Effect of pH. It is well known that the pH of the solution is one of the most important parameters in the photocatalytic degradation of organic compounds. This is attributed to the fact that the pH not only determines chemical properties of the photocatalyst but also influences adsorption behaviour of the pollutants. Therefore, the effect of pH on the degradation of methyl violet was studied at pH range from 3.5 to 7.5.

As shown in Figure 5, the most effective pH condition is at 5.5. This may be ascribed to the fact that the pH value could influence the amount of hydroxyl radicals (OH^\cdot) formed and the stable of $\text{H}_4\text{SiW}_{12}\text{O}_{40}$. So the optimum pH of the solution is 5.5.

3.2.4. Effect of Catalyst Dosage. The catalyst dosage is also an important parameter for optimizing the operational conditions. Therefore, the effect of catalyst dosage on the degradation of methyl violet was investigated in the catalyst dosage from 0.15 to 0.60 g, and the result shown was in Figure 6. The results indicated that the degradation rate gradually increased with increase of catalyst dosage from 0.15 to 0.30 g. However, the degradation efficiency gradually decreased with increase

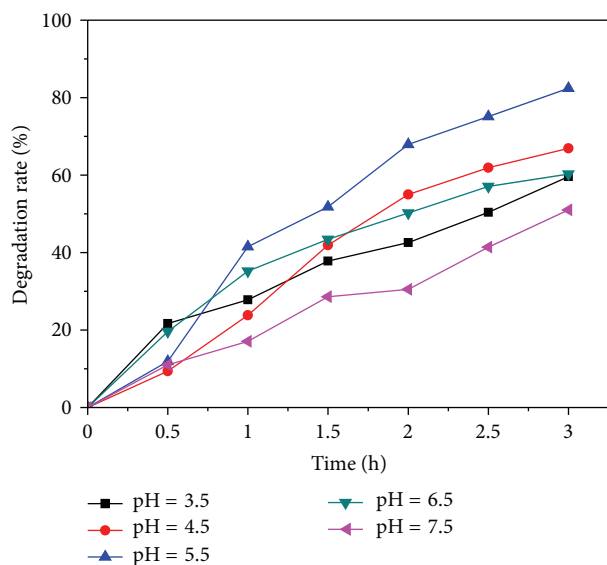


FIGURE 5: Effect of the solution pH on the photocatalytic degradation rate of methyl violet.

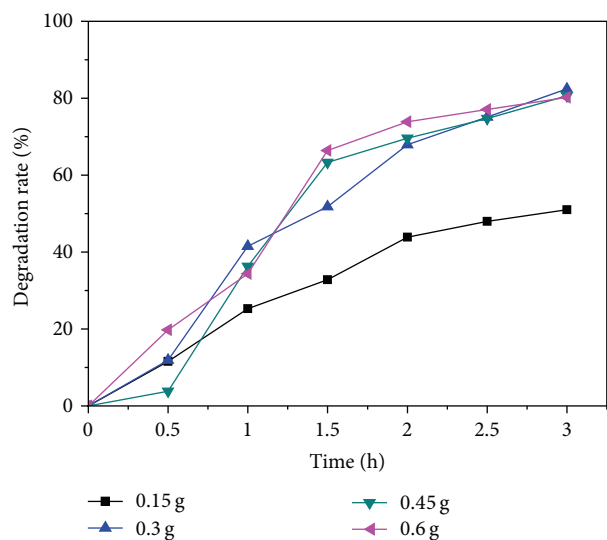


FIGURE 6: Effect of catalyst dosage on the photocatalytic degradation rate of methyl violet.

of catalyst dosage from 0.30 to 0.60 g. This may be attributed to the fact that the surplus catalyst can scatter the photons in the photoreaction system.

3.2.5. Kinetic Analysis. It is well known that the photodegradation of organic dyes mainly follows first-order kinetics. The kinetics of photocatalytic degradation of methyl violet was also studied under optimized conditions. The results are shown in Figure 7.

The results showed that the photocatalytic degradation of methyl violet over $\text{TiSiW}_{12}\text{O}_{40}/\text{TiO}_2$ under simulated sunlight irradiation can be described by the first-order kinetic

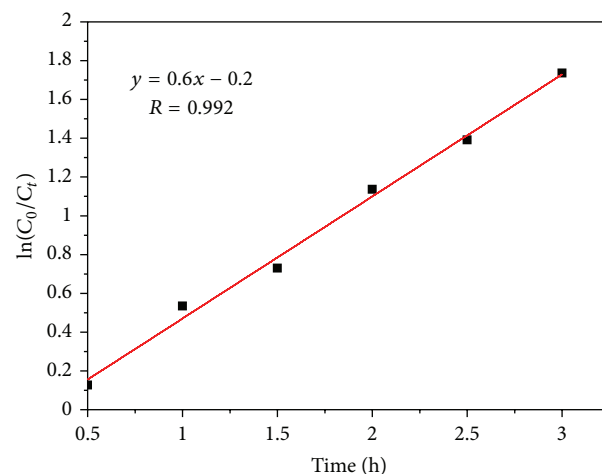


FIGURE 7: Relation curve of $\ln(C_0/C_t)$ and time (t).

model, $\ln(C_0/C_t) = kt$, where k is the rate constant (h^{-1}), C_0 is the initial concentration, and C_t is the concentration of dye at time t . It can be seen from Figure 7 that the plots represented a straight line. The correlation constant for the line was 0.992. The rate constant was 0.6 h^{-1} .

3.2.6. Comparison of Photocatalytic Activity of Catalysts. The photodegradation rate of $\text{TiSiW}_{12}\text{O}_{40}/\text{TiO}_2$ was compared with those of Co-SBA-15 [18], Fe-doped anatase TiO_2 [19], TiO_2 , and $\text{H}_4\text{SiW}_{12}\text{O}_{40}$, and the results are shown in Table 1.

The catalytic activity of $\text{TiSiW}_{12}\text{O}_{40}/\text{TiO}_2$ is much higher than that of $\text{H}_4\text{SiW}_{12}\text{O}_{40}$ and TiO_2 under simulated natural light irradiation. This might be ascribed to the synergistic effect between $\text{H}_4\text{SiW}_{12}\text{O}_{40}$ and TiO_2 . It was also observed that $\text{TiSiW}_{12}\text{O}_{40}/\text{TiO}_2$ shows a higher photocatalytic efficiency of degradation dyes than Co-SBA-15, and Fe-doped anatase TiO_2 . The results indicate that $\text{TiSiW}_{12}\text{O}_{40}/\text{TiO}_2$ has an excellent photocatalytic performance with a degradation of methyl violet more than 82% in 3 h, suggesting that the catalyst $\text{TiSiW}_{12}\text{O}_{40}/\text{TiO}_2$ has an excellent application in environmental protection.

4. Conclusion

The photocatalytic degradation of methyl violet using $\text{TiSiW}_{12}\text{O}_{40}/\text{TiO}_2$ as a novel eco-friendly catalyst under simulated natural light irradiation was investigated. The results demonstrated that at optimal condition (initial concentration of methyl violet is 20 mg/L, catalyst dosage is 0.3 g, and the pH is 5.5), the degradation rate of methyl violet is as high as 82.4% after 3 h under simulated natural light irradiation. The reaction of photocatalysis for methyl violet can be expressed as first-order kinetic mode.

Acknowledgments

This work was financially supported by the Young and Middle-Aged Natural Science Foundation of Hubei Province

TABLE 1: Comparison of photocatalytic activity of catalysts.

Type of catalyst	Catalyst dosage	Reaction conditions	Degradation rate
Co-SBA-15	1 g/L	Initial concentration 50 mg/L, within 150 min of solar light irradiation	61%
Fe-doped anatase TiO ₂	0.18 g	Initial concentration 4 mg/L, pH is 5.5, within 4 h visible light	59.4%
TiO ₂	0.3 g	Initial concentration 20 mg/L, pH is 5.5, within 3 h simulated natural light irradiation	58.8%
H ₄ SiW ₁₂ O ₄₀	0.3 g	Initial concentration 20 mg/L, pH is 5.5, within 3 h simulated natural light irradiation	21.5%
TiSiW ₁₂ O ₄₀ /TiO ₂	0.3 g	Initial concentration 20 mg/L, pH is 5.5, within 3 h simulated natural light irradiation	82.4%

Education Department (nos. Q20112507 and Q20082202) and Hubei Key Laboratory of Pollutant Analysis and Reuse Technology (no. KY2010G13).

References

- [1] F. H. Hussein, "Comparison between solar and artificial photocatalytic decolorization of textile industrial wastewater," *International Journal of Photoenergy*, vol. 2012, Article ID 793648, 10 pages, 2012.
- [2] M. N. Chong, B. Jin, C. W. K. Chow, and C. Saint, "Recent developments in photocatalytic water treatment technology: a review," *Water Research*, vol. 44, no. 10, pp. 2997–3027, 2010.
- [3] H. Lachheb, E. Puzenat, A. Houas et al., "Photocatalytic degradation of various types of dyes (Alizarin S, Crocein Orange G, Methyl Red, Congo Red, Methylene Blue) in water by UV-irradiated titania," *Applied Catalysis B*, vol. 39, no. 1, pp. 75–90, 2002.
- [4] Q. Zhang, Y. H. Jing, A. Shiue, C.-T. Chang, B.-Y. Chen, and C.-C. Hsueh, "Deciphering effects of chemical structure on azo dye decolorization/degradation characteristics: bacterial vs. photocatalytic method," *Journal of the Taiwan Institute of Chemical Engineers*, vol. 43, no. 5, pp. 760–766, 2012.
- [5] C. C. Hsueh and B. Y. Chen, "Comparative study on reaction selectivity of azo dye decolorization by *Pseudomonas luteola*," *Journal of Hazardous Materials*, vol. 141, no. 3, pp. 842–849, 2007.
- [6] C. McCullagh, N. Skillen, M. Adams, and P. K. Robertson, "Photocatalytic reactors for environmental remediation: a review," *Journal of Chemical Technology and Biotechnology*, vol. 86, no. 8, pp. 1002–1017, 2011.
- [7] S. H. S. Chan, T. Y. Wu, J. C. Juan, and C. Y. Teh, "Recent developments of metal oxide semiconductors as photocatalysts in advanced oxidation processes (AOPs) for treatment of dye waste-water," *Journal of Chemical Technology and Biotechnology*, vol. 86, no. 9, pp. 1130–1158, 2011.
- [8] M. Y. Guo, A. M. C. Ng, F. Liu, A. B. Djurišić, and W. K. Chan, "Photocatalytic activity of metal oxides—the role of holes and OH• radicals," *Applied Catalysis B*, vol. 107, no. 1–2, pp. 150–157, 2011.
- [9] J. Fenoll, P. Hellin, C. M. Martínez, P. Flores, and S. Navarro, "Semiconductor oxides-sensitized photodegradation of fenamiphos in leaching water under natural sunlight," *Applied Catalysis B*, vol. 115–116, pp. 31–37, 2012.
- [10] L. N. Wang, F. Lu, and F. M. Meng, "Synthesis and photocatalytic activity of TiO_x powders with different oxygen defects," *International Journal of Photoenergy*, vol. 2012, Article ID 208987, 7 pages, 2012.
- [11] X. M. Zhou, J. Y. Lan, G. Liu et al., "Facet-mediated photodegradation of organic dye over hematite architectures by visible light," *Angewandte Chemie*, vol. 124, no. 1, pp. 182–186, 2012.
- [12] H. G. Yu, R. Liu, X. F. Wang, P. Wang, and J. Yu, "Enhanced visible-light photocatalytic activity of Bi₂WO₆ nanoparticles by Ag₂O cocatalyst," *Applied Catalysis B*, vol. 111–112, no. 28, pp. 326–333, 2012.
- [13] X. F. Wang, S. F. Li, H. G. Yu, J. Yu, and S. Liu, "Ag₂O as a novel visible-light photocatalyst: self-stability and high photocatalytic activity," *Chemistry: A European Journal*, vol. 17, no. 28, pp. 7777–7780, 2011.
- [14] Q. Xiang, J. Yu, W. Wang, and M. Jaroniec, "Nitrogen self-doped nanosized TiO₂ sheets with exposed {001} facets for enhanced visible-light photocatalytic activity," *Chemical Communications*, vol. 47, no. 24, pp. 6906–6908, 2011.
- [15] P. Lei, C. Chen, J. Yang, W. Ma, J. Zhao, and L. Zang, "Degradation of dye pollutants by immobilized polyoxometalate with H₂O₂ under visible-light irradiation," *Environmental Science and Technology*, vol. 39, no. 21, pp. 8466–8474, 2005.
- [16] S. Jiang, Y. Guo, C. Wang, X. Qu, and L. Li, "One-step sol-gel preparation and enhanced photocatalytic activity of porous polyoxometalate-tantalum pentoxide nanocomposites," *Journal of Colloid and Interface Science*, vol. 308, no. 1, pp. 208–215, 2007.
- [17] E. B. Wang, C. W. Hu, and L. Xu, *Polyhydric Chemistry Introduction*, Chemical Industry Press, Beijing, China, 1998.
- [18] F. Xia, E. Ou, L. Wang, and J. Wang, "Photocatalytic degradation of dyes over cobalt doped mesoporous SBA-15 under sunlight," *Dyes and Pigments*, vol. 76, no. 1, pp. 76–81, 2008.
- [19] Y. Zhang and B. Chen, "Factors of affecting photocatalytic degradation on methyl violet by titania," *Applied Chemical Industry*, vol. 44, pp. 814–817, 2001 (Chinese).

Research Article

Physicochemical Study of Photocatalytic Activity of TiO₂ Supported Palygorskite Clay Mineral

Lahcen Bouna,¹ Benaissa Rhouta,¹ and Francis Maury²

¹ *Laboratoire de Matière Condensée et Nanostructures (LMCN), Faculté des Sciences et Techniques Guéliz, Université Cadi Ayyad, BP 549, 40 000 Marrakech, Morocco*

² *CIRIMAT, Université de Toulouse, CNRS-UPS-INP, ENSIACET, 4 allée Emile Monso, BP 44362, 31030 Toulouse Cedex 4, France*

Correspondence should be addressed to Francis Maury; francis.maury@ensiacet.fr

Received 8 February 2013; Accepted 28 March 2013

Academic Editor: Christos Trapalis

Copyright © 2013 Lahcen Bouna et al. This is an open access article distributed under the Creative Commons Attribution License, which permits unrestricted use, distribution, and reproduction in any medium, provided the original work is properly cited.

This study deals with the influence of physicochemical parameters, namely, the photocatalyst loading, dye concentration, and pH of polluted solutions, on the degradation efficiency of Orange G (OG) solutions containing TiO₂ nanoparticles supported on palygorskite clay mineral (TiO₂-Pal). The TiO₂ photocatalyst attached to natural palygorskite fibers was elaborated by colloidal sol-gel route. It exhibits the anatase structure that is the most photoactive crystallographic form. The highest performances of supported photocatalyst on OG degradation were found using an optimum amount of TiO₂-Pal around 0.8 g·L⁻¹, which corresponds properly to ca. 0.4 g·L⁻¹ of TiO₂. This amount is interestingly lower than the 2.5 g·L⁻¹ generally reported when using pure unsupported TiO₂ powder. The photodegradation rate increases by decreasing OG initial concentration, and it was found significantly higher when the OG solution is either acidic (pH < 4) or basic (pH ≈ 11). For OG concentrations in the range 5 × 10⁻⁶–5 × 10⁻⁴ M, the kinetic law of the OG degradation in presence of TiO₂-Pal is similar to that reported for unsupported TiO₂ nanopowder. It follows a Langmuir-Hinshelwood model with a first-order reaction and an apparent rate constant of about 2.9 × 10⁻² min⁻¹.

1. Introduction

Heterogeneous photocatalytic oxidation recently has emerged as an efficient alternative process for wastewater treatment [1–5]. The principle of this technique relies on the creation of reactive species as holes (h⁺) and hydroxyl radicals (OH[•]) upon irradiating a semiconductor oxide with an energy source (hν) higher than its energy band gap [1, 5]. In optimized processes, the reactive species so-generated are able to induce complete mineralization of organic pollutants into CO₂ and H₂O [1]. TiO₂ anatase is the most active semiconductor oxide in photocatalysis and is besides widely used owing to its numerous advantages, namely, nonharmfulness, low cost, and chemical inertness [1]. However, its use in the form of nanopowder (e.g., commercial Degussa P25 powder) raises several problems such as agglomeration of the particles during the process, which reduces photocatalytic efficiency. Additionally, recovering of micron sized aggregated particles from water decontaminated by TiO₂ slurry needs to implement costly microfiltration processes [1, 4, 6, 7]. To

overcome these drawbacks, researches focus on improving photocatalytic activity by the development of TiO₂ supported photocatalysts in particular starting with natural materials as support.

Among the support materials envisaged, clay minerals are considered promising owing to their interesting inherent properties as their adsorption capacity, high surface area, multiscale porosity, and ability to be bound to chemical compounds [6–9]. In this respect, we reported recently the immobilization of TiO₂ anatase nanoparticles (NPs) with an average size of 10 nm onto particle surfaces of beidellite [10] and fiber surfaces of palygorskite [11] via a colloidal sol-gel route. Beidellite and palygorskite were both natural clay minerals sampled in Morocco from Agadir basin and Marrakech High Atlas regions, respectively. They were purified, characterized, and functionalized to be used as catalytic support [12, 13]. Preliminary photocatalytic tests for the degradation of Orange G dye (OG) were promising. In comparative tests with Degussa P25 powder, the TiO₂-Pal photocatalyst exhibited a higher activity.

Because the optimization of experimental conditions is very important in designing a slurry reactor for effective and efficient use [4], we have investigated in the present work the effects of physicochemical parameters on photocatalytic activity of TiO_2 supported palygorskite fibers in order to find out the best conditions permitting an efficient removal of OG dye. This pollutant was selected as model compound because it is widely used in the textile industry.

2. Experimental Details

2.1. TiO_2 Supported Palygorskite Photocatalyst. The principle of the synthesis method is first to modify palygorskite with surfactant to afford an organophilic functionalization advantageous to the hydrolysis and polycondensation of titanium precursor. Thus, upon annealing, the amorphous hydroxoxo Ti-based thin film grafted on the palygorskite surface is converted into TiO_2 nanoparticles uniformly distributed onto palygorskite fiber surfaces with a high conformal coverage.

In summary, TiO_2 supported palygorskite composite material (labeled TiO_2 -Pal) was prepared starting from Na^+ -exchanged purified palygorskite (Na^+ -Pal) isolated from raw clay picked up in Marrakech High Atlas region (Morocco) [11]. The supported photocatalyst was elaborated according to a colloidal sol-gel procedure in two steps described in detail elsewhere [11]. Briefly, the synthesis route first involved the preparation of organopalygorskite (CTA^+ -Pal) by ion exchange of Na^+ -Pal aqueous dispersion (1 wt.%) with 0.2 g of hexadecyltrimethylammonium bromide (CTAB). Thereafter, 5 cm^3 of titanium tetraisopropoxide (TTIP) in isopropanol was added to 1 g of CTA^+ -Pal dispersed in 7 cm^3 of isopropanol, and it was hydrolyzed by adding some water droplets, and afterwards it was condensed to give rise to the gel precursor CTA^+ -Pal-Ti. Thereafter, the annealing at 600°C for 1 h converted CTA^+ -Pal-Ti into TiO_2 -palygorskite nanocomposite (TiO_2 -Pal).

TEM and *in situ* XRD versus temperature analyses demonstrated the good conformal coverage and wrapping of palygorskite fibers with remarkably stable TiO_2 anatase NPs that exhibited an average size of *ca.* 10 nm (Figure 1) [11].

2.2. Photocatalytic Tests. The photocatalytic activity was evaluated by measuring the decomposition rate of Orange G (OG) aqueous solutions containing a dispersion of the supported photocatalyst. The degradation reaction was carried out in a batch quartz reactor ($40 \times 20 \times 36 \text{ mm}^3$) placed in a thermostated chamber (25°C) under the UV light of a lamp (HPLN Philips 125 W) emitting at 365 nm. The reactor was irradiated with a photon flux of $1 \text{ mW}\cdot\text{cm}^{-2}$ by adjusting the distance to the lamp so that it simulates the UV intensity of solar spectrum on the earth [14]. This lamp was chosen because the OG absorption is negligible at this wavelength and, as a result, the direct photolysis of the OG aqueous solution (without photocatalyst) was found negligible for more than 24 h. The dispersion was agitated with an inert Teflon magnetic stirrer.

Even though the OG dye adsorption is generally negligible on our clayey materials, the photocatalyst dispersed in

OG aqueous solution was first cautiously kept in the dark inside a thermostated chamber for approximately 1 h before starting the irradiation with UV light. To determine the dye concentration, aliquots were taken from the mixture at regular time intervals and centrifuged at 12 500 rpm for 5 min. The OG concentration in the supernatant was determined by measuring the absorbance at 480 nm using a UV-VIS-NIR spectrophotometer (Perking Elmer lambda 19) and by applying Beer-Lambert's law. More details on this test are reported in [15].

3. Results and Discussion

3.1. Influence of Photocatalyst Amount. Figure 2 depicts the variation of OG concentration versus irradiation time upon photocatalytic tests without and in presence of different amounts of TiO_2 -Pal nanocomposite. In the absence of the photocatalyst, the OG concentration remains constant confirming that OG photolysis is quite negligible using our UV source. In the presence of supported photocatalyst, the removal of OG is confirmed by the decrease of its concentration when irradiation time increases. This degradation tends to be even more important as the photocatalyst amount increases. For instance, 96% of OG has been removed from a 10^{-5} M aqueous solution after 90 min using $1.5 \text{ g}\cdot\text{L}^{-1}$ of supported photocatalyst. This is more clearly shown by depicting the initial rate (R_i) deduced from the slope of linear parts in the early stages versus photocatalyst amount (Figure 3) in agreement with a pioneering report [1]. Indeed, below a photocatalyst amount of *ca.* $0.5 \text{ g}\cdot\text{L}^{-1}$, the initial degradation rate of OG increases with the increase of supported photocatalyst concentration. This reveals a heterogeneous catalytic regime [1]. However beyond $0.5 \text{ g}\cdot\text{L}^{-1}$, the initial degradation rate of OG reaches a plateau and becomes independent of photocatalyst quantity.

Another illustration reveals a critical amount of the supported photocatalyst; this is the influence of the photocatalyst quantity on the time required to degrade for instance 60% of OG ($t_{60\%}$). Figure 4 reveals that below $0.8 \text{ g}\cdot\text{L}^{-1}$ the $t_{60\%}$ time decreases by increasing the amount of photocatalyst and it practically stabilizes beyond this threshold value. This indicates that even if the initial degradation rate R_i does not vary significantly for catalyst amount ranging from 0.5 to $0.8 \text{ g}\cdot\text{L}^{-1}$ (Figure 3), the photocatalytic efficiency still increases with the catalyst amount up to the critical quantity of $0.8 \text{ g}\cdot\text{L}^{-1}$ (Figure 4). For nanocomposite amounts lower than $0.8 \text{ g}\cdot\text{L}^{-1}$, the increase of OG photodegradation with the catalyst amount could be explained by a photons flux in excess with respect to the specific surface area of particles dispersed in the reacting media so that all the TiO_2 -Pal particles are exposed to radiation. However, for higher photocatalyst amounts ($>0.8 \text{ g}\cdot\text{L}^{-1}$), both shadowing effects can occur and particles can aggregate which in turn reduces the interfacial area between the solution and the photocatalyst. Thus the number of active sites on the catalyst surface is decreased [16]. In other words, an excess of particles results in a screening effect masking part of the photosensitive surface [1] and increases opacity of the solution and

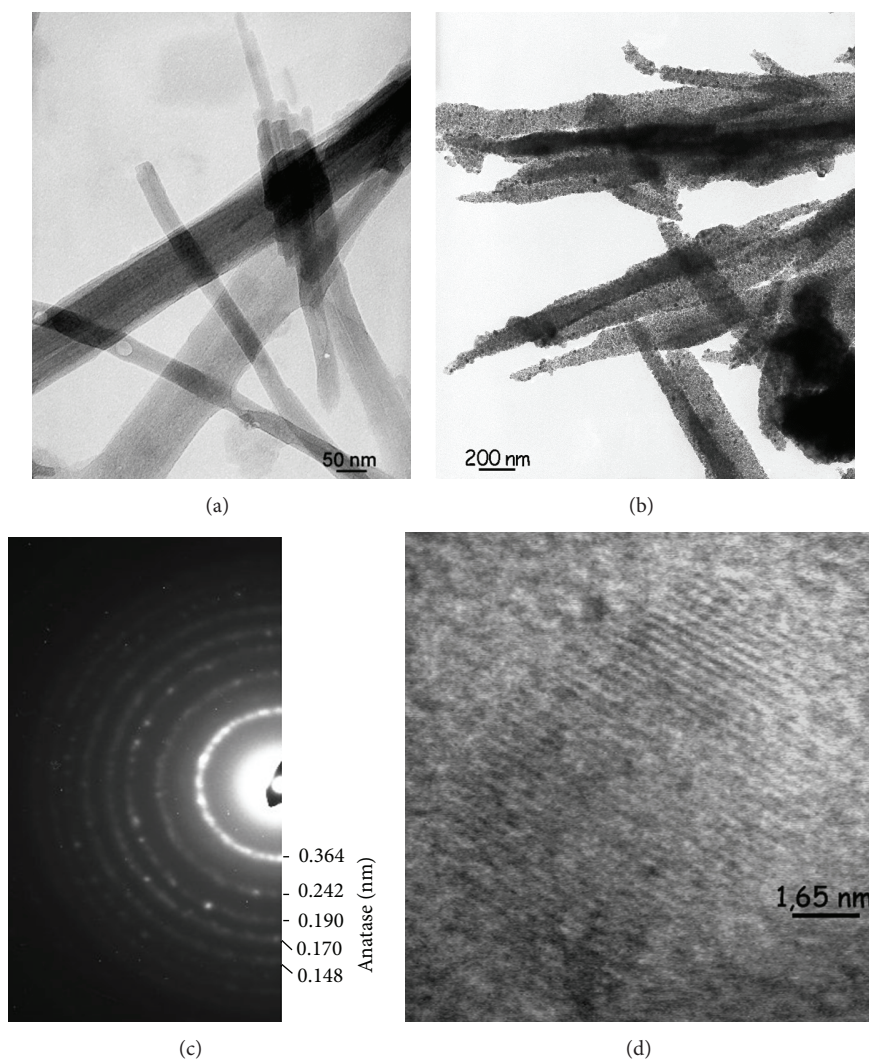


FIGURE 1: TEM micrographs of pristine palygorskite Na^+ -Pal (a) and TiO_2 -Pal (b) samples. Selected area electron diffraction pattern indexed with anatase (c) of a TiO_2 -Pal sample and high resolution electron micrograph (d) showing a nodular anatase NP (8–12 nm in diameter) and the {101} planes with a reticular distance of *ca.* 0.3 nm [11].

light scattering [16] yielding to lower degradation rate of OG.

ICP analysis of TiO_2 -Pal supported photocatalyst gave a TiO_2 content of *ca.* 47 wt.%. Therefore, the optimum concentration of nanocomposite TiO_2 -palygorskite photocatalyst determined herein at $0.8 \text{ g}\cdot\text{L}^{-1}$ properly corresponds to $0.37 \text{ g}\cdot\text{L}^{-1}$ of TiO_2 attached to palygorskite fibers, since the nanocomposite contains 47 wt.% of anatase. This TiO_2 amount of *ca.* $0.4 \text{ g}\cdot\text{L}^{-1}$ is significantly lower than the optimum concentration ($2.5 \text{ g}\cdot\text{L}^{-1}$) previously reported in the case of unsupported TiO_2 slurry [1]. Interestingly this result indicates that photodegradation efficiency could be achieved with lower amount of TiO_2 when it is immobilized onto palygorskite fibers in comparison with which is required for unsupported TiO_2 .

The time dependence of logarithmic plot $\log(C_0/C)$ corresponding to the degradation of an OG solution (10^{-5} M) with a TiO_2 -Pal catalyst loading of $1 \text{ g}\cdot\text{L}^{-1}$ reveals a linear

variation (Figure 5). This behavior is similar to that of unsupported TiO_2 powder slurry and suggests a first-order reaction. The apparent rate constant deduced from the slope is around $2.9 \times 10^{-2} \text{ min}^{-1}$.

3.2. Influence of Initial OG Concentration. Figure 6 shows OG degradation curves as a function of initial dye concentration using a TiO_2 -palygorskite loading of $1 \text{ g}\cdot\text{L}^{-1}$. It is shown that the lower the initial dye concentration, the faster the OG removal. Indeed, after 75 min of irradiation, a total OG degradation is observed for a $5 \times 10^{-6} \text{ M}$ solution, while only 87%, 83%, and 57% of OG degradation were recorded for initial dye concentration of 10^{-5} , 3×10^{-4} , and $5 \times 10^{-4} \text{ M}$, respectively. As beforehand evidenced, OG photolysis is negligible (Figure 2). Therefore, the decrease of OG photodegradation by increasing its initial concentration could be explained by significant absorption of photons flux by the dye. Photocatalysis is a heterogeneous process that

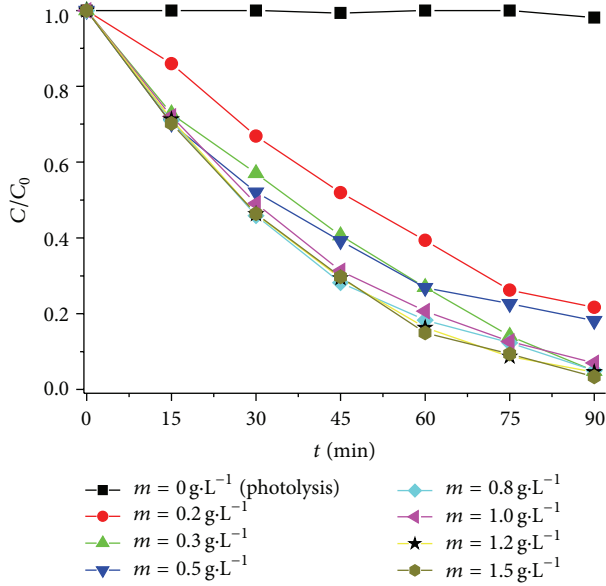


FIGURE 2: Influence of the supported photocatalyst amount on photocatalytic activity of TiO_2 supported palygorskite on the removal of Orange G from aqueous solution. OG degradation is given by its concentration at different time (C) divided by its initial concentration ($C_0 = 10^{-5} \text{ M}$).

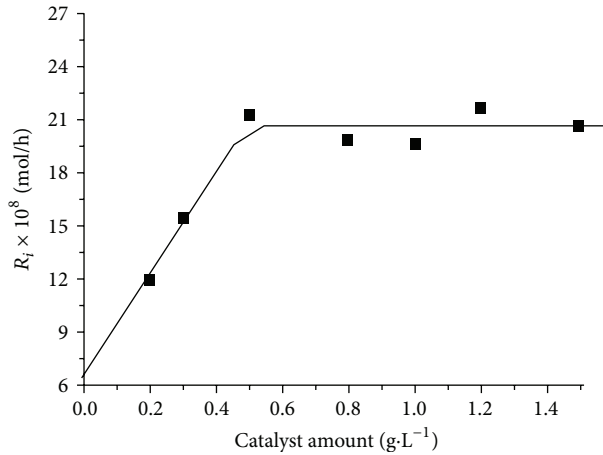


FIGURE 3: Variation of initial rate (R_i) of OG photodegradation versus the supported photocatalyst amount.

requires the combination of both photons and adsorption on catalytic sites. If photons flux decreases on the surface of supported photocatalyst due to absorption by the dye solution the efficiency of electron-hole photogeneration will also decrease and subsequently the formation of the required highly oxidant species, for example, OH^\bullet and $\text{O}_2^{\bullet-}$, will be reduced at the surface of photocatalyst [16].

Moreover, the photocatalysis kinetics generally follows a Langmuir-Hinshelwood mechanism with a reaction rate (R) varying proportionally with the coverage θ according to [1, 4]:

$$R = k\theta = k \left(\frac{KC}{1 + KC} \right), \quad (1)$$

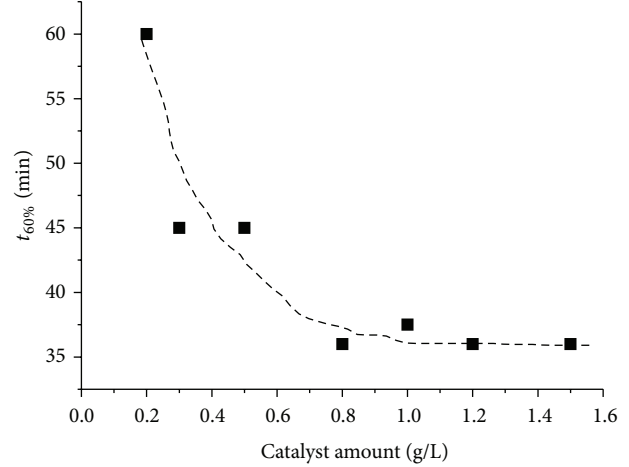


FIGURE 4: Influence of the supported photocatalyst amount on the time required to degrade 60% of OG ($t_{60\%}$).

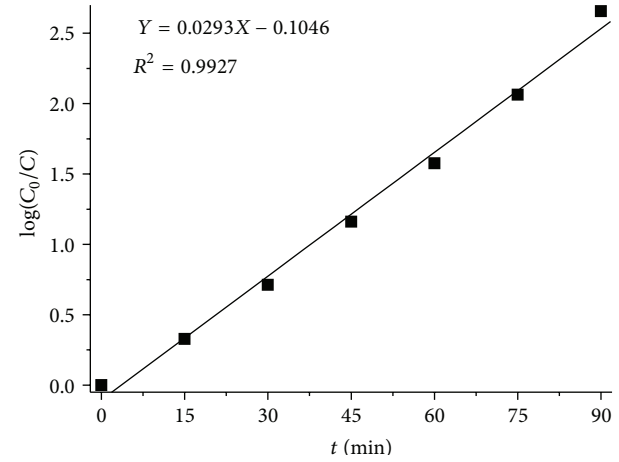


FIGURE 5: Logarithmic variation of OG relative concentration versus UV illumination time determined for a TiO_2 -supported palygorskite loading of $1 \text{ g}\cdot\text{L}^{-1}$ ($C_0 = 10^{-5} \text{ M}$).

where C is the pollutant concentration, k the rate constant, and K the equilibrium constant. Hence, the number of available catalytic sites decreases as the dye concentration increases, which in turn reduces OG photodegradation rate. As all OG solutions considered herein are diluted ($C < 10^{-3} \text{ M}$), the term KC becomes $\ll 1$ and consequently $R = k \cdot K \cdot C$. The reaction between photogenerated electron-hole and OG species (supposed to control the process) has an apparent first order as beforehand evidenced (Figure 5) [1, 4].

3.3. pH Effect of the Solution. The pH effect on photocatalytic degradation rate of OG solution (10^{-5} M) containing $1 \text{ g}\cdot\text{L}^{-1}$ of TiO_2 -supported palygorskite was studied by varying the pH from 2 to 11 by adding NaOH (basic pH) or HCl (acidic pH) (Figure 7(a)). The dependency on the pH is more clearly shown in Figure 7(b). The initial degradation rate of OG is high both for acidic pH (< 4) and basic pH (≈ 11). For median

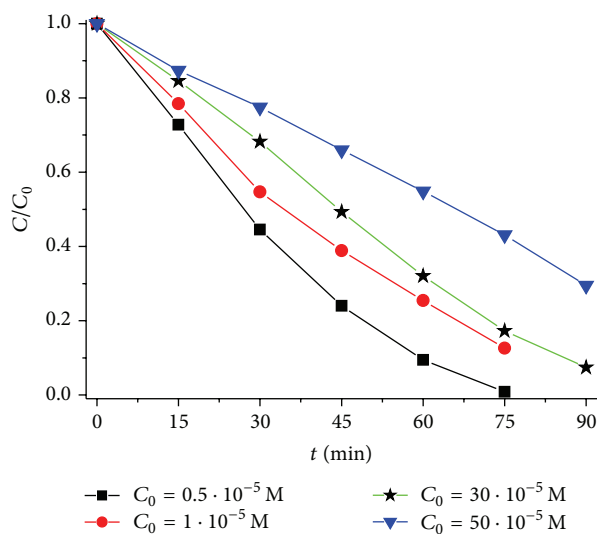


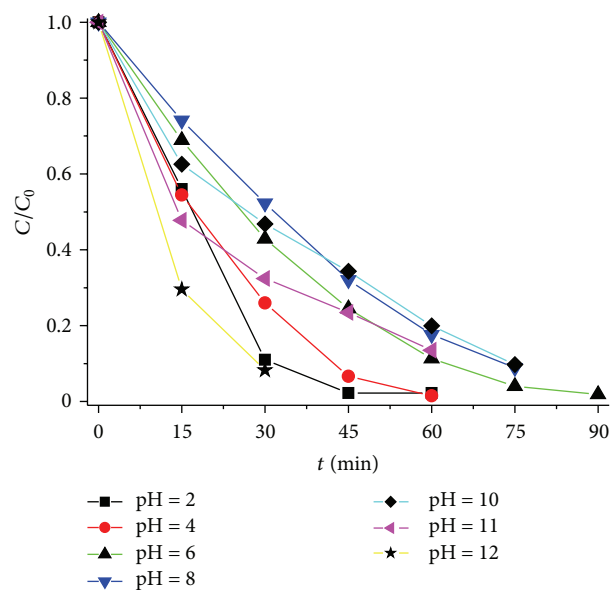
FIGURE 6: Influence of initial OG concentration on photocatalytic activity of $1 \text{ g} \cdot \text{L}^{-1}$ of TiO_2 supported palygorskite on the OG removal from aqueous solution.

values, the rate decreases by increasing pH from 4 to 8, then it increases to reach the highest level in the basic range.

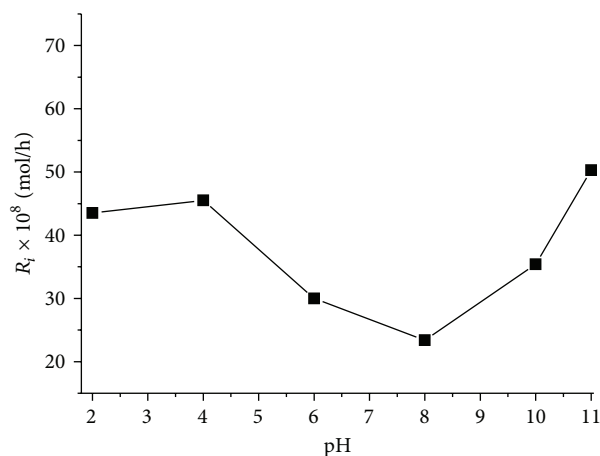
This may be ascribed to the pH effect on surface charge properties of TiO_2 nanoparticles wrapping palygorskite fibers (Figure 1). Indeed, in pH range 6–8, which includes the point of zero charge PZC (pH_{PZC}) of TiO_2 [17, 18], TiO_2 NPs surfaces are not charged, since they are mainly formed of neutral hydroxyl TiOH groups [19]. Hence, electrostatic interactions between particles are minimized and their agglomeration in the form of clusters is favored. This agglomeration reduces the transmission and absorption of light [20] and hence causes the decrease of dye degradation efficiency. Nevertheless, in strongly basic pH, TiO_2 nanoparticles surfaces are negatively charged in the form of TiO^- as a result of deprotonation of surface hydroxyl groups (TiOH) [19]. Consequently, electrostatic repulsions occur between particles, favoring their dispersion and hence the transmission and absorption of light which in turn enhance degradation rate of the OG dye. The same phenomenon likely occurs in acidic pH, but in this case, TiO_2 nanoparticles surfaces are positively charged in the form of TiOH_2^+ due to surface hydroxyls protonation [19]. In this case, besides the stability of TiO_2 -Pal dispersion, the adsorption of anionic species as OG molecules is likely much favored on positively charged surfaces sites of TiO_2 -Pal nanoparticles [21], which further improve the performance in photocatalysis.

4. Conclusion

This study shows that the photoactivity of TiO_2 NPs supported on palygorskite fibers depends on catalyst amount, OG dye concentration, and pH of the polluted solution. The photodegradation of OG was found to be the highest for an optimum photocatalyst loading of *ca.* $0.8 \text{ g} \cdot \text{L}^{-1}$. This corresponds to TiO_2 loading of only $0.37 \text{ g} \cdot \text{L}^{-1}$, which is significantly lower than literature data reported for unsupported



(a)



(b)

FIGURE 7: effect of pH: (a) photocatalytic OG degradation versus UV irradiation time as a function of the pH of aqueous solutions; (b) influence of pH of OG solutions on initial photocatalytic rate (R_i). The TiO_2 -Pal loading was $1 \text{ g} \cdot \text{L}^{-1}$ and initial OG concentration was 10^{-5} M .

TiO_2 nanopowders. The OG photocatalytic decomposition increases by decreasing the initial OG concentration of the polluted solution, and it is significantly improved by acidic and basic pH. These data are important to design and implement a slurry photoreactor and to determine its optimum operating conditions.

Acknowledgments

The financial supports from the “Convention de Coopération CNRST, Maroc/CNRS, France” (chemistry project no. 04/08), the “Programme de Coopération Scientifique Inter-universitaire de l’Agence Universitaire de la Francophonie”

(no. 63 13PS826), and the “Programme d’Action Intégrée Volubilis” (no. MA-08-185) are gratefully acknowledged.

References

- [1] J. M. Herrmann, “Heterogeneous photocatalysis: fundamentals and applications to the removal of various types of aqueous pollutants,” *Catalysis Today*, vol. 53, no. 1, pp. 115–129, 1999.
- [2] A. Fujishima, T. N. Rao, and D. A. Tryk, “Titanium dioxide photocatalysis,” *Journal of Photochemistry and Photobiology C*, vol. 1, no. 1, pp. 1–21, 2000.
- [3] Y. Paz, “Preferential photodegradation—why and how?” *Comptes Rendus Chimie*, vol. 9, no. 5-6, pp. 774–787, 2006.
- [4] O. Carp, C. L. Huisman, and A. Reller, “Photoinduced reactivity of titanium dioxide,” *Progress in Solid State Chemistry*, vol. 32, no. 1-2, pp. 33–177, 2004.
- [5] P. K. J. Robertson, “Semiconductor photocatalysis: an environmentally acceptable alternative production technique and effluent treatment process,” *Journal of Cleaner Production*, vol. 4, no. 3-4, pp. 203–212, 1996.
- [6] T. An, J. Chen, G. Li et al., “Characterization and the photocatalytic activity of TiO₂ immobilized hydrophobic montmorillonite photocatalysts. Degradation of decabromodiphenyl ether (BDE 209),” *Catalysis Today*, vol. 139, pp. 69–76, 2008.
- [7] P. Aranda, R. Kun, M. A. Martin-Luengo, S. Letaïef, I. Dékány, and E. Ruiz-Hitzky, “Titania-sepiolite nanocomposites prepared by a surfactant templating colloidal route,” *Chemistry of Materials*, vol. 20, pp. 84–91, 2008.
- [8] J. Liu, M. Dong, S. Zuo, and Y. Yu, “Solvothermal preparation of TiO₂/montmorillonite and photocatalytic activity,” *Applied Clay Science*, vol. 43, no. 2, pp. 156–159, 2009.
- [9] M. Nieto-Suárez, G. Palmisano, M. L. Ferrer et al., “Self-assembled titania-silica-sepiolite based nanocomposites for water decontamination,” *Journal of Materials Chemistry*, vol. 19, no. 14, pp. 2070–2075, 2009.
- [10] L. Bouna, B. Rhouta, M. Amjoud et al., “Synthèse, caractérisations et tests photocatalytiques d’un matériau argileux d’origine naturelle à base de la beidellite fonctionnalisée par TiO₂,” *Matériaux Et Techniques*, vol. 100, pp. 241–225, 2012.
- [11] L. Bouna, B. Rhouta, M. Amjoud et al., “Synthesis, characterization and photocatalytic activity of TiO₂ supported natural palygorskite microfibers,” *Applied Clay Science*, vol. 52, no. 3, pp. 301–311, 2011.
- [12] L. Bouna, B. Rhouta, L. Daoudi et al., “Mineralogical and physico-chemical characterizations of ferruginous beidellite-rich clay from Agadir basin (Moroc),” *Clays and Clay Minerals*, vol. 60, pp. 278–290, 2012.
- [13] E. Zatile, B. Rhouta, L. Bouna et al., “Comprehensive physicochemical study of dioctahedral palygorskite-rich clay from Marrakech High-Atlas (Morocco),” *Physics and Chemistry of Minerals*, 2013.
- [14] K. Hofstadler, R. Bauer, S. Novalic, and G. Heisler, “New reactor design for photocatalytic wastewater treatment with TiO₂ immobilized on fused-silica glass fibers: photomineralization of 4-chlorophenol,” *Environmental Science Technology*, vol. 28, no. 4, pp. 670–674, 1994.
- [15] C. Sarantopoulos, E. Puzenat, C. Guillard, J. M. Herrmann, A. N. Gleizes, and F. Maury, “Microfibrous TiO₂ supported photocatalysts prepared by metal-organic chemical vapor infiltration for indoor air and waste water purification,” *Applied Catalysis B*, vol. 91, no. 1-2, pp. 225–233, 2009.
- [16] M. Faisal, M. Abu Tariq, and M. Muneer, “Photocatalysed degradation of two selected dyes in UV-irradiated aqueous suspensions of titania,” *Dyes and Pigments*, vol. 72, no. 2, pp. 233–239, 2007.
- [17] A. Fernández-Nieves, C. Richter, and F. J. De Las Nieves, “Point of zero charge estimation for a TiO₂/water interface,” *Progress in Colloid and Polymer Science*, vol. 110, pp. 21–24, 1998.
- [18] L. A. García Rodenas, A. D. Weisz, G. E. Magaz, and M. A. Blesa, “Effect of light on the electrokinetic behavior of TiO₂ particles in contact with Cr(VI) aqueous solutions,” *Journal of Colloid and Interface Science*, vol. 230, no. 1, pp. 181–185, 2000.
- [19] C. Kormann, D. W. Bahnemann, and M. R. Hoffmann, “Photolysis of chloroform and other organic molecules in aqueous TiO₂ suspensions,” *Environmental Science and Technology*, vol. 25, no. 3, pp. 494–500, 1991.
- [20] W. Xi and S. U. Geissen, “Separation of TiO₂ from photocatalytically treated water by cross-flow microfiltration,” *Water Research*, vol. 35, no. 5, pp. 1256–1262, 2001.
- [21] L. Bouna, B. Rhouta, M. Amjoud et al., “Correlation between electrokinetic mobility and ionic dyes adsorption of Moroccan stevensite,” *Applied Clay Science*, vol. 48, no. 3, pp. 527–530, 2010.

Research Article

Synthesis of Nanostructured Anatase Mesoporous Membranes with Photocatalytic and Separation Capabilities for Water Ultrafiltration Process

Vahideh Tajer-Kajinebaf,¹ Hossein Sarpoolaky,¹ and Toraj Mohammadi²

¹ School of Metallurgy and Materials Engineering, Iran University of Science and Technology, Tehran 16846-13114, Iran

² Research Laboratory for Separation Processes, Faculty of Chemical Engineering, Iran University of Science and Technology, Tehran 16846-13114, Iran

Correspondence should be addressed to Hossein Sarpoolaky; hsarpoolaky@iust.ac.ir

Received 14 December 2012; Accepted 26 January 2013

Academic Editor: Jiaguo Yu

Copyright © 2013 Vahideh Tajer-Kajinebaf et al. This is an open access article distributed under the Creative Commons Attribution License, which permits unrestricted use, distribution, and reproduction in any medium, provided the original work is properly cited.

In this work, the nanostructured anatase mesoporous membranes were prepared for water ultrafiltration (UF) process with photocatalytic and physical separation capabilities. A macroporous substrate was synthesized from α - Al_2O_3 , then a colloidal titania sol was used for the preparation of the intermediate layer. Also, the membrane top layer was synthesized by deposition and calcination of titania polymeric sol on the intermediate layer. The characterization was performed by DLS, TG-DTA, XRD, BET, FESEM, TEM, and AFM techniques. Also, the filtration experiments were carried out based on separation of methyl orange from aqueous solution by a membrane setup with a dead-end filtration cell. Photocatalytic activity of the membranes was evaluated by methyl orange photodegradation using UV-visible spectrophotometer. The mean particle size of the colloidal and polymeric sols was 14 and 1.5 nm, respectively. The anatase membranes exhibited homogeneity, with the surface area of $32.8 \text{ m}^2/\text{g}$, the mean pore size of 8.17 nm, and the crystallite size of 9.6 nm. The methyl orange removal efficiency by the mesoporous membrane based on physical separation was determined to be 52% that was improved up to 83% by a coupling photocatalytic technique. Thus, the UF membrane showed a high potential due to its multifunctional capability for water purification applications.

1. Introduction

Nowadays, due to the rapid industrialization, the demand for high-quality water has increased. The wastewater that usually consists of fine particles, microorganisms, or organic pollutants has seriously polluted the drain water [1]. Also, industrial dyes have been recognized as one of the largest sources of water contamination [2].

Physical separation technique is an effective technology for the removal of water pollutants. Compared with conventional treatment technology, membrane processes can provide easy operational control, low energy costs, potential material recovery, and more compact assembly [3, 4]. However, the membrane's inherent shortcoming that the pollutants could merely be separated from water without further degradation makes it prone to cause secondary pollution. Thus, it needs to make an attempt with regard to its potential

for degradation of pollutants to overcome the drawback of filtration [5].

Photocatalytic degradation of toxic organic compounds has received a great attention for the past several years [6]. Hence, removal efficiency of pollutants can increase by coupling photocatalytic technique with separation process. Separation and photocatalytic processes can be promising technologies for the purification of wastewater. These processes can be coupled together to produce photocatalytic membranes [7, 8]. Among different materials for this object, titania has received significant attention due to its high water flux, chemical stability, high photocatalytic activity [9, 10], strong oxidizing power, cost effectiveness, long-term stability, and especially energy band edges, which well match the redox potentials of water [11]. These properties cause promising application of titania membranes for water treatment [12, 13]. Although titania has been known as the most effective

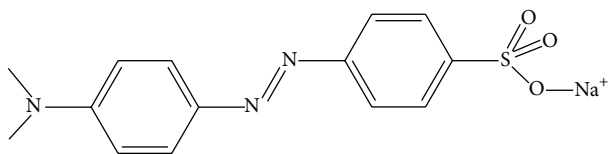


FIGURE 1: Chemical structure of methyl orange.

material for these objects, among different forms of titania, anatase is the most photoactive one [14–16]. Stabilization of anatase phase with high effective surface area is an important object in the synthesis process of titania membranes. Studies show the sol-gel method such as colloidal and polymeric ones can be a suitable route for the synthesis of the nanostructured anatase membranes with high effective surface area [7, 8, 17].

In the present work, the nanostructured anatase membranes were prepared by deposition and calcination of the polymeric titania sol on the colloidal titania-coated alumina substrates and then were characterized by DTA-TG, XRD, FESEM, TEM, AFM, BET, and UV-Vis spectroscopy. Also, the photocatalytic and separation capabilities of the mesoporous anatase membranes were evaluated by the determination of the removal efficiency of methyl orange based on its concentration changes in aqueous solution.

2. Experimental Procedures

2.1. Materials. Granulate powder of α - Al_2O_3 (KMS-92, Martinswerk) with chemical composition shown in Table 1 was chosen as raw material for the preparation of the membrane substrate.

Titanium tetraisopropoxide (TTIP, Merck 821895), isopropanol (IPA, Merck 109634), nitric acid (65% solution, Merck 100456), hydrochloric acid (37% solution, Merck 100317), and deionized water as raw materials as well as hydroxypropyl cellulose (HPC, Aldrich 435007) and polyvinyl alcohol (PVA, Acros 821038) as binders were used for the preparation of the colloidal and polymeric titania sols. Methyl orange (MO, Merck 101322) with chemical formula of $\text{C}_{14}\text{H}_{14}\text{N}_3\text{NaO}_3\text{S}$ (see Figure 1) and molar mass of 327.34 g/mol was used as the model pollutant for investigation of photocatalytic decolorization and separation capabilities of the synthesized anatase membranes.

2.2. Membrane Preparation

2.2.1. Alumina Substrate. To prepare the membrane substrate, α - Al_2O_3 granulate powder was shaped into a disk with 17 mm in diameter and 2 mm in thickness using a uniaxial press under the pressure of 150 psi. The sintering process was carried out with a heating rate of $10^\circ\text{C}/\text{min}$ up to 1000°C and was then followed with a rate of $5^\circ\text{C}/\text{min}$ up to 1380°C . Also, the retention time at the maximum temperature was set to be 1 h.

2.2.2. Membrane Interlayer. The membrane interlayer was prepared by the deposition of the colloidal titania sol on

TABLE 1: Chemical composition of α - Al_2O_3 powder.

Oxides	Al_2O_3	SiO_2	CaO	MgO	Fe_2O_3	Na_2O
Weight (%)	92	3.6	2.5	1.5	<0.2	<0.1

the alumina substrate. The colloidal sol was obtained by hydrolysis of TTIP via the addition of an excess H_2O ($[\text{H}_2\text{O}]/[\text{Ti}] > 4$). A solution of TTIP in IPA was added dropwise to a solution of water in IPA while stirring at high speed. Then, the alcohol was removed from the solution by rotary system and the washed product was dispersed in water to achieve the Ti concentration to 0.4 mol/lit. The solution was peptized with acid by adjusted pH to 1.5 and was refluxed at about 70°C for 20 h, which resulted in a semiopaque titania dispersion. Then, the sol was poured in beaker glass and subsequently was held for 30 min in an ultrasonic bath to break the weakly agglomerated particles. Finally, a clear blue stable sol was obtained. Consequently, a solution of HPC and PVA was added to the obtained sol as binder. For applying the titania layer, the colloidal sol was deposited on the alumina substrate for four steps by dipcoating process at a constant rate of 6 mm/min and immersion time of 30 s. Also, the unsupported gel layer was prepared by pouring the colloidal sol in a petri dish. Both the supported and unsupported gel layers were dried at room temperature for 48 h then were heat-treated at different temperatures for 1 h with a heating rate of $1^\circ\text{C}/\text{min}$. Finally, the colloidal titania-coated alumina substrates were prepared.

2.2.3. Membrane Top Layer. Membrane top layer was prepared by the deposition of polymeric titania sol on the intermediate layer. First, the polymeric sol was obtained by hydrolysis of TTIP via the addition of a less than equivalent amount of H_2O ($[\text{H}_2\text{O}]/[\text{Ti}] < 4$) in order to obtain a precipitate-free polymeric sol. A solution of water and hydrochloric acid as a catalyst in IPA was added dropwise to a solution of TTIP in IPA during high speed stirring. The molar ratio for TTIP : IPA : H_2O : HCl of the final sol was 1 : 31 : 0.8 : 0.23, respectively. Stirring was continued for 4 h to get a stabilized sol. Finally, the obtained transparent sol was deposited on the colloidal titania-coated alumina substrates for four steps by dip-coating process with a constant rate 6 mm/min and time immersion of 30 s. Also, the unsupported gel layer was prepared by pouring the polymeric sol in a petri dish. The supported and unsupported polymeric titania gel layers were dried at room temperature for 24 h. Finally, heat treatment was done at different temperatures for 1 h with a heating rate of $1^\circ\text{C}/\text{min}$.

2.3. Characterization. The substrate porosity was measured according to the ASTM C373-88 standard by the Archimedes method. The mechanical strength of the substrate was measured according to ASTM C1505-01 by SANTAM universal testing machine, STM-400 series. Particle size distribution of the prepared colloidal and polymeric titania sols was determined by dynamic light scattering technique (DLS, ZS3600, Malvern). Thermal properties of the dried gels were characterized by thermogravimetry and differential

TABLE 2: The optimized preparation conditions and the properties of alumina substrates.

Material	Size		Pressure	Heat treatment	Strength	Pore diameter	AWA ¹	MOP ²
	Diameter	Thickness						
α -Al ₂ O ₃	17 mm	2 mm	150 psi	1380°C, 1 h	38 MPa	1–3 μ m	15%	40%

¹ Average water absorption. ² Mean open porosity.

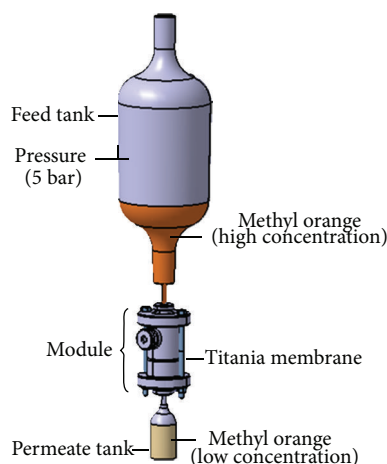


FIGURE 2: Schematic image of a membrane setup with a dead-end filtration cell used for filtration experiments.

thermal analysis (TG-DTA, PERKINELMER) in a nitrogen flow with a heating rate of 7.5°C/min up to 900°C. The phase composition and the average crystallite size of the membranes were identified using X-ray diffraction technique with Cu K α wavelength (Philips PW1800). The morphology of the samples was characterized by field emission scanning electron microscopy (FESEM, WEGA\\TESCAN) and transmission electron microscopy (TEM, EM 208, Philips) with an accelerating voltage of 30 kV and 100 kV, respectively. Surface roughness and morphology of the prepared membranes were evaluated by atomic force microscopy (AFM, DualScope C-26, DME). Also, N₂-sorption measurements (Belsorp mini II, BEL Japan, Inc.) were performed to determine the Brunauer-Emmett-Teller (BET) surface area and the pore size of the membrane top layer. The separation experiments were carried out using a membrane setup with a dead-end filtration cell under 5-bar pressure according to Figure 2.

Moreover, the feed solution containing 20 mg/L of MO aqueous solution was transported through membrane module, and then concentration of the permeate solution was determined by recording UV-Vis absorption spectra using UV-visible spectrophotometer (Agilent, 8453). Also, the photocatalytic activity of the membranes was measured by the photodegradation of MO aqueous solution. The prepared membrane in an MO solution (20 mg/L) was irradiated by a UV source (Sunny, 360–415 nm, 125 W), and then removal efficiency was evaluated by determination of concentration changes of MO solution by UV-visible spectrophotometer. Also, water permeation measurements were carried out using the as-prepared membrane setup. The feed side of

the membrane was kept at a constant pressure of 5 bar and the permeate side was set at atmospheric pressure. The permeation flux was measured at room temperature using the following [18]:

$$\text{Permeation flux} = \frac{Q}{A} \cdot \Delta t, \quad (1)$$

where Q is the quantity of permeate (cm³), A is the effective membrane area (m²), and Δt is the sampling time (h). Effective area of the membrane in the module was 1.76 cm².

3. Results and Discussion

3.1. Substrate. Alumina was chosen as a membrane substrate due to high chemical stability in acidic and basic environment [19, 20]. FESEM images of the surface and cross-section of the prepared α -Al₂O₃ substrate are shown in Figure 3.

Based on FESEM results, the distribution pore size of the alumina substrate is in the range of 1–3 μ m that can be a macroporous substrate according to IUPAC [21]. The support pore size should be large enough to build a pore size gradient from the support through the membrane layer. The gradient in the pore size effectively prevents early clogging of the membrane during its performance [7]. The mechanical strength of the substrate was determined to be 38 MPa according to the three-point bending test. Also, the mean open porosity and average water absorption of the substrate were determined to be 40% and 15%, respectively. The optimized preparation conditions as well as the properties of alumina substrates are given in Table 2.

3.2. Membrane Interlayer

3.2.1. Particle Size Distribution. Particle size distribution of the colloidal titania sol according to Figure 4 is in the range of 9–50 nm with a mean particle size of 14 nm.

In colloidal sol-gel route due to the presence of excess water, hydrolysis occurs fast and leads to the formation of relatively large particles that can easily cover the surface of alumina substrates without infiltration.

3.2.2. Thermal Analysis. The thermogravimetry and differential thermal analysis were used to obtain qualitative and quantitative information about the effects of heat treatment on the colloidal titania such as the combustion temperature of the organic compounds and the decomposition of hydroxyl groups as well as to determine the optimum calcination temperature of the intermediate layer. DTA-TG curves of the dried colloidal titania gel are given in Figure 5.

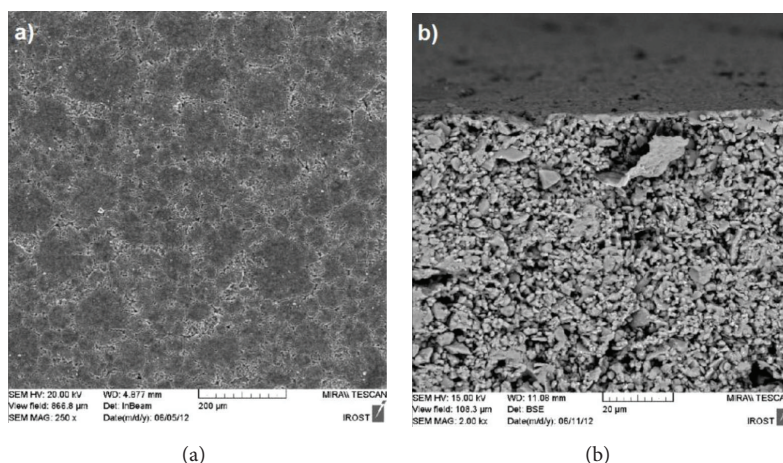


FIGURE 3: FESEM images of the (a) surface and (b) cross-section of the alumina substrate.

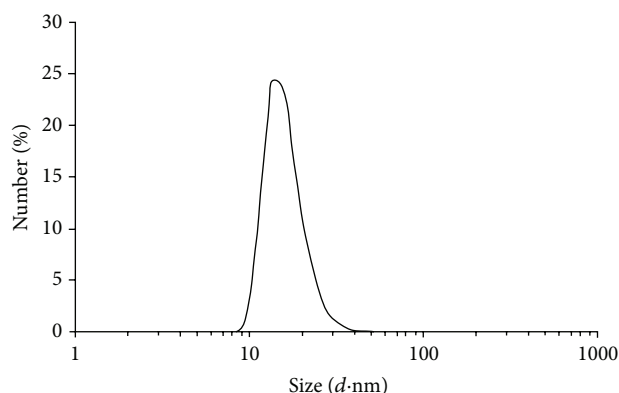


FIGURE 4: Particle size distribution of the colloidal titania sol.

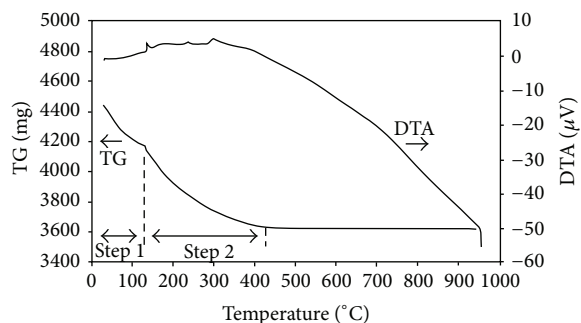


FIGURE 5: The thermogravimetry and differential thermal analysis of the dried colloidal titania gel.

According to Figure 5, the thermogravimetric curve follows 19% weight loss during two steps. The first step extends up to about 130°C that is attributed to the removal of adsorbed water corresponding to endothermic peak [22–24]. The second step extends up to 420°C that is according to the expulsion of organics and the dehydroxylation of $\text{Ti}(\text{OH})_4$. This step is along with TiO_2 phase transition according to exothermic peaks at 220 and 300°C. The former corresponds

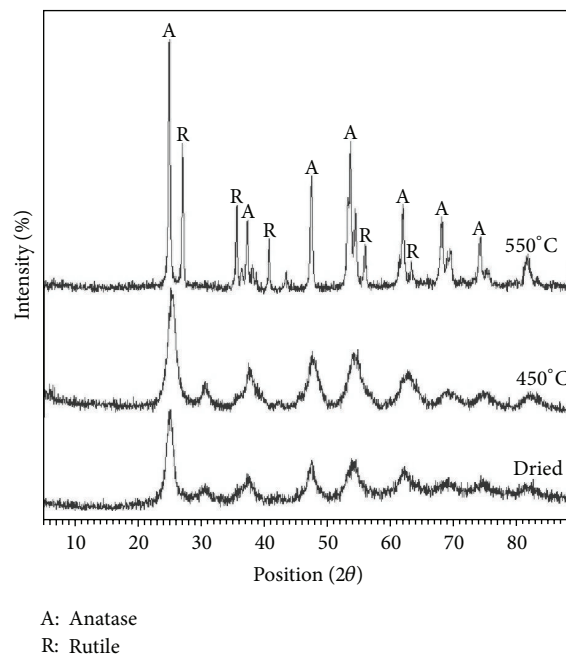


FIGURE 6: XRD patterns of the dried and calcined colloidal titania gels.

to the removal of organics and the latter can be due to phase transition from amorphous to anatase. Finally, the weight loss ends at about 420°C which can be a minimum calcination temperature for intermediate layer according to the complete removal of the organics.

3.2.3. Phase Analysis. The XRD patterns of the dried and calcined colloidal titania gels are shown in Figure 6. The strongest peaks of anatase and rutile phases are located at $2\theta = 25.3^\circ$ (101) and 27.4° (110), respectively [25].

According to Figure 6, phase structure of the dried colloidal titania gel is anatase while during calcination and by increasing the temperature, anatase peaks become sharper

and then rutile peaks are formed. Based on XRD results, at 450°C, titania is fully crystalline in the anatase form while rutile phase peaks are seen at 550°C. Several factors should be considered to select an optimum temperature for the calcination of membrane interlayer. First, the organic additives and hydroxyl groups should be completely removed and, second, titania should remain in the anatase form with a minimal crystallite size. Based on XRD and TG-DTA results as well as considering the above factors, the calcination of the intermediate layer was carried out at 450°C for 1 h. Also, a low heating rate (1°C/min) was chosen to prevent cracking of the interlayer during sintering process.

3.2.4. Microstructural Analysis. The top surface and cross-section FESEM images of the colloidal titania-coated alumina substrates are shown in Figure 7.

According to Figure 7(a), it can be seen that the surface of the alumina substrate is completely covered with the colloidal titania, implying that a continuous layer was formed on the surface. Also, it can be estimated that the thickness of the colloidal titania layer is about 2.5 μm (see Figure 7(b)). Our researches showed that the layer thickness increases with increasing the sol concentration and the dipping steps. Although few researchers mentioned that addition of PVA is sufficient for dipping solution [26, 27], others added both HPC and PVA to colloidal sol for dipping process [7, 28]. Alem et al. reported that PVA as a single additive that causes flocculation of the titania sol, but in combination with HPC no flocculation occurs. HPC hinders the interaction between PVA and titania and therefore can prevent flocculation of the sol. Also, Sekulić-Kuzmanović reported that a high PVA content causes flocculation of the colloidal titania sol, and a high HPC content decreases the viscosity of sol [29]. In the present work, a crack-free layer was achieved by addition of both HPC and PVA additives to the colloidal titania sol during four-step coating with the dipping time of 30 s. Therefore, the drying process was performed in a high humidity atmosphere, and then calcination process was carried out at an optimized temperature of 450°C for 1 h with a low heating rate of 1°C/min.

3.2.5. AFM Analysis. AFM micrographs showing the surface morphology of the colloidal titania-coated alumina substrate are given in Figure 8.

Figure 8 shows that the surface is quite rough at the micrometer scale, with a granular structure consisting of interconnected grain particles. The particles build up high mountains and deep valleys that seem to allow a better ability to absorb membrane top layer.

3.3. Membrane Top Layer

3.3.1. Particle Size Distribution. As shown in Figure 9, the particle size distribution of the polymeric titania sol is in the range of 1–3 nm with the mean particle size of 1.5 nm.

The polymeric titania sol has much smaller particles (nanometer-sized) compared to the colloidal one (see Figure 4). Thus, the deposition of the polymeric titania sol on

TABLE 3: Phase analysis results of the polymeric titania membrane at different calcination temperatures.

Temperature (°C)	450	550	650
Phase	Anatase	Anatase	Anatase
Crystallite size (nm)	9.6	15.8	31.8

the colloidal titania-coated substrate could produce a defect free top layer with the small pore size.

3.3.2. Thermal Analysis. The thermogravimetric and DTA curves of the dried polymeric titania gel are given in Figure 10.

The thermogravimetric curve follows 45% weight loss during three steps. The first step that extends up to 210°C can be attributed to the removal of alcohol and adsorbed water [29]. The second step to 250°C corresponds to removal of isopropoxy groups ($-\text{OC}_3\text{H}_7$) [29] and the third step that extends up to 440°C is attributed to the dehydroxylation of $\text{Ti}(\text{OH})_4$. Also, the board exothermic peak seen in DTA curve can be attributed to TiO_2 phase transition from amorphous to anatase. Based on TG curve, the weight loss beyond 440°C is negligible that is in agreement with the literature [29]. No significant thermal effects of the anatase-rutile transformation are detected up to 900°C.

3.3.3. Phase Analysis. According to Figure 11, XRD patterns of the polymeric titania show only anatase phase at different calcination temperatures.

The crystallite size of the prepared anatase membranes at different calcination temperatures was determined by Scherrer's equation [30, 31] of which results are recorded in Table 3.

The highest photocatalytic activity of titania is seen in the anatase form with optimal crystallite size in the range 8–10 nm [32]. Moreover, titania calcined at 450°C shows the fully crystalline anatase phase with the crystallite size of 9.6 nm. Thus, based on TG-DTA and XRD results, 450°C temperature was selected as an optimum temperature for calcination of the membrane top layer. However, the low calcination temperature of titania makes it possible to prepare membranes with the reduced pore and crystallite sizes [7].

3.3.4. Microstructural Study. Figure 12 shows the FESEM micrographs of the cross-section and top surface of the synthesized anatase membranes. As shown, a crack-free anatase layer with the thickness of about 0.5 μm is formed on the top surface of the colloidal titania-coated alumina substrate.

It is important to control the thickness of membrane top layer which has a significant effect on membrane permeability. The increasing thickness of top layer decreases membrane permeability as well as increases probability cracking during drying and calcination steps. Also, an optimum thickness provides better photocatalytic activity and overcomes the

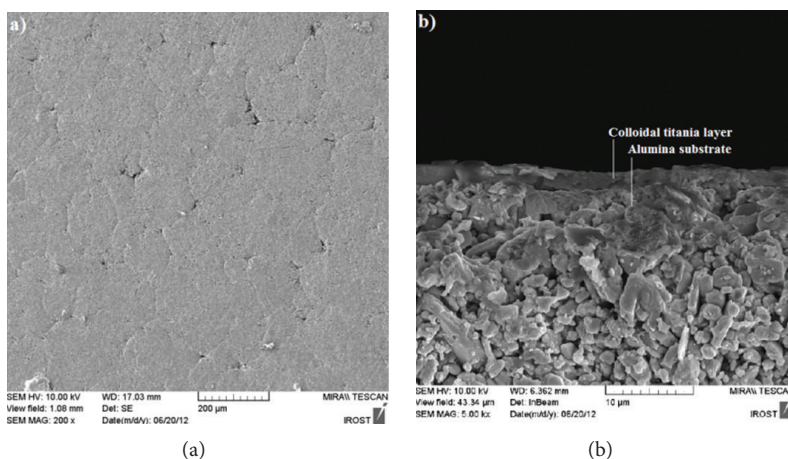


FIGURE 7: The FESEM images of the (a) top surface and (b) cross-section of the colloidal titania-coated alumina substrates.

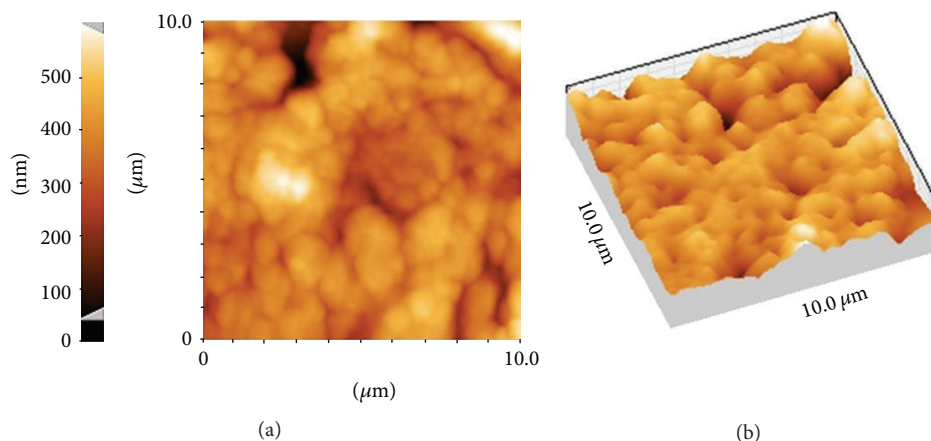


FIGURE 8: AFM micrographs (a) 2D and (b) 3D of the surface morphology of the colloidal titania-coated alumina substrate.

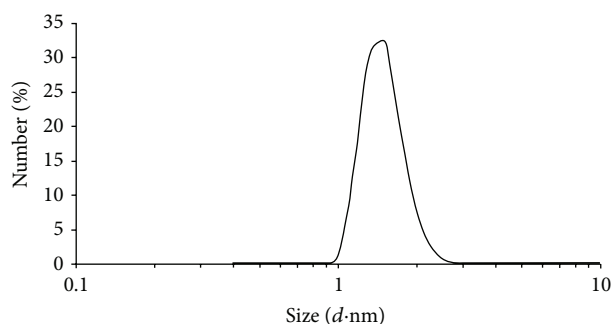


FIGURE 9: Particle size distribution of the polymeric titania sol.

irregularities and roughness of the surface. Our observations indicated that is increasing time and number of dipping steps increases top layer thickness. In the present study, an optimum thickness (about 500 nm) was obtained with four-step coating and dipping time of 30 s.

Also, TEM images in Figure 13 show that the membrane top layer consists of large particles that are agglomerations of smaller particles in nanometer scale (10–20 nm). Also, it

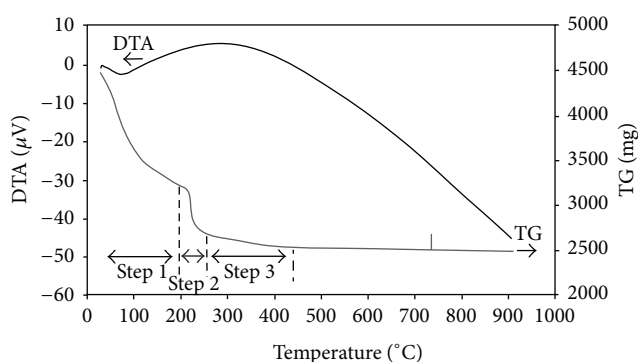


FIGURE 10: The thermogravimetric and DTA curves of the dried polymeric titania gel.

can be observed that crystallites are isotropic. According to Figure 13, the nanoparticles are well crystallized that are in agreement with XRD results.

3.3.5. AFM. AFM micrographs of surface morphology of the prepared anatase membrane are shown in Figure 14.

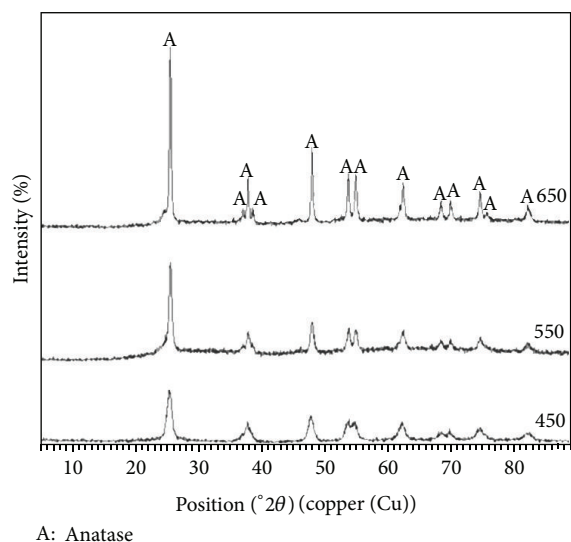
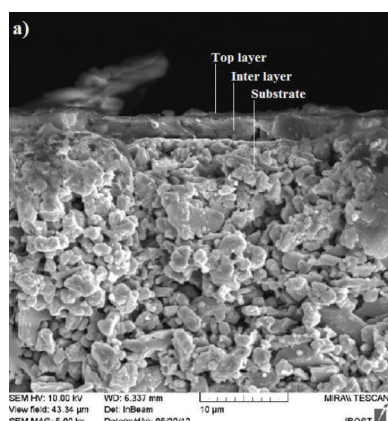
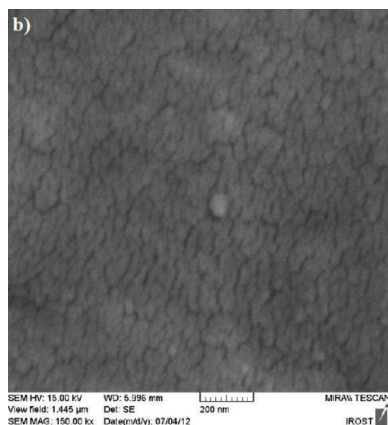


FIGURE 11: XRD patterns of the unsupported polymeric titania membranes at different calcination temperatures.



(a)



(b)

FIGURE 12: FESEM micrographs of (a) cross-section and (b) top surface of the synthesized anatase membrane.

The surface plot shows that the prepared anatase membrane has rough surface consisting of interconnected granular particles. As revealed by AFM, the membrane top layer shows the pores in the range of 20–200 nm that is categorized in UF membranes group according to IUPAC. The high surface roughness of the synthesized anatase membrane allows a good ability to absorb photons for photocatalytic activity.

3.3.6. Nitrogen Adsorption and Desorption. N_2 adsorption and desorption isotherms as well as BJH pore size distribution of the unsupported anatase membranes were obtained by BET method (see Figure 15).

As shown in Figure 15(a), N_2 hysteresis loop closes at a relative pressure, p/p_0 , of around 0.4 that it is associated with capillary condensation. The nature of adsorption isotherm displays a type IV adsorption isotherm with a hysteresis loop classified as type H_2 according to IUPAC [33], showing that major fraction of the pores are in the mesopore region. The adsorption and desorption isotherms do not coincide over a certain region of external pressures. At low pressures, first an adsorbate monolayer is formed on the pore surface, which is followed by the multilayer formation. The concept of monolayer adsorption works only on the perfect planar surface. A real surface possesses some degree of roughness, which makes adsorption to progress not homogeneously. The amount of molecules adsorbed on the external sample surface is negligible in comparison to that on the pore wall. The onset of the hysteresis loop usually marks the beginning of the capillary condensation in the pores. At the external pressure corresponding to the upper closure point of the hysteresis loop, the pores are completely filled with liquid [34]. Based on this analysis, BET specific surface area, pore volume, and mean pore diameter of the unsupported anatase membrane were determined to be around $32.8 \text{ m}^2/\text{g}$, $0.067 \text{ cm}^3/\text{g}$ and 8.1762 nm , respectively. Figure 15(b) shows the BJH pore size distribution curve of the unsupported anatase membrane calculated from the adsorption curve. It is found that the anatase membrane has a relatively narrow pore distribution in the range of 1–9 nm with a maximum at around 3.55 nm. According to IUPAC, pores in the range of 2–50 nm are categorized into mesopores [35]. The results obtained of BET method are summarized in Table 4.

Thus, based on BET analysis, the prepared anatase membranes are classified as mesoporous membranes.

3.3.7. Photocatalytic Properties. Photocatalytic activity of the nanostructured anatase mesoporous membranes was evaluated by the absorbance changes of MO aqueous solution under UV radiation after 30 minutes according to Figure 16.

The MO removal efficiency was estimated by applying the following:

$$\text{Removal efficiency (\%)} = \left[\frac{(C_0 - C)}{C} \right] \times 100, \quad (2)$$

where C_0 is the original MO concentration and C is the residual MO concentration in the feed solution [36]. So, the MO removal efficiency by the photocatalytic capability

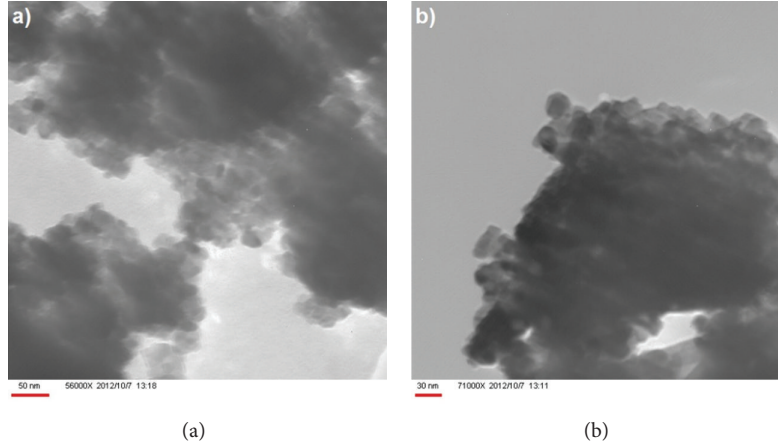


FIGURE 13: TEM micrographs of the membrane top layer.

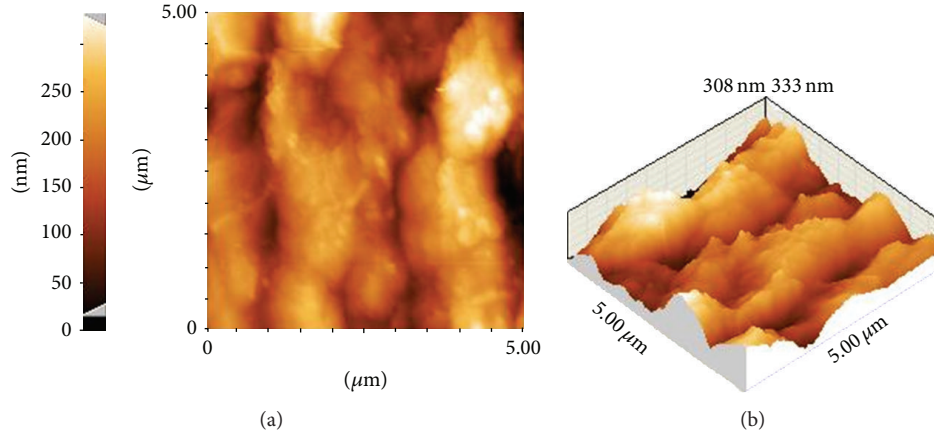


FIGURE 14: AFM micrographs (a) 2D and (b) 3D of the surface morphology of the nanostructured anatase membrane.

of the nanostructured anatase membranes was determined to be 61% after 30 min UV irradiation. It seems that the high roughness of membrane top layer (according to the AFM results in Figure 14) provides a better ability to capture the incident photon energy since a larger surface extension facilitates the photodegradation process. In fact, this surface not only enables the adsorption of a greater number of pollutant molecules but also creates a rough environment that causes a multiple light reflection and thus increases the amount of absorbed photons for photodegradation.

3.4. Membrane Experiments. The physical separation capability of the prepared anatase membranes was evaluated by direct measurement of MO concentration in the feed solution after passing through membrane at 5-bar pressure in constant time (see Figure 2). Figure 17 compares concentration of MO solution after passing through the membrane substrate, interlayer, and top layer.

Based on physical separation capability, the MO removal efficiency in the presence of alumina substrate, interlayer, and top layer was determined to be 4%, 20%, and 52%, respectively.

TABLE 4: The properties of the unsupported anatase membrane obtained of BET analysis.

Specific surface area (m^2/g)	Total pore volume (cm^3/g)	Mean pore diameter (nm)	Pore distribution (nm)
32.8	0.067	8.1762	1–9

Moreover, permeation flux in the presence of the membrane substrate, interlayer, and top layer was measured under 5-bar pressure according to (1) that the results are seen in Figure 18.

According to Figure 18, the alumina substrate shows a high permeability, while permeability considerably decreases in the presence of interlayer with $2.5 \mu\text{m}$ thickness. Moreover, the results indicate that depositing the top layer with $0.5 \mu\text{m}$ thickness on the interlayer has a small effect on the permeability reduction. Based on this experiment, the permeation flux was calculated to be 1470 , 1069 , and $935 \text{ cm}^3/\text{hm}^3$ for the membrane substrate, interlayer, and top layer, respectively. The decreasing permeation flux can be attributed to the reduction of pores size. Permeation experiment is one of

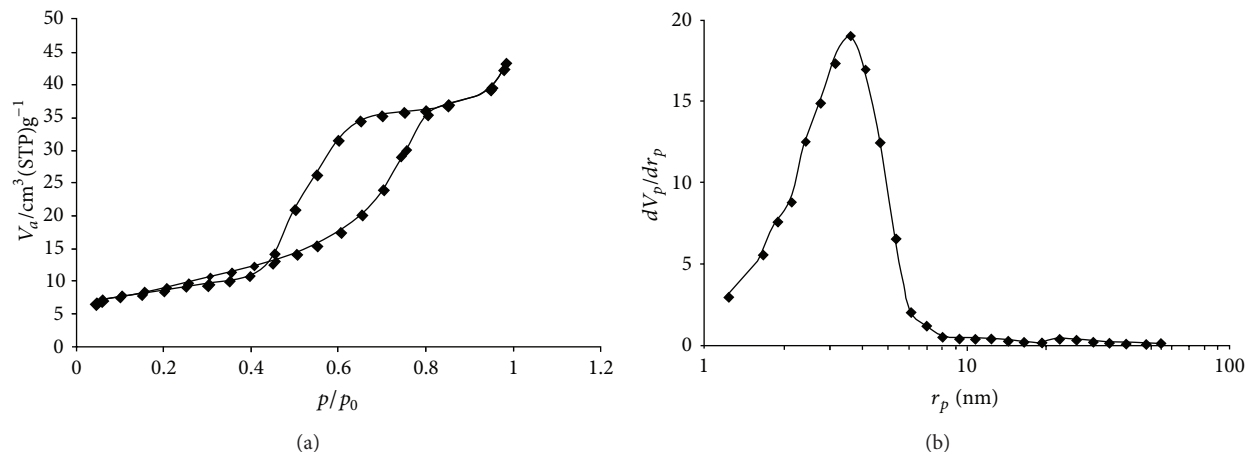


FIGURE 15: (a) The results obtained by BET method: N_2 adsorption and desorption isotherms and (b) BJH pore diameter distribution of the unsupported anatase membrane.

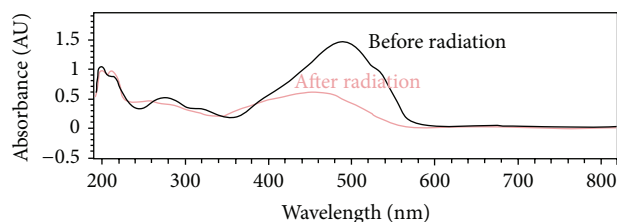


FIGURE 16: Absorbance curves of MO aqueous solution in the presence of the anatase membrane before and after UV radiation.

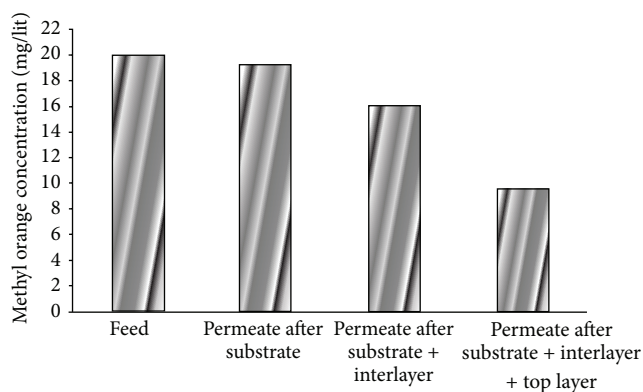


FIGURE 17: Concentration changes of MO solution before and after passing through the membrane substrate, interlayer, and top layer.

the most important methods for finding the structure and morphology of prepared membranes. Permeation flux is obviously affected by membrane structure and subsequently by preparation variables [37].

By coupling physical separation with photocatalytic technique, the MO removal efficiency was remarkably improved up to 83%, while it was 61% and 52% with individual photocatalysis and separation techniques, respectively. Figure 19 compares MO removal efficiency by the different techniques using the anatase mesoporous membrane.

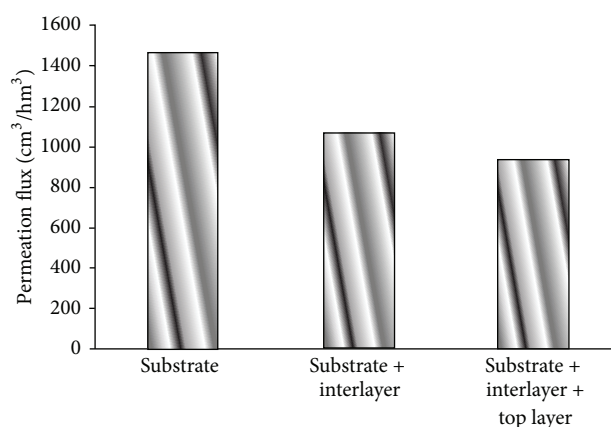


FIGURE 18: Permeation flux in the presence of substrate, substrate + interlayer and substrate + interlayer + top layer.

As observed, the anatase membrane synthesized in this work showed a high potential due to its multifunctional capability consisting of photodegradation and physical separation in water purification process.

4. Conclusion

In this research, the nanostructured anatase mesoporous membranes were prepared for water UF process with photocatalytic and physical separation capabilities. A colloidal titania sol was deposited on $\alpha\text{-Al}_2\text{O}_3$ substrates as the membrane interlayer. Also, membrane top layer was synthesized by deposition and calcination of titania polymeric sol on the intermediate layer. The mean particle size of the colloidal and polymeric titania sols was determined to be 14 and 1.5 nm, respectively. The synthesized anatase membranes exhibited homogeneity, with the surface area of $32.8 \text{ m}^2/\text{g}$, the maximum pore volume of $0.067 \text{ cm}^3/\text{g}$, the mean pore size of 8.17 nm, and the crystallite size of 9.6 nm. The removal efficiency of methyl orange based on physical separation

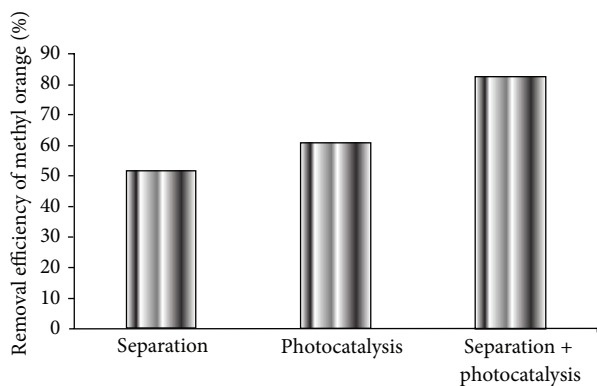


FIGURE 19: MO removal efficiency in the presence of anatase membrane by the different techniques.

by the mesoporous anatase membrane was determined to be 52% that by coupling photocatalytic technique, it was improved up to 83%. Thus, the prepared UF membranes showed a high potential due to its multifunctional capability such as photodegradation and physical separation for water purification applications.

Conflict of Interests

The authors have no conflict of interests in relation with the instrumental companies directly or indirectly.

References

- [1] C. C. Liu, Y. H. Hsieh, P. F. Lai, C. H. Li, and C. L. Kao, "Photodegradation treatment of azo dye wastewater by UV/TiO₂ process," *Dyes and Pigments*, vol. 68, no. 2-3, pp. 191-195, 2006.
- [2] Q. Wang, D. Gao, Ch. Gao et al., "Removal of a cationic dye by adsorption/photodegradation using electrospun PAN/O-MMT composite nanofibrous membranes coated with TiO₂," *International Journal of Photoenergy*, vol. 2012, Article ID 680419, 8 pages, 2012.
- [3] X. Huang, M. Leal, and Q. Li, "Degradation of natural organic matter by TiO₂ photocatalytic oxidation and its effect on fouling of low-pressure membranes," *Water Research*, vol. 42, no. 4-5, pp. 1142-1150, 2008.
- [4] B. S. Karnik, S. H. R. Davies, K. C. Chen, D. R. Jaglowski, M. J. Baumann, and S. J. Masten, "Effects of ozonation on the permeate flux of nanocrystalline ceramic membranes," *Water Research*, vol. 39, no. 4, pp. 728-734, 2005.
- [5] N. Ma, X. Quan, Y. Zhang, S. Chen, and H. Zhao, "Integration of separation and photocatalysis using an inorganic membrane modified with Si-doped TiO₂ for water purification," *Journal of Membrane Science*, vol. 335, no. 1-2, pp. 58-67, 2009.
- [6] W. Xin, D. Zhu, G. Liu, Y. Hua, and W. Zhou, "Synthesis and characterization of Mn-C-Co doped TiO₂ nanoparticles and photocatalytic degradation of methyl orange dye under sunlight irradiation," *International Journal of Photoenergy*, vol. 2012, Article ID 767905, 7 pages, 2012.
- [7] A. Alem, H. Sarpoolaky, and M. Keshmiri, "Titania ultrafiltration membrane: preparation, characterization and photocatalytic activity," *Journal of the European Ceramic Society*, vol. 29, no. 4, pp. 629-635, 2009.
- [8] A. Alem, H. Sarpoolaky, and M. Keshmiri, "Sol-gel preparation of titania multilayer membrane for photocatalytic applications," *Ceramics International*, vol. 35, no. 5, pp. 1837-1843, 2009.
- [9] S. H. Hyun and B. S. Kang, "Synthesis of titania composite membranes by the pressurized sol-gel technique," *Journal of the American Ceramic Society*, vol. 79, no. 1, pp. 279-282, 1996.
- [10] R. S. Sonawane, S. G. Hegde, and M. K. Dongare, "Preparation of titanium(IV) oxide thin film photocatalyst by sol-gel dip coating," *Materials Chemistry and Physics*, vol. 77, no. 3, pp. 744-750, 2003.
- [11] J. Yu, M. Jaroniec, and G. Lu, "TiO₂ photocatalytic materials," *International Journal of Photoenergy*, vol. 2012, Article ID 206183, 5 pages, 2012.
- [12] C. P. Athanasekou, G. E. Romanos, F. K. Katsaros, K. Kordatos, V. Likodimos, and P. Falarasa, "Very efficient composite titania membranes in hybrid ultrafiltration/photocatalysis water treatment processes," *Journal of Membrane Science*, vol. 392-393, pp. 192-203, 2012.
- [13] H. Choi, E. Stathatos, and D. D. Dionysiou, "Photocatalytic TiO₂ films and membranes for the development of efficient wastewater treatment and reuse systems," *Desalination*, vol. 202, no. 1-3, pp. 199-206, 2007.
- [14] A. L. Castro, M. R. Nunes, A. P. Carvalho, F. M. Costa, and M. H. Florêncio, "Synthesis of anatase TiO₂ nanoparticles with high temperature stability and photocatalytic activity," *Solid State Sciences*, vol. 10, no. 5, pp. 602-606, 2008.
- [15] L. Djafer, A. Ayral, and A. Ouagued, "Robust synthesis and performance of a titania-based ultrafiltration membrane with photocatalytic properties," *Separation and Purification Technology*, vol. 75, no. 2, pp. 198-203, 2010.
- [16] C. He, B. Tian, and J. Zhang, "Thermally stable SiO₂-doped mesoporous anatase TiO₂ with large surface area and excellent photocatalytic activity," *Journal of Colloid and Interface Science*, vol. 344, no. 2, pp. 382-389, 2010.
- [17] L. Caldeira, D. C. L. Vasconcelos, E. H. M. Nunes et al., "Processing and characterization of sol-gel titania membranes," *Ceramics International*, vol. 38, no. 4, pp. 3251-3260, 2012.
- [18] M. Sivakumar, D. R. Mohan, and R. Rangarajan, "Studies on cellulose acetate-polysulfone ultrafiltration membranes: II. Effect of additive concentration," *Journal of Membrane Science*, vol. 268, no. 2, pp. 208-219, 2006.
- [19] T. Tsuru, D. Hironaka, T. Yoshioka, and M. Asaeda, "Titania membranes for liquid phase separation: effect of surface charge on flux," *Separation and Purification Technology*, vol. 25, no. 1-3, pp. 307-314, 2001.
- [20] T. van Gestel, C. Vandecasteele, A. Buekenhoudt et al., "Alumina and titania multilayer membranes for nanofiltration: preparation, characterization and chemical stability," *Journal of Membrane Science*, vol. 207, no. 1, pp. 73-89, 2002.
- [21] W. J. Koros, Y. H. Ma, and T. Shimidzu, "Terminology for membranes and membrane process," IUPAC, Commission on membrane nomenclature, 1995.
- [22] K. G. K. Warrier, S. R. Kumar, C. P. Sibu, and G. Werner, "High temperature stabilisation of pores in sol-gel titania in presence of silica," *Journal of Porous Materials*, vol. 8, no. 4, pp. 311-317, 2001.
- [23] S. Mayadevi, S. S. Kulkarni, A. J. Patil et al., "Controlled chemical precipitation of titania for membrane applications—effect of heat treatment and fabrication conditions on its performance," *Journal of Materials Science*, vol. 35, no. 15, pp. 3943-3949, 2000.

- [24] A. Kermanpur, E. Ghassemali, and S. Salemizadeh, "Synthesis and characterisation of microporous titania membranes by dip-coating of anodised alumina substrates using sol-gel method," *Journal of Alloys and Compounds*, vol. 461, no. 1-2, pp. 331-335, 2008.
- [25] S. Mozia, A. W. Morawski, M. Toyoda, and M. Inagaki, "Application of anatase-phase TiO_2 for decomposition of azo dye in a photocatalytic membrane reactor," *Desalination*, vol. 241, no. 1-3, pp. 97-105, 2009.
- [26] V. T. Zaspalis, W. van Praag, K. Keizer, J. R. H. Ross, and A. J. Burggraaf, "Synthesis and characterization of primary alumina, titania and binary membranes," *Journal of Materials Science*, vol. 27, no. 4, pp. 1023-1035, 1992.
- [27] J. L. Zhang, W. Li, X. K. Meng, L. Wang, and L. Zhu, "Synthesis of mesoporous silica membranes oriented by self-assembles of surfactants," *Journal of Membrane Science*, vol. 222, no. 1-2, pp. 219-224, 2003.
- [28] A. A. Habibpanah, S. Pourhashem, and H. Sarpoolaky, "Preparation and characterization of photocatalytic titania-alumina composite membranes by sol-gel methods," *Journal of the European Ceramic Society*, vol. 31, no. 15, pp. 2867-2875, 2011.
- [29] J. Sekulić Kuzmanović, *Mesoporous and microporous titania membranes [Ph.D. thesis]*, 2004.
- [30] B. D. Cullity, *Elements of X-Ray Diffraction*, Addison-Wesley, Reading, Mass, USA, 1978.
- [31] Zh. Li, B. Hou, Y. Xu et al., "Comparative study of sol-gel-hydrothermal and sol-gel synthesis of titania-silica composite nanoparticles," *Journal of Solid State Chemistry*, vol. 178, no. 5, pp. 1395-1405, 2005.
- [32] F. Bosc, A. Ayral, P. A. Albouy, and C. Guizard, "A simple route for low-temperature synthesis of mesoporous and nanocrystalline anatase thin films," *Chemistry of Materials*, vol. 15, no. 12, pp. 2463-2468, 2003.
- [33] K. S. W. Sing, D. H. Everett, R. A. W. Haul et al., "Reporting physisorption data for gas/solid systems with special reference to the determination of surface area and porosity," *Pure and Applied Chemistry*, vol. 57, no. 4, pp. 603-619, 1985.
- [34] S. Naumov, *Hysteresis phenomena in mesoporous materials [Dissertation]*, Universitat Leipzig, 2009.
- [35] T. Tsuru, "Nano/subnano-tuning of porous ceramic membranes for molecular separation," *Journal of Sol-Gel Science and Technology*, vol. 46, no. 3, pp. 349-361, 2008.
- [36] A. A. Ismail, I. A. Ibrahim, M. S. Ahmed, R. M. Mohamed, and H. El-Shall, "Sol-gel synthesis of titania-silica photocatalyst for cyanide photodegradation," *Journal of Photochemistry and Photobiology A*, vol. 163, no. 3, pp. 445-451, 2004.
- [37] E. Saljoughi, M. Sadrzadeh, and T. Mohammadi, "Effect of preparation variables on morphology and pure water permeation flux through asymmetric cellulose acetate membranes," *Journal of Membrane Science*, vol. 326, no. 2, pp. 627-634, 2009.

Research Article

Correlation of Photocatalysis and Photoluminescence Effect in Relation to the Surface Properties of $\text{TiO}_2\text{:Tb}$ Thin Films

Damian Wojcieszak, Danuta Kaczmarek, Jaroslaw Domaradzki, and Michal Mazur

Faculty of Microsystem Electronics and Photonics, Wrocław University of Technology, Janiszewskiego 11/17, 50-372 Wrocław, Poland

Correspondence should be addressed to Damian Wojcieszak; damian.wojcieszak@pwr.wroc.pl

Received 24 November 2012; Accepted 7 February 2013

Academic Editor: Christos Trapalis

Copyright © 2013 Damian Wojcieszak et al. This is an open access article distributed under the Creative Commons Attribution License, which permits unrestricted use, distribution, and reproduction in any medium, provided the original work is properly cited.

In this paper structural, optical, photoluminescence, and photocatalytic properties of TiO_2 and $\text{TiO}_2\text{:}(2.6 \text{ at. \% Tb})$ thin films have been compared. Thin films were prepared by high-energy reactive magnetron sputtering process, which enables obtaining highly nanocrystalline rutile structure of deposited films. Crystallites sizes were 8.7 nm and 6.6 nm for TiO_2 and $\text{TiO}_2\text{:Tb}$, respectively. Surface of prepared thin films was homogenous with small roughness of ca. 7.2 and 2.1 nm in case of TiO_2 and $\text{TiO}_2\text{:Tb}$ samples, respectively. Optical properties measurements have shown that the incorporation of Tb into TiO_2 matrix has not changed significantly the thin films transparency. It also enables obtaining photoluminescence effect in wide range from 350 to 800 nm, what is unique phenomenon in case of TiO_2 with rutile structure. Moreover, it has been found that the incorporation of 2.6 at. % of Tb has increased the photocatalytic activity more than two times as compared to undoped TiO_2 . Additionally, for the first time in the current state of the art, the relationship between photoluminescence effect, photocatalytic activity, and surface properties of $\text{TiO}_2\text{:Tb}$ thin films has been theoretically explained.

1. Introduction

In the recent years there has been a continuous increase of the application possibilities of various metal oxide thin films with certain properties. Thin films play a key role in the development of innovative technologies, for example, in ophthalmic or protective coatings. One of the most important coating materials is titanium dioxide (TiO_2). It is caused by its many advantages like high transparency, high refraction index, thermal, chemical, and mechanical stability, and high photocatalytic activity [1–6].

Proper selection of technological process parameters can influence the TiO_2 crystal structure (brookite, anatase, rutile, or amorphous) and the crystallites sizes. Depending on the type of the crystal structure titanium dioxide may exhibit different properties, for example, optical, electrical, and chemical. Also doping the TiO_2 with various materials influences its structural, optical, and electrical properties [7–9]. Moreover, the properties of thin films based on titanium dioxide can be further modified by the application of postprocess annealing [10–12]. The changes are then caused

mainly by the increase in the crystallites sizes and as a result of the structure phase transformation, which usually takes place in elevated temperature.

Some desired properties of titanium dioxide can be obtained by doping with rare earth elements (REs). The application of the REs especially enables obtaining the photoluminescence effect. In practice, such materials can be used, for example, as light emitters in displays or in medical diagnostics. During the past two decades, a dynamic increase in interest of doping such oxides like SiO_2 , ZrO_2 , SnO_2 , ZnO , and TiO_2 with lanthanides has been observed [9, 12–23]. In the present paper TiO_2 doped with terbium (Tb) has been described. Terbium is an f-electron element with the oxidation states of +3 and +4. The doping of oxides with terbium gives a broad photoluminescence spectrum with the maximum emission at the wavelength range corresponding to green light. However, there are rare examples in literature resources of light emission observed from terbium-doped TiO_2 thin films [24].

Incorporation of lanthanides into TiO_2 matrix also allows the modification of surface properties, what is crucial in

photocatalysis processes. Photoinduced carriers formed in the matrix can undergo the recombination process, which reduce the photocatalytic activity. Carriers can be also intercepted by the trapping centers, which allows to avoid the recombination, or take part in reaction of pollutants decomposition and form oxidizing compounds. According to Liqiang et al. [25], photocatalytic activity of TiO_2 depends directly on amount of generated carriers, but its efficiency is determined by process of separation, recombination, capture, and transfer of carriers to the surface. It results from the fact that all oxidizing and reducing processes take place at the surface of TiO_2 [4, 26, 27]. Only pollutants, which are in contact with TiO_2 crystallites, can be decomposed. Significant factor in photocatalytic reaction is oxygen amount adsorbed at TiO_2 surface, because it inhibits the carriers recombination [28]. Also holes play significant role, because reaction based on those kinds of carriers is characterized by high quantum efficiency, particularly in oxidizing reaction of TiO_2 surface [28]. Active oxygen, hydroxide radicals, and hydrogen peroxide are the most reactive species formed in photocatalysis process.

For the purpose of the present work, thin films have been manufactured by magnetron sputtering method. In industrial application, sputtering processes are commonly used for deposition of thin oxide films [29–34]. These methods allow for deposition of films on the basis of infusible materials in relatively simple and cost-effective way. Additionally, magnetron sputtering gives the opportunity to control structure and stoichiometry of manufactured thin films. Huge advantage of this process is the possibility of deposition of dielectric, semiconductor, and metal films on large surfaces with different shapes. Proper selection of the magnetron sputtering process parameters enables the densification of thin-film crystal structure. The use of the modified process can result in nanocrystalline structure of deposited films with crystallites sizes varied from few to several nanometers [35, 36]. Densification of the structure is obtained by an increase in the sputtered species energy, that condenses at the substrate surface. This can be obtained by, for example, decrease of working gas pressure, increase in magnetron powering conditions, and application of voltage bias to the substrate.

In this paper, the influence of 2.6 at. % of Tb dopant on structural, optical, and photocatalytic properties of TiO_2 has been presented. Due to the lack of such description in the current state of the art, novel theoretical explanation of the relationship of photoluminescence effect and photocatalytic activity and the surface properties of TiO_2 doped with terbium has been presented.

2. Experimental

Titanium dioxide thin films doped with terbium have been deposited by high-energy reactive magnetron sputtering process (HERMS) [36–38]. Thin films were deposited in pure oxygen plasma (without argon as a working gas) by sputtering of metallic titanium target. Doping was obtained by sputtering of Ti-Tb mosaic target. Several sets of TiO_2 thin films doped with different amount of terbium were

prepared. Samples consisted of 2.6 at. % of Tb were selected for further investigation due to simultaneous existence of photoluminescence and photocatalytic effects. Thickness of TiO_2 and TiO_2 :Tb thin films was equal to 377 nm and 585 nm, respectively. The amount of the terbium dopant has been analyzed using energy-dispersive spectrometer.

X-ray diffraction (XRD) measurements were performed with the aid of Dron-2 powder diffractometer with Fe-filtered $\text{Co K}\alpha$ radiation. Average crystallite sizes were determined using the standard Sheerer formula. Surface morphology of deposited samples was examined by atomic force microscope UHV VT AFM/STM Omicron operating in contact mode.

Optical properties of TiO_2 :Tb thin films were investigated on the basis of transmission spectra. Transmission is the basic parameter defining the transparency level of the thin films and is defined as the ratio of light passing through the sample to the light incident the sample.

Emission properties of TiO_2 :Tb thin films deposited on silica substrates were investigated by the photoluminescence (PL) method. For photoluminescence measurements UV argon laser with the excitation wavelength of 302 nm was used. Thin films were measured at room temperature.

The influence of terbium doping on photocatalytic properties of nanocrystalline TiO_2 thin films was estimated based on phenol decomposition reaction. The experimental setup consisted of a UV-Vis light source (6×20 W Phillips lamps with intensity of UV and Vis radiation: 183 W/m^2 and 167 W/m^2 , resp.) and cylindrical reservoir which contained 100 mL of solution with the phenol concentration of 10 mg/L. To avoid the heating of the solution, the reaction temperature was controlled by circulation of water through the jacket at constant temperature of ca. 15°C . All experiments were carried out under agitation with a magnetic stirrer operating at 500 rpm in order to provide a good mixing of the suspension. No external oxygen supply was used. The phenol concentration was calculated from the absorption peak at 270 nm by means of a calibration curve. After 30 minutes of premixing at constant temperature, lights were switched on to initiate the reaction. To determine the change of the phenol concentration, samples of phenol solutions were withdrawn regularly every 60 minutes for 5 hours from the reactor. The final transparent solution was poured into a quartz cuvette and analyzed by UV-Vis spectrophotometer, in the wavelength range of 200–700 nm.

3. Results

As it was mentioned above, doping with lanthanides can result in modification of structural properties of TiO_2 thin films in a wide range. The significant role plays the amount of the dopant incorporated into titanium dioxide matrix. By selection of the dopant amount the specified crystal structure of TiO_2 directly after deposition process can be obtained. In Figure 1 results of XRD measurements of undoped TiO_2 and TiO_2 :Tb deposited on silica substrates have been presented.

Broad peaks in the XRD patterns have shown that both thin films had nanocrystalline structure. Undoped TiO_2 have rutile structure with crystallites sizes of 8.7 nm. Doping with 2.6 at. % of terbium the TiO_2 matrix resulted in 25% decrease

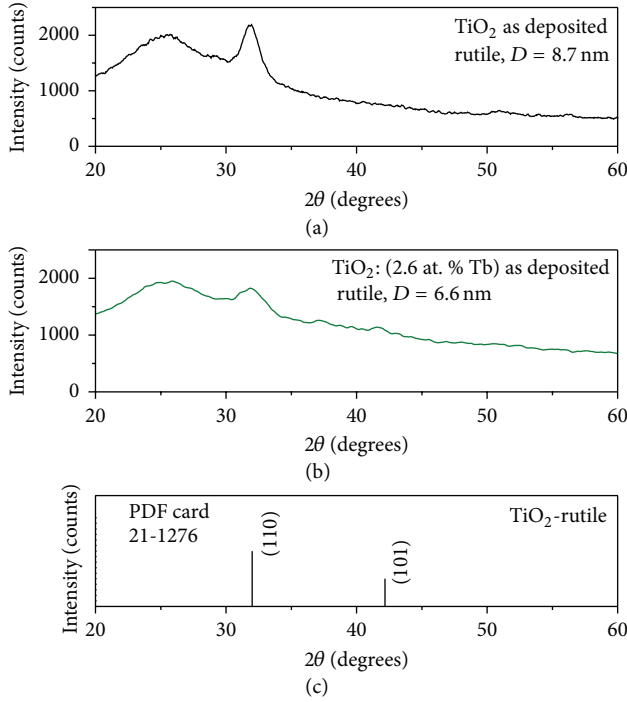


FIGURE 1: XRD measurements results of (a) undoped TiO₂ thin film, (b) TiO₂:Tb thin film, and (c) standard patterns for TiO₂-rutile structure. D : crystallite size.

of crystallites sizes to 6.6 nm; however, the structure was still the rutile [37, 39, 40]. No diffraction peaks of Tb or Tb-O compounds have been found. These indicate that Tb (or its compounds) particles were too small to be detected by XRD or that Tb ions were incorporated into TiO₂ nanocrystals. Taking into account the ionic radius of Tb³⁺ the latter is less probable. It is more reasonable to assume that Tb dopant is localized at the surface of TiO₂ nanocrystals.

Structure densification is clearly seen on AFM images presented in Figure 2. Despite nanocrystalline structure, as-deposited thin films are very homogenous with small surface roughness. Root mean square (RMS) value is 3 times lower in case of terbium-doped titanium dioxide in comparison to undoped matrix. It was 7.2 and 2.1 for TiO₂ and TiO₂:Tb thin films, respectively. Symmetrical shape of grains size histogram in Z direction testifies about homogenous distribution of grains in deposited thin films.

Influence of terbium doping on transparency of TiO₂ thin films was determined on the basis of transmission characteristics presented in Figure 3(a). Visible minima and maxima are connected with light interferences. Measurements have shown that the incorporation of Tb into TiO₂ matrix with the rutile structure has not changed significantly the transparency of the thin films. Moreover, doping has shifted the cutoff wavelength through longer wavelengths.

Transmission measurements results allow for estimation of absorption coefficient, and on this basis the width of optical energy gap (E_g^{opt}) has been determined. Characteristics, which were used to define optical energy gap, are presented

in Figure 3(b). Results have shown that lower E_g^{opt} value was obtained for TiO₂:Tb and was equal to 2.96 eV.

As the result of TiO₂ matrix excitation with ultraviolet illumination, the photoluminescence spectrum in wide emission range, from 350 to 800 nm, has been observed (Figure 4). This spectrum is the superposition of six emission lines of various wavelengths, which corresponds to radiative recombination of carriers from different energy levels. Characteristic emission lines of Tb³⁺ ions, which occur at the wavelength of: 418 nm, 431 nm, 491 nm, 545 nm, and 619, correspond to electron transitions between ⁵D₃-⁷F₅, ⁵D₃-⁷F₄, ⁵D₄-⁷F₆, ⁵D₄-⁷F₅, and ⁵D₄-⁷F₃ levels, respectively. Moreover, light emission at 370 nm is connected with defect states transitions of titanium dioxide. Photoluminescence of terbium ions in TiO₂ matrix with rutile structure is unique phenomenon. Sheng et al. [24] have confirmed that such unique phenomenon was obtained only by authors of current paper.

Kinetics of photocatalytic decomposition of organic compounds at the TiO₂ surface is usually consistent with Langmuire-Hinshelwood relationship [27, 41, 42]:

$$r = -\frac{dc}{dt} = \frac{kKc}{1 + Kc}, \quad (1)$$

where r is oxidizing rate, c is solution concentration, t is exposure time, k is reaction rate constant, and K is absorption coefficient.

For solutions with low initial concentration c_0 (at 10^{-3} mol level) the above equation can be simplified as follows [14, 28, 41]:

$$\ln\left(\frac{c_0}{c}\right) = k \cdot K \cdot t = k_{\text{RRC}} \cdot t \quad (2)$$

or

$$c_t = c_0 \cdot \exp(-k_{\text{RRC}}t), \quad (3)$$

where k_{RRC} is corrected reaction rate constant and c_t is solution concentration after time t .

The value of corrected reaction rate constant can be determined from slope of $\ln(c/c_0)$ characteristic in the function of light exposure t .

Results of phenol decomposition have shown that investigated thin films were photocatalytic. Photocatalytic activity was determined under the exposure to UV light based on dependence of $\ln(c/c_0)$ in time function. Measurement results for TiO₂ and TiO₂: (2.6 at. % Tb) thin films have been shown in Figure 5. Those results were used to calculate phenol decomposition as thin film's photocatalytic activity, which can be defined as

$$\frac{(c/c_0)}{p} \cdot 100\%, \quad (4)$$

where p is area of thin film.

By the reason of small sample size of approximately 1 cm², the phenol decomposition was estimated as %/cm². It has been found that the incorporation of 2.6 at. % of Tb has increased the photocatalytic activity more than two times as

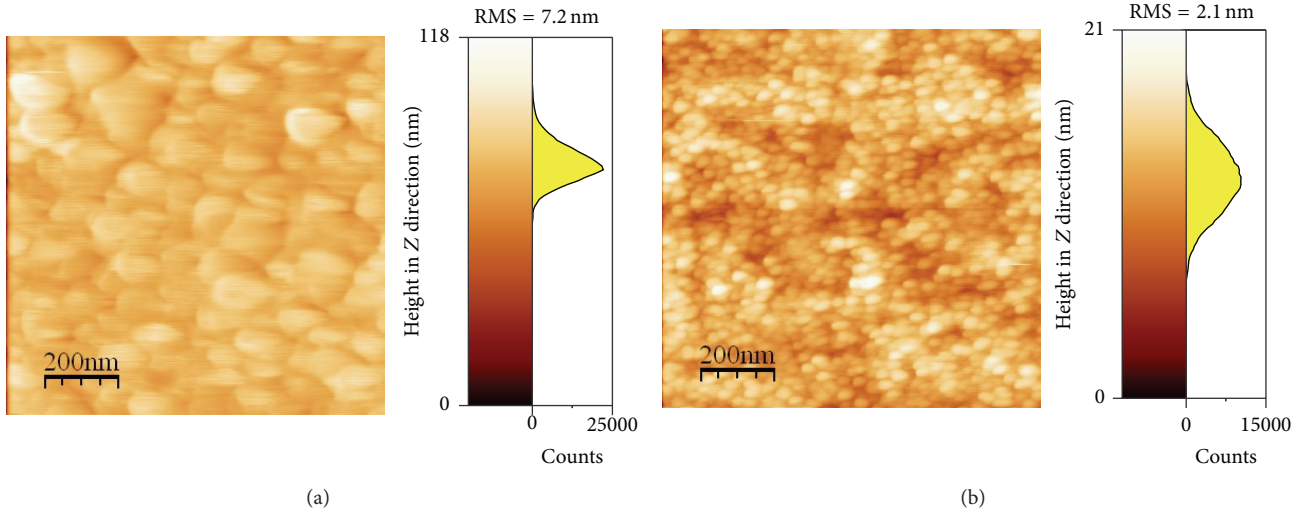


FIGURE 2: AFM images of (a) TiO_2 thin film and (b) $\text{TiO}_2\text{:Tb}$ thin film with height distribution of grains size in Z direction and surface roughness determined by RMS factor.

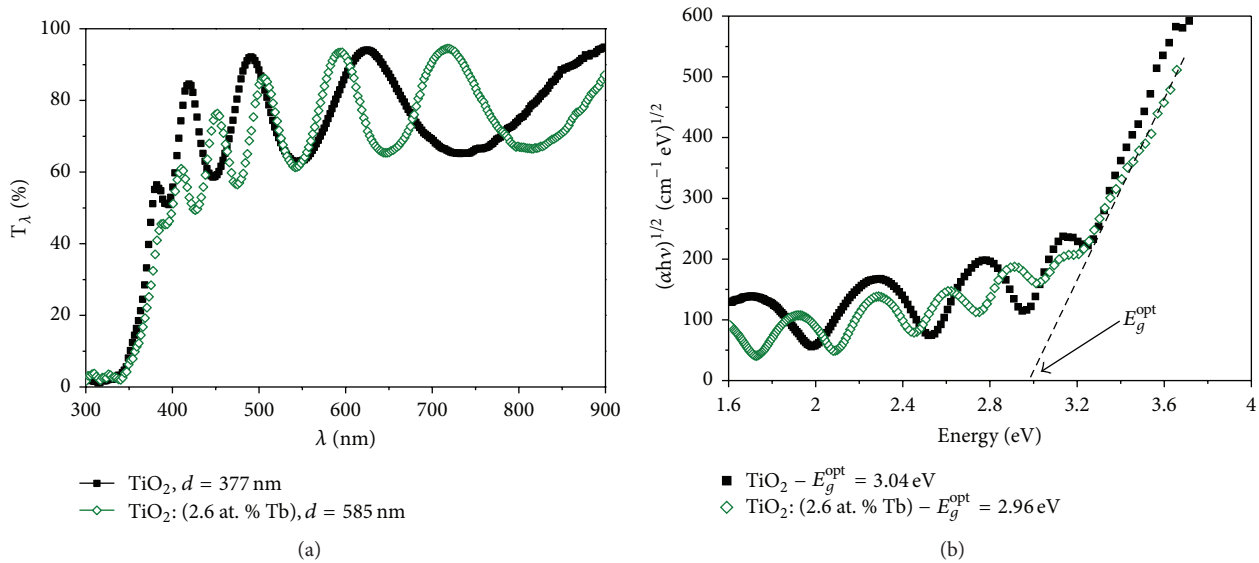


FIGURE 3: Optical properties of TiO_2 and $\text{TiO}_2\text{:Tb}$: (a) transmission characteristics and (b) Tauc plots for allowed indirect transitions. d : thin film thickness.

compared to undoped TiO_2 matrix. After five hours TiO_2 doped with terbium has decomposed ca. 4.7% of phenol, while, in the same time, undoped TiO_2 has decomposed just 2.2% of phenol. Such results are unique in case of TiO_2 with the rutile structure. Corrected reaction rate constant was also two times higher for $\text{TiO}_2\text{:Tb}$ in comparison to TiO_2 thin film.

4. Discussion

Nanocrystalline TiO_2 thin film doped with Tb exhibits photoluminescence properties and increased photocatalytic activity in comparison to undoped nanocrystalline TiO_2 thin film with rutile structure. From the state of the art it is

well known that materials with nanocrystalline structure composed of crystallites in size of less than 10 nm exhibit higher photoluminescence or photocatalytic activity as compared to materials with larger crystallites [43–45]. In case of materials with such nanocrystalline structure, the influence of quantum size effect on luminescence properties was first described by Bhargawa et al. [46]. According to the literature [43–45], both specific energy levels and the decrease of energy band gap in nanocrystalline oxide matrix can be observed as size of the crystallites is in the range from 2 to 10 nm. Size of the crystallites has an essential influence on series of different properties of metal oxides connected with the degree of the surface area development. Similarly, as in case of photoluminescence, also photocatalytic activity of the thin

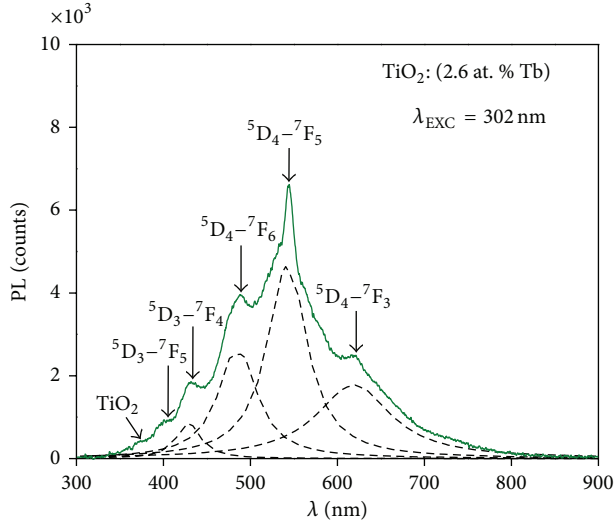


FIGURE 4: $\text{TiO}_2\text{:Tb}$ thin film photoluminescence spectrum under the excitation of Ar laser.

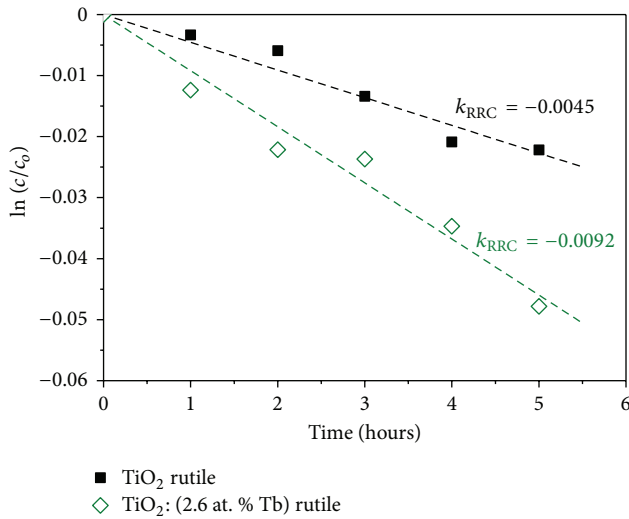


FIGURE 5: Photocatalytic activity of TiO_2 and $\text{TiO}_2\text{:Tb}$ thin films with rutile structure exposed to UV light time function based on dependence of $\ln(c/c_0)$.

films based on TiO_2 is the highest for matrix composed of crystallites in size that ranges from 5 to 10 nm [42, 43, 47].

In current state of the art only one article [25] can be found, which tries to describe mutual relationship between the photocatalysis and the photoluminescence. The key factor for conjunction of photoluminescence effect and the decomposition of pollutants, which proceeds at the surface of material, is the oxygen vacancies concentration [25]. These defects are the trapping centers, which inhibit recombination and simultaneously enables on efficient joining electrons with oxygen. Moreover, they are active centers for surface absorption of water particles and OH^- groups, which are necessary for carrying out of the photocatalytic reaction.

One of the main limits for these both effects is relatively low total quantum efficiency connected with high level of

recombination of the electron-hole pairs generated at the TiO_2 surface [25]. Therefore, increasing of light emission intensity or photocatalytic activity of thin films based on TiO_2 can be obtained by, for example, decrease of crystallites size [48, 49] or by doping [8, 50, 51]. It is because, for nanomaterials, diffusion rate is much larger than recombination rate. The most often, thin films with high photocatalytic activity exhibit weak photoluminescence effect, which is connected with low carriers recombination efficiency [52, 53]. However, in the current state of the art there are also examples of materials characterized by strong photoluminescence effect and high photocatalytic activity [54, 55]. It indicates that these results are inconsistent, and explanation of reasons of such different interpretations needs much more detailed analysis of carriers: excitation and recombination mechanisms. For $\text{TiO}_2\text{:}(2.6\% \text{ at. \% Tb})$ strong photoluminescence and high photocatalytic activity have been found simultaneously; hence, it is necessary to elaborate on the model, which takes into consideration the relationship between these two phenomena.

Explanation of relationship between photoluminescence effect and photocatalysis phenomenon needs the complex analysis of different types of recombination, which occurs in titanium dioxide [25, 56–59]. In such material, electrons and holes are generated under the photoexcitation. Photoexcited electrons transit to the conduction band and fill the energy levels, which correspond to excitation energy. These carriers can easily recombine and return to valence band in different ways, and their energy can be emitted as photons or phonons. Excited electrons can transit directly to valence band with release of energy in the form of light emission. This type of direct transitions can take place also in case of electrons with higher energy than E_g ; however, transfer of carriers proceeds then directly from levels situated above the bottom edge of conduction band. The recombination process can also occur via sublevels in energy band gap (defect states of the matrix) and it is an indirect radiative transition.

In case of photoluminescence effect, which is present as the result of direct radiative recombination, lower recombination of generated carriers causes the decrease of light emission intensity. However, this process simultaneously increases the photocatalytic activity of the semiconductor [53]. Whereas, in case of indirect radiative recombination, the relation between photoluminescence effect intensity and photocatalytic activity depends on the type of the incorporated dopant. According to Liqiang et al. [25], lower recombination cause smaller photoluminescence intensity and higher photocatalytic activity of semiconductor. Although, sometimes also the increase of defects amount and oxygen vacancies at the thin film surface allow to obtain higher intensity of photoluminescence and photocatalytic activity [25]. Such relations can be applied for analysis of TiO_2 thin films doped with rare earth elements, in which emission levels are below defect states of the matrix. For prepared $\text{TiO}_2\text{:}(2.6 \text{ at. \% Tb})$ thin film, none of the abovementioned explanations can be accepted as a basis for analysis of relation between photoluminescence and photocatalysis phenomena. Therefore, it was necessary to elaborate on individual model, which takes into consideration properties of prepared thin films and mechanisms occurring during both discussed processes.

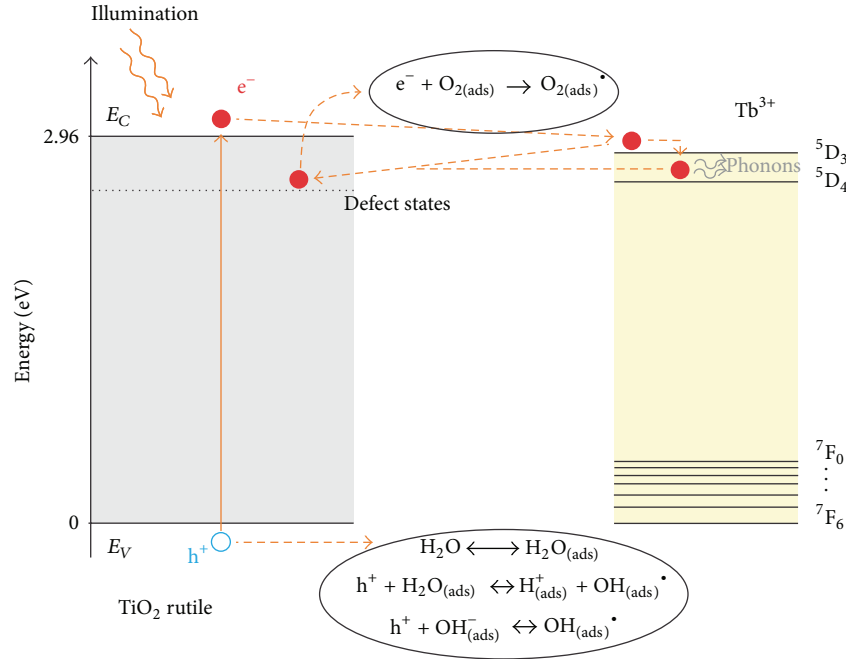


FIGURE 6: The scheme of processes proceeding at the $\text{TiO}_2\text{:Tb}$ surface with rutile structure. Designations: E_c , E_v , energy of the bottom edge of the conduction band and the top of the valence band, respectively; e^- , electron; h^+ , hole; O_2 , oxygen; O_2^* , oxygen radical; H_2O , water; H^+ , hydrogen; OH^- , hydroxide group; OH^* , hydroxide radical; (ads), surface adsorption.

The abovementioned processes proceed at the titanium dioxide nanograin surface with rutile structure. Under the exposure to light, generated electrons in matrix pass from the valence to conduction band and take part in reaction with oxygen adsorbed at the film surface, creating oxygen radicals (O_2^*) [28]. On the other hand, holes from valence band take part in reaction with water and hydroxide groups (OH^-) adsorbed at the surface. Consequently hydroxide radicals (OH^*) are formed [28]. Moreover, electrons trapped by the matrix's defect states also can take part in process of oxygen radicals formation, which is caused by considerably shorter time of diffusion than recombination in case of nanograins. In the following stages, at the surface of nanocrystalline film, the decomposition of contaminations proceeds with the participation of oxygen (O_2^*) and hydroxide (OH^*) radicals. Final products of these reactions are CO_2 and H_2O .

Doping TiO_2 matrix with 2.6 at. % of terbium allows obtaining thin film with photoluminescence properties, which exhibits two times higher photocatalytic activity as compared to undoped titanium dioxide. The incorporation of terbium dopant causes increase in the number of energy levels to which electrons generated in TiO_2 matrix can be transferred. Therefore, photocatalytic rate increases and favorably influences thin film activity. In Figure 6 scheme of processes proceeding at the $\text{TiO}_2\text{:Tb}$ surface with the rutile structure is presented.

In case of photocatalysis process, presence of terbium at the surface causes changes of the surface energy parameters. Both terbium ions on +3 and +4 oxidation states can accept and return electrons. Presence of these ions facilitates the

transfer of carriers, which is necessary in photocatalysis reaction.

Briefly, based on structural and optical properties analysis of the $\text{TiO}_2\text{:Tb}$ thin films, it was found that the incorporation of terbium dopant during high-energy reactive magnetron sputtering process allowed for preparing of homogenous, densely packed films, which were composed of crystallites in size of 6.6 nm. Such small crystallites sizes and significantly higher degree of order of film structure (in comparison to undoped titanium dioxide) favorably influence both discussed phenomena by the increasing of active area. Smaller crystallites size causes that the range of transition to make for electrons is also smaller [25, 42, 43]. Therefore, the probability of carrier transfer between the TiO_2 crystallites and Tb ions localized at the surface is large. Except nanocrystalline structure, the key role for both phenomena plays amount of the dopant, which should be incorporated into TiO_2 matrix in high-energy deposition process. It is necessary to incorporate the sufficient amount of the dopant to obtain the suitable number of the ions at the +3 oxidation state.

5. Conclusions

In present paper analysis of the influence of 2.6 at. % terbium dopant on the $\text{TiO}_2\text{:Tb}$ thin films properties has been outlined. Thin films deposited in high-energy reactive magnetron sputtering process were homogenous and densely packed. $\text{TiO}_2\text{:Tb}$ film had rutile structure with crystallites size of 6.6 nm.

Investigations of photocatalytic properties have shown that doping with terbium favorably influence the increase

of TiO_2 matrix surface activity. Moreover, based on optical properties analysis, it was found that terbium did not deteriorate the high transparency of TiO_2 , but influence the position shift of cutoff wavelength and width of optical band gap. The incorporation of terbium allowed for obtaining photoluminescence effect of Tb^{3+} in TiO_2 matrix with the rutile structure, which is unique and has not been reported yet by other authors. $\text{TiO}_2\text{:Tb}$ after 5 hours of the photocatalytic activity investigation has decomposed two times more phenol as compared to undoped TiO_2 .

Results of investigations have shown that, to increase the photocatalytic activity of $\text{TiO}_2\text{:Tb}$ thin films the presence of Tb^{3+} at the surface of TiO_2 nanocrystals is necessary. The addition of terbium to TiO_2 matrix caused that additional energy levels have appeared and favorably influenced energy transfer mechanism. Thanks to terbium doping of titanium dioxide, it was possible to obtain effective photoinduced carriers transfer mechanism, which is necessary requirement for the presence of both phenomena: photocatalysis and photoluminescence.

Acknowledgments

The authors would like to thank E. L. Prociow from Wrocław University of Technology for his help in the experimental part of this work. This work was financed from the sources granted by the NCN in the years 2011–2013 as a research project no. N N515 4963 40, in years 2013–2015 as a research project no. 2012/05/N/ST7/00173, and from the statute sources given by the MNiSW in the years 2012–2013.

References

- [1] H. Bieber, P. Gilliot, M. Gallart et al., "Temperature dependent photoluminescence of photocatalytically active titania nanopowders," *Catalysis Today*, vol. 122, no. 1-2, pp. 101–108, 2007.
- [2] U. Diebold, "The surface science of titanium dioxide," *Surface Science Reports*, vol. 48, pp. 53–229, 2003.
- [3] K. Eufinger, D. Poelman, H. Poelman, R. De Gryse, and G. B. Marin, "Photocatalytic activity of dc magnetron sputter deposited amorphous TiO_2 thin films," *Applied Surface Science*, vol. 254, no. 1, pp. 148–152, 2007.
- [4] A. Fujishima, T. N. Rao, and D. A. Tryk, "Titanium dioxide photocatalysis," *Journal of Photochemistry and Photobiology C*, vol. 1, no. 1, pp. 1–21, 2000.
- [5] G. Li, L. Chen, M. E. Graham, and K. A. Gray, "A comparison of mixed phase titania photocatalysts prepared by physical and chemical methods: the importance of the solid-solid interface," *Journal of Molecular Catalysis A*, vol. 275, no. 1-2, pp. 30–35, 2007.
- [6] Y. Xie and C. Yuan, "Transparent TiO_2 sol nanocrystal-lites mediated homogeneous-like photocatalytic reaction and hydrosol recycling process," *Journal of Materials Science*, vol. 40, no. 24, pp. 6375–6383, 2005.
- [7] T. L. Chen, Y. Furubayashi, Y. Hirose, T. Hitosugi, T. Shimada, and T. Hasegawa, "Anatase phase stability and doping concentration dependent refractivity in codoped transparent conducting TiO_2 films," *Journal of Physics D*, vol. 40, no. 19, article 026, pp. 5961–5964, 2007.
- [8] W. Choi, A. Termin, and M. R. Hoffmann, "The role of metal ion dopants in quantum-sized TiO_2 : correlation between photoreactivity and charge carrier recombination dynamics," *Journal of Physical Chemistry*, vol. 98, no. 51, pp. 13669–13679, 1994.
- [9] K. L. Frindell, M. H. Bartl, M. R. Robinson, G. C. Bazan, A. Popitsch, and G. D. Stucky, "Visible and near-IR luminescence via energy transfer in rare earth doped mesoporous titania thin films with nanocrystalline walls," *Journal of Solid State Chemistry*, vol. 172, no. 1, pp. 81–88, 2003.
- [10] J. Domaradzki, D. Kaczmarek, A. Borkowska et al., "Influence of annealing on the structure and stoichiometry of europium-doped titanium dioxide thin films," *Vacuum*, vol. 82, no. 10, pp. 1007–1012, 2008.
- [11] Y. Q. Hou, D. M. Zhuang, G. Zhang, M. Zhao, and M. S. Wu, "Influence of annealing temperature on the properties of titanium oxide thin film," *Applied Surface Science*, vol. 218, no. 1–4, pp. 97–105, 2003.
- [12] A. Podhorodecki, G. Zatoryb, J. Misiewicz, J. Domaradzki, D. Kaczmarek, and A. Borkowska, "Influence of annealing on europium photoexcitation doped into nanocrystalline titania film prepared by magnetron sputtering," *Journal of the Electrochemical Society*, vol. 156, no. 3, pp. H214–H219, 2009.
- [13] G. Feng, S. F. Wang, M. K. Lu et al., "Luminescent characteristics of Eu^{3+} in SnO_2 nanoparticles," *Optical Materials*, vol. 25, no. 1, pp. 59–64, 2004.
- [14] F. Gourbilleau, P. Choppinet, C. Dufour et al., "Emission of Er- and Si-doped silicate glass films obtained by magnetron co-sputtering," *Materials Science and Engineering B*, vol. 105, no. 1–3, pp. 44–47, 2003.
- [15] P. G. Kik and A. Polman, "Exciton-erbium energy transfer in Si nanocrystal-doped SiO_2 ," *Materials Science and Engineering*, vol. 81, no. 1–3, pp. 3–8, 2001.
- [16] K. Kuratani, M. Mizuhata, A. Kajinami, and S. Deki, "Synthesis and luminescence property of $\text{Eu}^{3+}/\text{ZrO}_2$ thin film by the liquid phase deposition method," *Journal of Alloys and Compounds*, vol. 408–412, pp. 711–716, 2006.
- [17] Z. Liu, J. Zhang, B. Han et al., "Solvothermal synthesis of mesoporous $\text{Eu}_2\text{O}_3\text{-TiO}_2$ composites," *Microporous and Mesoporous Materials*, vol. 81, no. 1–3, pp. 169–174, 2005.
- [18] A. Peng, E. Xie, C. Jia, R. Jiang, and H. Lin, "Photoluminescence properties of $\text{TiO}_2\text{:Eu}^{3+}$ thin films deposited on different substrates," *Materials Letters*, vol. 59, no. 29–30, pp. 3866–3869, 2005.
- [19] B. Schaudel, P. Goldner, M. Prassas, and F. Auzel, "Cooperative luminescence as a probe of clustering in Yb^{3+} doped glasses," *Journal of Alloys and Compounds*, vol. 300, pp. 443–449, 2000.
- [20] M. Sendova-Vassileva, M. Nikolaeva, D. Dimova-Malinovska, M. Tzolov, and J. C. Pivin, "Room-temperature photoluminescence from Tb^{3+} ions in SiO_2 and a-SiC:H thin films deposited by magnetron co-sputtering," *Materials Science and Engineering B*, vol. 81, no. 1–3, pp. 185–187, 2001.
- [21] D. Kaczmarek, J. Domaradzki, A. Borkowska, A. Podhorodecki, J. Misiewicz, and K. Sieradzka, "Optical emission from Eu, Tb, Nd luminescence centers in TiO_2 prepared by magnetron sputtering," *Optica Applicata*, vol. 37, no. 4, pp. 433–438, 2007.
- [22] J. Domaradzki, E. L. Prociow, D. Kaczmarek et al., "X-ray, optical and electrical characterization of doped nanocrystalline titanium oxide thin films," *Materials Science and Engineering B*, vol. 109, no. 1–3, pp. 249–251, 2004.
- [23] J. Domaradzki, D. Wojcieszak, E. Prociow, and D. Kaczmarek, "Characterization of transparent and nanocrystalline $\text{TiO}_2\text{:Nd}$

- thin films prepared by magnetron sputtering," *Acta Physica Polonica A*, vol. 116, pp. S75–S77, 2009.
- [24] Y. Sheng, L. Zhang, H. Li et al., "Photoluminescence of TiO_2 films co-doped with $\text{Tb}^{3+}/\text{Gd}^{3+}$ and energy transfer from $\text{TiO}_2/\text{Gd}^{3+}$ to Tb^{3+} ions," *Thin Solid Films*, vol. 519, no. 22, pp. 7966–7970, 2011.
 - [25] J. Liqiang, Q. Yichun, W. Baiqi et al., "Review of photoluminescence performance of nano-sized semiconductor materials and its relationships with photocatalytic activity," *Solar Energy Materials and Solar Cells*, vol. 90, no. 12, pp. 1773–1787, 2006.
 - [26] A. Fujishima, X. Zhang, and D. A. Tryk, " TiO_2 photocatalysis and related surface phenomena," *Surface Science Reports*, vol. 63, no. 12, pp. 515–582, 2008.
 - [27] H. Ohsaki, N. Kanai, Y. Fukunaga, M. Suzuki, T. Watanabe, and K. Hashimoto, "Photocatalytic properties of $\text{SnO}_2/\text{TiO}_2$ multilayers," *Thin Solid Films*, vol. 502, no. 1–2, pp. 138–142, 2006.
 - [28] U. I. Gaya and A. H. Abdullah, "Heterogeneous photocatalytic degradation of organic contaminants over titanium dioxide: a review of fundamentals, progress and problems," *Journal of Photochemistry and Photobiology C*, vol. 9, no. 1, pp. 1–12, 2008.
 - [29] L. Chen, M. E. Graham, G. Li, and K. A. Gray, "Fabricating highly active mixed phase TiO_2 photocatalysts by reactive DC magnetron sputter deposition," *Thin Solid Films*, vol. 515, no. 3, pp. 1176–1181, 2006.
 - [30] M. Gómez, J. Rodríguez, S.-E. Lindquist, and C. G. Granqvist, "Photoelectrochemical studies of dye-sensitized polycrystalline titanium oxide thin films prepared by sputtering," *Thin Solid Films*, vol. 342, no. 1, pp. 148–152, 1999.
 - [31] C. H. Heo, S.-B. Lee, and J. H. Boo, "Deposition of TiO_2 thin films using RF magnetron sputtering method and study of their surface characteristics," *Thin Solid Films*, vol. 475, no. 1–2, pp. 183–188, 2005.
 - [32] E. P. Lokshin and T. A. Sedneva, "On stabilization of anatase with the fluoride ion," *Russian Journal of Applied Chemistry*, vol. 79, no. 8, pp. 1220–1224, 2006.
 - [33] M. D. Stamate, "On the non-linear I - V characteristics of dc magnetron sputtered TiO_2 thin films," *Applied Surface Science*, vol. 205, no. 1–4, pp. 353–357, 2003.
 - [34] S. F. Wang, Y. F. Hsu, and Y. S. Lee, "Microstructural evolution and optical properties of doped TiO_2 films prepared by RF magnetron sputtering," *Ceramics International*, vol. 32, no. 2, pp. 121–125, 2006.
 - [35] J. Domaradzki, D. Kaczmarek, E. L. Prociow, and Z. J. Radzinski, "Study of structure densification in TiO_2 coatings prepared by magnetron sputtering under low pressure of oxygen plasma discharge," *Acta Physica Polonica A*, vol. 120, no. 1, pp. 49–52, 2011.
 - [36] D. Kaczmarek, E. Prociów, J. Domaradzki, A. Borkowska, W. Mielcarek, and D. Wojcieszak, "Influence of substrate type and its placement on structural properties of TiO_2 thin films prepared by the high energy reactive magnetron sputtering method," *Materials Science-Poland*, vol. 26, no. 1, pp. 113–117, 2008.
 - [37] D. Kaczmarek, D. Wojcieszak, J. Domaradzki et al., "Influence of nanocrystalline structure and composition on hardness of thin films based on TiO_2 ," *Central European Journal of Physics*, vol. 9, no. 2, pp. 349–353, 2011.
 - [38] R. Wasielewski, J. Domaradzki, D. Wojcieszak et al., "Surface characterization of TiO_2 thin films obtained by high-energy reactive magnetron sputtering," *Applied Surface Science*, vol. 254, no. 14, pp. 4396–4400, 2008.
 - [39] J. Domaradzki, D. Kaczmarek, E. Prociów et al., "Study of structural and optical properties of $\text{TiO}_2:\text{tb}$ thin films prepared by high energy reactive magnetron sputtering method," *Optica Applicata*, vol. 39, no. 4, pp. 815–823, 2009.
 - [40] D. Kaczmarek, J. Domaradzki, D. Wojcieszak et al., "Structural investigations of $\text{TiO}_2:\text{Tb}$ thin films by X-ray diffraction and atomic force microscopy," *Applied Surface Science*, vol. 254, no. 14, pp. 4303–4307, 2008.
 - [41] I. K. Konstantinou and T. A. Albanis, "Photocatalytic transformation of pesticides in aqueous titanium dioxide suspensions using artificial and solar light: intermediates and degradation pathways," *Applied Catalysis B*, vol. 42, no. 4, pp. 319–335, 2003.
 - [42] A. Mills and S. Le Hunte, "An overview of semiconductor photocatalysis," *Journal of Photochemistry and Photobiology A*, vol. 108, no. 1, pp. 1–35, 1997.
 - [43] H. R. Kim, T. G. Lee, and Y. G. Shul J, "Photoluminescence of La/Ti mixed oxides prepared using sol-gel process and their pCBA photodecomposition," *Journal of Photochemistry and Photobiology A*, vol. 185, no. 2–3, pp. 156–160, 2007.
 - [44] T. Y. Wei, C. Y. Kuo, Y. J. Hsu, S. Y. Lu, and Y. C. Chang, "Tin oxide nanocrystals embedded in silica aerogel: photoluminescence and photocatalysis," *Microporous and Mesoporous Materials*, vol. 112, no. 1–3, pp. 580–588, 2008.
 - [45] M. Zalewska and A. M. Klonkowski, "Energy transfer from TiO_2 nanocrystals to Tb^{3+} ions incorporated into silica," *Optical Materials*, vol. 30, no. 5, pp. 725–729, 2008.
 - [46] R. N. Bhargawa, D. Gallagher, X. Hong, and A. Nurmiikko, "Optical properties of manganese-doped nanocrystals of ZnS ," *Physical Review Letters*, vol. 72, no. 3, pp. 416–419, 1994.
 - [47] K. M. Reddy, C. V. G. Reddy, and S. V. Manorama, "Preparation, characterization, and spectral studies on nanocrystalline anatase TiO_2 ," *Journal of Solid State Chemistry*, vol. 158, no. 2, pp. 180–186, 2001.
 - [48] A. J. Maira, K. L. Yeung, C. Y. Lee, P. L. Yue, and C. K. Chan, "Size effects in gas-phase photo-oxidation of trichloroethylene using nanometer-sized TiO_2 catalysts," *Journal of Catalysis*, vol. 192, no. 1, pp. 185–196, 2000.
 - [49] Z. Xu, J. Shang, C. Liu, C. Kang, H. Guo, and Y. Du, "The preparation and characterization of TiO_2 ultrafine particles," *Materials Science and Engineering B*, vol. 63, no. 3, pp. 211–214, 1999.
 - [50] J. Soria, J. C. Conesa, V. Augugliaro, L. Palmisano, M. Schiavello, and A. Sclafani, "Dinitrogen photoreduction to ammonia over titanium dioxide powders doped with ferric ions," *Journal of Physical Chemistry*, vol. 95, no. 1, pp. 274–282, 1991.
 - [51] J. C. Yu, J. G. Yu, K. W. Ho, Z. T. Jiang, and L. Z. Zhang, "Effects of F^- Doping on the photocatalytic activity and microstructures of nanocrystalline TiO_2 powders," *Chemistry of Materials*, vol. 14, no. 9, pp. 3808–3816, 2002.
 - [52] X. Z. Li, F. B. Li, C. L. Yang, and W. K. Ge J, "Photocatalytic activity of WO_x - TiO_2 under visible light irradiation," *Journal of Photochemistry and Photobiology A*, vol. 141, no. 2–3, pp. 209–217, 2001.
 - [53] J. G. Yu, H. G. Yu, B. Chen, X. J. Zhao, J. C. Yu, and W. K. Ho J, "calcination temperature on the surface microstructure and photocatalytic activity of TiO_2 thin films prepared by liquid phase deposition," *The Journal of Physical Chemistry B*, vol. 107, no. 50, pp. 13871–13879, 2003.
 - [54] J. Liqiang, S. Xiaojun, X. Baifu, W. Baiqi, C. Weimin, and F. Honggang, "The preparation and characterization of la doped TiO_2 nanoparticles and their photocatalytic activity," *Journal of Solid State Chemistry*, vol. 177, no. 10, pp. 3375–3382, 2004.

- [55] L. Q. Jing, F. L. Yuan, H. G. Hou, B. F. Xin, W. M. Cai, and H. G. Fu, "Relationships of surface oxygen vacancies with photoluminescence and photocatalytic performance of ZnO nanoparticles," *Science China Chemistry*, vol. 48, no. 1, pp. 25–30, 2005.
- [56] M. R. Hoffmann, S. T. Martin, W. Choi, and D. W. Bahnemann, "Environmental applications of semiconductor photocatalysis," *Chemical Reviews*, vol. 95, no. 1, pp. 69–96, 1995.
- [57] A. L. Linsebigler, G. Lu, and J. T. Yates, "Photocatalysis on TiO₂ surfaces: principles, mechanisms, and selected results," *Chemical Reviews*, vol. 95, no. 3, pp. 735–758, 1995.
- [58] M. I. Litter, "Heterogeneous photocatalysis: transition metal ions in photocatalytic systems," *Applied Catalysis B*, vol. 23, no. 2-3, pp. 89–114, 1999.
- [59] D. Wojcieszak, D. Kaczmarek, J. Domaradzki, E. Prociów, A. W. Morawski, and M. Janus, "Photocatalytic properties of nanocrystalline TiO₂ thin films doped with Tb," *Central European Journal of Physics*, vol. 9, no. 2, pp. 354–359, 2011.

Research Article

Release of Volatile Compounds from Polymeric Microcapsules Mediated by Photocatalytic Nanoparticles

J. Marques,¹ L. F. Oliveira,¹ R. T. Pinto,¹ P. J. G. Coutinho,¹ P. Parpot,² J. R. Góis,³
J. F. J. Coelho,³ F. D. Magalhães,⁴ and C. J. Tavares¹

¹ Centre of Physics, University of Minho, 4800-058 Guimarães, Portugal

² Centre of Chemistry, University of Minho, 4710-057 Braga, Portugal

³ Chemical Engineering Department, Polo II, University of Coimbra, 3030-790 Coimbra, Portugal

⁴ LEPAE, Chemical Engineering Department, Faculty of Engineering, University of Porto, Rua Dr. Roberto Frias s/n, 4200-465 Porto, Portugal

Correspondence should be addressed to C. J. Tavares; ctavares@fisica.uminho.pt

Received 14 January 2013; Accepted 24 January 2013

Academic Editor: Jiaguo Yu

Copyright © 2013 J. Marques et al. This is an open access article distributed under the Creative Commons Attribution License, which permits unrestricted use, distribution, and reproduction in any medium, provided the original work is properly cited.

In this study we propose a suitable method for the solar-activated controlled release of volatile compounds from polymeric microcapsules bonded with photocatalytic nanoparticles. These reservoirs can find applications, for example, in the controlled release of insecticides, repellents, or fragrances, amongst other substances. The surfaces of the microcapsules have been functionalized with TiO₂ nanoparticles. Upon ultraviolet irradiation, redox mechanisms are initiated on the semiconductor surface resulting in the dissociation of the polymer chains of the capsule wall and, finally, volatilization of the encapsulated compounds. The quantification of the output release has been performed by gas chromatography analysis coupled with mass spectroscopy.

1. Introduction

Microencapsulation and release has been an area of growing interest in the last years due to the many application perspectives, like in pharmaceutical products for drug controlled release, such as of insulin and other proteins, or cosmetics [1–3]. Different approaches of microencapsulation have been reported in the last decade. The complex coacervation method is a technique that has been used to produce polymeric microcapsules [4, 5]. This process uses the interaction of different polymers with opposite charges to form insoluble complexes and originate a phase separation. The encapsulation is achieved by the deposition of such complexes around a hydrophobic core. Despite the simple fabrication and ease of use in time-release and thermal-release applications, this method presents a significant number of disadvantages like wide-size distributions, weak shell wall, and low kinetics of shell wall formation [6, 7]. Solvent evaporation is one of the most popular processes to achieve encapsulation. A core material, solid or liquid, and capsule wall material

are mixed in a water-immiscible solvent and the resulting solution is emulsified in an aqueous solution [8, 9]. After solvent evaporation, the solid microcapsules are produced. However this method requires quite complex processes and is expensive. Hence, interfacial polymerization emerged as an easy method to prepare microcapsules. It allows a high degree of control over the physical/chemical properties using mild reaction conditions [10]. This method involves the condensation reaction between two monomers dissolved in immiscible solvents at the interface, creating a thin polymer film. Due to its intrinsic advantages, this method was used in this work and the relationship between the properties of the water/oil phase and the polymeric capsule wall was carefully studied. It is well known that the experimental conditions are an important factor for controlling shape, permeability, and physical properties of the microcapsule [11, 12]. Dodecane was used as oil phase and also as model organic volatile compound in which acyl chloride monomer was dissolved. An amine was dissolved in the water phase, resulting in the

formation of polyamide film at the interface; as exemplified in Figure 1 [13].

The immobilization of titanium dioxide nanoparticles in microcapsules can offer a wide range of practical applications and combines the main advantages of photocatalytic reactions with the possibility of controlled release by solar activation. These photoactive nanomaterials can be deposited onto several types of surfaces, including tents, curtains, and windows, amongst other surfaces [14]. Semiconductor photocatalysts have attracted a great deal of attention because of their potential applications for removing toxic organic and inorganic pollutants [15, 16].

The main objective of this work was to produce polymeric microreservoir systems for the controlled release of volatile compounds (e.g., insecticides, deodorants, fragrances, etc.) upon solar activation. The TiO_2 nanoparticles were synthesized by a modified sol-gel method and its microstructure was characterized by X-ray diffraction for different calcination temperatures. The controlled release of the encapsulated dodecane was studied in the presence of TiO_2 catalysts with and without ultraviolet (UV) irradiation. In order to extend the semiconductor absorbance into the visible light region, aiming to reduce the semiconductor band gap, the TiO_2 nanoparticles were doped with nitrogen anions [17].

2. Experimental

2.1. Materials. Titanium (IV) isopropoxide (>99%, Sigma-Aldrich), propyl alcohol (>98%, Sigma-Aldrich), triethylamine (>99%, Sigma-Aldrich), hydrochloric acid (37%, Sigma), poly(vinyl alcohol) (>98%, Sigma-Aldrich), ethylenediamine (>99.5%, Sigma-Aldrich), dodecane (>99%, Sigma-Aldrich), and sebacoyl chloride (>95%, Sigma-Aldrich) were used as received. Commercial TiO_2 P25 powder was purchased from Degussa and used as reference photocatalytic material.

2.2. Synthesis of the N-Doped TiO_2 Powders. The N-doped TiO_2 nanoparticles were synthesized by a modified sol-gel method [18]. Triethylamine was used as nitrogen source for the attempted anionic doping of the TiO_2 lattice. In a typical procedure, a solution was prepared with water and propyl alcohol (1:10) at pH 2.4 (adjusted by addition of HCl). N-doped TiO_2 nanoparticles were prepared by dissolving 1 mL of titanium isopropoxide in 1.25 mL of solution under vigorous stirring followed by a dropwise addition of 3 mL of nitrogen precursor. The reaction was carried out under gentle stirring for two days to attain the particle doped with nitrogen.

After the sol-gel synthesis, the N-doped TiO_2 nanoparticles were collected by repeated centrifugation and washed with propyl alcohol. Amorphous powders were first annealed at 80°C in a conventional electric oven for 8 h and later calcined at 300°C, 500°C, 700°C, and 800°C during 2 h to produce nanometric powders. The resulting samples were named considering the calcination temperature as NP300,

NP500, NP700, and NP800, respectively. The sample without any thermal treatment was identified as NPRT.

2.3. Photocatalytic Activity. The photocatalytic oxidation of methylene blue (MB) in the presence of the N-doped TiO_2 nanoparticles under UV irradiation was investigated in order to evaluate the photocatalytic activity at different calcination temperatures [19–22]. The same procedure was performed for the reference TiO_2 P25 powder.

In a typical experiment, 2 mg of photocatalyst was suspended in aqueous methylene blue solution (10^{-5} M) in a quartz cell (40 mm × 40 mm × 10 mm) at pH 7.2 [23, 24]. The suspension was irradiated with a high power LED source (Thorlabs, 700 mA) with an excitation centered at 365 nm (UV-A). The averaged irradiance was $\sim 4 \text{ mW} \cdot \text{cm}^{-2}$.

The absorbance of the MB was monitored at intervals of 5 min using a spectrophotometer (ScanSpec UV-Vis, ScanSci) in the range of 300–900 nm. The rate of photodegradation of MB was analyzed by monitoring the intensity variation of the main absorption peak at 665 nm.

The kinetics of photocatalytic degradation of MB is a pseudo-first-order reaction and can be expressed according to the equation [24, 25]:

$$\ln \left(\frac{C}{C_0} \right) = -kt, \quad (1)$$

where C represents the dye's concentration at the time t , which is proportional to its optical absorbance, and k is the first-order rate constant of the reaction.

2.4. Detection of Hydroxyl Radicals. Photoluminescence technique (PL) was used for the detection of hydroxyl radicals ($\cdot\text{OH}$) produced during the photocatalysis reaction. Coumarin was chosen as molecular probe, which readily reacted with $\cdot\text{OH}$ radicals to produce a highly fluorescent subproduct, 7-hydroxycoumarin (7HC), which shows a strong PL signal at 456 nm [26]. At room temperature, 5 mg of photocatalyst powder was dispersed in 4 mL of 10^{-3} M coumarin aqueous solution in a quartz cell (40 mm × 10 mm × 10 mm). The pH was adjusted to 3.3 with a HCl 0.1 M solution. Initially, the coumarin solution with the modified N- TiO_2 and reference P25 particles was kept in dark for 30 min to establish adsorption-desorption equilibrium. After this stabilization period, and at given intervals of UV irradiation, the suspension was centrifuged and then analyzed on a FluoroLog-3 fluorescence spectrophotometer with an excitation wavelength of 332 nm. The measurements were performed at room temperature and the emission and excitation slits were set to 2.0 nm.

2.5. Polymeric Microcapsules. The microcapsules were prepared by using an adapted method based on interfacial polycondensation in an ultrasonic bath at a frequency of 30 kHz [13, 27, 28]. The encapsulation of dodecane into the microcapsules was achieved by the reaction between sebacoyl chloride and ethylenediamine, in presence of poly(vinyl) alcohol (PVA) as a surfactant. 415 μL (6.2×10^{-3} mol) of

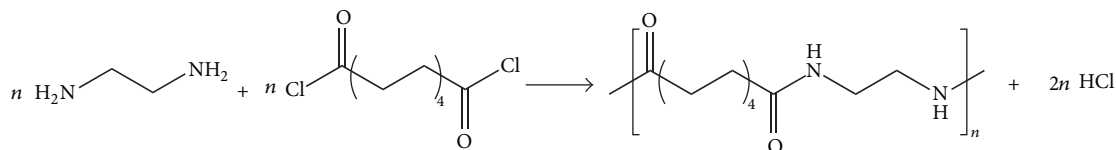


FIGURE 1: Scheme of the polymerization reaction.

ethylenediamine was added to the 25 mL of the 2% PVA solution. In the organic phase, 1.5 mL of dodecane and 265 μL (1.2×10^{-3} mol) of sebacyl chloride were added drop by drop to the previous solution. The water/oil emulsion was emulsified for 5 min under the same ultrasonic conditions followed by 5 minutes under magnetic stirring at 300 rpm. The resulting microcapsules were rinsed several times with deionized water to remove the unreacted amine.

2.5.1. Characterization Methods. The gas chromatography coupled with mass spectrometry (GC-MS) analysis of dodecane output release from within the microcapsules was performed using a Varian 4000 Performance apparatus, equipped with a CP8944 VF-5 column and an ion trap mass spectrometer as detector. The carrier gas was helium, at a flow rate of $1 \text{ mL} \cdot \text{min}^{-1}$. Column temperature was initially 40°C , and then gradually increased to 270°C at $8^\circ\text{C} \cdot \text{min}^{-1}$. For GC-MS detection an electron impact ionization system was used with ionization energy of 70 eV.

The crystalline structure of the photocatalysts was characterized by X-ray diffraction analysis (XRD, Bruker D8 Discover diffractometer) using $\text{Cu K}\alpha$ radiation. The morphological properties of microcapsules were studied using a scanning electron microscope (SEM, NanoSEM-FEI Nova 200) at SEMAT/UM. Fourier-transform infrared spectroscopy (FTIR) of vacuum-dried microcapsules loaded with optimized N-doped TiO_2 nanoparticles (at 30°C for 5 days) was performed at 132 scans and with a 4 cm^{-1} resolution between 500 and 4000 cm^{-1} , using a JASCO 4200 FTIR spectrophotometer, operating in the ATR mode (MKII Golden Gate Single Reflection ATR System).

3. Results and Discussion

3.1. XRD Analysis. Figure 2 shows the XRD patterns of the prepared N-doped TiO_2 photocatalyst powders annealed at 300, 500, 700, and 800°C . The powders without calcination (curve a) exhibit an amorphous structure, with only minor traces of the most prominent anatase diffraction peaks. Therefore, the thermal treatment process is necessary to convert the amorphous TiO_2 into a crystallized structure. For samples annealed at 300°C (curve b), clear diffraction peaks appear at 25.2° and 37.8° , which are attributed to (101) and (004) lattice planes of the anatase structure, revealing the formation of crystalline anatase phase at an early stage of the heat treatment; the peak observed at 35° is ascribed to Ti (100) planes. At this temperature no evidence of rutile

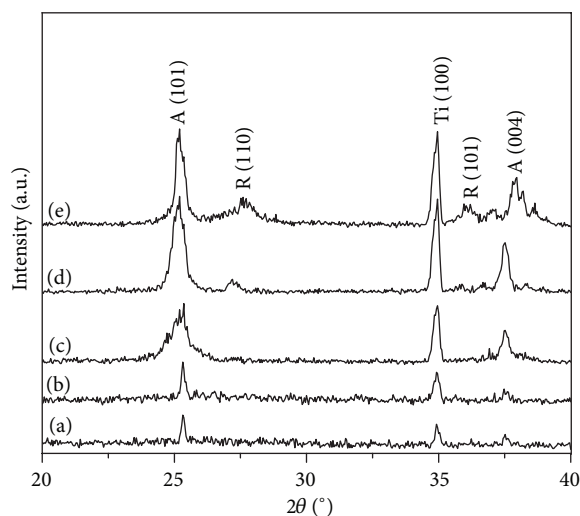


FIGURE 2: XRD patterns of the N-doped TiO_2 powders calcined at (a) room temperature (b) 300°C (c) 500°C (d) 700°C , and (e) 800°C . A: anatase; R: rutile.

phase is discerned. Moreover, upon increasing the calcination temperature, the intensity of these anatase diffraction peaks also increases. However, for the highest temperature of 800°C (NP800—curve e) the diffraction peak associated with the rutile phase (110) at 27.5° is more prominent, albeit lower than anatase preferential growth, indicating the starting transition of anatase phase to a more stable rutile phase. The diffraction pattern obtained for sample NP700 (curve d) is similar to the reference P25 material (not shown). The anatase average crystallite domain size varies very little with calcination temperature, increasing from 30 nm in its as-synthesized state to 50 nm for the highest temperature thermal treatment. At 800°C the rutile domain size is smaller than that corresponding to anatase, having a value of $\sim 37 \text{ nm}$.

3.2. Evaluation of the Photocatalytic Activity of the TiO_2 Powders

3.2.1. Adsorption of Methylene Blue on TiO_2 Nanopowders. Comparative studies of the adsorption of methylene blue on the synthesized nanocatalyst powders were performed. A solution of methylene blue (10^{-5} M) was stirred with the different TiO_2 nanoparticles ($0.15 \text{ g} \cdot \text{L}^{-1}$) in the dark to ensure complete surface adsorption of dye. The change in methylene blue concentration was investigated by monitoring the

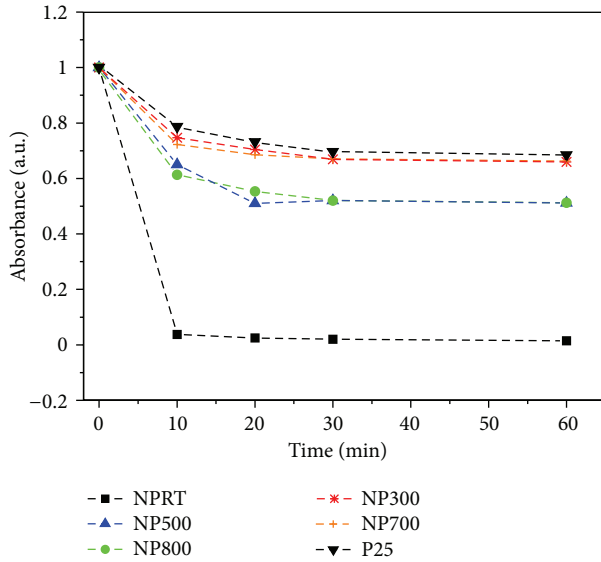


FIGURE 3: UV-vis absorption variation at 665 nm measured in the dark of MB (10^{-5} M, pH 7.2) solution as a function of time for nano- TiO_2 powders annealed at different temperatures. This experiment has also been performed for the P25 reference powder.

maximum of absorbance of this dye at 665 nm, as plotted in Figure 3. An important change can be observed after 10 minutes, where the absorbance of methylene blue drops from 2.33 to values lower than 1.85, approximately 20% of the initial concentration value.

These results indicate that the TiO_2 nanoparticles strongly adsorb the methylene blue molecules at the surface. This can be explained by the pH effect on methylene blue/ TiO_2 nanoparticle suspensions. The pH of the solution influences significantly the characteristics of the TiO_2 surface charge. Point of zero charge (PZC) is the value of pH at which the surface charge is zero. The knowledge of PZC of titania (PZC = 6.8) helps to predict the type and nature of the charge transfer that occurs preferentially. Since the photocatalytic assays were performed at pH higher than the reference PZC of titania, the surface of TiO_2 nanoparticles has a negative charge and there is an electrostatic adsorption between negative-charged surfaces of TiO_2 and methylene blue cations that carry a positive charge (2) [29–31]:



Thus, Figure 3 further indicates that 30 minutes was sufficient to reach the adsorption equilibrium between methylene blue and TiO_2 nanoparticles. Therefore, for all photocatalytic experiments, the dye solutions with TiO_2 nanoparticles were first stirred in the dark for 30 min before UV-A irradiation assays.

3.2.2. Photocatalysis Assays. The photocatalytic reaction is very sensitive to the catalyst surface. The MB reacts with electrons and superoxide anions generated on the modified TiO_2 particles under UV irradiation. The photocatalytic degradation reactions of MB on UV were investigated using

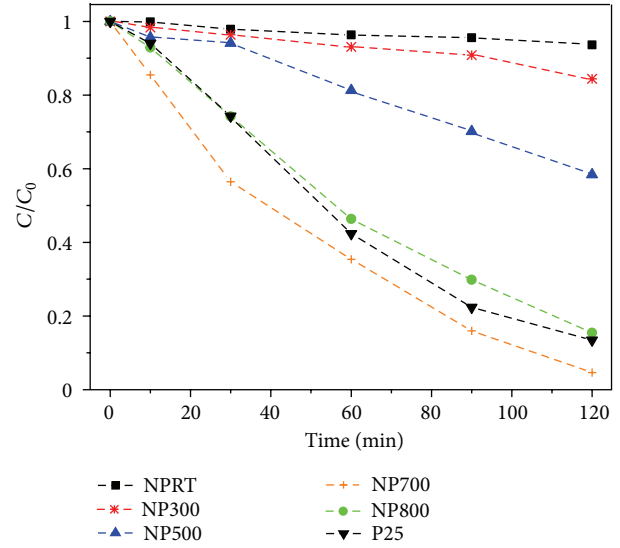


FIGURE 4: Photodegradation of MB (10^{-5} M, pH 7.2) solution as a function of UV-A irradiation time for TiO_2 powders annealed at different temperatures and reference P25.

TABLE 1: Rate constant (k) and degradation (%) of the MB (10^{-5} M, pH 7.2) solution for TiO_2 powders annealed at different temperatures.

Samples	k values (min^{-1})	Degradation (%) of MB solution after 120 min.
NPRT	—	2
NP300	1.6×10^{-3}	16
NP500	6.0×10^{-3}	40
NP700	2.4×10^{-2}	95
NP800	1.5×10^{-2}	85
TiO_2 P25	1.7×10^{-2}	88

the prepared N-doped TiO_2 powders at different calcination temperature. In order to compare their UV light activities, the experiments were also carried out using the TiO_2 powders without thermal treatment and the reference TiO_2 P25 in the same way as using the N-doped TiO_2 . The evolution of MB concentration with time for each sample at 665 nm is presented in Figure 4.

The photocatalytic degradation is a pseudo-first-order reaction and its kinetics, k values (1), and the degradation (%) of MB showing the catalytic activity of each sample are given in Table 1. Although MB was quickly degraded during UV-A irradiation for all the nanoparticles with thermal treatment, it is evident that NP700 showed the highest photocatalytic activity. The increased photocatalytic efficiency of the powders annealed at higher temperatures can be related to the surface morphology and crystal structure. This effect is attributed to the higher content of the crystalline anatase phase for the samples calcined at 700°C compared to those at 300 and 500°C . According to the XRD results, the phase transformation from amorphous TiO_2 to anatase was not complete at 300°C . At 800°C , some of

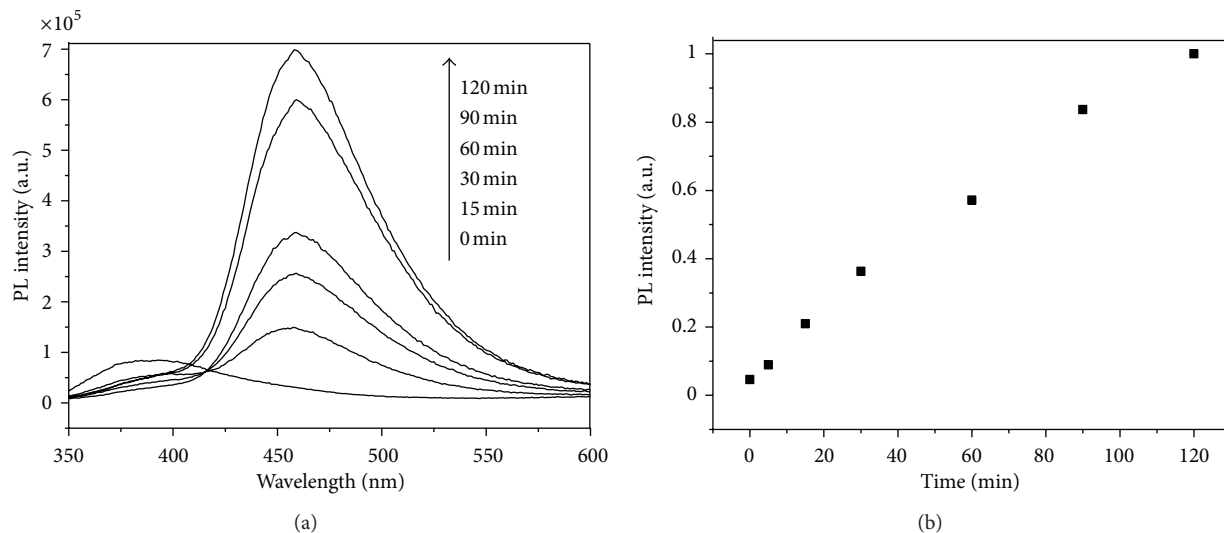
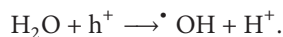
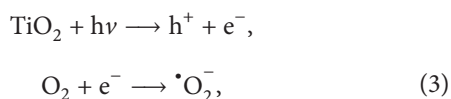


FIGURE 5: (a) Photoluminescence spectra of coumarin solution (10^{-3} mol L⁻¹, pH 3.3) after UV-A irradiation and (b) the time dependence of the photoluminescence intensity of 7-hydroxycoumarin at 456 nm, in the presence of the NP700 powder.

anatase phase starts to transform to the more stable but photocatalytically less active rutile phase. The photolysis experiments (not shown), in the absence of TiO₂ catalyst or samples without pre-treatment, revealed that the self-degradation of MB was almost insignificant under UV-A illumination.

3.3. Photoluminescence of Coumarin. Under ultraviolet irradiation the valence-band electrons of TiO₂ are excited to conduction band, leading to the formation of photogenerated electrons (e⁻) and holes (h⁺) pairs. In aqueous medium [•]OH radicals are generated by the reaction between photogenerated holes and H₂O. Related reactions may be summarized as follows:



The detection by coumarin fluorescence is based on the fact that its hydroxylation generates various subproducts, in which only one is strongly fluorescent, 7-hydroxycoumarin, as follows:



After the correction of the coumarin PL signal, which is almost negligible, the 7-hydroxycoumarin fluorescence signal can be used to determine the quantity of [•]OH generated in reaction. Figure 5 shows the changes of PL spectra from a coumarin solution with UV-A irradiation time in the presence of NP700. It is evident that a gradual increase in the fluorescence occurs over the time at ~456 nm. This signal can be related to 7-hydroxycoumarin and suggests that fluorescent product was formed during TiO₂ photocatalysis due to

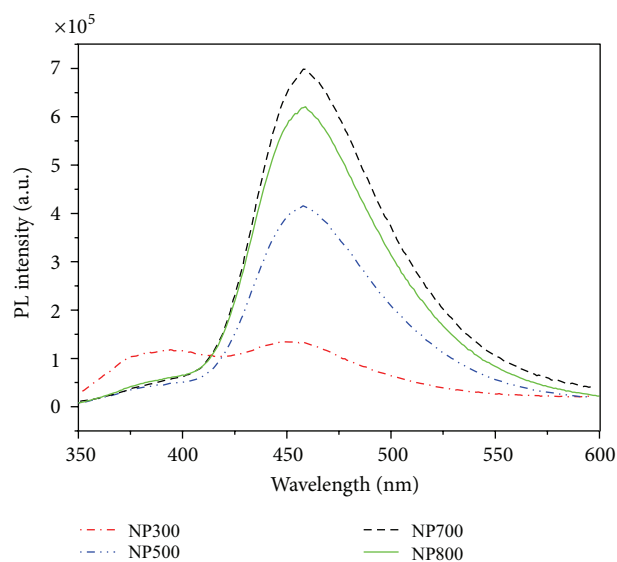


FIGURE 6: Photoluminescence spectra of coumarin solution (10^{-3} mol L⁻¹, pH 3.3) after 120 min of UV-A irradiation in the presence of N-TiO₂ powders annealed at different temperatures.

the specific reaction between hydroxyl radical and coumarin. It is clearly seen in Figure 5(b) that the fluorescence intensity increases linearly with the irradiation time.

In order to investigate the effect of temperature annealing on the formation rate of radicals, PL experiments were performed in same conditions of NP700 for all N-doped TiO₂ prepared by sol-gel method. After 2 h of irradiation PL spectra were recorded and compared (Figure 6).

It is clear that the NP700 sample yields a higher PL intensity, implying a high formation rate of 7HC and [•]OH. It is interesting to note that the PL intensity decreased when

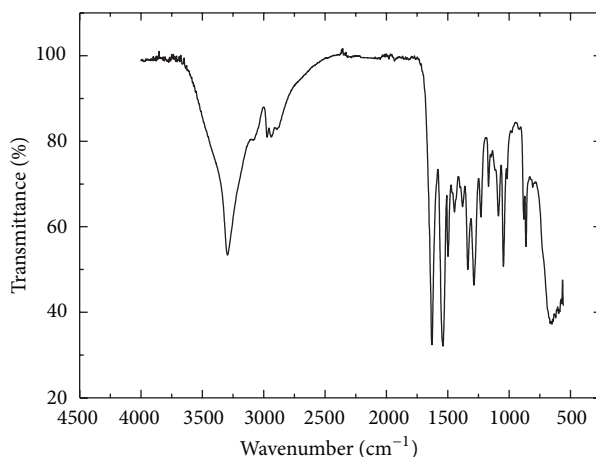


FIGURE 7: IR spectra of microcapsules with TiO_2 prepared by interfacial polymerization.

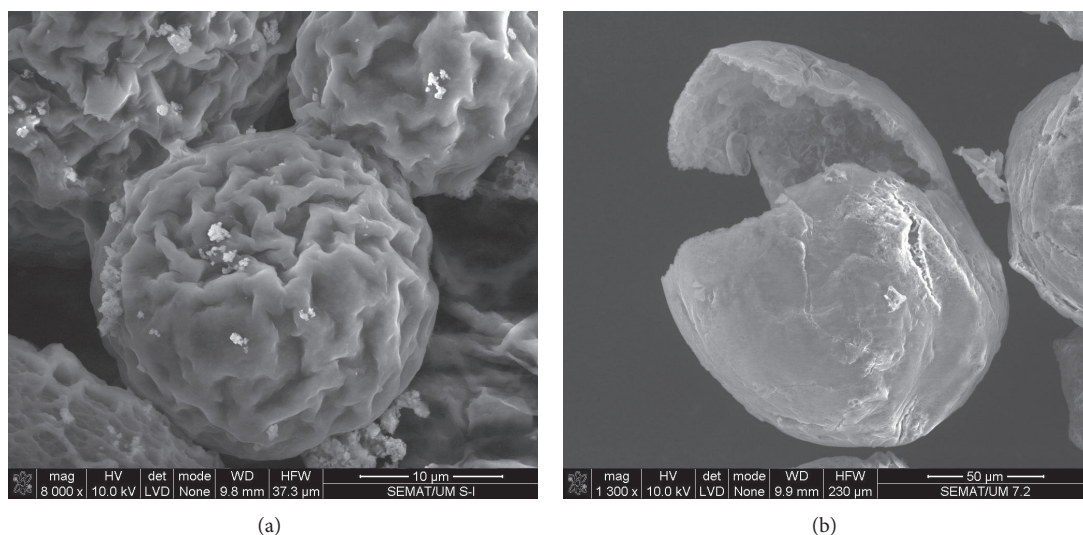


FIGURE 8: Scanning electron microscopy micrographs of dodecane-loaded polyamide microcapsules (a) with N-doped TiO_2 nanoparticles adsorbed onto its surface and (b) microcapsule degradation upon UV-A irradiation.

NP800 was used. This can be explained by the fact that NP800 contains a two-phase mixture of anatase and rutile, which can be related to the increase of the recombination in photogenerated electrons and holes and subsequently block of $\cdot\text{OH}$ production on the TiO_2 surface. The $\cdot\text{OH}$ formation rate on rutile phase is much lower than that on anatase phase. The observed PL signal was lower for calcined powders at temperatures below 700°C , meaning that a prominent anatase phase is directly correlated with enhanced $\cdot\text{OH}$ production.

3.4. FTIR-ATR Analysis of Polyamide Microcapsules. The FTIR spectrum of the synthesized polyamide microcapsules functionalized with TiO_2 is presented in Figure 7.

Figure 7 presents the absorption band related with $-\text{C}=\text{O}$ stretching vibration of the secondary amide group at

1630 cm^{-1} and the corresponding N-H stretching vibration at 1544 cm^{-1} , which shows the success of the interfacial polymerization, with formation of polyamide.

The spectral region between 3500 and 3060 cm^{-1} corresponds to the $-\text{NH}$ stretching vibration of the primary and secondary amines, which could be related to the excess of amine used. The large band at 3310 cm^{-1} is ascribed to the $-\text{C}=\text{O}$ characteristic band. The peaks from 2970 cm^{-1} to 2830 cm^{-1} are attributed to the TiO_2 showing that the nanoparticles were successfully adsorbed on the surface.

3.5. SEM Analysis of Polymeric Microcapsules. Figure 8 shows a SEM micrograph of the microcapsules (a) with N-doped TiO_2 powders adsorbed onto polymeric wall and (b) microcapsule degradation upon UV-A irradiation. The resulting microcapsules have sizes ranging from $20\text{--}100\text{ }\mu\text{m}$

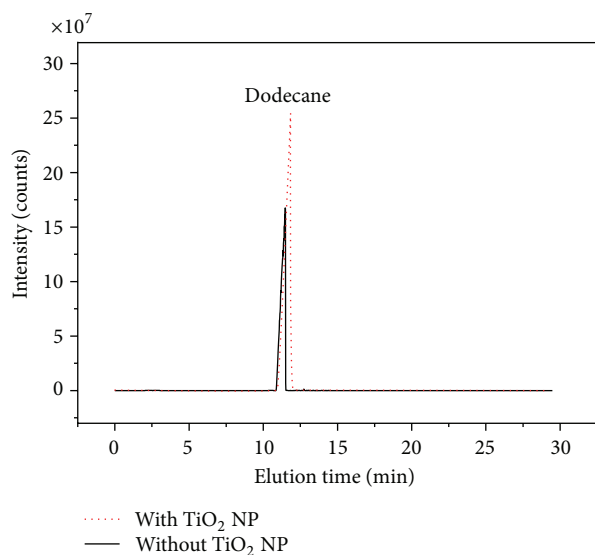


FIGURE 9: Chromatograms obtained by GC-MS for UV-A-irradiated dodecane-loaded polyamide microcapsules in the presence and absence of N-doped TiO₂ nanoparticles (NP700).

and spherical shape with a porous surface. The results presented in Figure 8(b) suggest that the microcapsule wall collapses after 2 h under UV-A irradiation. This can be related to the photocatalyst-driven oxidation-reduction mechanisms that are developed on the catalyst surface and subsequent $\cdot\text{OH}$ radicals production that initiate the dissociation and subsequent breach of the polymeric wall.

3.6. Evaluation of Dodecane Release by GC-MS. The GC-MS analysis of the UV-A-irradiated samples containing dodecane-loaded microcapsules adsorbed with TiO₂ nanoparticles on the surface revealed the presence of dodecane as a principal compound from the output yield. In order to compare the results with a commercial sample of TiO₂ P25, GC-MS experiments were performed only for the sample NP700, since it showed the best results in the photocatalysis and photoluminescence assays discussed before (Figures 4 and 6). Figure 9 shows the chromatograms obtained by GC-MS for irradiated microcapsules in the presence and absence of photocatalyst nanoparticles, while Figure 10 demonstrates the UV-A illumination effect on the output release of dodecane from within the aforementioned microcapsules adsorbed with the photocatalyst nanoparticles.

From the analysis of Figures 9 and 10 it is demonstrated that the integrated area of dodecane peak is much higher when the microcapsules are adsorbed with the photocatalyst nanoparticles and under UV-A irradiation. These results strengthen the fact that under UV-A irradiation the surface of photocatalyst develops oxidation-reduction processes that originate the cleave of chemical bonds and thus the collapse of the polymeric capsule, yielding the release of the volatile compound (dodecane).

Figure 11 shows the output release concentrations in ppm of dodecane from the polyamide microcapsules, for different

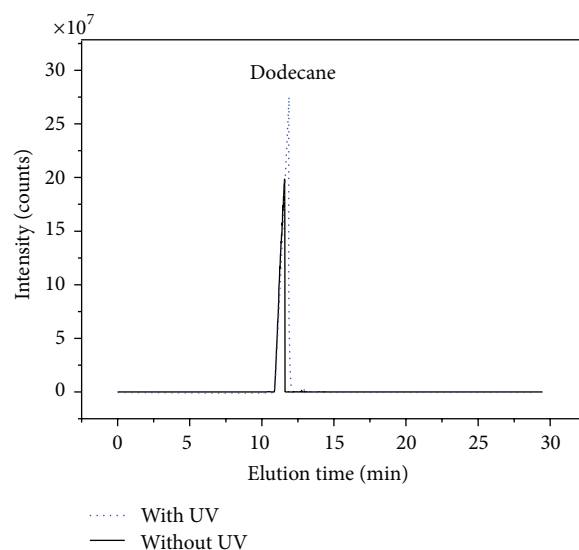


FIGURE 10: GC-MS chromatograms obtained for dodecane-loaded polyamide microcapsules adsorbed with N-doped TiO₂ nanoparticles (NP700), with and without UV-A irradiation.

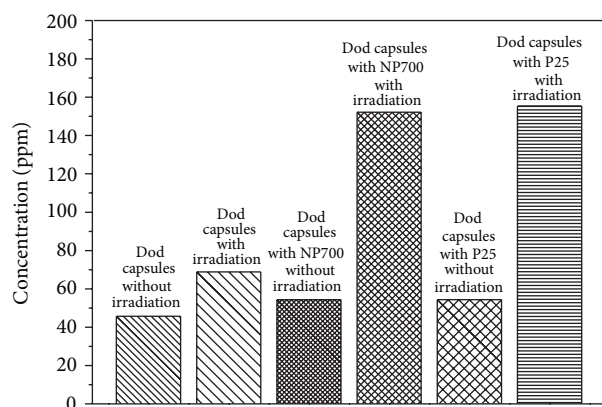


FIGURE 11: Concentration (ppm) of the output release of dodecane (Dod) from the polyamide microcapsules, for different samples and experimental conditions.

samples and experimental conditions. Due to the fact that these polymeric capsules may have some porosity, since the synthesis process is not fully optimized, it was found that dodecane can be released slowly either without the presence of the TiO₂ nanoparticles or in its presence but without UV-A irradiation. The irradiation of the microcapsules with UV-A alone, in absence of titanium dioxide, is expected to degrade the polymeric wall, releasing the dodecane. However, upon the UV-A irradiation, the release rate of the volatile agent is much higher. The results obtained for the NP700 and TiO₂ P25 confirm that nanoparticles prepared in this work present similar efficiency when compared with the commercial sample.

4. Conclusions

A simple method was developed for the synthesis of a stable nanocrystalline N-doped TiO₂ photocatalysts by a modified

sol-gel method, which were adsorbed on dodecane-loaded polyamide-based microcapsules. The effect of annealing temperature on the photocatalytic activity of the nanoparticles under ultraviolet irradiation was investigated. It was found that photocatalytic activity of these nanoparticles is strongly dependent on the calcination temperature. The nanoparticles calcined at 700°C revealed the highest photocatalytic activity upon degrading methylene blue under UV-A irradiation. Furthermore, the formation of $\cdot\text{OH}$ radicals on the photocatalyst surface under UV-A irradiation was also monitored by fluorescence experiments. In the same way of MB degradation, the N-doped TiO_2 powders calcined at 700°C form a higher number of hydroxyl radicals on its surface than powders annealed at lower and higher temperatures (800°C). This result can be related to the more stable and prominent anatase phase in this sample, in detriment to rutile formation at a higher temperature.

This work has shown that polyamide based microcapsules with TiO_2 adsorbed on the surface can be successfully used to trigger the release of a model organic volatile compounds by UV-A irradiation. By means of GC-MS experiments it was possible to identify and quantify the amount of volatile compound released.

The proof of concept presented in this work can be extended to afford the preparation of microcapsules loaded with organic compounds that can be released in a controlled manner through UV-A irradiation.

Acknowledgments

This work was supported by FEDER through the COMPETE Program and by the Portuguese Foundation for Science and Technology (FCT) in the framework of the Strategic Project PEST-C/FIS/UI607/2011 and PTDC/CTM-NAN/119979/2010 Project.

References

- [1] T. Brandau, "Preparation of monodisperse controlled release microcapsules," *International Journal of Pharmaceutics*, vol. 242, no. 1-2, pp. 179-184, 2002.
- [2] K. Aiedeh, E. Gianasi, I. Orienti, and V. Zecchi, "Chitosan microcapsules as controlled release systems for insulin," *Journal of Microencapsulation*, vol. 14, no. 5, pp. 567-576, 1997.
- [3] U. Jeong, S. H. Im, P. H. C. Camargo, J. H. Kim, and Y. Xia, "Microscale fish bowls: a new class of latex particles with hollow interiors and engineered porous structures in their surfaces," *Langmuir*, vol. 23, no. 22, pp. 10968-10975, 2007.
- [4] R. Dubey, T. C. Shami, and K. U. Bhasker Rao, "Microencapsulation technology and applications," *Defence Science Journal*, vol. 59, no. 1, pp. 82-95, 2009.
- [5] D. G. Yu, S. H. Kim, and J. H. An, "Preparation and characterization of electronic inks encapsulation for microcapsule-type electrophoretic displays (EPDs)," *Journal of Industrial and Engineering Chemistry*, vol. 13, no. 3, pp. 438-443, 2007.
- [6] H. Bungerberg de Jong, "Crystallization-coacervation-flocculation," *Colloid Science*, vol. 2, pp. 280-283, 1949.
- [7] S. Leclercq, K. R. Harlander, and G. A. Reineccius, "Formation and characterization of microcapsules by complex coacervation with liquid or solid aroma cores," *Flavour and Fragrance Journal*, vol. 24, no. 1, pp. 17-24, 2009.
- [8] F. Tiarks, K. Landfester, and M. Antonietti, "Preparation of polymeric nanocapsules by miniemulsion polymerization," *Langmuir*, vol. 17, no. 3, pp. 908-918, 2001.
- [9] R. Arshady, "Microspheres and microcapsules, a survey of manufacturing techniques. Part III. Solvent evaporation," *Polymer Engineering and Science*, vol. 30, no. 15, pp. 915-924, 1990.
- [10] H. Strohm, M. Sgraja, J. Bertling, and P. Löbmann, "Preparation of TiO_2 -polymer hybrid microcapsules," *Journal of Materials Science*, vol. 38, no. 8, pp. 1605-1609, 2003.
- [11] A. Toubeli and C. Kiparissides, "Synthesis and characterization of polyterephthalamide membranes for encapsulation use: effect of the amine type and composition on the membrane permeability," *Journal of Membrane Science*, vol. 146, no. 1, pp. 15-29, 1998.
- [12] P. Persico, C. Carfagna, L. Danicher, and Y. Frere, "Polyamide microcapsules containing jojoba oil prepared by inter-facial polymerization," *Journal of Microencapsulation*, vol. 22, no. 5, pp. 471-486, 2005.
- [13] M. L. Soto-Portas, J. F. Argillier, F. Méchin, and N. Zydowicz, "Preparation of oily core polyamide microcapsules via interfacial polycondensation," *Polymer International*, vol. 52, no. 4, pp. 522-527, 2003.
- [14] C. J. Tavares and F. J. S. Pina, "Photocatalytic coating for the controlled release of volatile agents," International Patent WO 2011/012935 A2, PCT/IB2009/055716, World Intellectual Property Organization, 2011.
- [15] M. A. Fox and M. T. Dulay, "Heterogeneous photocatalysis," *Chemical Reviews*, vol. 93, no. 1, pp. 341-357, 1993.
- [16] A. L. Linsebigler, G. Lu, and J. T. Yates, "Photocatalysis on TiO_2 surfaces: principles, mechanisms, and selected results," *Chemical Reviews*, vol. 95, no. 3, pp. 735-758, 1995.
- [17] R. Asahi, T. Morikawa, T. Ohwaki, K. Aoki, and Y. Taga, "Visible-light photocatalysis in nitrogen-doped titanium oxides," *Science*, vol. 293, no. 5528, pp. 269-271, 2001.
- [18] C. Cantau, T. Pigot, J. C. Dupin, and S. Lacombe, "N-doped TiO_2 by low temperature synthesis: stability, photo-reactivity and singlet oxygen formation in the visible range," *Journal of Photochemistry and Photobiology A*, vol. 216, no. 2-4, pp. 201-208, 2010.
- [19] X. Zhang, K. Udagawa, Z. Liua et al., "Photocatalytic and photoelectrochemical studies on N-doped TiO_2 photocatalyst," *Journal of Photochemistry and Photobiology A*, vol. 202, no. 1, pp. 39-47, 2009.
- [20] T. Ihara, M. Miyoshi, Y. Iriyama, O. Matsumoto, and S. Sugihara, "Visible-light-active titanium oxide photocatalyst realized by an oxygen-deficient structure and by nitrogen doping," *Applied Catalysis B*, vol. 42, no. 4, pp. 403-409, 2003.
- [21] B. Fu, L. Gao, and S. Yang, "CNTs/ Ta_3N_5 nanocomposite with enhanced photocatalytic activity under visible light irradiation," *Journal of the American Ceramic Society*, vol. 90, no. 4, pp. 1309-1311, 2007.
- [22] Y. Cong, L. Xiao, J. Zhang, F. Chen, and M. Anpo, "Preparation and characterization of nitrogen-doped TiO_2 photocatalyst in different acid environments," *Research on Chemical Intermediates*, vol. 32, no. 8, pp. 717-724, 2006.
- [23] A. Mills and J. Wang, "Photobleaching of methylene blue sensitized by TiO_2 : an ambiguous system?" *Journal of Photochemistry and Photobiology A*, vol. 127, no. 1-3, pp. 123-134, 1999.

- [24] H. Hashemipour and M. Mirzaee, "Experimental study of influencing factors and kinetics in catalytic removal of methylene blue with TiO_2 nanopowder," *American Journal of Environmental Engineering*, vol. 2, no. 1, pp. 1–7, 2012.
- [25] C. H. Wu and J. M. Chern, "Kinetics of photocatalytic decomposition of methylene blue," *Industrial and Engineering Chemistry Research*, vol. 45, no. 19, pp. 6450–6457, 2006.
- [26] H. Czili and A. Horváth, "Applicability of coumarin for detecting and measuring hydroxyl radicals generated by photoexcitation of TiO_2 nanoparticles," *Applied Catalysis B*, vol. 81, no. 3–4, pp. 295–302, 2008.
- [27] H. Essawy and K. Tauer, "Polyamide capsules via soft templating with oil drops-1. Morphological studies of the capsule wall," *Colloid and Polymer Science*, vol. 288, no. 3, pp. 317–331, 2010.
- [28] I. Hanno, C. Anselmi, and K. Bouchemal, "Polyamide nanocapsules and nano-emulsions containing Parsol MCX and Parsol 1789: in vitro release, ex vivo skin penetration and photostability studies," *Pharmaceutical Research*, vol. 29, pp. 559–573, 2012.
- [29] A. H. Mahvi, M. Ghanbarian, S. Nasser, and A. Khairi, "Mineralization and discoloration of textile wastewater by TiO_2 nanoparticles," *Desalination*, vol. 238, no. 1–3, pp. 309–316, 2009.
- [30] H. Kumazawa, H. Otsuki, and E. Sada, "Preparation of monosized spherical titania fine particles by controlled hydrolysis of titanium tetraethoxide in ethanol," *Journal of Materials Science Letters*, vol. 12, no. 11, pp. 839–840, 1993.
- [31] A. Houas, H. Lachheb, M. Ksibi, E. Elaloui, C. Guillard, and J. M. Herrmann, "Photocatalytic degradation pathway of methylene blue in water," *Applied Catalysis B*, vol. 31, no. 2, pp. 145–157, 2001.

Research Article

The Photocatalytic Property of Nitrogen-Doped TiO₂ Nanoball Film

Haiying Wang and Yanchun Hu

College of Physics and Electronic Engineering, Henan Normal University, Xinxiang, Henan 453007, China

Correspondence should be addressed to Haiying Wang; why@htu.cn

Received 14 October 2012; Revised 8 December 2012; Accepted 8 December 2012

Academic Editor: Jiaguo Yu

Copyright © 2013 H. Wang and Y. Hu. This is an open access article distributed under the Creative Commons Attribution License, which permits unrestricted use, distribution, and reproduction in any medium, provided the original work is properly cited.

TiO₂ nanoball films of nitrogen doping and no doping were prepared by anodic oxidation method. The nitrogen-doped samples exhibited significant enhanced absorption in visible light range, narrowing band gap from 3.2 eV to 2.8 eV and the smaller nanoball diameter size. The concentrations of methyl blue reduce to nearly 44% after 4-hour photodecomposition test by nitrogen-doped sample. It is indicated that there may be two main reasons for the enhanced photocatalytic activity: the increase of O vacancy and photocatalytic reactivity surface area in nitrogen-doped samples.

1. Introduction

Due to the strong photocatalytic activity, antiphotocorrosion ability, biologic compatibility, and chemical stability of TiO₂, TiO₂ has become the most promising photocatalyst [1–4]. However, the wideband gap of TiO₂ (3.2 eV for the anatase phase and 3.0 eV for the rutile phase) needs ultraviolet (UV) light for electron-hole separation, which is only 5% of the natural solar light [5]. It is of great significance to enlarge the TiO₂ absorption band border to visible light range and to improve the photocatalytic efficiency of the TiO₂ that can be used in visible light irradiation.

Recently, it was recognized that compared with metal doping (Ca²⁺, Sr²⁺, and Ba²⁺) [6], transition metal ions (Fe³⁺, Cr⁶⁺, Co³⁺, and Mo⁵⁺ [7–10]), rare earth cations (La³⁺, Ce³⁺, Er³⁺, Pr³⁺, Gd³⁺, Nd³⁺, and Sm³⁺) [11], and some nonmetal doping (C [12], S [13], and F [14, 15]), nitrogen-doped TiO₂ exhibited a valid process for narrowing the band gap and demonstrated a more appropriate solution for extending the photocatalytic activity of TiO₂ into the visible region [16–22]. Macak et al., and Shankar et al., and Allam and El-Sayed pointed out that the morphology, crystallinity, composition, and illumination geometry of nanotube arrays were critical factors in their performance as photoelectrodes [23–25]. TiO₂ nanostructure materials displayed high performance for their potential in improving photocatalytic activity because of their high surface area.

In this work, the N-doped nanoball films were prepared and their photocatalytic activities were evaluated by the degradation of methyl blue under visible light irradiation.

2. Experimental

The titanium foils (0.6 mm thick, 99.5% purity, and cut in 1 cm × 2 cm) were used as the substrates for the growth of the TiO₂ nanowire arrays. The titanium sheets were cleaned by sonicating in 1 : 1 acetone and ethanol solution, followed by being rinsed with deionized water and dried in airstream. The anodization was carried out in a two-electrode electrochemical cell with a graphite sheet as the cathode at a constant potential 60 V. A DC power supply (WYK-6010, 0–60 V, and 0–10 A) was used to control the experimental current and voltage for 1.2 h. The electrolyte contained 0.5 wt% NH₄F, 5 mL H₂O, and 195 mL ethylene glycol. After anodization, the specimens were cleaned in 10% HCl by ultrasonic immediately for 20 minutes and dried in airstream. Postannealing in air at 700°C was employed to transform the amorphous titania to nanocrystalline TiO₂ and remove most of the organic and inorganic species encapsulated in the arrays. Nitrogen doping was carried out by annealing the samples in ammonia atmosphere at 520°C. The reagents—acetone (CH₃COCH₃), ethanol (C₂H₅OH), ammonium fluoride (NH₄F), and ethylene glycol (C₂H₆O₂)

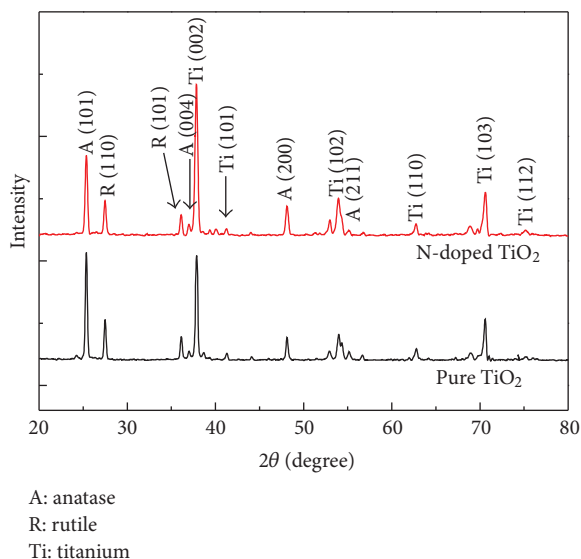


FIGURE 1: XRD patterns of nitrogen-doped and undoped TiO_2 nanoball films.

were of analytical grade without further purification. The water used in all the experiments was deionized water.

The crystal structures of samples were characterized by X-ray diffraction (XRD, Bruker AXS D8 Advance diffractions) using $\text{Cu K}\alpha$ radiation. The surface morphologies and thickness of the nanoball films were observed by scanning electron microscopy (SEM, S-4800). The X-ray photoelectron spectroscopy (XPS) experiments were performed on a VG MultiLab 2000 spectrometer to obtain the information on chemical binding energy of the TiO_2 nanoballs which was calibrated with the reference to the C 1s peak at 284.6 eV. The UV-visible absorption spectra were measured using a Cary 5000 UV-Vis-NIR spectrophotometer; BaSO_4 was used as a reflectance standard in a UV-visible diffuse reflectance experiment. The photocatalytic activities under visible light irradiation were evaluated by the degradation of methyl blue irradiated by a 450 W xenon lamp. In the process, a TiO_2 nanoball film with dimensions of $0.5 \text{ cm} \times 0.5 \text{ cm}$ was immersed into a quartz colorimetric cuvette filled with 3 mL 10 mg/L methylene blue (MB) solution and placed below xenon lamp. The distance between the film and the lamp is 10 cm distance. And the intensity of the light incident on the samples is measured about 900 mW/cm^2 . The solution in the photoreactor was placed in dark for 30 minutes to reach the absorption-desorption equilibrium of the dye molecules on the sample surface. After 30-minute visible-light irradiation and 5-minute waiting, the content of methyl blue was measured by Cary 5000 UV-Vis-NIR spectrophotometer and the deionized water was used as a reflectance standard. Then the process was repeated for 8 times to get degradation data.

3. Results and Discussion

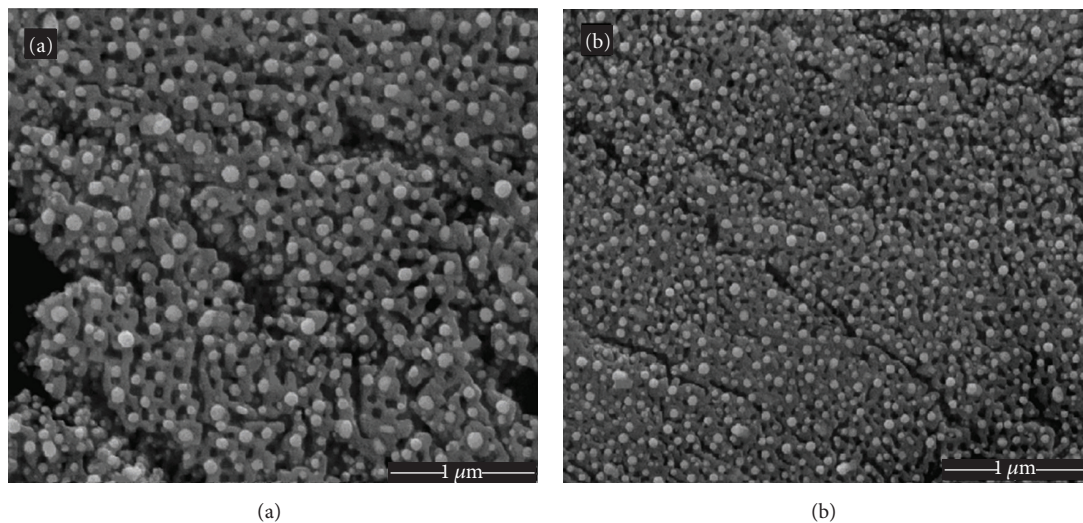
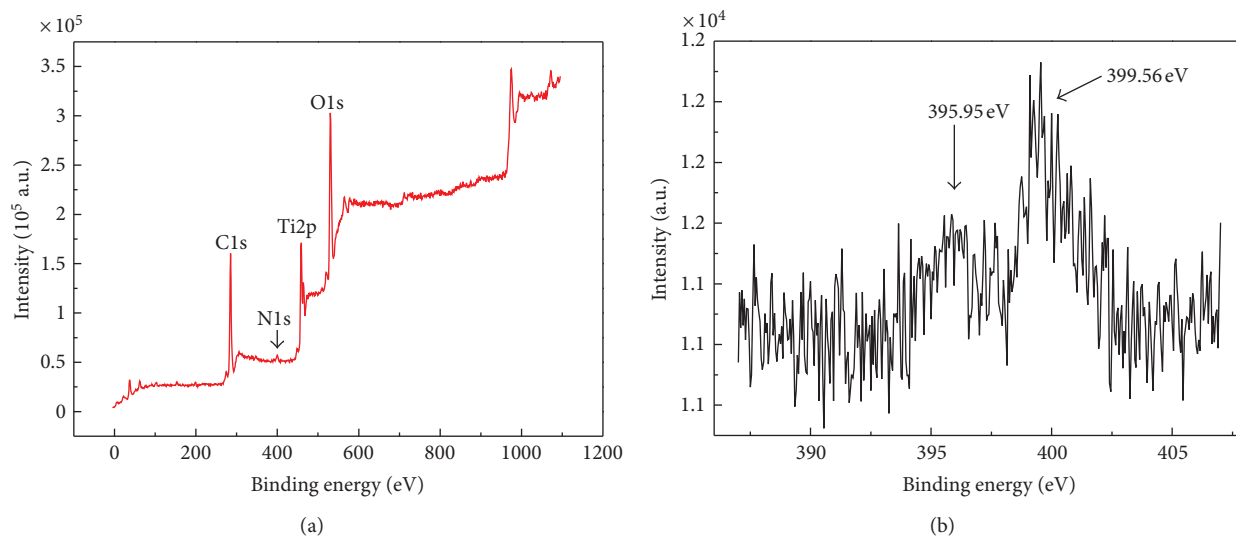
Figure 1 shows the XRD patterns of nitrogen-doped and undoped TiO_2 nanoball films. For the pure sample annealed

at 700°C , an anatase characteristic diffraction peak appears at 25.38° and a rutile diffraction peak appears at 27.48° , which are in well accordance with the (101) diffraction peak position of anatase TiO_2 (JCPDS 21-1272) and the (110) diffraction peak position of rutile TiO_2 (JCPDS 21-1276). The contents of rutile phase and anatase phase are calculated by the XRD results, using the method described by Zhu et al. [26]. The calculation results indicate that both films contain major anatase phase with minor rutile (about 20% content) and the titanium substrate peaks showing up without other phases. The smaller full width at half maximum (FWHM) ($\Delta\theta = 0.134^\circ$) of (101) peak of pure TiO_2 samples indicates a larger crystallite size of undoped nanoballs compared with nitrogen-doped samples ($\Delta\theta = 0.161^\circ$).

SEM images of pure and nitrogen-doped TiO_2 nanoball films are shown in Figure 2. It is found that for both films with the pure nanoball particles and nitrogen-doped nanoball particles, the shape of the nanoballs does not show any obvious change after the treatment in NH_3 flow at 520°C . But it can be seen that the size of nitrogen-doped nanoball (the ball diameter is about 50 nm and the film thickness is about 500 nm) is obviously smaller than undoped TiO_2 nanoballs (the ball diameter is about 100 nm), in accordance with the XRD results. The doping of N element may retard the growth of nanoballs, which is similar with the report in papers [27, 28].

In order to get the composition and the chemical states information, XPS measurements were performed. Figure 3(a) shows the XPS survey spectrum of the nitrogen-doped sample, where the peaks at 458.86 eV, 530.01 eV, 399.69 eV, and 284.7 eV correspond to the binding energy of $\text{Ti}2\text{p}_{3/2}$, O 1s, N 1s, and C 1s, respectively. The C 1s peak is a signal of adventitious elemental carbon as reported in other works [17, 29, 30]. The existence of N element and the entering of N ion into the structure of anatase TiO_2 within the limits of instrumental error were confirmed.

To further investigate the N 1s core level states, the XPS spectrum of N 1s core level electron for N-doped sample is measured and is shown in Figure 3(b). Although, the N doping in TiO_2 has been reported by many papers, the XPS peak of N 1s has still been under debate. Typically, there are two forms of N doping. One is the substitutional doping (O-Ti-N) in which the N atom is bound to Ti atoms directly and replaces the lattice oxygen atoms with a binding energy of N about 396 eV; the other one is the interstitial doping (Ti-O-N) in which the N atoms are bound to lattice oxygen atoms and locate in the TiO_2 lattice interstice with a binding energy of N of about 400 eV [31–36]. In this work, the N 1s XPS spectrum has a major peak at 399.56 eV which can be assigned to the substitutional nitrogen atoms in the anatase lattice of TiO_2 , and a minor peak at 395.95 eV which can be ascribed to the contributions of the nitrogen atoms in the interstitial sites forming the Ti-O-N oxynitrides. The doping content of N is 1.98%, calculating from the N 1s peaks spectrum. In this work, the doped N atoms are inclined to be in the substitutional sites forming the N-Ti-O oxynitrides, and after the N atoms in the substitutional sites forming the N-Ti-O oxynitrides become saturated (the content is close to 1.53%), the excessive N atoms were then present in the

FIGURE 2: SEM images of pure (a) and nitrogen-doped (b) TiO₂ nanoball films.FIGURE 3: XPS spectra of nitrogen-doped TiO₂ nanoball film. (a) Survey; (b) N 1s peaks.

substitutional sites forming the N–Ti–N structure, as it was reported in paper [37].

Figure 4(a) illustrates the UV-Vis absorption spectroscopy of undoped and N-doped TiO₂ with the wavelength in the range of 200–800 nm. The undoped TiO₂ samples exhibit the characteristic spectrum of TiO₂ with its fundamental absorption sharp edge around 380 nm. However, the nitrogen-doped samples exhibit the absorption edge around 440 nm. This absorption edge shifted toward visible light range indicates that a significant enhancement of absorption visible light range is observed. According to the equation $\lambda = 1240/E_g$, the band gaps of the pure and N-doped TiO₂ are 3.23 eV and 2.82 eV, respectively. These band gaps are determined by fitting the absorption spectra data according to the equation $(\alpha h\nu)^2 = B(h\nu - E_g)$ (α is the absorption coefficient; $h\nu$ is the photo energy; B is a constant number;

E_g is the absorption band gap energy). Figure 4(b) illustrates the $(\alpha h\nu)^{1/2}$ versus $h\nu$ curves. As it can be seen, the band gaps of the pure and N-doped TiO₂ are 3.2 eV and 2.8 eV individually, which are in accordance with the results in Figure 4(a) and similar to those reported in [38]. The band gap energy of the nitrogen-doped samples has been narrowed compared with undoped sample. The reason for this change has been discussed elsewhere [39]. For the presence of nitrogen atoms in the lattice, the results of density functional theory (DFT) calculations [37] have shown a large decrease in the formation energy for oxygen vacancies. It has been reported that oxygen vacancy induced by N doping or self-doping plays an important role in the photocatalytic activity of TiO₂ catalyst by trapping the photoinduced electron and acting as a reactive center for the photocatalytic process. And it is known that N has a lower valence state than O so that the

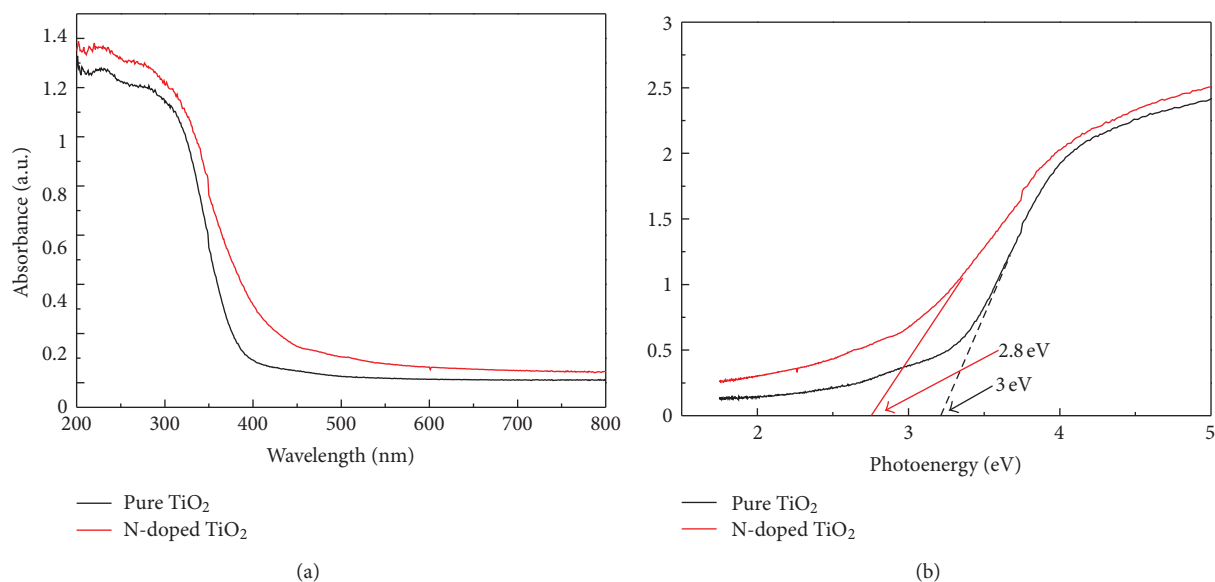


FIGURE 4: UV-vis absorption spectroscopy of undoped and N-doped TiO₂ with the wavelength in the range of (a) 200–800 nm and (b) $(\alpha h\nu)^{1/2}$ versus $h\nu$ curves.

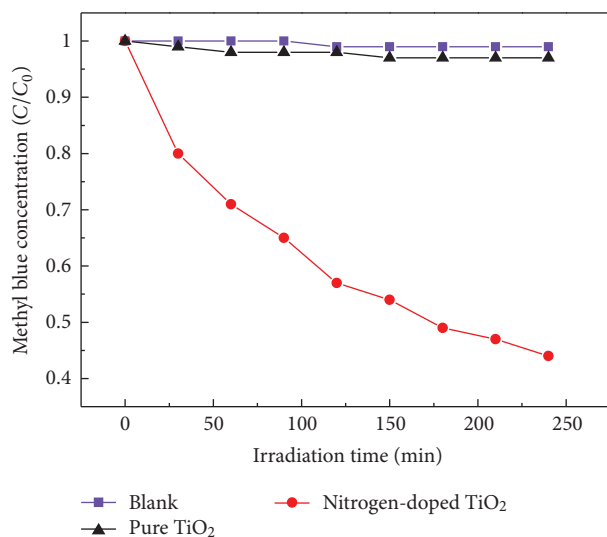


FIGURE 5: Concentrations of methyl blue photodegraded by the pure TiO₂ and nitrogen-doped TiO₂.

incorporation of N must promote the synchronous formation of oxygen vacancies for the charge equilibrium in TiO₂ [40]. That is to say, for nitrogen-doped TiO₂, the increase of visible light response for N-doped TiO₂ is attributed to both oxygen vacancies and the N 2p states.

Figure 5 shows the concentrations of methyl blue photodegraded in an aqueous solution under visible light irradiation by insert a filter ($\lambda \leq 400$ nm) between the Xe-lamp and the samples by the pure TiO₂ and nitrogen-doped TiO₂. The blank test without photocatalyst is carried and the result is shown in Figure 5 as a compared data. The concentration of

methyl blue decreases to nearly 44% in 4 hours for nitrogen-doped samples, while for the pure TiO₂ nanoball film, almost no photocatalytic activity has been observed. The methyl blue degradation rate constants of the nitrogen-doped sample ($3.657 \times 10^{-3} \text{ min}^{-1}$) is much higher than that of the pure sample ($0.128 \times 10^{-3} \text{ min}^{-1}$), calculated from Figure 5. For the nitrogen-doped sample, the size of nanoball diameter is about 50 nm which is only half of the size of undoped nanoball, the surface area to volume ratio associated with the nanosize of titania crystals increased, which assures the higher total amount of the surface active sites available for adsorption of reactant molecules and facilitates the mass transfer, hence enhancing the photocatalytic efficiency [41–45]. At the same time, after nitrogen doping, the visible light absorption band as evidenced in Figure 4 can be reasonably thought to arise from the localized states of N 2p above the valence band and also concomitant oxygen vacancy states below the conduction band [41]. Hence, as the results show that nitrogen-doped sample has a superior photocatalytic property than pure sample under visible light irradiation.

4. Conclusions

In conclusion, TiO₂ nanoball films were synthesized by an anodic oxidation method. The nitrogen doping could significantly enhance absorption in visible light range, narrowband gap from 3.2 eV to 2.8 eV and reduce nanoball diameter compared with that of the pure samples. The N-doped TiO₂ nanoball films possess a stronger photocatalytic activity for catalyzing the degradation of methyl blue. The concentration of methyl blue reduces to nearly 44% in 4 hours for nitrogen-doped sample. The increasement of O vacancies and surface area for photocatalytic reactivity may be the important two

reasons for the increase of photocatalytic activity in the nitrogen-doped TiO₂ nanoball films.

Acknowledgments

The authors would like to acknowledge the financial support from the Henan Normal University Doctor Science Foundation (01026500121).

References

- [1] A. Fujishima and K. Honda, "Electrochemical photolysis of water at a semiconductor electrode," *Nature*, vol. 238, no. 5358, pp. 37–38, 1972.
- [2] S. Sreekantan, R. Hazan, and Z. Lockman, "Photoactivity of anatase-rutile TiO₂ nanotubes formed by anodization method," *Thin Solid Films*, vol. 518, no. 1, pp. 16–21, 2009.
- [3] A. Fujishima, T. N. Rao, and D. A. Tryk, "Titanium dioxide photocatalysis," *Journal of Photochemistry and Photobiology C*, vol. 1, no. 1, pp. 1–21, 2000.
- [4] J. G. Yu, M. Jaroniec, and G. X. Lu, "TiO₂ photocatalytic materials," *International Journal of Photoenergy*, vol. 2012, Article ID 206183, 5 pages, 2012.
- [5] X. Chen and S. S. Mao, "Titanium dioxide nanomaterials: synthesis, properties, modifications and applications," *Chemical Reviews*, vol. 107, no. 7, pp. 2891–2959, 2007.
- [6] N. I. Al-Salim, S. A. Bagshaw, A. Bittar et al., "Characterisation and activity of sol-gel-prepared TiO₂ photocatalysts modified with Ca, Sr or Ba ion additives," *Journal of Materials Chemistry*, vol. 10, no. 10, pp. 2358–2363, 2000.
- [7] M. Kang, "Synthesis of Fe/TiO₂ photocatalyst with nanometer size by solvothermal method and the effect of H₂O addition on structural stability and photodecomposition of methanol," *Journal of Molecular Catalysis A*, vol. 197, no. 1-2, pp. 173–183, 2003.
- [8] K. Wilke and H. D. Breuer, "The influence of transition metal doping on the physical and photocatalytic properties of titania," *Journal of Photochemistry and Photobiology A*, vol. 121, no. 1, pp. 49–53, 1999.
- [9] J. Wang, S. Uma, and K. J. Klabunde, "Visible light photocatalysis in transition metal incorporated titania-silica aerogels," *Applied Catalysis B*, vol. 48, no. 2, pp. 151–154, 2004.
- [10] Y. Yang, X. J. Li, J. T. Chen, and L. Y. Wang, "Effect of doping mode on the photocatalytic activities of Mo/TiO₂," *Journal of Photochemistry and Photobiology A*, vol. 163, no. 3, pp. 517–522, 2004.
- [11] A. W. Xu, Y. Gao, and H. Q. Liu, "The preparation, characterization, and their photocatalytic activities of rare-earth-doped TiO₂ nanoparticles," *Journal of Catalysis*, vol. 207, no. 2, pp. 151–157, 2002.
- [12] S. U. M. Khan, M. Al-Shahry, and W. B. Ingler, "Efficient photochemical water splitting by a chemically modified n-TiO₂," *Science*, vol. 297, no. 5590, pp. 2243–2245, 2002.
- [13] T. Umebayashi, T. Yamaki, H. Itoh, and K. Asai, "Band gap narrowing of titanium dioxide by sulfur doping," *Applied Physics Letters*, vol. 81, no. 3, pp. 454–456, 2002.
- [14] T. Yamaki, T. Sumita, and S. Yamamoto, "Formation of TiO_{2-x}F_x compounds in fluorine-implanted TiO₂," *Journal of Materials Science Letters*, vol. 21, pp. 33–35, 2002.
- [15] G. Ren, Y. Gao, X. Liu, A. Xing, H. Liu, and J. Yin, "Synthesis of high-activity F-doped TiO₂ photocatalyst via a simple one-step hydrothermal process," *Reaction Kinetics, Mechanisms and Catalysis*, vol. 100, no. 2, pp. 487–497, 2010.
- [16] L. DONG, G. X. CAO, Y. MA, X. L. JIA, G. T. YE, and S. K. GUAN, "Enhanced photocatalytic degradation properties of nitrogen-doped titania nanotube arrays," *Transactions of Non-ferrous Metals Society of China*, vol. 19, no. 6, pp. 1583–1587, 2009.
- [17] H. Y. Wang, Y. C. Yang, J. H. Wei et al., "Effective photocatalytic properties of N doped Titanium dioxide nanotube arrays prepared by anodization," *Reaction Kinetics, Mechanisms and Catalysis*, vol. 106, no. 2, pp. 341–353, 2012.
- [18] J. J. Qian, G. J. Cui, M. J. Jing, Y. Wang, M. Zhang, and J. J. Yang, "Hydrothermal synthesis of nitrogen-doped titanium dioxide and evaluation of its visible light photocatalytic activity," *International Journal of Photoenergy*, vol. 2012, Article ID 198497, 6 pages, 2012.
- [19] X. W. Cheng, X. J. Yu, Z. P. Xing, and L. S. Yang, "Enhanced visible light photocatalytic activity of mesoporous anatase TiO₂ codoped with nitrogen and chlorine," *International Journal of Photoenergy*, vol. 2012, Article ID 593245, 6 pages, 2012.
- [20] K. R. Wu, C. H. Hung, C. W. Yeh, C. C. Wang, and J. K. Wu, "Effect of N, C-ITO on Composite N,C-TiO₂/N,C-ITO/ITO electrode used for photoelectrochemical degradation of aqueous pollutant with simultaneous hydrogen production," *International Journal of Photoenergy*, vol. 2012, Article ID 829327, 10 pages, 2012.
- [21] J. Y. Wei, B. B. Huang, P. Wang et al., "Photocatalytic properties of nitrogen-doped Bi₁₂TiO₁₂ synthesized by urea addition sol-gel method," *International Journal of Photoenergy*, vol. 2012, Article ID 135132, 8 pages, 2012.
- [22] G. F. Shang, H. B. Fu, S. G. Yang, and T. G. Xu, "Mechanistic study of visible-light-induced photodegradation of 4-chlorophenol by TiO_{2-x}N_x with low nitrogen concentration," *International Journal of Photoenergy*, vol. 2012, Article ID 759306, 9 pages, 2012.
- [23] J. M. Macak, H. Tsuchiya, A. Ghicov et al., "TiO₂ nanotubes: self-organized electrochemical formation, properties and applications," *Current Opinion in Solid State and Materials Science*, vol. 11, no. 1-2, pp. 3–18, 2007.
- [24] K. Shankar, J. I. Basham, N. K. Allam et al., "Recent advances in the use of TiO₂ nanotube and nanowire arrays for oxidative photoelectrochemistry," *Journal of Physical Chemistry C*, vol. 113, no. 16, pp. 6327–6359, 2009.
- [25] N. K. Allam and M. A. El-Sayed, "Photoelectrochemical water oxidation characteristics of anodically fabricated TiO₂ nanotube arrays: structural and optical properties," *Journal of Physical Chemistry C*, vol. 114, no. 27, pp. 12024–12029, 2010.
- [26] J. Zhu, W. Zheng, B. He, J. Zhang, and M. Anpo, "Characterization of Fe-TiO₂ photocatalysts synthesized by hydrothermal method and their photocatalytic reactivity for photodegradation of XRG dye diluted in water," *Journal of Molecular Catalysis A*, vol. 216, no. 1, pp. 35–43, 2004.
- [27] J. Yu, M. Zhou, H. Yu, Q. Zhang, and Y. Yu, "Enhanced photoinduced super-hydrophilicity of the sol-gel-derived TiO₂ thin films by Fe-doping," *Materials Chemistry and Physics*, vol. 95, no. 2-3, pp. 193–196, 2006.
- [28] W. Q. Peng, M. Yanagida, and L. Y. Han, "Rutile-anatase TiO₂ photoanodes for dye-sensitized solar cells," *Journal of Nonlinear Optical Physics And Materials*, vol. 19, no. 4, pp. 673–679, 2010.

- [29] W. Ren, Z. Ai, F. Jia, L. Zhang, X. Fan, and Z. Zou, "Low temperature preparation and visible light photocatalytic activity of mesoporous carbon-doped crystalline TiO_2 ," *Applied Catalysis B*, vol. 69, no. 3-4, pp. 138-144, 2007.
- [30] H. Irie, Y. Watanabe, and K. Hashimoto, "Carbon-doped anatase TiO_2 powders as a visible-light sensitive photocatalyst," *Chemistry Letters*, vol. 32, no. 8, pp. 772-773, 2003.
- [31] J. F. Molder, W. F. Stickle, P. E. Sobol, and K. D. Bomben, *Handbook of X-Ray Photoelectron Spectroscopy*, Perkin-Elmer, Eden Prairie, Minn, USA, 2nd edition, 1992.
- [32] D. Li, N. Ohashi, S. Hishita, T. Kolodiazny, and H. Haneda, "Origin of visible-light-driven photocatalysis: a comparative study on N/F-doped and N-F-codoped TiO_2 powders by means of experimental characterizations and theoretical calculations," *Journal of Solid State Chemistry*, vol. 178, no. 11, pp. 3293-3302, 2005.
- [33] F. Esaka, K. Furuya, H. Shimada et al., "Comparison of surface oxidation of titanium nitride and chromium nitride films studied by x-ray absorption and photoelectron spectroscopy," *Journal of Vacuum Science and Technology A*, vol. 15, no. 5, pp. 2521-2528, 1997.
- [34] A. Fujishima, X. Zhang, and D. A. Tryk, " TiO_2 photocatalysis and related surface phenomena," *Surface Science Reports*, vol. 63, no. 12, pp. 515-582, 2008.
- [35] J. Wang, D. N. Tafen, J. P. Lewis et al., "Origin of photocatalytic activity of Nitrogen-doped TiO_2 nanobelts," *Journal of the American Chemical Society*, vol. 131, no. 34, pp. 12290-12297, 2009.
- [36] P. Wu, R. Xie, and J. K. Shang, "Enhanced visible-light photocatalytic disinfection of bacterial spores by palladium-modified nitrogen-doped titanium oxide," *Journal of the American Ceramic Society*, vol. 91, no. 9, pp. 2957-2962, 2008.
- [37] C. Di Valentin, G. Pacchioni, A. Selloni, S. Livraghi, and E. Giamello, "Characterization of paramagnetic species in N-doped TiO_2 powders by EPR spectroscopy and DFT calculations," *Journal of Physical Chemistry B*, vol. 109, no. 23, pp. 11414-11419, 2005.
- [38] J. Yu, Q. Xiang, and M. Zhou, "Preparation, characterization and visible-light-driven photocatalytic activity of Fe-doped titania nanorods and first-principles study for electronic structures," *Applied Catalysis B*, vol. 90, no. 3-4, pp. 595-602, 2009.
- [39] R. Asahi, T. Morikawa, T. Ohwaki, K. Aoki, and Y. Taga, "Visible-light photocatalysis in nitrogen-doped titanium oxides," *Science*, vol. 293, no. 5528, pp. 269-271, 2001.
- [40] T. Ihara, M. Miyoshi, Y. Iriyama, O. Matsumoto, and S. Sugihara, "Visible-light-active titanium oxide photocatalyst realized by an oxygen-deficient structure and by nitrogen doping," *Applied Catalysis B*, vol. 42, no. 4, pp. 403-409, 2003.
- [41] G. Liu, G. Y. Hua, X. Wang et al., "Visible light responsive nitrogen doped anatase TiO_2 sheets with dominant 001 facets derived from TiN ," *Journal of the American Chemical Society*, vol. 131, no. 36, pp. 12868-12869, 2009.
- [42] Q. Xiang, J. Yu, W. Wang, and M. Jaroniec, "Nitrogen self-doped nanosized TiO_2 sheets with exposed 001 facets for enhanced visible-light photocatalytic activity," *Chemical Communications*, vol. 47, no. 24, pp. 6906-6908, 2011.
- [43] Q. Xiang, J. Yu, and M. Jaroniec, "Nitrogen and sulfur co-doped TiO_2 nanosheets with exposed 001 facets: synthesis, characterization and visible-light photocatalytic activity," *Physical Chemistry Chemical Physics*, vol. 13, no. 11, pp. 4853-4861, 2011.
- [44] X. Chen and C. Burda, "The electronic origin of the visible-light absorption properties of C-, N- and S-doped TiO_2 nanomaterials," *Journal of the American Chemical Society*, vol. 130, no. 15, pp. 5018-5019, 2008.
- [45] S. Liu, J. Yu, and W. Wang, "Effects of annealing on the microstructures and photoactivity of fluorinated N-doped TiO_2 ," *Physical Chemistry Chemical Physics*, vol. 12, no. 38, pp. 12308-12315, 2010.